

DISS. ETH No. 22572

# **GAS-PARTICLE SUSPENSIONS AS HIGH-TEMPERATURE HEAT TRANSFER MEDIA FOR CONCENTRATED SOLAR POWER APPLICATIONS**

A thesis submitted to attain the degree of  
DOCTOR OF SCIENCES of ETH ZURICH  
(Dr. sc. ETH Zurich)

presented by

JAN MARTI

MSc ETH ME

born on 10.01.1987

citizen of Etziken (SO)

accepted on the recommendation of

Prof. Dr. Aldo Steinfeld, examiner

Dr. Andreas Z'Graggen, co-examiner

Dr. Andreas Haselbacher, co-examiner

2015



*In memory of Richi Marti (1947–2007)*





# Abstract

A major improvement of the solar-to-electricity efficiency of conventional concentrated solar power (CSP) plants requires an increase of the operating temperature to enable the use of a more efficient thermodynamic cycle. In addition, cost-effective thermal-energy storage systems are required to reduce the cost of dispatchable electricity generation by CSP plants. Finally, this enables the replacement of fossil-fired power plants. These requirements can be achieved by using a slowly upward-moving, dense gas-particle suspension as heat transfer medium (HTM) to absorb and store the solar energy. The gas-particle suspension is heated up by moving through directly irradiated riser tubes located in the solar receiver of a solar power tower. This dense gas-particle suspension behaves thereby like an upward-moving bubbling fluidized bed. By using a HTM based on heat-resistant particles with a high heat capacity like silicon carbide (SiC) particles, the operating temperature of the CSP plant can be increased to about 1000 °C. Additionally, the hot particles can directly be used as thermal-energy storage media.

To advance the development of this new HTM for CSP plants, this thesis investigates the detailed hydrodynamics and heat-transfer mechanisms in dense gas-particle suspensions. Therefore, a two-phase Euler-Euler model for dense gas-particle systems is built on the open-source code OpenFOAM. The model is capable of predicting the complex hydrodynamic behavior of bubble formation, coalescence, and breakup together with conduction, convection, and radiation heat transfer.

To accurately model the radiation heat transfer, an experimental-numerical approach is developed to determine the volume-averaged radiation properties: extinction coefficient, scattering albedo, and approximated scattering phase function of SiC particle suspensions with different solid fractions. A spectroscopic goniometry system is used to measure the angular intensity distribution around irradiated SiC particle suspensions. In a second step, this experimental intensity distribution is compared to the numerical intensity distribution of a Monte Carlo ray-tracing model matching the experimental setup and representing the particle suspension by a participating medium. The radiation properties of the participating medium are adjusted in a fitting routine until the resulting numerical intensity distribution is in good agreement with the experimental distribution. This procedure is done for different suspension thicknesses with different solid fractions. In this way, the resulting set of radiation properties can directly be applied to solve the radiation transfer equation in gas-particle systems with changing solid fractions using existing popular methods like the spherical harmonics, discrete ordinate, or statistical Monte Carlo methods.

At each time step, the two-phase model calculates the effective radiation properties as a function of the local solid fraction based on the determined radiation properties of the SiC particle suspensions. Therefore, the model captures radiation penetrating through gas bubbles near the riser wall and radiation being absorbed within a few millimeters by the dense gas-particle suspension.

In addition to separate verification and validation studies of hydrodynamics and heat transfer, comparisons with on-sun experimental results indicate that the model accurately predicts coupled hydrodynamics and heat transfer in dense gas-particle systems.

In a parameter study, the model is used to investigate the influence of the riser-wall temperature and riser diameter on the heat-transfer coefficient, solid temperature, solid mass flow rate, and solid fraction. Increasing the riser-wall temperature leads for a constant mass flow rate to a decrease of the heat-transfer coefficient as the logarithmic mean temperature difference

---

over the irradiated riser section strongly increases. An increase of the riser diameter from 36 mm to 72 mm leads for a constant gas inlet velocity and riser-wall temperature to a solid temperature reduction of about 30 %.

A detailed investigation of the involved heat-transfer mechanisms shows that the majority of the heat transfer takes place within a distance of a few particle diameters from the heated riser wall. In this region, the particles are heated by solid conduction and heat is then transferred by solid convection to the colder flow in the center of the riser. Even at a riser-wall temperature of 1281 K, radiation heat transfer is found to be a minor contribution to the overall heat transfer in the solid phase. This results from a reduced temperature difference between the wall and the adjacent solid phase together with a high extinction coefficient that prevents radiation heat transfer between solid regions farther apart. It is shown that with a moderate riser wall temperature of 581 K and a particle diameter of 64  $\mu\text{m}$ , solid conduction accounts for about 97 % of the wall-to-suspension heat flux. Increasing the wall temperature to 981 K together with a particle diameter of 400  $\mu\text{m}$  leads to an increase of the radiation heat-flux contribution up to about 10 % of the total wall-to-suspension heat flux.

A comparison of sequential snapshots of the solid-fraction, solid-temperature, and solid-velocity field show the complex interplay between the wall heat flux and the examined solid and gas-phase property fields. The path of the rising bubbles has thereby an essential influence on the local wall heat flux by inducing a replacement of heated solid regions at the wall with colder ones from the center of the riser.



# Zusammenfassung

Um eine deutliche Effizienzsteigerung der Stromproduktion von Sonnenwärmekraftwerke zu erreichen, muss die Betriebstemperatur erhöht werden. Diese Temperaturerhöhung ermöglicht die Verwendung eines effizienteren thermodynamischen Kreisprozesses zur Umwandlung von Wärme in Arbeit und letztendlich in Elektrizität. Zusätzlich werden kosteneffiziente Systeme zur Wärmespeicherung benötigt, damit die Kosten der kontinuierlichen Stromerzeugung durch Sonnenwärmekraftwerke reduziert werden können. Die dadurch gewonnene Kostenreduktion ermöglicht die mit fossilen Energieträgern betriebenen Elektrizitätswerke durch Sonnenwärmekraftwerke zu ersetzen. Die dafür notwendigen Anforderungen können mittels Verwendung eines neuartigen Wärmeübertragungsmediums erreicht werden, das aus einer dichten Suspension von Gas und Partikeln besteht, welche die Sonnenenergie absorbieren und speichern. Die Gas-Partikel-Suspension verhält sich wie eine aufwärts bewegende, blasenbildende Wirbelschicht, die beim Durchströmen von direkt bestrahlten Steigrohren aufgeheizt wird. Die Steigrohre befinden sich im zentralen Absorber zuoberst auf einem Solarturm. Durch die Verwendung eines Wärmeübertragungsmediums, basierend auf hitzebeständigen Partikeln, wie Siliziumkarbid-Partikeln, kann die Betriebstemperatur bis auf etwa 1000 °C erhöht werden. Zusätzlich können die heißen Partikel dank der hohen Wärmekapazität von Siliziumkarbid direkt als WärmespeichermEDIUM verwendet werden.

Um die Entwicklung dieses neuartigen Wärmeübertragungsmediums für Sonnenwärmekraftwerke voranzutreiben untersucht diese Doktorarbeit die

detaillierten Mechanismen der Hydrodynamik und der Wärmeübertragung in dichten Gas-Partikel-Suspensionen. Dafür wurde mit Hilfe des Softwarepaketes OpenFOAM ein Zweiphasen-Euler-Euler-Modell für dichte Gas-Partikel-Systeme erstellt. Das Modell ist in der Lage, die komplexen hydrodynamischen Verhaltensweisen von Blasenbildung, Blasenkoaleszenz und Blasenzerfall zusammen mit dem Wärmetransport durch Konduktion, Konvektion und Strahlung zu berechnen.

Die genaue Modellierung des Wärmetransportes durch Strahlung erfordert die Bestimmung der volumengemittelten Strahlungseigenschaften ‘Extinktionskoeffizient’, ‘Albedo’ und approximierte ‘Streuungsfunktion’. Diese Strahlungseigenschaften werden durch eine experimentell-numerische Methode als Funktion des Feststoffanteils der Siliziumkarbid-Partikel bestimmt. In einem ersten Schritt wird ein goniometrischer Messaufbau verwendet, mit dem die winkelabhängige Strahlungsintensität von bestrahlten Siliziumkarbid-Partikel-Suspensionen gemessen wird. In einem zweiten Schritt wird die gemessene mit der numerischen Intensitätsverteilung eines Monte Carlo Modells zur Strahlenverfolgung verglichen. Das Monte Carlo Modell stimmt mit dem Messaufbau überein. Die Partikel-Suspension wird durch ein sogenanntes teilnehmendes Medium repräsentiert. Die Strahlungseigenschaften des teilnehmenden Mediums werden angepasst, bis die numerische mit der experimentellen Intensitätsverteilung in adäquater Übereinstimmung ist. Diese Vorgehensweise wird für verschiedene Schichtdicken und Feststoffanteile der Suspension durchgeführt. Die daraus resultierenden Strahlungseigenschaften können direkt für die Lösung der Strahlungstransportgleichung in Gas-Partikel-Systemen genutzt werden.

Das entwickelte Zweiphasenmodell berechnet für jeden Zeitschritt, in Abhängigkeit vom lokalen Feststoffanteil, die effektiven Strahlungseigenschaften, basierend auf den zuvor bestimmten Strahlungseigenschaften der Siliziumkarbid-Partikel-Suspensionen. Somit erfasst das Modell entweder den Strahlungsdurchgang durch die Gasblasen, die sich an der Wand des Steigrohres befinden oder es erfasst die Strahlungsabsorption durch die dichte Gas-Partikel-Suspension.

Zusätzlich zu Verifizierungs- und Validierungsstudien zeigen Vergleiche mit experimentellen Resultaten, dass das Modell die Hydrodynamik und den Wärmetransport in dichten Gas-Partikel-Systemen genau berechnen kann. In einer Parameterstudie wird dieses Modell verwendet, um den Einfluss der Wandtemperatur und den Durchmesser des Steigrohres auf den Wärmeübergangskoeffizienten, die Temperatur der Festphase, den Massendurchfluss der Festphase und den Feststoffanteil zu untersuchen. Dabei führt die Erhöhung der Wandtemperatur bei konstantem Massendurchfluss zu einem Rückgang des Wärmeübergangskoeffizienten, da die mittlere Temperaturdifferenz über den erhitzten Abschnitt des Steigrohres sich stark erhöht. Die Vergrößerung des Steigrohrdurchmessers von 36 mm auf 72 mm führt bei einer gleichbleibenden Wandtemperatur und konstanten Strömungsgeschwindigkeiten zu einer Temperaturreduktion der Festphase um etwa 30 %.

Eine detaillierte Untersuchung der involvierten Wärmetransportmechanismen zeigt, dass der wesentliche Wärmetransport in einem Bereich von ein paar Partikeldurchmessern von der heissen Steigrohrwand stattfindet. Dort werden die Partikel hauptsächlich durch Konduktion aufgeheizt. Die Wärme wird durch Konvektion der Festphase zur kühleren Strömung in der Mitte des Steigrohres transportiert. Der Wärmetransport durch Strahlung ist, auch bei einer Wandtemperatur von 1281 K, von geringer Bedeutung. Die reduzierte Temperaturdifferenz zwischen der Steigrohrwand und der angrenzenden Festphase, in Kombination mit einem hohen Extinktionskoeffizienten, verhindert einen Strahlungsaustausch zwischen entfernteren Regionen. Bei moderaten Wandtemperaturen von 581 K und Partikeldurchmessern von  $64\text{ }\mu\text{m}$  macht die Wärmeleitung durch die Festphase rund 97 % des totalen Wärmestroms der Steigrohrwand zur Suspension aus. Eine Erhöhung der Wandtemperatur auf 981 K in Kombination mit Partikeldurchmessern von  $400\text{ }\mu\text{m}$ , führt zu einer Erhöhung des Wärmestroms durch Strahlung bis zu 10 % des totalen Wärmestroms.

Ein Vergleich zwischen aufeinander folgenden Momentaufnahmen der Verteilung des Feststoffanteils, der Feststofftemperatur und der Feststoffgeschwindigkeit im Steigrohr legt die komplexen Wechselwirkungen zwischen

den untersuchten Feststoffeigenschaften und dem Wandwärmestrom offen. Der Weg der aufsteigenden Gasblasen hat einen wesentlichen Einfluss auf den lokalen Wandwärmestrom. Die aufsteigenden Gasblasen erzeugen einen Austausch von heissen Feststoffregionen in Wandnähe mit kühleren Feststoffregionen aus der Mitte des Steigrohres.



# Acknowledgements

First of all, I would like to thank Prof. Dr. Aldo Steinfeld for giving me the opportunity to perform my doctoral thesis under his supervision and providing an exceptional research environment at the Professorship of Renewable Energy Carriers (PREC) at ETH Zurich. His support and confidence in my work were essential for this thesis.

I am very grateful to Dr. Andreas Z'Graggen for reviewing the manuscript of this thesis and acting as co-examiner.

Special thanks go to Dr. Andreas Haselbacher for his guidance, countless fruitful discussions, and for being co-examiner. His support and expertise were extremely important for the success of this work.

I thank Dr. Matthew Roesle for his support and motivation during the first one and a half years of my doctoral studies and Dr. Zoran Jovanovic for the discussions about fluidized beds.

Thanks go to all the partners of the CSP2 project for their collaboration and especially to Hadrien Benoit for providing experimental data.

I thank my present and former colleagues of the PREC group. Special thanks go to my office mates Emilie Zermatten and Simon Ackermann for helpful discussions and the pleasant working atmosphere in our office.

I acknowledge the work done by Francesco Andreoli, performing his Master thesis, Raghav Khanna and Vikas Patil, performing their Semester projects, and Maximilian Taillandier, performing his Bachelor thesis under my supervision.

I gratefully acknowledge the financial support of the European Commis-

sion (FP7, Project N° 282932).

Finally, I would like to thank my family and closest friends, Rita, Nora, Anaïs, Loek, Carol, Cedric, Manuel, Milena, Ömer, Timo, and Yael, for their support and encouragement.

# Contents

|  |           |
|--|-----------|
| <b>Abstract</b>  | <b>i</b>  |
| <b>Zusammenfassung</b>   | <b>v</b>  |
| <b>Acknowledgements</b>  | <b>ix</b> |
| <b>Nomenclature</b>  | <b>xx</b> |
| <b>1 Introduction</b>  | <b>1</b>  |
| 1.1 Motivation for high-temperature concentrated solar power . .                       | 1         |
| 1.2 Motivation for dense gas-particle suspensions as heat transfer<br>medium . . . . . | 2         |
| 1.3 Detailed model of hydrodynamics and heat transfer . . . . .                        | 6         |
| 1.4 Thesis goals and outline . . . . .   | 9         |
| <b>I Determination of radiation properties</b>   | <b>13</b> |
| <b>2 Theory and background</b>   | <b>15</b> |
| 2.1 Fundamentals of radiation transfer . . . . .                                       | 15        |
| 2.2 Radiation transfer equation in participating media . . . . .                       | 16        |
| 2.3 Radiation properties of particle clouds . . . . .                                  | 19        |
| 2.3.1 Independent scattering . . . . .   | 19        |
| 2.3.2 Dependent scattering . . . . .   | 22        |

|           |  |           |
|-----------|--|-----------|
| <b>3</b>  | <b>Experimental method and numerical model</b> | <b>25</b> |
| 3.1       | Particle characterization . . . . .            | 25        |
| 3.2       | Sample preparation . . . . .                   | 26        |
| 3.3       | Experimental setup . . . . .                   | 32        |
| 3.4       | Modeling approach . . . . .                    | 36        |
| 3.4.1     | Monte Carlo model . . . . .                    | 36        |
| 3.4.2     | Numerical fitting procedure . . . . .          | 39        |
| <b>4</b>  | <b>Results</b>                                 | <b>41</b> |
| 4.1       | Validation study . . . . .                     | 41        |
| 4.2       | Spectral dependence . . . . .                  | 45        |
| 4.3       | Extinction coefficient . . . . .               | 47        |
| 4.4       | Experimental-numerical approach . . . . .      | 53        |
| 4.4.1     | Measurements . . . . .                         | 53        |
| 4.4.2     | Simulations . . . . .                          | 54        |
| 4.5       | Conclusion . . . . .                           | 71        |
| <b>II</b> | <b>Model of dense gas-particle suspensions</b> | <b>73</b> |
| <b>5</b>  | <b>Model and numerical methods</b>             | <b>75</b> |
| 5.1       | Conservation equations . . . . .               | 76        |
| 5.1.1     | Mass conservation . . . . .                    | 76        |
| 5.1.2     | Momentum conservation . . . . .                | 78        |
| 5.1.3     | Energy conservation . . . . .                  | 79        |
| 5.2       | Closure relations for hydrodynamics . . . . .  | 81        |
| 5.2.1     | Solid-phase stress . . . . .                   | 81        |
| 5.2.2     | Interphase drag . . . . .                      | 84        |
| 5.3       | Closure relations for heat transfer . . . . .  | 85        |
| 5.3.1     | Radiation model . . . . .                      | 85        |
| 5.3.2     | Effective conductivity . . . . .               | 86        |
| 5.3.3     | Interphase heat transfer . . . . .             | 87        |
| 5.4       | Solution procedure . . . . .                   | 88        |

---

|          |  |            |
|----------|--|------------|
| 5.5      | Time and space average . . . . .                           | 90         |
| <b>6</b> | <b>Model verification and validation</b>                   | <b>93</b>  |
| 6.1      | Hydrodynamics . . . . .                                    | 94         |
| 6.1.1    | Single-phase flow verification . . . . .                   | 94         |
| 6.1.2    | Bubbling fluidized bed validation . . . . .                | 94         |
| 6.2      | Heat transfer . . . . .                                    | 115        |
| 6.2.1    | Transient convective heat-transfer verification . . . . .  | 115        |
| 6.2.2    | Radiation heat-transfer verification . . . . .             | 116        |
| 6.2.3    | Steady-state conduction and radiation validation . . . . . | 118        |
| 6.3      | Conclusion . . . . .                                       | 122        |
| <b>7</b> | <b>Results</b>   | <b>123</b> |
| 7.1      | Simulation of CSP plant . . . . .                          | 123        |
| 7.1.1    | Grid-refinement and averaging study . . . . .              | 126        |
| 7.1.2    | Comparison with experimental results . . . . .             | 149        |
| 7.2      | Parameter study . . . . .                                  | 158        |
| 7.2.1    | Influence of riser-wall temperature . . . . .              | 158        |
| 7.2.2    | Influence of riser diameter . . . . .                      | 161        |
| 7.3      | Time-averaged heat-transfer mechanisms . . . . .           | 163        |
| 7.3.1    | Temperature distribution in the solid phase . . . . .      | 163        |
| 7.3.2    | Heat-transfer contributions in the solid phase . . . . .   | 166        |
| 7.3.3    | Local wall-to-suspension heat flux . . . . .               | 175        |
| 7.4      | Instantaneous heat-transfer mechanisms . . . . .           | 176        |
| 7.5      | Conclusion . . . . .                                       | 184        |
| <b>8</b> | <b>Summary and outlook</b>                                 | <b>187</b> |
| 8.1      | Summary . . . . .  | 187        |
| 8.1.1    | Determination of radiation properties . . . . .            | 188        |
| 8.1.2    | Model of dense gas-particle suspensions . . . . .          | 189        |
| 8.2      | Outlook . . . . .  | 192        |
| 8.2.1    | Determination of radiation properties . . . . .            | 192        |
| 8.2.2    | Model of dense gas-particle suspensions . . . . .          | 193        |

|                             |            |
|-----------------------------|------------|
| <b>List of figures</b>      | <b>208</b> |
| <b>List of tables</b>       | <b>210</b> |
| <b>References</b>           | <b>227</b> |
| <b>List of publications</b> | <b>229</b> |

# Nomenclature

## Abbreviations

|        |   |
|--------|---|
| CFD    | Computational fluid dynamics                              |
| CSP    | Concentrated solar power                                  |
| DHG    | Double Henyey-Greenstein                                  |
| HG     | Henyey-Greenstein   |
| HTM    | Heat transfer medium                                      |
| LMTD   | Logarithmic mean temperature difference                   |
| MULES  | Multidimensional universal limiter with explicit solution |
| PISO   | Pressure-implicit split-operator                          |
| RMSE   | Root mean square error                                    |
| SEM    | Scanning electron microscope                              |
| SIMPLE | Semi-implicit method for pressure-linked equations        |

## Greek characters

|            |  |                                |
|------------|--|--------------------------------|
| $\alpha$   | Phase fraction                             | —                              |
| $\beta$    | Extinction coefficient                     | $\text{m}^{-1}$                |
| $\chi$     | Effective conductivity parameter           | —                              |
| $\Delta$   | Difference                                 | —                              |
| $\delta$   | Forward scattering fraction                | —                              |
| $\epsilon$ | Emissivity                                 | —                              |
| $\Gamma$   | Generic diffusion coefficient              | $\text{m}^2/\text{s}$          |
| $\gamma$   | Particle collision dissipation coefficient | $\text{kg}/\text{m}^3\text{s}$ |
| $\gamma$   | Scaling factor                             | —                              |

|                              |                              |                           |
|------------------------------|------------------------------|---------------------------|
| $\kappa$                     | Absorption coefficient       | $\text{m}^{-1}$           |
| $\mu$                        | Dynamic viscosity            | $\text{kg/s m}$           |
| $\nabla$                     | Nabla operator               | $\text{m}^{-1}$           |
| $\nu$                        | Kinematic viscosity          | $\text{m}^2/\text{s}$     |
| $\Omega$                     | Solid angle                  | $\text{sr}$               |
| $\omega$                     | Scattering albedo            | —                         |
| $\overline{\overline{\tau}}$ | Viscous stress tensor        | $\text{Pa}$               |
| $\Phi$                       | Scattering phase function    | $\text{sr}^{-1}$          |
| $\phi$                       | Generic scalar               | —                         |
| $\psi$                       | Particle shape factor        | —                         |
| $\rho$                       | Density                      | $\text{kg/m}^3$           |
| $\sigma$                     | Stefan-Boltzmann constant    | $\text{W/m}^2 \text{K}^4$ |
| $\sigma_s$                   | Scattering coefficient       | $\text{m}^{-1}$           |
| $\tau$                       | Optical thickness            | —                         |
| $\Theta$                     | Granular temperature         | $\text{m}^2/\text{s}^2$   |
| $\theta_s$                   | Scattering angle             | $^\circ$                  |
| $\xi$                        | Gas- or solid-phase quantity |                           |

### Latin characters

|                                    |   |                |
|------------------------------------|---|----------------|
| $\overline{\overline{\mathbf{I}}}$ | Identity tensor                           | —              |
| $\mathbf{g}$                       | Gravitational acceleration vector         | $\text{m/s}^2$ |
| $\mathbf{n}$                       | Unit normal vector                        | —              |
| $\mathbf{q}$                       | Heat flux vector                          | $\text{W/m}^2$ |
| $\mathbf{r}$                       | Position vector                           | $\text{m}$     |
| $\mathbf{s}$                       | Unit vector                               | —              |
| $\mathbf{U}$                       | Interstitial velocity vector              | $\text{m/s}$   |
| $\mathbf{V}$                       | Generic vector                            |                |
| $A$                                | Area                                      | $\text{m}^2$   |
| $a, b$                             | Coefficients                              | —              |
| $A_1$                              | Linear-anisotropic scattering coefficient | —              |
| $B$                                | Bias limit                                | —              |
| $C$                                | Cross section                             | $\text{m}^2$   |
| $C$                                | Heat capacity rate                        | $\text{J/K s}$ |



|                  |                                       |  |
|------------------|---------------------------------------|--|
| $C_D$            | Dimensionless drag coefficient        | –                                      |
| $c_p$            | Specific heat capacity                | J/kg K                                 |
| $d$              | Diameter                              | m                                      |
| $E$              | Incoming irradiation                  | W/m <sup>2</sup>                       |
| $E$              | Total energy                          | J/kg                                   |
| $e$              | Specific internal energy              | J/kg <sup>3</sup>                      |
| $e_r$            | Restitution coefficient               | –                                      |
| $f$              | Frequency                             | s <sup>–1</sup>                        |
| $G$              | Incident radiation                    | W/m <sup>2</sup>                       |
| $g$              | Asymmetry factor                      | –                                      |
| $H$              | Height                                | m                                      |
| $h$              | Heat-transfer coefficient             | W/m <sup>2</sup> K, W/m <sup>3</sup> K |
| $I$              | Radiation intensity                   | W/m <sup>2</sup> sr                    |
| $J_1$            | Granular temperature dissipation term | kg/m <sup>3</sup> s                    |
| $J_2$            | Granular temperature source term      | kg/m s <sup>3</sup>                    |
| $k$              | Heat conductivity                     | W/m K                                  |
| $k_\Theta$       | Granular temperature conductivity     | kg/s m                                 |
| $K_D$            | Interphase drag coefficient           | kg/m <sup>3</sup> s                    |
| $L$              | Length                                | m                                      |
| $m$              | Mass                                  | kg                                     |
| $n$              | Refractive index                      | –                                      |
| $N_i$            | Number of cells                       | –                                      |
| $N_t$            | Number of time steps                  | –                                      |
| $P$              | Precision limit                       | –                                      |
| $P$              | Pressure coefficient                  | kg/m <sup>3</sup>                      |
| $p$              | Pressure                              | Pa                                     |
| $Q$              | Power                                 | W                                      |
| $q$              | Heat flux                             | W/m <sup>2</sup>                       |
| $Q_0$            | Cumulative distribution               | –                                      |
| $q_0$            | Density distribution                  | –                                      |
| $Q_{\text{ext}}$ | Extinction efficiency factor          | –                                      |
| $q_v$            | Volumetric flux                       | m <sup>3</sup> /m <sup>2</sup> s       |

---

|       |                                 |                  |
|-------|---------------------------------|------------------|
| $R$   | Random number                   | —                |
| $S$   | Energy source term              | W/m <sup>3</sup> |
| $s$   | Geometric path length           | m                |
| $T$   | Temperature                     | K                |
| $T$   | Transmittance                   | —                |
| $t$   | Time                            | s                |
| $U$   | Uncertainty                     | —                |
| $V$   | Detector signal                 | V                |
| $v_r$ | Dimensionless terminal velocity | —                |
| $x$   | Radial coordinate               | m                |
| $x$   | Size parameter                  | —                |
| $y$   | Axial coordinate                | m                |
| Nu    | Nusselt number                  | —                |
| Pr    | Prandtl number                  | —                |
| Re    | Reynolds number                 | —                |

### Subscripts

|           |                      |
|-----------|----------------------|
| $\lambda$ | Spectral             |
| $\Theta$  | Granular temperature |
| $b$       | Backward             |
| $E$       | Epoxy                |
| $f$       | Forward              |
| $G$       | Glass                |
| $g$       | Gas phase            |
| $i$       | Cell number          |
| $i$       | Incoming direction   |
| $L$       | Lens                 |
| $p$       | Particle             |
| $r$       | Relative             |
| $s$       | Solid phase          |
| $t$       | Time step            |
| $w$       | Wall                 |
| 0         | Initial              |

---

|       |   |
|-------|---|
| aer   | Aeration                                |
| atm   | Atmosphere                              |
| ave   | Averaging                               |
| bed   | Bed                                     |
| bulk  | Bulk                                    |
| cold  | Cold surface                            |
| comp  | Computational                           |
| cond  | Conduction                              |
| conv  | Conduction                              |
| diff  | Diffuse                                 |
| dom   | Domain                                  |
| eff   | Effective                               |
| el    | Electrical                              |
| end   | End                                     |
| hot   | Hot surface                             |
| in    | Inlet                                   |
| ind   | Independent                             |
| int   | Internal energy                         |
| intf  | Interfacial                             |
| iso   | Isotropic                               |
| kin   | Kinetic energy                          |
| leak  | Leakage                                 |
| LMTD  | Logarithmic mean temperature difference |
| max   | Maximum                                 |
| mean  | Mean                                    |
| norm  | Normalized                              |
| out   | Outlet                                  |
| pres  | Pressure                                |
| rad   | Radiation                               |
| riser | Riser                                   |
| sg    | Solid-gas interphase                    |
| start | Start                                   |

|     |            |
|-----|------------|
| sus | Suspension |
| th  | Thermal    |
| tot | Total      |

**Superscripts**

|     |                 |
|-----|-----------------|
| ''' | Per volume      |
| -   | Time average    |
| ·   | Flow rate       |
| ^   | Spatial average |

# Chapter 1

## Introduction

### 1.1 Motivation for high-temperature CSP

To overcome the negative environmental impact of electricity generation by conventional fossil-fired power plants, their electricity generation capacity must be replaced with renewable and carbon-neutral technologies. A promising renewable and carbon-neutral energy technology is concentrated solar power (CSP). To become cost competitive, the solar-to-electricity efficiency of CSP plants must increase. A major improvement of this efficiency requires an increase of the working-fluid temperature to use more efficient thermodynamic cycles. A thermodynamic cycle is used to convert heat into mechanical work. CSP plants are typically based on subcritical Rankine cycles with a working-fluid temperature below 500 °C and a thermal-to-electricity efficiency in the range of 30–40 % [1]. An increase of the working fluid temperature above 600 °C enables the use of supercritical or even ultra-supercritical Rankine cycles. As a consequence, the thermal-to-electricity efficiency increases about 10 % compared to a subcritical Rankine cycle [2, 3]. Furthermore, to allow cost-effective and round-the-clock dispatchable electricity generation using CSP, such plants must incorporate thermal-energy storage systems. Several types of storage systems have been developed, but

their widespread adoption is at present limited by high costs [2].

For large-scale high-temperature CSP plants, solar power towers are particularly suitable due to their maturity, high solar concentration ratio, and a favorable design for thermal-energy storage [4]. A solar power tower contains a receiver unit into which sun-tracking heliostats reflect the incident sunlight. Inside the receiver unit, the solar energy heats either a working fluid (e.g., steam) or a heat transfer medium (HTM). The working fluid can be used directly in a thermodynamic cycle whereas the HTM acts as intermediate storage of thermal energy in an indirect cycle. After passing the receiver unit, the HTM can be either stored for later use or routed through a heat exchanger. In the later case, the thermal energy of the HTM is transferred to a working fluid that is subsequently used in a thermodynamic cycle to generate electricity [5, 6]. Existing CSP plants based on solar power towers typically use either molten nitrate salt as HTM in an indirect cycle or water/steam as a working fluid in a direct cycle [7]. Figure 1.1 shows a photograph of a commercial solar power tower CSP plant using molten nitrate salt as HTM constructed in Spain by Torresol Energy. The power plant has 2650 heliostats, each with a mirror surface area of  $120\text{ m}^2$ , surrounding the 140 m high central tower. The power plant has an electrical power output of  $20 \times 10^6\text{ W}$  at peak periods [8, 9].

## 1.2 Motivation for dense gas-particle suspensions as HTM

At temperatures above  $600^\circ\text{C}$ , nitrate salts become unstable and decompose [10] and direct steam production is impractical for thermal-energy storage due to very high pressures at critical conditions and low volumetric heat capacities [11]. Therefore, highly-efficient CSP plants require alternative HTM that are better suited to operation at high temperatures. This has motivated the investigation of liquid metals as high-temperature HTM [12]. However, the use of liquid metals entails substantial safety risks due to their

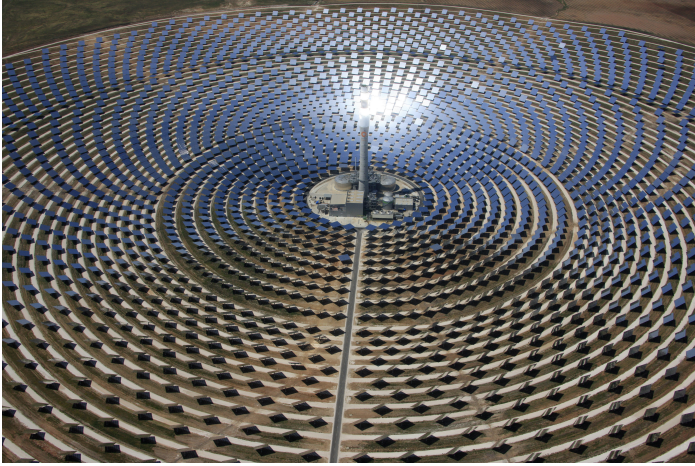


Figure 1.1: Aerial view of Gemasolar, a  $20\text{ MW}_{\text{el}}$  solar power tower CSP plant using molten nitrate salt as HTM. The plant was constructed and is operated by Torresol Energy [9].

reactivity with oxygen and, similar to molten nitrate salts, the problem of solidification at low temperatures [1]. The development of a HTM for CSP at high temperatures is therefore still an open problem.

The above-mentioned problems can be avoided by using particles to absorb and store the solar energy. The potential of dilute gas-particle suspensions with submicron particles as working fluid for solar applications without intermediate storage was studied independently by [13, 14] and [15] in the late 1970s. The use of particles as an intermediate HTM was first mentioned in the early 1980s, where in an experimental study particles were fluidized in a directly irradiated tube. The radiation was absorbed by the tube and the particles inside were heated up by the hot tube wall [16]. At the same time, a different study investigated the application of a freely falling, directly irradiated curtain of particles to store the solar energy [17, 18]. Due to their stability at temperatures up to  $1000^\circ\text{C}$ , particles made of alumina, silica, silicon carbide (SiC), or zircon, are especially at-

tractive for high-temperature CSP plants [19]. Because typical specific heat capacities of these materials are comparable to molten nitrate salts, particles are suitable as thermal-energy storage media [20, 12]. Particles made of SiC are of particular interest because they are inexpensive and widely available [6]. The price of SiC particles depends significantly on the supplier, the purchase quantity, and the material grade. In large quantities, Wuxi Wanli Hongji Ltd. offers SiC particles in the price range 0.4–0.8 \$/kg. This is slightly lower than commercial available molten nitrate salts with a price range of 0.5–1.2 \$/kg [21].

A recent experimental on-sun study demonstrated a new CSP concept based on dense gas-particle suspensions of air and SiC particles to store and transport thermal energy [6]. Figure 1.2 shows a schematic of the concept using a slowly upward-moving, dense gas-particle suspension as HTM. This dense gas-particle suspension behaves like an upward-moving bubbling fluidized bed. Directly irradiated riser tubes heat up the particles by combined conduction, convection, and radiation. After passing through the riser tubes, the hot particles are transferred to a high-temperature storage tank that in turn feeds a heat exchanger in which the thermal energy is transmitted to a working fluid. The cooled particles are transferred to a low-temperature storage tank that supplies the solar receiver and closes the continuous particle circulation. The SiC particles had a mean diameter in the range 50–150  $\mu\text{m}$ , a density of 3210  $\text{kg}/\text{m}^3$ , and a fluidization velocity of a few  $\text{cm}/\text{s}$  when using air as the fluidization medium. They are classified as Geldart Group A–B particles that can therefore be fluidized easily [22]. The solid volume fraction in the riser tubes is approximately 0.3–0.4, indicating that the fluidization medium has only a minor impact on the overall heat transport. With thermal-energy storage, the CSP plant can produce electricity at night and on overcast weather. The thermal efficiency of the riser-tubes solar receiver of such a CSP plant operating with a dense gas-particle suspension was predicted to reach about 80 % [23]. Compared to a CSP plant operating with molten nitrate salt, the parasitic power consumption of a CSP plant using a dense gas-particle suspension is lower. The



molten-salt circuit of the power plant shown in Figure 1.1 has a parasitic power consumption of about 0.8 % of the thermal input power [24]. This is in a relative perspective approximately four times more than the estimated parasitic power consumption for the particle transportation of a 10 MW<sub>th</sub> solar power tower operated with a dense gas-particle suspension as HTM [23]. An economic analysis of large-scale CSP plants using this technology estimated an electricity cost reduction of over 10 % compared to conventional molten-salt CSP plants [25]. The proposed system can be adapted to different working fluids like water/steam to power a steam turbine, air in combination with a gas turbine, or both in a combined cycle.

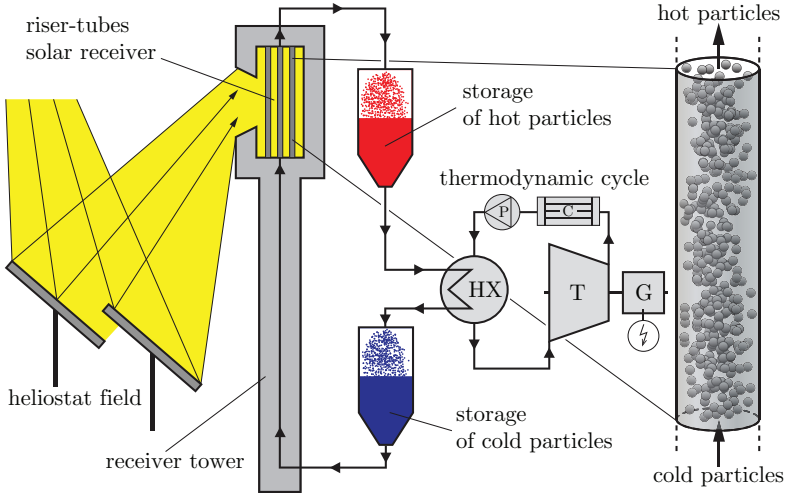


Figure 1.2: Schematic of a CSP plant using a dense gas-particle suspension as HTM with a storage of hot and cold particles and a generic thermodynamic cycle (HX: heat exchanger, T: turbine, C: condenser, P: pump, G: generator).

The above-mentioned experimental study of the new CSP concept [6] focused on the measurement of the wall-to-bed heat-transfer coefficient because it has a substantial influence on the overall plant efficiency. Due to the difficulties in measuring particle-temperature distributions and time-

dependent solid flow rates without interfering with the gas-particle flow field, only general trends of the wall-to-bed heat-transfer coefficient were determined. To assess this new CSP concept in more detail, a better understanding of its hydrodynamics and heat-transfer behavior is required. Accurate simulations can provide this improved understanding.

## 1.3 Detailed model of hydrodynamics and heat transfer

Numerous publications deal with the modeling and prediction of the wall-to-bed heat-transfer in dense gas-particle systems like bubbling fluidized beds. Various mechanistic and empirical correlations for the wall-to-bed heat-transfer coefficient are available and reviewed by [26, 27, 28]. These models are generally restricted to a narrow range of fluidization velocities, particle sizes, and solid or gas temperatures. Their suitability for predicting the performance of this new CSP concept for a range of operating conditions and for optimization and scale-up studies is unknown. A more general and accurate model must be capable of resolving the dynamics of bubble formation, coalescence, and breakup together with conduction, convection, and radiation heat transfer in dense gas-particle systems. Such a model enables insights that cannot be gained experimentally and it can therefore contribute to evaluate the applicability of this new high-temperature HTM for CSP plants.

There are two basic classes of simulations for dense gas-particle suspensions: the Euler-Lagrange and the Euler-Euler approach. These two approaches differ only in their representation of the solid phase because both treat the fluid phase as continuum. The Euler-Lagrange approach treats all particles as discrete elements and uses the second law of Newton to track their motion and interaction. There are two subclasses of the Euler-Lagrange approach for dense gas-particle systems: the unresolved and the resolved discrete-particle approach. In the unresolved approach, the compu-

tational grid spacing of the fluid phase is bigger than the particle diameter and several particles can simultaneously be located within one computational grid cell. In the resolved approach, the grid spacing of the fluid phase is smaller than the particle diameter and the fluid flow around each particle is resolved [29, 30]. The Euler-Euler approach, on the other hand, uses a continuous solid phase in which the motion and collision of individual particles has been averaged out. Therefore, the gas and particle phase form two interpenetrating continua. Although the tracking of individual particles is in principle more accurate, it suffers from very high computational costs and is impractical for more than about  $10^6$  particles [31]. One riser tube in the new CSP concept contains roughly  $10^{10}$  particles at any instant. As a result, the model in this thesis is based on the Euler-Euler approach to reduce the computational cost.

Several previous numerical studies applied the Euler-Euler approach to investigate heat transfer in bubbling fluidized beds. The flow of a gas adjacent to a heated wall was used to investigate the influence of bubbles on the local and instantaneous [32, 33, 34], time-averaged [35], and periodic [36] wall-to-bed heat-transfer coefficients. Other numerical studies determined the heat transfer from one [37] or more [38, 39] immersed tubes to a bubbling fluidized bed. A comparison with experimental results showed that the measured heat-transfer coefficient was overpredicted. Possible reasons for this discrepancy are the method used to calculate the effective conductivity of the solid phase and experimental difficulties. An accurate prediction of the heat transfer in gas-particle systems requires an effective conductivity that accounts for solid-fraction variations [33]. There are several different studies using the Euler-Euler approach to investigate heat transfer in industrial applications like a heavy-oil riser [40], a fluidized-bed reactor for polymerization [41], or a fluidized-bed reactor for fast pyrolysis of biomass [42, 43]. The above-mentioned publications do not consider radiation heat transfer. This is justified with a wall and suspension temperature below approximately  $400^\circ\text{C}$  where radiation heat transfer is negligible [44, 45]. In high-temperature gas-particle systems, with operating temperatures above

600 °C, the radiation contribution to the total wall-to-bed heat transfer can exceed 20 % [46]. Therefore, in this new high-temperature CSP concept, radiation must be expected to have an important influence. There are only few Euler-Euler studies that include radiation heat transfer and they are typically for gas-particle suspensions with very low solid fractions [47, 48].

In this thesis, a detailed two-phase Euler-Euler model for dense gas-particle systems was developed, to investigate the heat transfer in slowly rising bubbling fluidized beds used as HTM for CSP plants. The model was built on the open-source code OpenFOAM 2.3.x [49] and includes conduction, convection, and radiation heat transfer.

An effective specification of radiation heat transfer in gas-particle systems requires accurate radiation properties of particle suspensions with different solid fractions. Based on empirical data, various studies have developed predictive correlations for radiation properties of mono- and poly-disperse particle suspensions [50, 51]. A different approach uses uniform participating media to describe the radiation behavior of complex gas-solid systems. For that purpose, correlations built on the independent scattering theory [52, 53] or Monte Carlo ray-tracing methods were implemented [54, 55]. In this thesis, a combined experimental-numerical approach was used to find the volume-averaged radiation properties: extinction coefficient, scattering albedo, and approximated scattering phase function of particle suspensions with different solid fractions. The experimental results were measured with a spectroscopic goniometry system that was previously used to find radiation properties of packed beds [55] and reticulated porous structures [56]. Samples of SiC particle suspensions with different solid fractions and sample thicknesses were examined and the intensity distribution around each sample was measured. The experimental results were used in a numerical fitting procedure to find the volume-averaged radiation properties of SiC particle suspensions as a function of the solid fraction. The fitting procedure used a Monte Carlo ray-tracing model that matches the experimental setup and represents the particle suspension with an idealized continuous participating medium. Two types of SiC particles with a different optical

appearance were analyzed and compared. The resulting radiation properties can improve the modeling of radiation heat transfer in gas-particle systems with changing solid fractions. Existing popular methods, like the spherical harmonics, discrete ordinate, or statistical Monte Carlo methods, can directly incorporate the determined radiation properties to solve the radiation transfer equation.

The detailed two-phase model calculates, based on the determined volume-averaged radiation properties of the SiC particle suspensions, the effective radiation properties at each time step depending on the solid volume fraction in each computational cell. Therefore, the model captures the penetration of radiation into the suspension through bubbles at the wall and the absorption or scattering of radiation close to the hot wall due to the high extinction coefficient of the dense suspension. By including radiation heat transfer, the present model can be applied to heat transfer in gas-particle systems with a wider range of wall and suspension temperatures than existing models. Furthermore, the present model can provide quantitative data on the relevant hydrodynamic and heat-transfer mechanisms at a level of detail that is beyond existing experimental techniques. Therefore, the model is well suited for the optimization and scale-up of this new high-temperature CSP concept.

## 1.4 Thesis goals and outline

This thesis is performed in the framework of the project ‘CSP2 — Concentrated Solar Power in Particles’, funded by the European Commission. The project involves collaborations with different partners with the objectives to develop and promote the technology for using a dense gas-particle suspension as new HTM for CSP plants. This includes the development of a detailed model of the hydrodynamics and heat transfer together with a simplified model describing basic heat and mass balances. Based on the review of prior work and to meet the project’s objectives, the goals of this thesis are to:

- Determine the volume-averaged radiation properties: extinction coefficient, scattering albedo, and approximated scattering phase function of SiC particle suspensions with different solid fractions.
- Develop a two-phase Euler-Euler model that is capable of capturing detailed hydrodynamic and heat-transfer mechanisms in dense gas-particle suspensions.
- Study the heat transfer in dense gas-particle systems to extract data for developing of heat-transfer correlations for CSP plants operating with a dense gas-particle suspension as HTM.
- Investigate the relative importance of convection, conduction, and radiation heat transfer from the wall to the suspension and within the fluidized solid phase.
- Examine the influence of local hydrodynamic mechanisms on the heat transfer.
- Provide input for a simplified model to further evaluate and scale up this technology.

This thesis is divided into two parts: Part I presents a combined experimental-numerical method to determine volume-averaged radiation properties of particle suspensions (Chapters 2–4) and Part II focuses on the detailed model of the hydrodynamics and heat transfer in dense gas-particle systems (Chapters 5–7).

In Part I, Chapter 2 gives an introduction into the theory of radiation heat transfer in participating media and discusses the background of radiation properties of particle clouds with focus on independent and dependent scattering. In Chapter 3, the developed experimental-numerical method to determine radiation properties of particle suspensions is explained. This includes a characterization of the used SiC particles, a description of the experimental setup, and an explanation of the Monte Carlo ray-tracing model. Chapter 4 presents the results of the applied experimental-numerical approach including a validation study to evaluate the accuracy of the approach and the complete set of volume-averaged radiation properties of SiC particle suspensions required by the detailed two-phase model of Part II.

---

In Part II, Chapter 5 describes the conservation equations, closure relations, and solution procedure of the two-phase model. Chapter 6 shows the verification and validation studies of the developed model where the hydrodynamics and heat transfer are examined separately. In Chapter 7, the numerical results of a modeled CSP plant are compared to measurements and the model is used for a parameter study as well as detailed investigations of the heat-transfer mechanisms. Finally, Chapter 8 gives an overall summery of this thesis and an outlook.





## Part I

# Determination of radiation properties



# Chapter 2

## Theory and background

### 2.1 Fundamentals of radiation transfer

When radiation travels through a medium, like gas, liquid, or solid, it can be transmitted, reflected, or absorbed. For radiation passing through a particle cloud, the direction of a photon, or an electromagnetic wave, can additionally change when interacting with particles. These interactions can be diffraction, refraction, or reflection. As a group they describe the scattering of radiation [57]. Diffraction is the contact-free redirection of an electromagnetic wave interacting with an obstacle that has a similar size than its wavelength. Refraction occurs when a photon penetrates a particle and the entry and exit direction differ. This is the case for semi-transparent particles with a different index of refraction than the surrounding medium [58]. Reflection describes the trajectory change of a photon that hits a particle surface and is thereby redirected. The travel direction of a photon after a scattering event is characterized by the scattering phase function  $\Phi$  that gives the probability that a photon incident from one direction will be directed into a specific other direction. The absorption and scattering of radiation traveling through a particle cloud leads to an exponential decay of the incident radiation. In the most basic case, this is described by the

transmittance  $T$  of a medium layer with thickness  $s$  given by

$$T = e^{-(\kappa + \sigma_s)s} = e^{-\beta s} \quad (2.1)$$

where  $\kappa$  is the absorption coefficient,  $\sigma_s$  is the scattering coefficient, and  $\beta = \kappa + \sigma_s$  is the extinction coefficient of this medium. The scattering ability of a particle cloud is defined as the ratio of the scattering coefficient and the extinction coefficient known as the scattering albedo  $\omega$  defined by

$$\omega = \frac{\sigma_s}{\kappa + \sigma_s} = \frac{\sigma_s}{\beta} \quad (2.2)$$

where  $\omega = 1$  indicates a purely scattering behavior without absorption and  $\omega = 0$  indicates no scattering while absorption can be present. If the considered particle cloud is at a temperature  $> 0$  K, the particles will also emit thermal radiation independent of the incident radiation. An emitting, absorbing, and scattering medium is known as a participating medium [59, 57].

## 2.2 Radiation transfer equation in participating media

A general expression of the radiation heat transfer in participating media requires the definition of the spectral radiative intensity  $I_\lambda$  describing the radiative energy flow per time, per solid angle, per unit area normal to the propagation direction, and per wavelength. The intensity distribution within a participating medium is determined with the radiation transfer equation (RTE) describing the conservation of the spectral radiation intensity in direction  $\mathbf{s}$  along the path  $s$  given by

$$\frac{dI_\lambda}{ds} = \kappa_\lambda I_{b,\lambda} - \kappa_\lambda I_\lambda - \sigma_{s,\lambda} I_\lambda + \frac{\sigma_{s,\lambda}}{4\pi} \int_0^{4\pi} I_\lambda(\mathbf{s}_i) \Phi_\lambda(\mathbf{s}_i, \mathbf{s}) d\Omega_i \quad (2.3)$$

where  $I_{b,\lambda}$  is the spectral radiative intensity of a black body and  $\Omega$  is the solid angle. The first term on the right-hand side of Eq. (2.3) accounts for

increasing the intensity by emission, the second and third terms accounts for decreasing the intensity due to absorption and scattering away from direction  $\mathbf{s}$ , and the fourth term accounts for an intensity increase due to in-scattering from direction  $\mathbf{s}_i$  into direction  $\mathbf{s}$  [57]. In the following, the subscript  $\lambda$ , indicating spectral dependency, will be omitted for brevity.

The investigation of radiation transfer in participating media includes two different tasks to consider:

- Determine the volumetric radiation properties of the participating media under consideration.
- Solve the integro-differential RTE given in Eq. (2.3).

There are two main approaches to solve the RTE in participating media. The first one is based on the classical continuum mechanics approach where the medium is treated as a continuous phase. Examples for this approach are the Rossland approximation, spherical harmonics, or discrete ordinates method. The second approach uses a discrete formulation of the RTE and applies ray tracing, like the Monte Carlo method, to find a solution of Eq. (2.3). Although these two methods are fundamentally different, both solution procedures require volumetric radiation properties [51, 57].

Several different approaches exist to find volumetric radiation properties of dispersed media like fluidized or packed beds. Two of the most common methods are listed here:

- Theoretical prediction based on the Maxwell equations describing the electromagnetic wave theory [60, 61]. Due to high computational costs, this method is in general only used for simple situations like an isolated sphere with a perfectly smooth surface. For this situation, Mie theory gives the exact solution [62]. Nevertheless, there are more advanced numerical methods that can be applied to solve the electromagnetic wave theory for non-spherical particles or even particle compounds [63].
- Monte Carlo ray tracing can be used to find radiation properties of structures where the interface of a dispersed medium is accurately known and can be described mathematically. Furthermore, the char-

acteristic length scale of the considered structure must be much larger than the radiation wavelength [64]. In combination with computed tomography scans, this method can be applied to find radiation properties of arbitrary and highly complex geometries [65, 66].

To use these radiation properties in a participating medium, a volume- or spatial-averaging procedure is required. For ray tracing based methods it is essential that the considered domain is bigger or equal to a representative elementary volume to avoid local effects influencing the volume-averaged properties of the complete structure [67, 65]. The theoretical predicted radiation effects are additive in the case of independent scattering and the radiation properties can be superimposed. An example is the application of radiation properties of a single sphere to find the volumetric radiation properties of a particle cloud consisting of a large number of identical spheres [57]. This procedure is not directly applicable for the condition of dependent scattering and can lead to large errors as explained in more detail in Section 2.3.2.

Even though the presented methods can be used for many applications, there are situations where they fail. For simple systems where a theoretical approach based on the electromagnetic wave theory is applicable, the complex index of refraction is required. This can be problematic for uncommon materials or materials with impurities leading to nonuniform material properties. The same issue has the ray-tracing approach. Furthermore, the geometric representation of the surface can be difficult or even impossible due to the lack of computed tomography scans or surface features that are smaller than the tomography resolution [68]. In such situations, it can be necessary to determine the radiation properties with an experimental approach. A summary of different experimental approaches is given in [69, 68, 57]. The standard experimental procedure at ambient conditions is to expose a sample with a radiation beam of known wavelength and measure the radiation distribution around the irradiated sample for defined angles with respect to the incoming direction. The measured signal corresponds to a sample-averaged value. In a second step, a numerical model, where

the sample is represented by a participating medium, is used to fit the radiation properties: extinction coefficient, scattering albedo, and scattering phase function. When the radiation distribution of the numerical model agrees with the experimentally determined distribution, the applied radiation properties of the participating medium can be assumed to represent the volume-averaged radiation properties of the respective sample.

## 2.3 Radiation properties of particle clouds

### 2.3.1 Independent scattering

Independent scattering describes the situation where the incident radiation interacts with particles in a particle cloud in the same manner as for a single particle. This implies that a single scattering event is not influenced by nearby particles. A common criterion for independent scattering is based on the ratio of the mean inter-particle distance  $c$  and the radiation wavelength  $\lambda$ . For a typical value of  $c/\lambda > 0.3$  independent scattering is assumed [70, 71]. A different characterization is based on the solid volume fraction  $\alpha_s$  where, in the geometric optics limit, independent scattering is present for  $\alpha_s < 0.065$  [52, 53]. By combining inter-particle distance to wavelength ratio and solid volume fraction, a different study showed that independent scattering can be assumed for  $\alpha_s < 0.006$  or  $c/\lambda > 0.5$  [72].

The scattering and absorption behavior of single particles depends on the particle size and the radiation wavelength described by the size parameter

$$x = \frac{\pi d_p}{\lambda} \quad (2.4)$$

Based on this size parameter, there are in general three different scattering regimes:

- Rayleigh theory,  $x \ll 1$ : Very small particles, like air molecules, scatter light proportional to  $1/\lambda^4$  [73].
- Lorenz-Mie theory,  $x \approx 1$ : Particles with a diameter in the range of the radiation wavelength require the solution of the electromagnetic

wave theory [62].

- Geometric optics,  $x \gg 1$ : Larger particles act like normal surfaces and radiation can be idealized with rays. In this regime Monte Carlo ray tracing is applicable [57].

Although the fundamental Lorenz-Mie theory can be used for all particles sizes, it is the most complex formulation and the computational time increases with an increasing size parameter. For very small and large particles it can therefore be preferable to use a simpler formulation like the Rayleigh theory or a geometric optics approach [59].

### Absorption and scattering coefficient

The scattering and absorption performance of a particle is usually expressed with a scattering  $C_{\text{sca}}$  and an absorption cross-section  $C_{\text{abs}}$ . For the independent scattering regime, the scattering and absorption coefficient of a uniform particle cloud is found by adding up the independent scattering or absorption cross-sections given by

$$\sigma_s = N_p''' C_{\text{sca}} \quad (2.5)$$

$$\kappa = N_p''' C_{\text{abs}} \quad (2.6)$$

where  $N_p'''$  is the number of particles per volume. The scattering and absorption cross-section depends on the projected surface area of the particle and an efficiency factor. The extinction coefficient is therefore expressed by

$$\beta = \sigma_s + \kappa = N_p''' (C_{\text{sca}} + C_{\text{abs}}) = \pi \frac{d_p^2}{4} N_p''' Q_{\text{ext}} \quad (2.7)$$

where  $Q_{\text{ext}}$  is the extinction efficiency factor. For large size parameters ( $x \gg 1$ ), like in the geometric optics limit, the extinction efficiency factor approaches  $Q_{\text{ext}} = 2$  [57]. Eq. (2.7) can be rewritten as a function of the solid volume fraction according to

$$\beta = \alpha_s \frac{3}{2d_p} Q_{\text{ext}} \quad (2.8)$$



## Scattering phase function

In the independent scattering regime, the scattering phase function of a monosized particle cloud is the same as for a single particle. The exact scattering phase function of a spherical particle depends on complex amplitude functions based on the complex index of refraction and the size parameter. A solution can be found by using for example a series of Legendre polynomials [74]. Monosized particle clouds show, as a result of diffraction peaks, oscillating scattering phase functions. For polysized particle clouds, the shift of diffraction peaks leads to a smoothing of the phase function [57]. The same effect leads to a smoothing of the phase function when a cloud of irregular shaped particles is considered [75]. Especially for technical applications different particle sizes with irregular shapes are present. The scattering phase function can thereby in general be approximated with a simplified function. The simplest case is for isotropic scattering where radiation is scattered equally in each direction and the scattering phase function is given by

$$\Phi_{\text{iso}} = 1 \quad (2.9)$$

This is the case for a large specularly reflecting opaque sphere. A large diffusely reflecting spheres scatters radiation according to

$$\Phi_{\text{diff}}(\theta_s) = \frac{8}{3\pi} (\sin \theta_s - \theta_s \cos \theta_s) \quad (2.10)$$

where this scattering phase function depends on the scattering angle  $\theta_s$  measured from the direction of transmission [57].

Large particles have normally a strong scattering peak in forward direction ( $\theta_s = 0^\circ$ ) that can often be described with approximation scattering phase functions like the Henyey-Greenstein (HG) phase function given by

$$\Phi_{\text{HG}}(\theta_s, g_f) = \frac{1 - g_f^2}{\left(1 + g_f^2 - 2g_f \cos \theta_s\right)^{3/2}} \quad (2.11)$$

where  $g_f$  is an asymmetry factor between zero and one [76]. Especially for dielectric particles, the HG phase function can lead to substantial errors

due to a missing backward scattering peak [77, 78]. This can be improved by combining a forward with a backward scattering peak as in the double Henyey-Greenstein (DHG) phase function defined as

$$\Phi_{\text{DHG}}(\theta_s, g_f, g_b, \delta) = \delta \Phi_{\text{HG}}(\theta_s, g_f) + (1 - \delta) \Phi_{\text{HG}}(\theta_s, -g_b) \quad (2.12)$$

where  $\delta$  is the forward scattered fraction,  $g_f$  the asymmetry factor of the forward peak, and  $g_b$  the asymmetry factor of the backward peak [79, 80]. Figure 2.1 shows a visual comparison of the presented scattering phase functions given in Eq. (2.9)–(2.12).

It can be beneficial to describe the scattering direction with a single parameter, likewise denoted as asymmetry factor, based on the average cosine of the scattering angle calculated from

$$\begin{aligned} A_1 = \overline{\cos \theta_s} &= \frac{1}{4\pi} \int_0^{4\pi} \Phi(\theta_s) \cos \theta_s d\Omega \\ &= \frac{1}{4\pi} \int_0^{2\pi} \int_0^\pi \Phi(\theta_s) \cos \theta_s \sin \theta_s d\theta_s d\phi_s \end{aligned} \quad (2.13)$$

where the asymmetry factor  $A_1$  lies within the range  $-1 \leq A_1 \leq 1$ . The rays are scattered in backward direction for  $A_1 = -1$ , in forward direction for  $A_1 = 1$ , and isotropically for  $A_1 = 0$  [57].

### 2.3.2 Dependent scattering

When the criteria for independent scattering are not satisfied, the scattering and absorption of single particles are influenced by nearby particles. Dependent scattering effects result from electromagnetic wave interference and multiple scattering events [51]. In practice, dependent scattering effects can be important in different applications like high-temperature packed beds or dense fluidized beds where a high solid fraction leads to a reduced inter-particle distance. Different approaches exist to approximate dependent scattering effects. An extensive compilation is given in [51]. A conventional approach to calculate dependent radiation properties is to apply correction

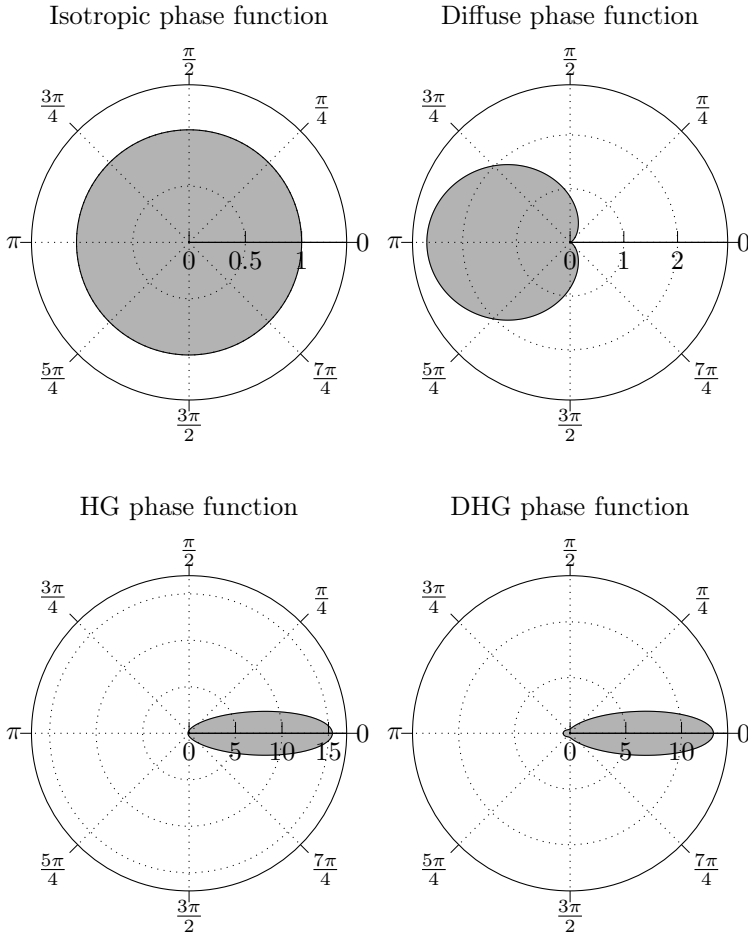


Figure 2.1: Polar plot of different scattering phase functions. The HG and DHG phase function have the same shape factor for the forward peak. The incident radiation travels from the left to the right.

terms to the radiation properties derived from the independent scattering theory according to

$$\beta = \beta_{\text{ind}}\gamma \quad (2.14)$$

where  $\beta_{\text{ind}}$  is the extinction coefficient for independent scattering given in Eq. (2.8) and  $\gamma$  is a scaling factor. Commonly used scaling factors are given by Brewster [81] based on theoretical calculations of the geometric mean ray length according to

$$\gamma = \frac{1}{1 - \alpha_s} \quad (2.15)$$

or by Singh and Kaviani [82, 52] based on Monte Carlo simulations according to

$$\gamma = 1 + 1.84\alpha_s - 3.15\alpha_s^2 + 7.20\alpha_s^3 \quad \text{for } \alpha_s < 0.7 \quad (2.16)$$

where both correlations are derived for opaque spheres and they correct only the extinction coefficient while the scattering albedo  $\omega$  and the scattering phase function  $\Phi$  are unchanged. An approach by Kamiuto [83, 84] calculates based on a correlated radiative transfer theory the hemispherical transmittances of randomly-packed beds of spheres and scales additionally to  $\beta$  the scattering albedo

$$\omega = 1 - \frac{1 - \omega_{\text{ind}}}{\gamma} \quad (2.17)$$

where  $\omega_{\text{ind}}$  is the scattering albedo for the independent scattering regime. The scaling factor is given by

$$\gamma = 1 + 1.5\alpha_s - 0.75\alpha_s^2 \quad \text{for } \alpha_s > 0.079 \quad (2.18)$$

that is likewise applied to Eq. (2.14) while the scattering phase function remains unaffected.

## Chapter 3

# Experimental method and numerical model<sup>1</sup>

### 3.1 Particle characterization

Two different types of SiC particles were considered: black particles with a purity of 97 % and green particles with a purity of 99 %. The impurities are mainly carbon, which is a by-product from the production process. Figure 3.1 depicts a photograph of the black and green SiC particles indicating the different colors. Scanning electron microscope (SEM) images of the black and green SiC particles are shown in Figure 3.2. The SEM images were captured with the Hitachi tabletop microscope TM–1000. The particles are sharp-edged since they were manufactured to be used as an abrasive. Additionally, the particles have very irregular shapes and are far from spherical. Both particle types have similar shapes while the black SiC particles include

---

<sup>1</sup>Material from this chapter has been published in:

J. Marti, M. Roesle, and A. Steinfeld, “Experimental determination of the radiative properties of particle suspensions for high-temperature solar receiver applications,” *Heat Transfer Engineering*, vol. 35, no. 3, pp. 272–280, 2014

J. Marti, M. Roesle, and A. Steinfeld, “Combined experimental–numerical approach to determine radiation properties of particle suspensions,” *Journal of Heat Transfer*, vol. 136, no. 9, pp. 092701–092708, 2014

some particles with a porous structure due to carbon impurities.

Figure 3.3 shows the cumulative and density distribution of the black and green SiC particles. The distributions are based on the number of particles and the particle sizes are measured with the laser diffraction analyzer HORIBA LA-950. The reported particle diameter is the volume equivalent sphere diameter. Table 3.1 lists the volume-mean, median, D10, and D90 diameters of the black and green SiC particles. Both SiC particle types have a very similar particle size distribution whereas the median diameter of the black particles is about 7 % smaller than the median diameters of the green particles.

Table 3.1: Measured volume-mean, median, D10, and D90 diameter based on the number distribution of the black and green SiC particles. The indicated particle diameters are volume equivalent sphere diameters.

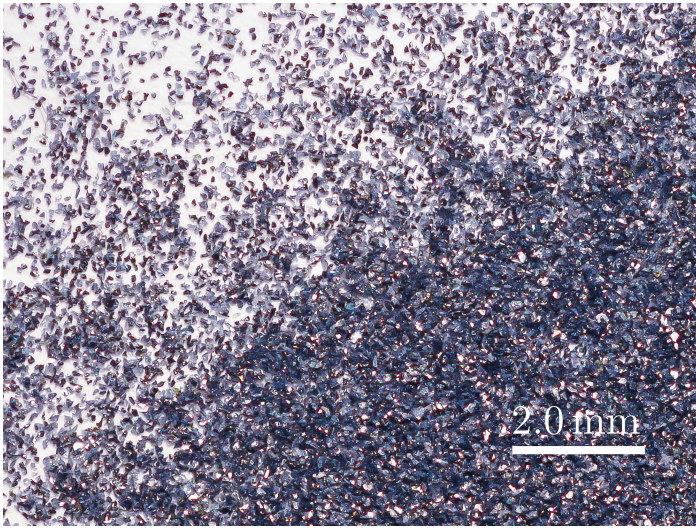
|                              | Black SiC ( $\mu\text{m}$ ) | Green SiC ( $\mu\text{m}$ ) |
|------------------------------|-----------------------------|-----------------------------|
| Volume-mean diameter, D(4,3) | 61.1                        | 66.4                        |
| Median diameter, D50         | 59.9                        | 64.5                        |
| D10                          | 29.5                        | 39.1                        |
| D90                          | 90.9                        | 95.6                        |

Altogether, the investigated SiC particles have very irregular shapes, the material properties are not fully known, and the material has impurities. The application of theoretical predictions or a pure ray-tracing approach to find the radiation properties, extinction coefficient, scattering albedo, and scattering phase function, are therefore not suitable. The alternative is to use an experimental-numerical approach as explained in the following.

## 3.2 Sample preparation

Fluidized beds are usually not homogeneous due to bubbles rising in an unsteady process. In such a system, the radiation properties depend strongly

(a) Black SiC



(b) Green SiC

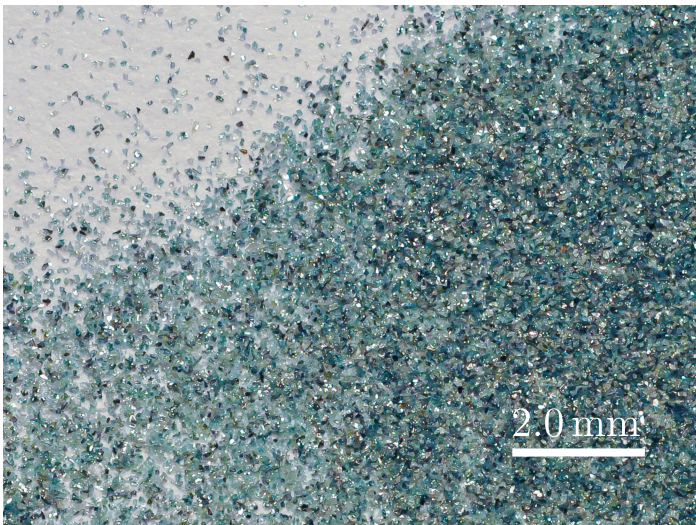
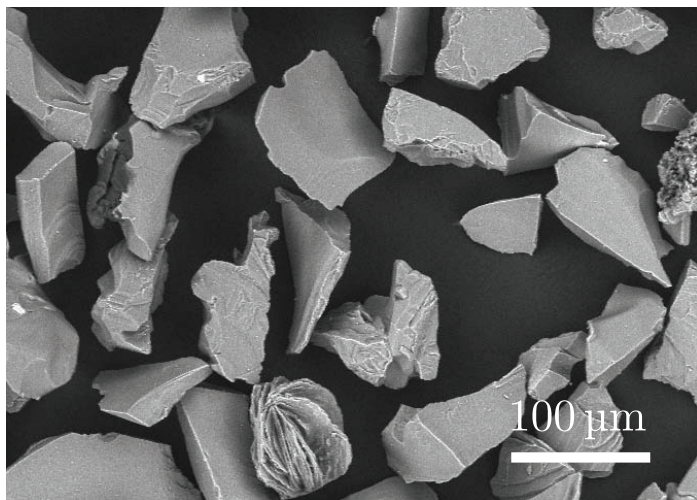


Figure 3.1: Photograph of the investigated black (a) and green (b) SiC particles with indicated scale.

(a) Black SiC



(b) Green SiC

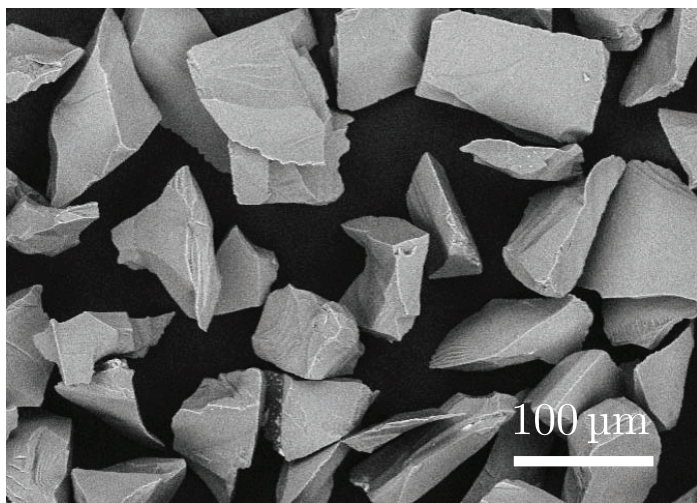


Figure 3.2: SEM images of the black (a) and green (b) SiC particles with indicated scale.



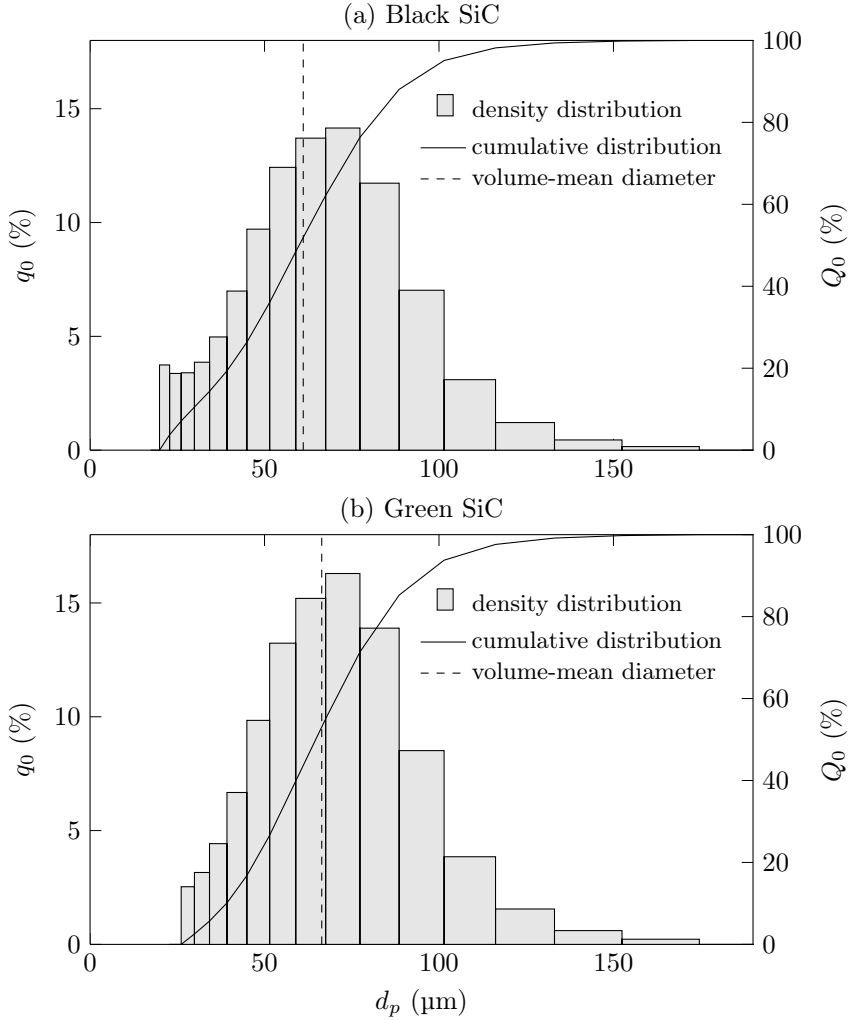


Figure 3.3: Density ( $q_0$ ) and cumulative ( $Q_0$ ) distribution of the black (a) and green (b) SiC volume-based particle diameter. The distributions are based on the number of particles. Also shown is the volume-mean particle diameter.

on the local particle volume fraction. It is therefore required to derive radiation properties as a function of the particle or solid volume fraction. To achieve a homogeneous particle suspension with a constant solid fraction, the SiC particles were mixed uniformly with a transparent epoxy resin (Biothan 2MD 1750-N and Biodur M-330 Optical) from Silitech AG. The viscosity of the epoxy resin is high enough to sustain the particles and avoid a particle settling due to gravity. To remove entrapped air introduced during the mixing process, the suspension was evacuated in a vacuum system. Very thin sample thicknesses had to be realized to allow sufficient radiation passing through the highly attenuating particle suspension and reaching the detector. This was achieved by pouring the viscous mixture onto a soda-lime glass microscope slide and cover it with a second microscope slide before the epoxy hardens. The distance between the glass slides was fixed with spacer discs at ranges from 0.1 mm up to 1.5 mm with a tolerance of  $\pm 0.01$  mm. Particles with a mean diameter larger than the smallest sample thickness represent less than 1 % of the total particles and can, due to their irregular shape, rotate to fit between the slides.

To evaluate the measurements, it is necessary to have for each solid fraction a sample series with different sample thicknesses. The solid volume fraction was controlled by mixing a measured mass of epoxy resin with a measured mass of particles and using the known material densities to calculate the volume fractions. For one sample series, the same mixture was used to guarantee an identical solid fraction for the different sample thicknesses.

Figure 3.4 depicts a photograph of one sample with black and one sample with green SiC particles. The microscope slides have a dimension of  $76 \times 26 \times 1$  mm and the edges of the samples were covered with an opaque film to avoid radiation from internal reflections within the glass slides reaching the detector.

With this procedure, the solid volume fraction and the sample thickness can be specified precisely. This is crucial for an accurate modeling procedure and data analysis. A sample series with three different sample thicknesses

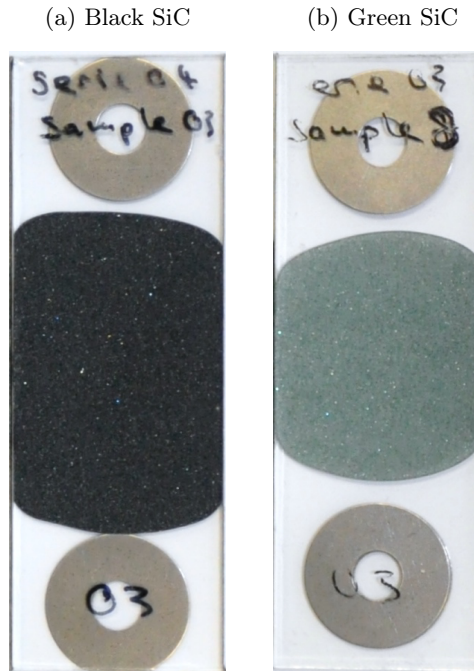


Figure 3.4: Photograph of the investigated black (a) and green (b) SiC particle samples. The sample height is 76 mm and the width is 26 mm.

was produced for each solid fraction and analyzed in the experimental setup.

### 3.3 Experimental setup

This study uses a spectroscopic goniometry system that was previously applied to measure intensity distributions of packed beds [55] and reticulated porous structures [56]. The spectroscopic goniometry system is schematically depicted in Figure 3.5. It consists of a xenon-arc lamp, a double monochromator, a mechanical beam chopper, two spherical  $\text{MgF}_2$  lens pairs, a sample, a detector, a lock-in amplifier, and a data acquisition system. The radiation source is the xenon-arc lamp connected to the double monochromator. The mechanical beam chopper pulses the near-monochromatic light at the monochromator exit slit. The cross section of the pulsed light is magnified and refocused with the first plano-convex spherical lens pair. The magnifying effect is achieved by using two lenses with focal lengths of 75 mm and 150 mm, respectively. The beam is focused at the rotation point of a rotary arm that supports the second plano-convex lens pair together with the detector. With this setup, angular measurements up to  $156^\circ$  from the incoming ray direction are possible. After the sample, the second lens pair captures the radiation leaving the sample and refocuses the light onto the dual Si/MCT detector. The first and second lenses of the second lens pair have focal lengths of 150 mm and 50 mm, respectively. This reduces the size of the beam cross section at the detector sufficiently to allow the detector to capture the whole beam cross section. The lens-detector system has a maximum half-cone acceptance angle of  $3.6^\circ$ . The lock-in amplifier measures the detector signal and accepts only the specific pulsed frequency from the mechanical beam chopper. The system is therefore only sensitive to radiation from the xenon-arc lamp that passes through the double monochromator and noise from other light sources is minimized.

The samples were held centered at the rotation point of the rotating arm with their face perpendicular to the incident ray direction. The rotation point coincides with the focal plane of the incident beam. Angu-

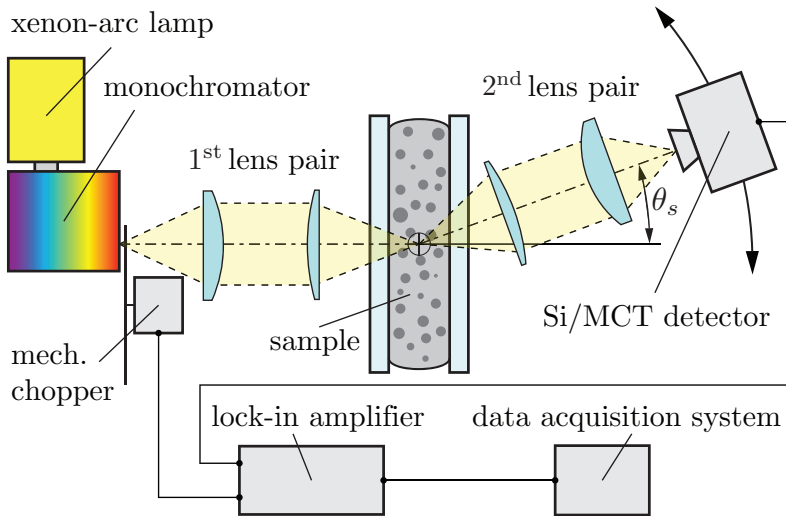


Figure 3.5: Schematic of the spectroscopic goniometry system with a xenon-arc lamp, double monochromator, mechanical chopper, plano-convex spherical  $\text{MgF}_2$  lens pairs, sample, dual Si/MCT sandwich detector, lock-in amplifier, and data acquisition system.

lar measurements were performed for every sample starting at  $\theta_s = 0^\circ$  up to  $\theta_s = 150^\circ$  measured from the incident ray direction as indicated in Figure 3.5. The measured signal was normalized with the reference signal  $V_0$  measured without a sample at an angle of  $\theta_s = 0^\circ$ . For each solid fraction, the set of measured intensity distributions were afterwards used in a numerical fitting procedure to determine the volume-averaged radiation properties as a function of the solid fraction.

A total of 40 measurements per sample and angle were performed. To account for possible local sample inhomogeneities, measurements were taken at four sample locations covering the central suspension region with an adequate distance from the slide or suspension edges to avoid any boundary artifacts. The detector signal was sampled at a frequency of 6.67 Hz over an interval of 1.5 s leading to ten measurements per sample location. The reference signal  $V_0$  was measured before and after each sample series to account for power fluctuations of the radiation source. Based on a confidence level of 95 %, the precision limit of the measured detector signal was approximated as twice the standard deviation. The bias limit of the goniometry system was estimated by taking the maximum difference of the experimental intensity distribution compared to a validation case using spherical glass particles as explained in Section 4.1. The maximum precision limit of the reference signal  $P_{V_0}$ , solid fraction  $\alpha_s$ , and sample thickness  $s$  are 3.1 %, 1.2 %, and 2.1 %, respectively. The 95 %-confidence based overall uncertainty of the normalized detector signal  $V/V_0$  was determined by accounting for the precision limit of the detector signal across the sample, the precision limit of the reference signal, and the bias limit of the system applying the propagation equation [87, 88]. The maximum precision limit of the measured detector signal, the bias limit, and the maximum overall uncertainty of the normalized detector signal are listed in Table 3.2 as a function of the viewing angle.

Table 3.2: Maximum precision limit of the measured detector signal  $P_V$ , bias limit  $B$ , and the overall uncertainty of the normalized detector signal  $U_{V/V_0}$  as a function of the viewing angle  $\theta_s$  for a confidence level of 95 %.

| $\theta_s$ ( $^\circ$ ) | $P_V$ (%) | $B$ (%) | $U_{V/V_0}$ (%) |
|-------------------------|-----------|---------|-----------------|
| 0                       | 42.0      | 27.0    | 49.9            |
| 10                      | 24.9      | 10.9    | 26.7            |
| 20                      | 24.1      | 14.1    | 28.1            |
| 30                      | 24.2      | 12.5    | 26.5            |
| 40                      | 26.3      | 5.5     | 27.4            |
| 50                      | 21.6      | 10.0    | 23.6            |
| 60                      | 21.2      | 16.4    | 24.5            |
| 70                      | 25.5      | 27.4    | 35.8            |
| 80                      | 22.6      | 41.8    | 45.3            |
| 90                      | —         | —       | —               |
| 100                     | 15.1      | 27.5    | 29.0            |
| 110                     | 14.1      | 11.2    | 17.4            |
| 120                     | 14.0      | 20.1    | 21.6            |
| 130                     | 19.2      | 21.8    | 26.5            |
| 140                     | 23.9      | 19.7    | 27.9            |
| 150                     | 18.1      | 5.4     | 19.6            |

## 3.4 Modeling approach

### 3.4.1 Monte Carlo model

The numerical model uses the collision-based Monte Carlo ray-tracing method and was realized with the in-house code VeGaS [89]. The particle suspension was modeled as a participating medium and a large number of stochastic rays were used to model the irradiation. The radiation properties of the participating medium were tuned until the numerical intensity distribution showed adequate agreement with the experimentally determined intensity distribution. The ray path is strongly influenced by the optical equipment and a proper representation of the experimental setup requires the modeling of the individual parts at their exact location. The only exception is the xenon-arc lamp and the double monochromator that were approximated as a rectangular ray source with the dimensions of the monochromator exit slit (1 mm  $\times$  4 mm). The emission direction of this ray source was previously determined [55] and modeled as a uniformly emitting disk near infinity with a half subtense angle of  $0.57^\circ$ . Furthermore, the geometry of the Monte Carlo model includes the two plano-convex spherical lens pairs, the sample including the microscope glass slides, and the detector. To account for refraction and internal reflection, the lenses are modeled as plano-convex Fresnel surfaces with the  $\text{MgF}_2$  index of refraction  $n_L = 1.38$ . Each microscope glass slide is modeled as a double-layer Fresnel surface with a nonabsorbing medium with refractive index of  $n_G = 1.52$  in between. The refractive index of the participating medium representing the particle suspension is assumed to correspond to the epoxy resin given by  $n_E = 1.55$ . The detector is modeled as a perfectly absorbing circular disc with the same dimensions as in the experimental case. Figure 3.6 shows on top the Monte Carlo setup with a description of the modeled optical equipment and below the result of an example run with a small number of rays. The solid (yellow) lines are rays that are either absorbed in the participating medium or by a detector and the dashed lines (black) are rays that are lost to the surrounding. As



shown in the figure, a second lens pair together with a detector plane is defined for each measured viewing angle. With such an arrangement, a single simulation run provides the same discrete angular intensity distribution around one sample like a complete set of experiments.

Figure 3.7 shows a schematic of the sample including the epoxy-particle suspension and the glass slides together with generic ray paths. Rays traveling through the participating medium are transmitted, scattered, or absorbed. The distance each ray travels before an absorption or scattering event is given by

$$s_\beta = \frac{1}{\beta} \ln \frac{1}{R_\beta} \quad (3.1)$$

where  $R_\beta$  is a random number between 0 and 1. If the distance  $s_\beta$  is longer than the travel distance through the participating medium, the ray will be transmitted without an absorption or scattering event. For each extinction event within the participating medium the condition

$$\omega \leq R_\omega \quad (3.2)$$

is evaluated to check whether absorption or scattering occurs. If the condition (3.2) is true the ray is absorbed and the ray path ends. Otherwise the ray is scattered and the new ray direction is determined by solving equation

$$R_\theta = \frac{\int_0^{\theta'_s} \Phi(\mathbf{s} \cdot \mathbf{s}') \sin \theta_s d\theta_s}{\int_0^\pi \Phi(\mathbf{s} \cdot \mathbf{s}') \sin \theta_s d\theta_s} \quad (3.3)$$

for the polar scattering angle  $\theta'_s$  where  $\mathbf{s} \cdot \mathbf{s}' = \cos \theta'_s$  and equation

$$R_\psi = \frac{\int_0^{\psi'_s} \int_0^\pi \Phi(\mathbf{s} \cdot \mathbf{s}') \sin \theta_s d\theta_s d\psi_s}{\int_0^{2\pi} \int_0^\pi \Phi(\mathbf{s} \cdot \mathbf{s}') \sin \theta_s d\theta_s d\psi_s} \quad (3.4)$$

for the azimuthal scattering angle  $\psi'_s$  where  $\mathbf{s}'$  is the new direction of the scattered ray. The polar scattering angle is in the range of  $0 \leq \theta'_s \leq \pi$  determined from the incoming ray direction  $\mathbf{s}$  while the azimuthal scattering angle points into a plane normal to  $\mathbf{s}$  within the range  $0 \leq \psi'_s \leq 2\pi$  [68, 57].

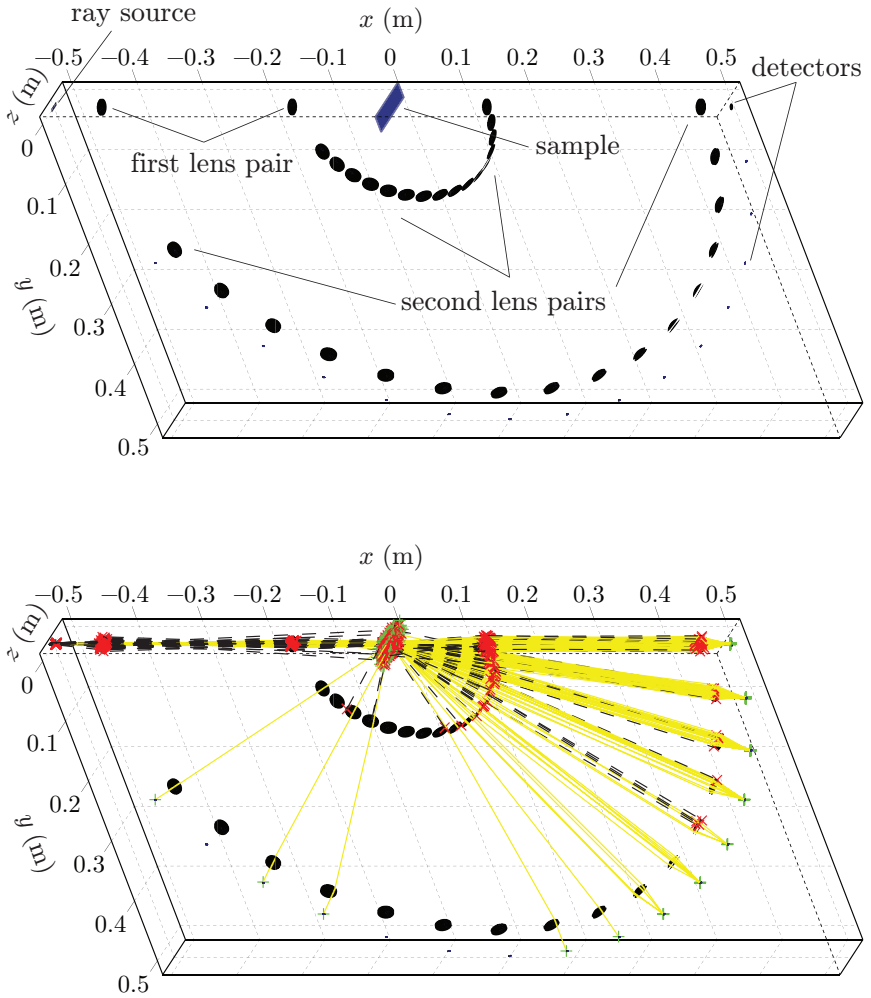


Figure 3.6: Geometric representation of the Monte Carlo model. With description on top and indicated stochastic rays below. Only a small number of rays are shown for clarity. The yellow lines are rays that are either absorbed in the participating medium or by a detector and the black lines are rays that are lost to the surrounding. A green plus sign indicates an absorption event and a red cross sign indicates the last scattering event of a ray that is lost to the surrounding.

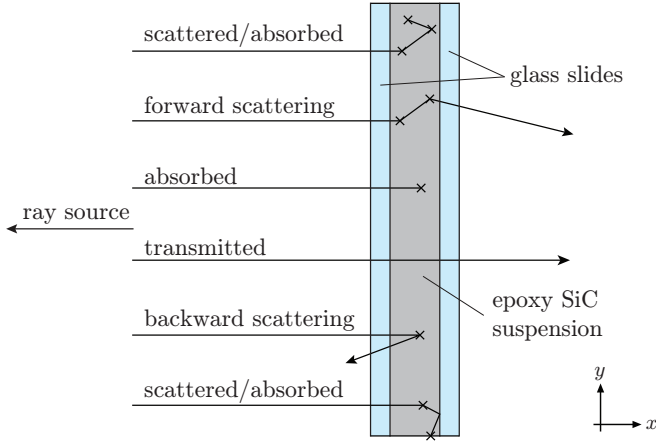


Figure 3.7: Schematic of the sample including the epoxy-particle suspension and the glass slides together with generic ray paths.

In the case of linear-anisotropic scattering, Eq. (3.4) simplifies to

$$R_\psi = \frac{\psi'_s}{2\pi} \quad (3.5)$$

A new set of random numbers ( $R_\beta$ ,  $R_\omega$ ,  $R_\theta$ , and  $R_\psi$ ) is generated for every ray and after every scattering event.

### 3.4.2 Numerical fitting procedure

A numerical fitting procedure was used for each solid fraction to find the volume-averaged radiation properties. Similar to the experimental measurements, a normalized detector signal was calculated by dividing the incident rays on each detector plane by the number of rays hitting the central detector plane ( $\theta_s = 0^\circ$ ) without sample.

The participating medium of the Monte Carlo model requires as an input a specific set of the radiation properties, namely:  $\beta$ ,  $\omega$ , and  $\Phi$ . Whereas  $\Phi$  was approximated with the DHG scattering phase function that requires three tuning parameters. This results in five independent parameters re-

sponsible for the radiation behavior of the participating medium. Each of these parameters was varied stepwise and the resulting normalized intensity distribution is compared to the normalized experimental measured intensity distribution. The extinction coefficient can be calculated directly (see Section 4.3) by using the experimental results for the limiting case of negligible in-scattering. This experimentally determined  $\beta$  is applied as an initial guess for the fitting procedure and  $\omega$  and the three tuning parameters of the DHG scattering phase function lie between zero and unity. The accuracy of each parameter set was evaluated by computing the root mean square error (RMSE) between the natural log of the experimental measured and the numerical results. The RMSE for each sample thickness was summed for one solid fraction. Thus, the resulting radiation properties represent all considered sample thicknesses for a given solid fraction. The investigated interval of  $\beta$  covered  $\pm 15\%$  of the experimentally determined value. The fitting procedure included an initial and a refinement run. The initial run covered the whole parameter range with a step size of  $10\%$  of the investigated range to obtain an approximation. In the subsequent refinement run, the investigated range was reduced to  $\pm 10\%$  of the initial determined value with a halving of the step size. A further refinement step showed negligible changes of the determined radiation properties. For each set of radiation properties, the ray path was calculated for at least  $5 \times 10^6$  stochastic rays. This number was determined with a convergence study where a further increase in stochastic rays showed a minor change of the obtained numerical result.

# Chapter 4

## Results<sup>1</sup>

### 4.1 Validation study

To assess the presented experimental-numerical approach to determine radiation properties of particle suspensions, a validation study with soda-lime glass microspheres from Whitehouse Scientific Ltd. was performed. The glass spheres are slightly larger than the SiC particles and have a very high sphericity as shown in the SEM image in Figure 4.1. The particle size distribution of the glass particles was measured by laser scattering (HORIBA LA-950) and Figure 4.2 depicts the number-based density and cumulative distribution together with the volume-mean particle diameter. The particle diameters are volume equivalent sphere diameters.

Mie theory can be applied to calculate the exact scattering phase function of a perfect sphere for independent scattering [57]. Therefore, a com-

---

<sup>1</sup>Material from this chapter has been published in:

J. Marti, M. Roesle, and A. Steinfeld, “Experimental determination of the radiative properties of particle suspensions for high-temperature solar receiver applications,” *Heat Transfer Engineering*, vol. 35, no. 3, pp. 272–280, 2014

J. Marti, M. Roesle, and A. Steinfeld, “Combined experimental–numerical approach to determine radiation properties of particle suspensions,” *Journal of Heat Transfer*, vol. 136, no. 9, pp. 092701–092708, 2014

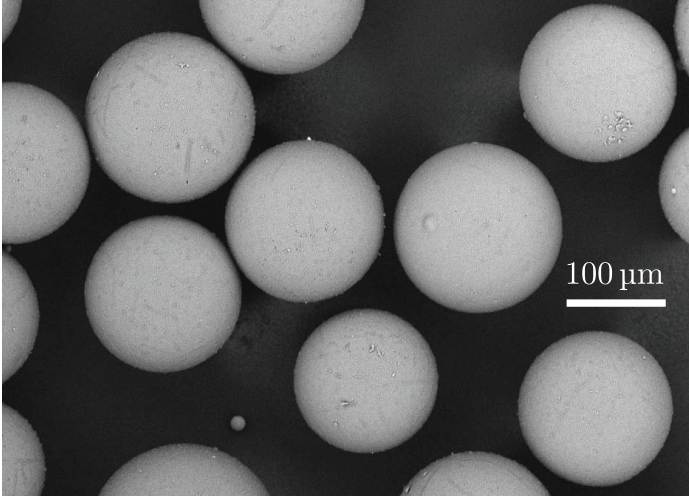


Figure 4.1: SEM image of the glass microspheres used for the validation study with indicated scale.

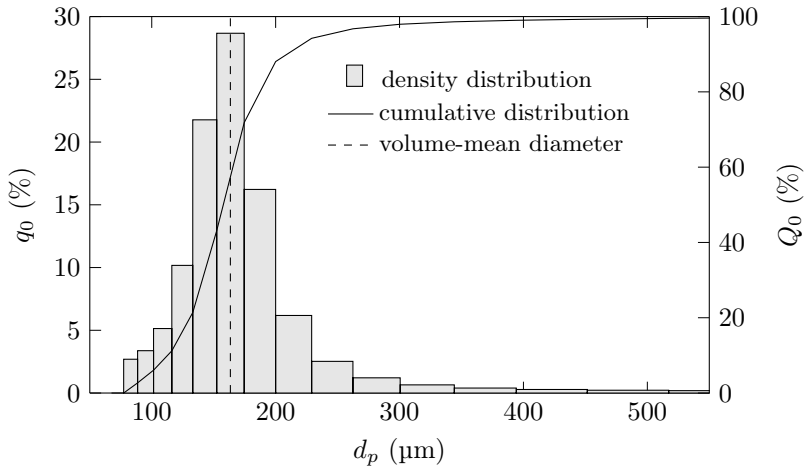


Figure 4.2: Density ( $q_0$ ) and cumulative ( $Q_0$ ) distribution of the glass microspheres volume-based particle size. The distributions are based on the number of particles. Also indicated is the volume-mean particle diameter.

puter program that integrates the results over the measured particle size distribution was implemented [90, 91, 92] to calculate the scattering phase function of the glass particles. Since the index of refraction of the epoxy resin is close to the refractive index of the glass spheres, the scattered intensity is too small to be measured accurately for glass particles suspended in the epoxy resin. Instead, a packed bed of glass microspheres was used to measure the scattering behavior. The boundaries of the packed bed are the same glass slides used for the SiC samples. The thickness of the packed bed was in the order of a few particle diameters to avoid a strong dependent scattering effect. The extinction coefficient was calculated by applying the scaling factor of Singh and Kaviani [82] given in Eq. (2.16). The glass microspheres have a negligible radiation absorption coefficient and a scattering albedo of  $\omega = 0.999$  was assumed. Compared to a perfectly nonabsorbing participating media with  $\omega = 1.0$ , this reduces the computational effort considerably while having an insignificant influence on the numerical result. With a complete set of radiation properties, the numerical intensity distribution can be computed and compared to the experimental determined distribution. A proper numerical model must be capable to accurately predict the experimental result. Furthermore, this comparison enables an estimation of the accuracy of the applied experimental-numerical approach to determine radiation properties.

Two packed beds of glass microspheres with different thicknesses were used for the validation procedure. The glass microspheres had a volume-mean diameter of  $d_p = 163.46 \mu\text{m}$  and the samples had a thickness of 0.65 mm and 1.23 mm, respectively. The measured mean solid fraction of the packed beds was  $\alpha_s = 0.45 \pm 0.01$ , which is lower than ordinary randomly packed beds due to the increased influence of the wall region for the thin sample thickness. The solid fraction was calculated by dividing the volume of the glass particles by the volume of the repository. The volume of the glass particles is determined by weight measurements divided by the density. To calculate the scattering phase function with Mie theory, the complex index of refraction of the glass spheres  $n_G = 1.515 - i1.5 \times 10^{-7}$

was used. Figure 4.3 depicts the calculated Mie scattering phase function for a wavelength of 500 nm. The phase function shows the characteristic shape for dielectric particles including a strong forward-scatter ( $\theta_s = 0^\circ$ ) peak and a weaker backward-scattering ( $\theta_s > 150^\circ$ ) peak [57].

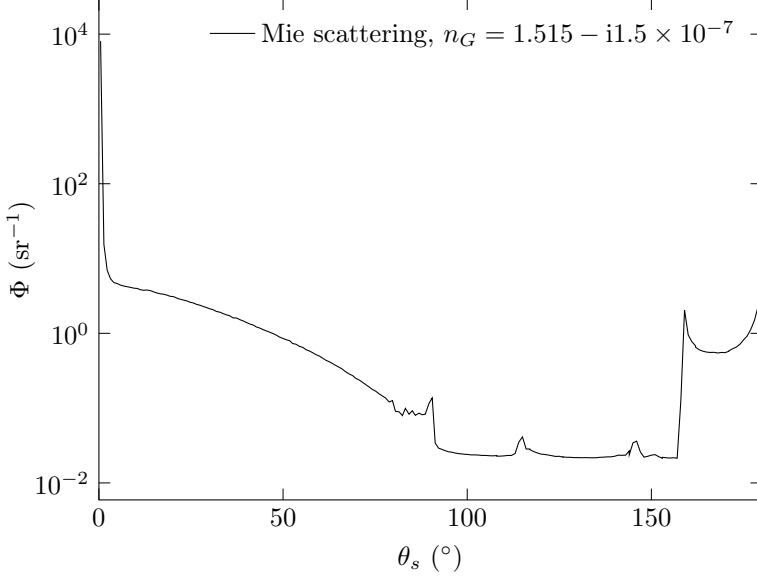


Figure 4.3: Mie scattering phase function of glass microspheres with a refractive index of  $n_G = 1.515 - i1.5 \times 10^{-7}$  and a wavelength of  $\lambda = 500$  nm.

Figure 4.4 shows the computed intensity as a function of the viewing angle compared to the experimental results for both sample thicknesses and a wavelength of 500 nm. The samples block scattered radiation at a viewing angle of  $90^\circ$  and the measured signal was therefore omitted. The model shows for both samples a good agreement with the experiments while the discrepancy of the thicker sample is slightly bigger. Since the applied Mie theory is strictly speaking only valid for independent scattering, it is expected that the stronger dependent scattering effect of the thicker sample leads to these bigger deviations. Nevertheless, the overall agreement is good



and the applied numerical method is expected to capture the scattering behavior of the SiC samples as well.

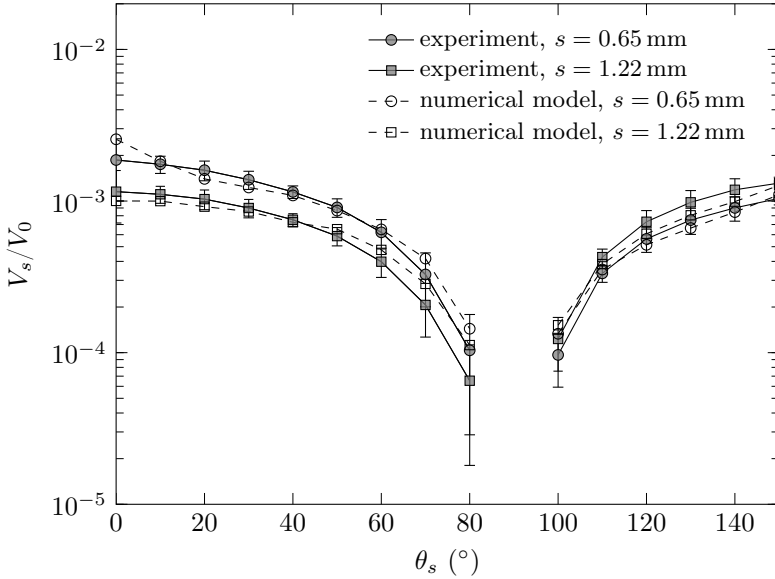


Figure 4.4: Measured normalized detector signal of packed beds with glass microspheres as a function of the viewing angle compared to the numerical results of the Monte Carlo model with Mie scattering.

## 4.2 Spectral dependence

In the gas-particle suspension used as HTM, the particles are surrounded by air that has an insignificant influence on the radiation. In the experimental setup, the particles are embedded in epoxy resin and covered with glass slides. For both the influence on the radiation transfer must be determined. Furthermore, the spectral dependence of the radiation interaction with the SiC particles needs to be investigated.

Figure 4.5 (a) shows the normalized detector signal of the transmitted

radiation through a single and double glass slide as well as a sample with epoxy only. The results are shown for a viewing angle of  $\theta_s = 0^\circ$  in the spectral interval 250–3000 nm. Figure 4.5 (b) shows the normalized detector signal of the transmitted radiation for black and green SiC samples with two different sample thicknesses in each case. In the visible ( $400 \text{ nm} < \lambda < 800 \text{ nm}$ ) and near-infrared ( $800 \text{ nm} < \lambda < 2500 \text{ nm}$ ) spectrum, the average fraction of the transmitted radiation for the single glass slide is  $V/V_0 = 0.918$ . This is in excellent agreement with the theoretical predicted normal transmittance at the interface of two perfect dielectrics ( $\beta = 0 \text{ m}^{-1}$ ) based on Fresnel's equation and Snell's law according to

$$\rho_n = \left( \frac{n_2 - n_1}{n_2 + n_1} \right)^2 \quad (4.1)$$

where  $\rho_n$  is the normal reflectivity and  $n_1$  and  $n_2$  are the refractive indexes of the two dielectrics [59]. The transmittance  $T$  is then calculated from

$$T = \frac{1 - \rho_n}{1 + \rho_n} \quad (4.2)$$

For the glass/air interface with  $n_1 = 1$  and  $n_2 = 1.52$  this leads to  $T = 0.918$ . The theoretical transmittance for two glass slides is given by  $T = 0.918^2 = 0.843$  and agrees with the measured detector signal of  $V/V_0 = 0.843$  over the spectral interval  $400 \text{ nm} < \lambda < 2500 \text{ nm}$ . For the sample with two glass slides and epoxy in between (solid line in Figure 4.5) the reflection losses between glass/epoxy and epoxy/glass are marginal since the two dielectrics have a very similar index of refraction  $n_G/n_E = 0.981$ . In the visible spectrum, the sample with epoxy behaves therefore similar than a single glass slide with a mean transmittance of  $T = 0.912$ . An increase or decrease of the epoxy thickness had thereby virtually no influence on the transmittance and implies that the extinction coefficient of the epoxy resin is negligible in the visible spectrum. Furthermore, the detector signal for  $\theta_s > 0^\circ$  dropped to an insignificant value indicating negligible light scattering by the epoxy resin. When increasing the wavelength to  $\lambda > 1000 \text{ nm}$ , the measured detector signal of the sample with epoxy decreases due to a reduced light transmittance in the near-infrared spectrum.

Figure 4.5 (b) shows the spectral dependence of the normalized detector signal for samples with black and green SiC particles. The chosen samples have a similar solid fraction and the two thicknesses are for both black and green SiC particles similar. For the thin samples, the agreement between black and green SiC particles is very good. The difference for the thicker samples is more pronounced and shows a constant shift between the normalized detector signal of the black and green SiC particles. This shift results from the reduced transmittance of the green SiC sample due to the slightly higher solid fraction and an increased sample thickness. In the spectral interval  $400\text{ nm} < \lambda < 1000\text{ nm}$  the transmittances of the SiC samples are very constant and show a negligible spectral dependency. In the spectral interval  $1000\text{ nm} < \lambda < 3000\text{ nm}$  the reduced transmittance of the epoxy resin is predominant and the normalized detector signals of the SiC samples show the characteristic peaks of the transmitted signal of the epoxy sample. An additional spectral dependence is not present. It is therefore assumed that the SiC particles have in the visible and near-infrared spectrum wavelength independent radiation properties and thus all measurements are performed at a single wavelength of 500 nm. Furthermore, a previous study [93] showed a very weak temperature dependence of the SiC emittance for up to 1500 °C. Based on Kirchhoff's law, this can also be assumed for the absorptance. It is therefore expected that the radiation properties determined at ambient conditions can be used at high temperatures as well.

### 4.3 Extinction coefficient

The solid fraction and sample thickness of the black and green SiC particles were kept as close as possible to simplify a comparison of the results. Nevertheless, due to manual sample preparation the maximal absolute differences of the solid fraction and sample thickness are 0.02 and 0.07 mm, respectively. Table 4.1 lists the investigated samples with the measured solid fractions and sample thicknesses together with the 95 % uncertainty of the measurements.

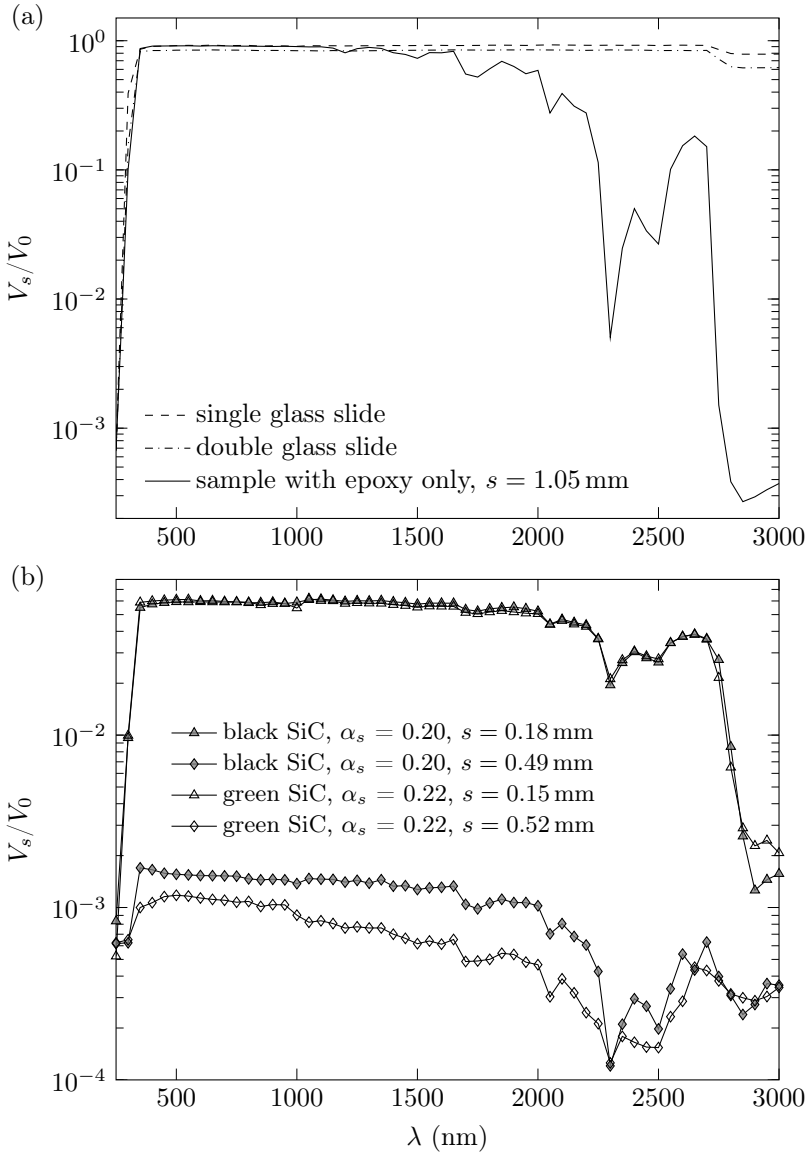


Figure 4.5: Spectral dependence of the normalized detector signal at  $\theta_s = 0^\circ$  for a) the glass slides, a sample with epoxy only, and b) samples with black and green SiC particles for different sample thicknesses.

Table 4.1: Solid fraction and sample thickness of the investigated black and green SiC particle suspensions with indicated 95 % uncertainty.

| SiC   | Sample | $\alpha_s$      | $s$ (mm)                    |
|-------|--------|-----------------|-----------------------------|
| Black | 1      | $0.05 \pm 0.01$ | $0.23, 0.52, 1.05 \pm 0.02$ |
|       | 2      | $0.09 \pm 0.01$ | $0.25, 0.57, 1.08 \pm 0.02$ |
|       | 3      | $0.20 \pm 0.01$ | $0.14, 0.18, 0.50 \pm 0.02$ |
|       | 4      | $0.30 \pm 0.01$ | $0.14, 0.18, 0.53 \pm 0.02$ |
| Green | 5      | $0.05 \pm 0.01$ | $0.28, 0.56, 1.07 \pm 0.02$ |
|       | 6      | $0.09 \pm 0.01$ | $0.25, 0.57, 1.04 \pm 0.02$ |
|       | 7      | $0.22 \pm 0.01$ | $0.14, 0.19, 0.52 \pm 0.02$ |
|       | 8      | $0.28 \pm 0.01$ | $0.13, 0.19, 0.52 \pm 0.02$ |

In the limiting case of a cold medium without in-scattering, the RTE given in Eq. (2.3) simplifies to

$$\frac{dI}{ds} = -\kappa I - \sigma_s I = -\beta I \quad (4.3)$$

This equation can easily be solved and leads to Bouguer's law given by

$$I(s) = I_0 e^{-\beta s} \quad (4.4)$$

where  $I_0$  is the intensity for  $s = 0$ . Bouguer's law describes the exponential decrease of the incident radiation intensity along the path  $s$  in a participating medium with an extinction coefficient  $\beta$  [68, 57]. For a detector with a small acceptance angle, the measured detector signal  $V$  can be approximated with the radiative intensity  $I$  and Eq. (4.4) can be rewritten as

$$V_s = V_0 e^{-\beta s} \quad (4.5)$$

where  $V_0$  is the detector signal measured without sample in direction of the incident radiation and  $V_s$  is the measured signal in the same direction after passing a sample with thickness  $s$ . The extinction coefficient can then be

determined by

$$\beta = -\frac{1}{s} \ln \frac{V_s}{V_0} \quad (4.6)$$

Eq. (4.6) is valid for a negligible augmentation of the intensity along the path  $s$  by incoming scattering [94, 68]. By using the optical thickness  $\tau = \beta s$ , Eq. (4.5) is simplified to

$$\frac{V_s}{V_0} = e^{-\tau} \quad (4.7)$$

where the expression  $V_s/V_0$  is equal to the sample transmittance  $T$  [57].

To avoid an influence of the glass slides and the epoxy resin on the experimental determined extinction coefficient, the detector signal  $V_0$  is scaled with the transmittance of the two glass slides with epoxy in between given by  $T_0 = 0.912$ . Figure 4.6 shows the normalized and scaled detector signal of the black (a) and green (b) SiC particles as a function of the sample thickness at a viewing angle of  $\theta_s = 0^\circ$  for different solid fractions. Each sample series includes an exponential fit. The fit shows for both particles and for every solid fraction a very good agreement with the measured data points. This agreement demonstrates the applicability of Bouguer's law due to reduced in-scattering effects. The slope of the exponential fit is exactly the extinction coefficient of the respective sample series. Table 4.2 lists the experimental derived extinction coefficient based on Bouguer's law for the black and green SiC particles together with the 95 % confidence uncertainty.

Figure 4.7 shows the experimentally determined extinction coefficients of the black and green SiC particle suspensions compared to the independent scattering theory given by Eq. (2.8) and the dependent scattering correlation from Singh and Kaviani given by Eq. (2.16). The experimental results include the 95 % confidence uncertainty. Both particle suspensions show for low solid fractions ( $\alpha_s < 0.1$ ) a very good agreement with the independent scattering theory and for higher solid fractions ( $\alpha_s > 0.2$ ) a very good agreement with the correlation from Singh and Kaviani. This is consistent with the previous characterized limit for independent scattering. The slightly higher extinction coefficient of the black SiC particle suspensions results from their smaller mean particle diameter.

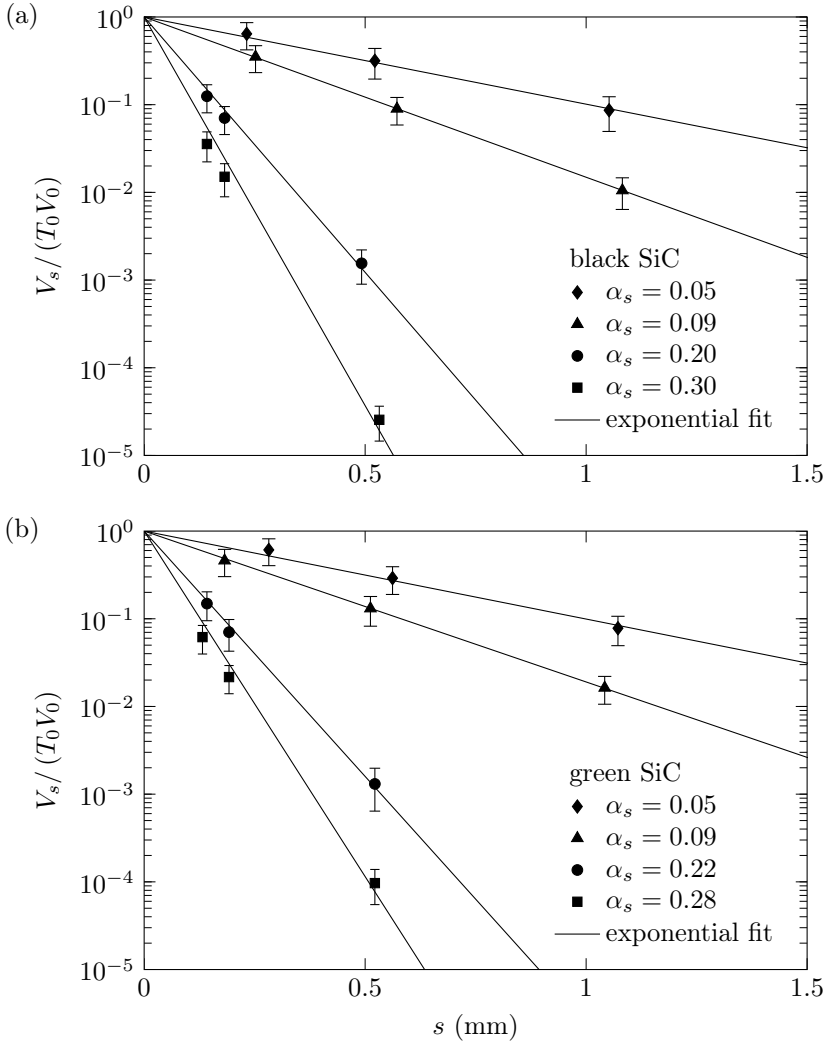


Figure 4.6: Normalized and scaled detector signal at a viewing angle of  $\theta_s = 0^\circ$  for different solid fractions as a function of the sample thickness together with an exponential fit through each sample series. (a) shows the results of the black SiC particles and (b) the results of the green SiC particles together with the 95 % confidence uncertainty.

Table 4.2: Experimental derived extinction coefficient  $\beta$  based on Bouguer's law for the black and green SiC particles together with the 95 % confidence uncertainty.

| SiC   | $\alpha_s$      | $\beta$ (mm <sup>-1</sup> ) |
|-------|-----------------|-----------------------------|
| Black | $0.05 \pm 0.01$ | $2.29 \pm 0.18$             |
|       | $0.09 \pm 0.01$ | $4.21 \pm 0.52$             |
|       | $0.20 \pm 0.01$ | $13.41 \pm 1.13$            |
|       | $0.30 \pm 0.01$ | $20.41 \pm 2.33$            |
| Green | $0.05 \pm 0.01$ | $2.31 \pm 0.33$             |
|       | $0.09 \pm 0.01$ | $3.96 \pm 0.09$             |
|       | $0.22 \pm 0.01$ | $12.89 \pm 0.73$            |
|       | $0.28 \pm 0.01$ | $18.14 \pm 1.92$            |

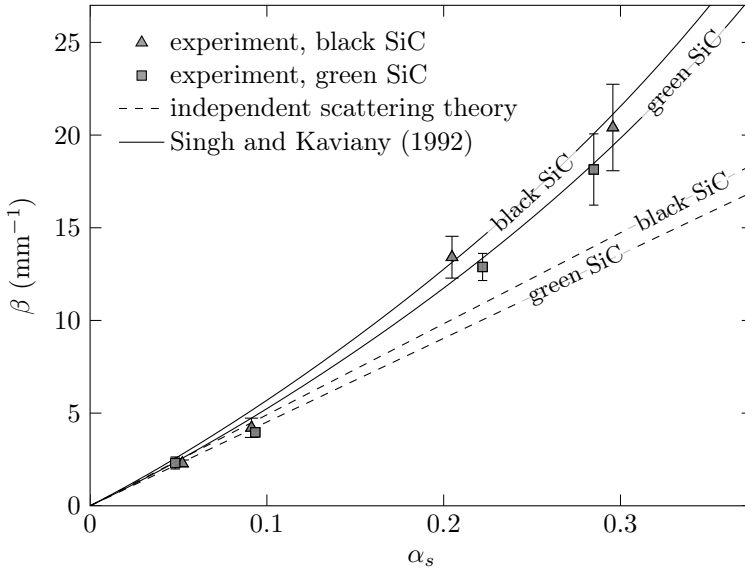


Figure 4.7: Experimentally determined extinction coefficients of the black and green SiC samples compared to the independent scattering theory and the dependent scattering correlation from Singh and Kaviani [52] with indicated 95 % confidence uncertainty of the experimental results.



## 4.4 Experimental-numerical approach

Having validated the overall approach, investigated spectral dependencies, examined the influences of the glass slides and the epoxy resin, and determined an initial guess of the extinction coefficient, attention is now turned to find the complete set of volume-averaged radiation properties of the SiC particle suspensions. This is achieved by using the explained numerical fitting procedure based on the experimental-determined discrete intensity distribution around the irradiated samples.

### 4.4.1 Measurements

Figure 4.8 and 4.9 show the experimental determined normalized detector signal of the black SiC samples as a function of the viewing angle for different solid fractions and sample thicknesses. Independent of the solid fraction and sample thickness, the normalized detector signal shows a strong peak in the forward direction for  $\theta_s = 0^\circ$ , a decrease as far as  $\theta_s = 80^\circ$ , and an increase in the backward direction for  $\theta_s \geq 100^\circ$ . Since the sample blocks radiation reaching the detector at a viewing angle of  $\theta_s = 90^\circ$ , these data points are neglected. The forward peak decreases for increasing the sample thickness and/or increasing the solid fraction, which corresponds to increasing the optical thickness. The decrease of the forward peak is due to a reduction of transmitted rays reaching the detector when increasing the optical thickness. Furthermore, increasing the optical thickness leads to an increase of the radiation scattering events, resulting in a more diffuse scattering behavior. This is especially noticeable for the sample with the biggest optical thickness in Figure 4.9 (b) where the normalized detector signal in forward direction shows a weaker dependence on the viewing angle compared to samples with a lower optical thickness. The normalized detector signal in backward direction is similar for all solid fractions. This similarity arises probably from the fact that most of the backscattering events are single scattering events taking place on the first layer of particles facing the

monochromator exit slit. As a consequence, the solid fraction and mainly the sample thickness have only a minor influence on the backscattering behavior. This expectation is supported by the reduced backward signal for the sample with the lowest optical thickness shown in Figure 4.8 (a) where a lot of unscattered rays reach the detector.

Figure 4.10 and 4.11 show the experimentally determined normalized detector signal of the green SiC samples as a function of the viewing angle for different solid fractions and sample thicknesses. The normalized detector signals of the green SiC samples show a very similar dependence on the viewing angle than the black SiC samples. However, between different sample thicknesses of the same solid fraction, the green SiC samples show, especially for lower solid fractions, a stronger difference of the backward detector signal and a reduced difference in forward direction compared to the black SiC samples. An explanation for this behavior would be a reduced absorption coefficient of the green SiC particle suspensions. This is backed up by the stronger detector signal of the green SiC samples in both forward and backward direction as seen in Figure 4.12 showing a direct comparison of the normalized detector signal of the black and green SiC samples for a solid fraction of  $\alpha_s = 0.09$  and similar sample thicknesses.

#### 4.4.2 Simulations

Before the actual fitting procedure, the different scattering phase functions presented in Section 2.3.1 were tested in the Monte Carlo model and their performance was compared to each other. Figure 4.13 (a) depicts the investigated scattering phase functions and (b) shows the normalized detector signal of a generic experimental sample (green SiC,  $\alpha_s = 0.28$ ,  $s = 0.19$  mm) together with the Monte Carlo model for the different scattering phase functions. For all numerical cases, the values of  $\beta$  and  $\omega$  were equal. The parameters of the HG and DHG phase functions were fitted to best approximate the experimental result. The isotropic and diffuse scattering phase functions underestimate the scattering in forward directions and overesti-

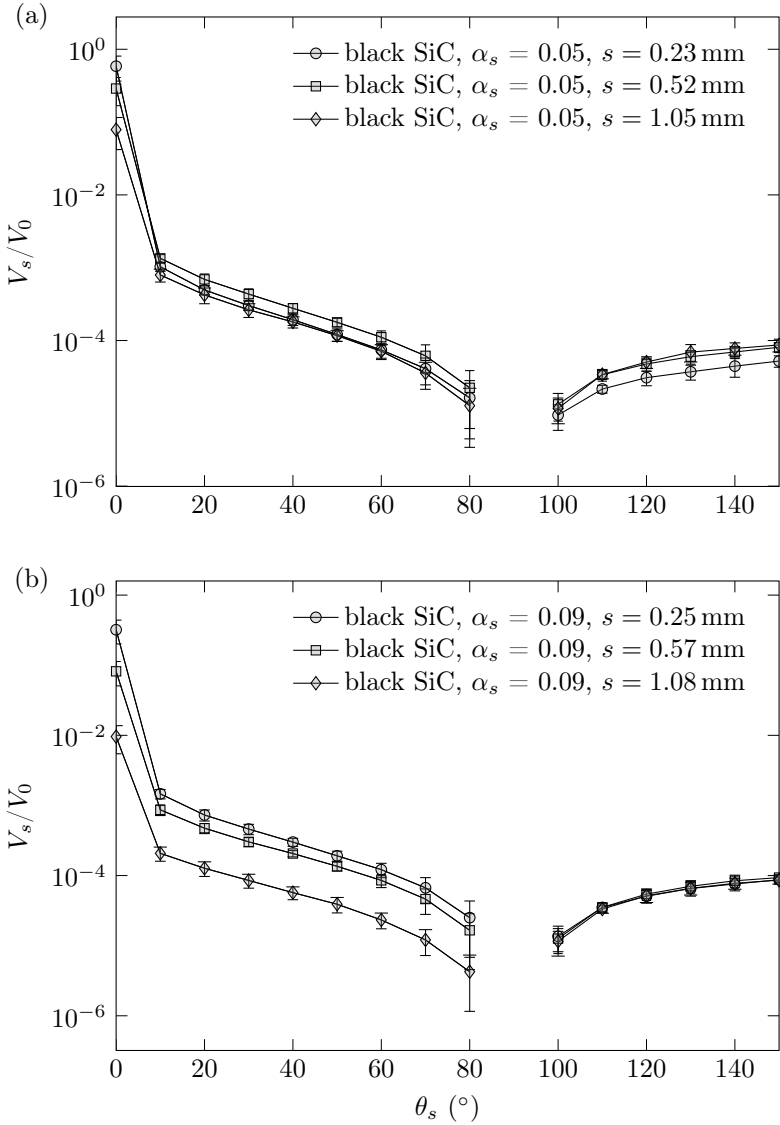


Figure 4.8: Normalized detector signal of the black SiC samples with  $\alpha_s = 0.05$  (a) and  $\alpha_s = 0.09$  (b) as a function of the viewing angle with indicated 95% confidence uncertainty.

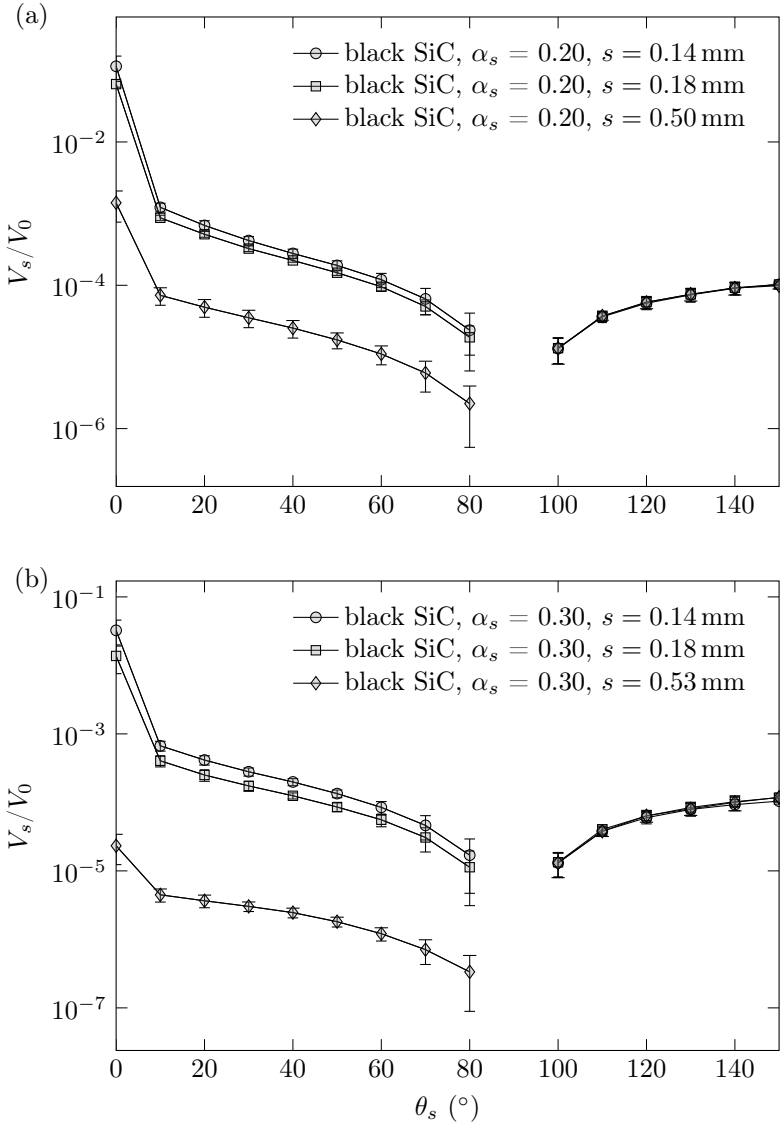


Figure 4.9: Normalized detector signal of the black SiC samples with  $\alpha_s = 0.20$  (a) and  $\alpha_s = 0.30$  (b) as a function of the viewing angle with indicated 95% confidence uncertainty.

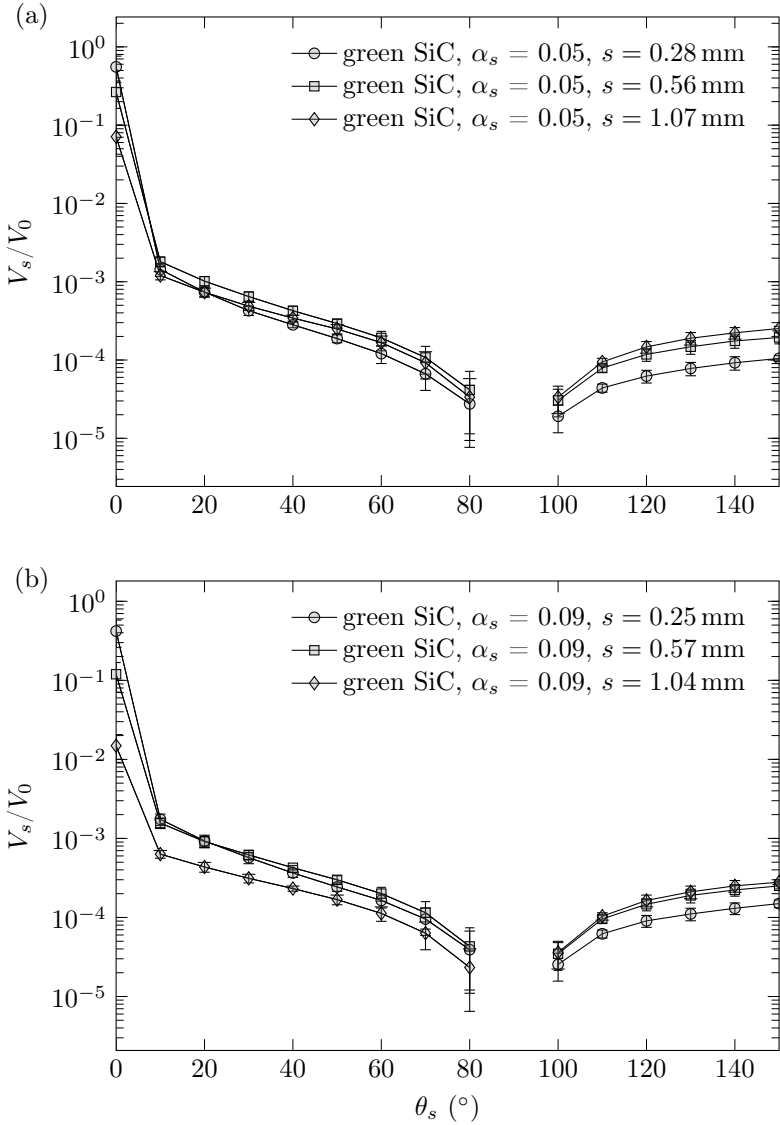


Figure 4.10: Normalized detector signal of the green SiC samples with  $\alpha_s = 0.05$  (a) and  $\alpha_s = 0.09$  (b) as a function of the viewing angle with indicated 95% confidence uncertainty.

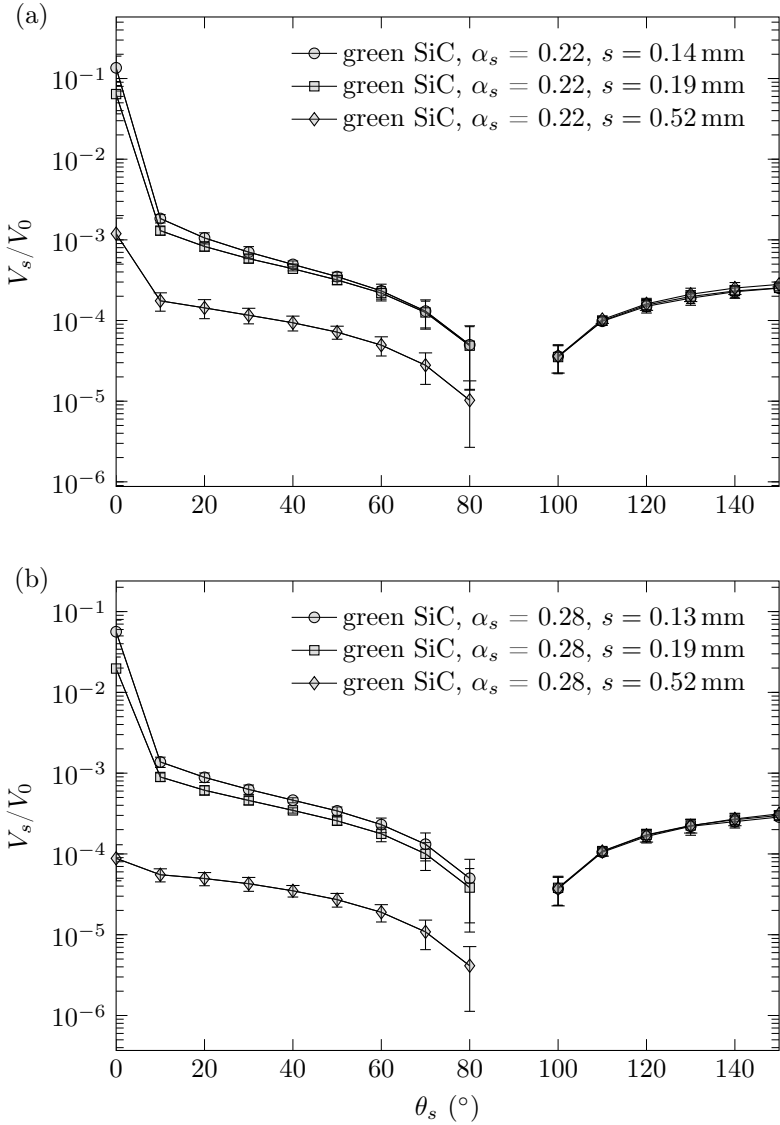


Figure 4.11: Normalized detector signal of the green SiC samples with  $\alpha_s = 0.22$  (a) and  $\alpha_s = 0.28$  (b) as a function of the viewing angle with indicated 95% confidence uncertainty.

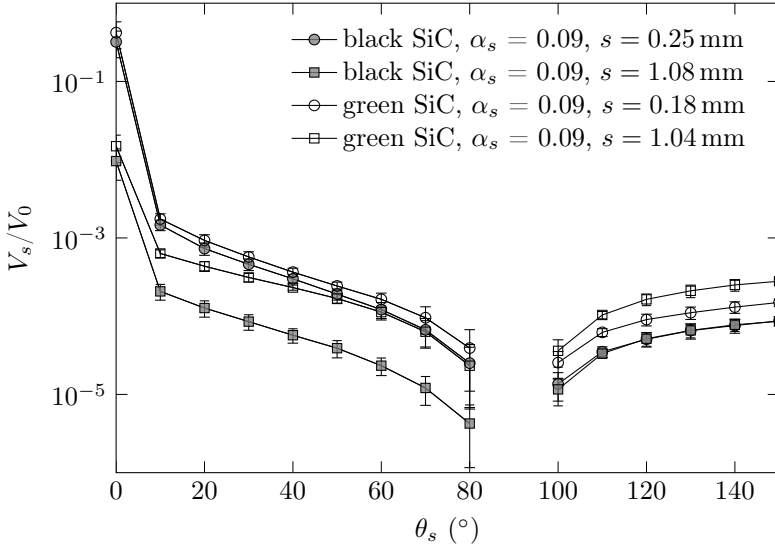


Figure 4.12: Normalized detector signal of the black and green SiC samples with a solid fraction of  $\alpha_s = 0.09$  and similar sample thicknesses as a function of the viewing angle with indicated 95 % confidence uncertainty.

mate the backscattering. The HG phase function behaves vice versa and overpredicts the forward scattering while the backward scattering is underestimated. This behavior is corrected with the additional backward peak of the DHG phase function that shows excellent agreement and was therefore used for the numerical fitting procedure to determine the approximated and volume-averaged radiation properties of the SiC particle suspensions.

Figure 4.14 shows the normalized detector signal for different solid fractions and similar sample thicknesses of the black SiC samples (a) and the green SiC samples (b) as a function of the viewing angle in comparison with the fitted result of the Monte Carlo model. The agreement of the numerical and experimental results is especially for the optical thin samples very good while the relative difference increases slightly with an increasing optical thickness.

### Scattering phase function

Figure 4.15 shows a comparison of the numerically derived DHG scattering phase functions of the black and green SiC particle suspensions for different solid fractions. Particularly for the black SiC particle suspensions, the approximated scattering phase function has a very weak dependence on the solid fraction. However, a reduction of the solid fraction shows for both SiC types an increase of the DHG forward scattering peak. This trend is especially obvious for the green SiC particle suspensions. It is expected that besides the weak dependence on the solid fraction, the particle size distribution and the particle shape mainly influence the scattering phase function.

Figure 4.16 shows the fitted scattering phase function of the black and green SiC particle suspensions for  $\alpha_s = 0.05$  in comparison with the theoretical calculation using Mie theory. The Mie scattering phase function is calculated for  $n_{\text{SiC}} = 2.70 - i0.1$  [95, 96] and integrated over the measured green SiC particle size distribution. Although the Mie scattering phase function differs considerably from the numerical derived DHG phase functions, both show a strong forward scattering peak with reduced probability



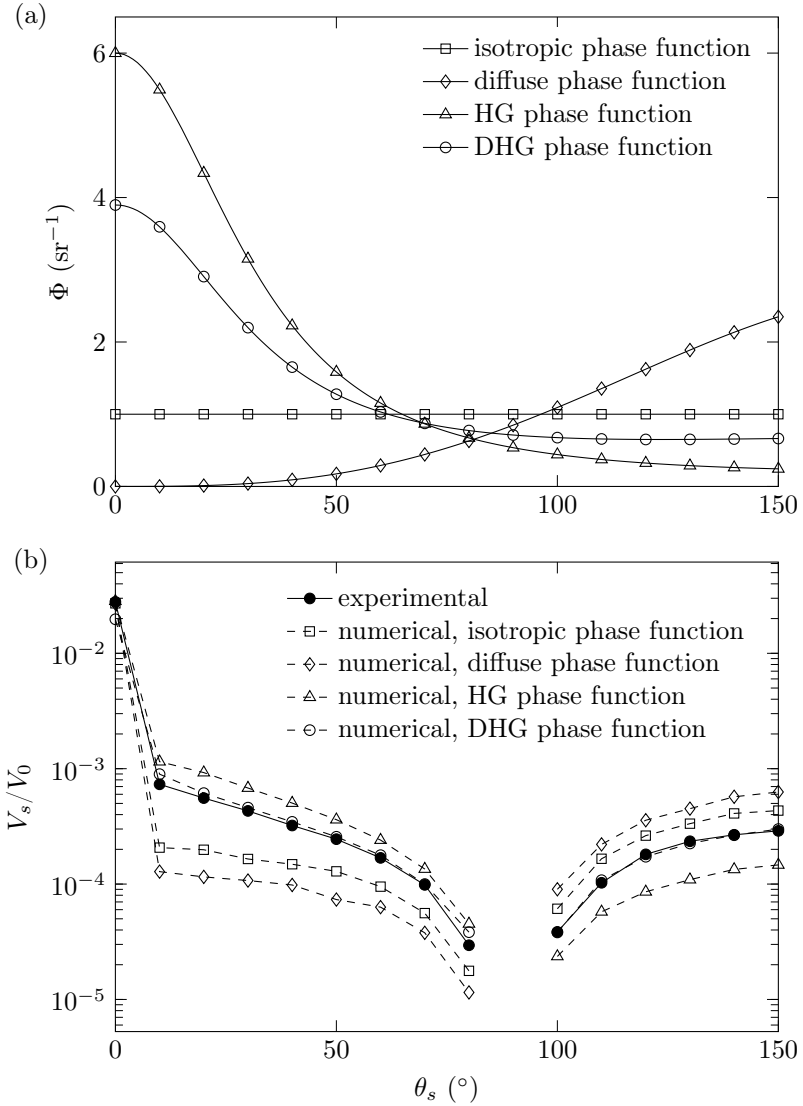


Figure 4.13: (a) Investigated scattering phase functions. (b) Experimental measured (green SiC,  $\alpha_s = 0.28$ ,  $s = 0.19\text{ mm}$ ) and normalized detector signal as a function of the viewing angle compared to the Monte Carlo model with the different scattering phase functions shown in (a).

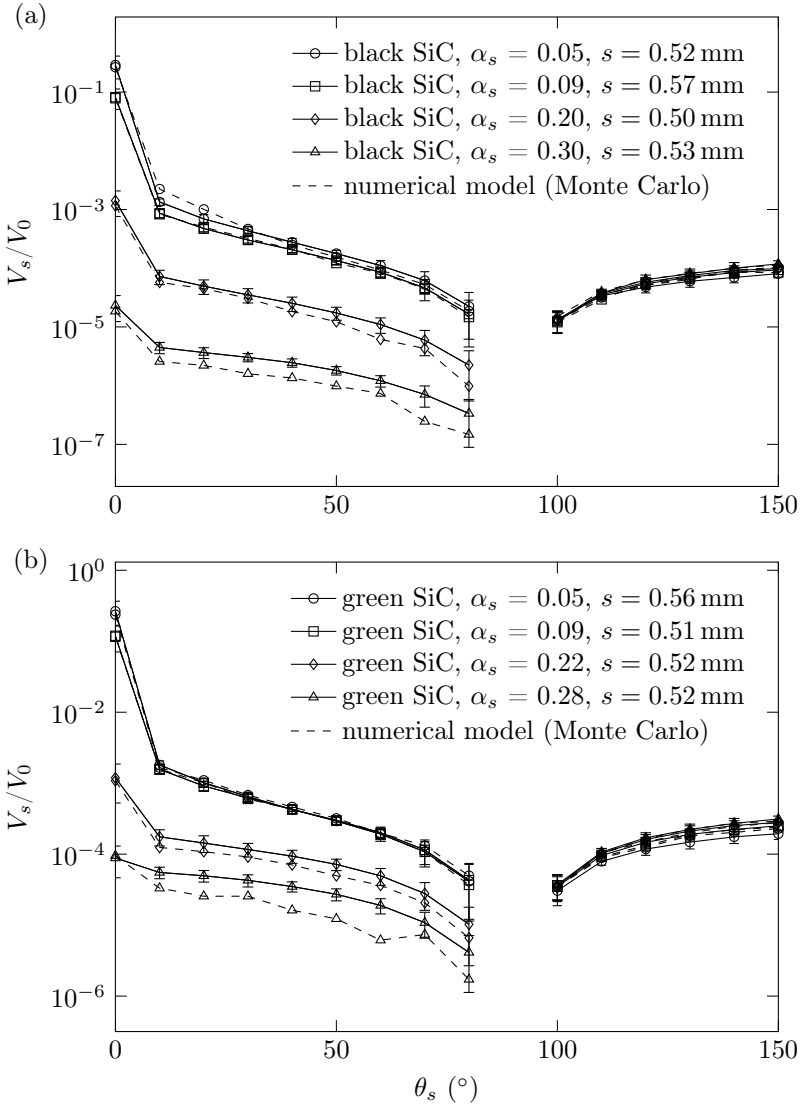


Figure 4.14: Normalized detector signal for different solid fractions and similar sample thicknesses of the black SiC (a) and green SiC (b) samples as a function of the viewing angle in comparison with the Monte Carlo model.

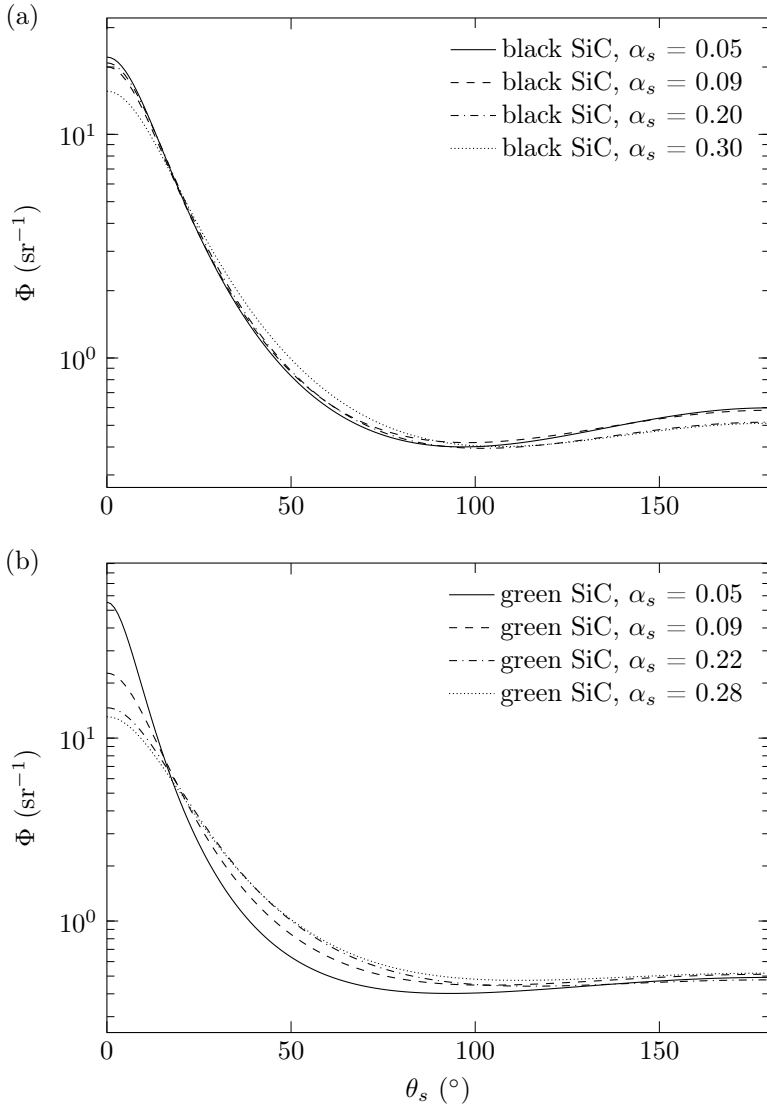


Figure 4.15: Comparison of the numerically derived DHG scattering phase function for black SiC (a) and green SiC (b) particle suspensions with different solid fractions as a function of the scattering angle.

of backscattering. The strong forward peak of the Mie scattering reflects mainly the refracted radiation. In contrast, the goniometry system used in this study has a larger acceptance angle, so the normalized detector signal at  $\theta_s = 0^\circ$  includes both unattenuated and refracted radiation. Further reasons for the difference between the approximated and the Mie scattering phase function may be the shape of the SiC particles, dependent scattering effects, and SiC particle impurities.

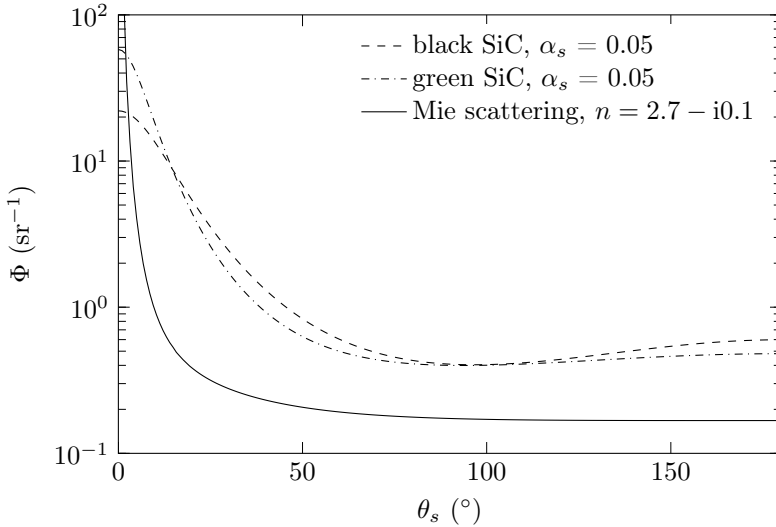


Figure 4.16: Numerically derived DHG scattering phase functions of the black and green SiC particle suspensions ( $\alpha_s = 0.05$ ) compared to the scattering phase function based on Mie theory for  $n_{\text{SiC}} = 2.7 - i0.1$  and using the measured green SiC particle size distribution.

Figure 4.17 shows the fitted DHG scattering phase function parameters for the black (a) and green SiC (b) particle suspensions together with linear fits as a function of the solid fraction. The trend of the individual parameters of both SiC types are similar: the forward asymmetry factor  $g_f$  decreases, the backward asymmetry factor  $g_b$  stays nearly constant, and the forward

scattering fraction  $\delta$  increases slightly with increasing solid fraction. The linear fits of the black SiC particle suspensions are given by

$$g_{f,\text{black}}(\alpha_s) = 0.77 - 0.18\alpha_s \quad \text{with RMSE} = 0.010 \quad (4.8)$$

$$g_{b,\text{black}}(\alpha_s) = 0.20 - 0.05\alpha_s \quad \text{with RMSE} = 0.009 \quad (4.9)$$

$$\delta_{\text{black}}(\alpha_s) = 0.70 + 0.20\alpha_s \quad \text{with RMSE} = 0.008 \quad (4.10)$$

and for the green SiC particle suspensions given by

$$g_{f,\text{green}}(\alpha_s) = 0.85 - 0.60\alpha_s \quad \text{with RMSE} = 0.031 \quad (4.11)$$

$$g_{b,\text{green}}(\alpha_s) = 0.11 \quad \text{with RMSE} = 0.0 \quad (4.12)$$

$$\delta_{\text{green}}(\alpha_s) = 0.67 + 0.10\alpha_s \quad \text{with RMSE} = 0.019 \quad (4.13)$$

where for each fit the RMSE is indicated. By including Eq. (4.8)–(4.13) into Eq. (2.12), the approximated DHG scattering phase function can be expressed as a function of  $\alpha_s$  and  $\theta_s$  leading to an expression given for the black SiC particle suspensions by

$$\begin{aligned} \Phi_{\text{DHG,black}}(\theta_s, \alpha_s) = & \frac{(0.20\alpha_s - 0.30) \left( (0.05\alpha_s - 0.20)^2 - 1 \right)}{\left( (0.05\alpha_s - 0.20)^2 - \cos \theta_s (0.10\alpha_s - 0.40) + 1 \right)^{\frac{3}{2}}} \\ & - \frac{(0.20\alpha_s + 0.70) \left( (0.18\alpha_s - 0.77)^2 - 1 \right)}{\left( \cos \theta_s (0.36\alpha_s - 1.54) + (0.18\alpha_s - 0.77)^2 + 1 \right)^{\frac{3}{2}}} \end{aligned} \quad (4.14)$$

and for the green SiC particle suspensions by

$$\begin{aligned} \Phi_{\text{DHG,green}}(\theta_s, \alpha_s) = & - \frac{9.88\alpha_s - 0.33}{(0.22 \cos \theta_s + 1.01)^{\frac{3}{2}}} \\ & - \frac{(10\alpha_s + 0.67) \left( (0.6\alpha_s - 0.85)^2 - 1 \right)}{\left( \cos \theta_s (1.20\alpha_s - 1.70) + (0.6\alpha_s - 0.85)^2 + 1 \right)^{\frac{3}{2}}} \end{aligned} \quad (4.15)$$

By using Eq. (2.13), the directional scattering trend can be described with a single asymmetry factor  $A_1$ . This leads for Eq. (4.14) to the expression

$$A_{1,\text{black}}(\alpha_s) = 0.48 + 0.08\alpha_s - 0.05\alpha_s^2 \quad (4.16)$$

and for Eq. (4.15) to the expression

$$A_{1,\text{green}}(\alpha_s) = 0.53 - 0.31\alpha_s - 0.06\alpha_s^2 \quad (4.17)$$

Figure 4.18 shows a comparison of this single asymmetry factors of the black and green SiC particle suspensions as a function of the solid fraction. The  $y$ -axis is scaled to show the possible range of  $-1 \leq A_1 \leq 1$ . The asymmetry factors of both particles show a forward scattering tendency ( $A_1 > 0$ ) and especially for the black SiC particle suspensions a weak dependence on the solid fraction. This trends agree with the DHG scattering phase functions shown in Figure 4.15.

### Scattering albedo

Figure 4.19 shows the scattering albedo as a function of the solid fraction for the black and green SiC particle suspensions. Both particle types show a slight increase of the scattering albedo with increasing solid fraction. The average absolute difference between the two SiC particle types is 0.26. With a similar extinction coefficient, this results in a significantly higher absorption coefficient for the black SiC particle suspensions and agrees with the much darker optical appearance and the observations from Section 4.4.1. The linear fit of the scattering albedo of the black SiC particle suspension is given by

$$\omega_{\text{black}}(\alpha_s) = 0.38\alpha_s + 0.49 \quad (4.18)$$

with a RMSE of 0.008 and the scattering albedo of the green SiC particle suspension is approximated with

$$\omega_{\text{green}}(\alpha_s) = 0.11\alpha_s + 0.79 \quad (4.19)$$

resulting in a RMSE of 0.023.

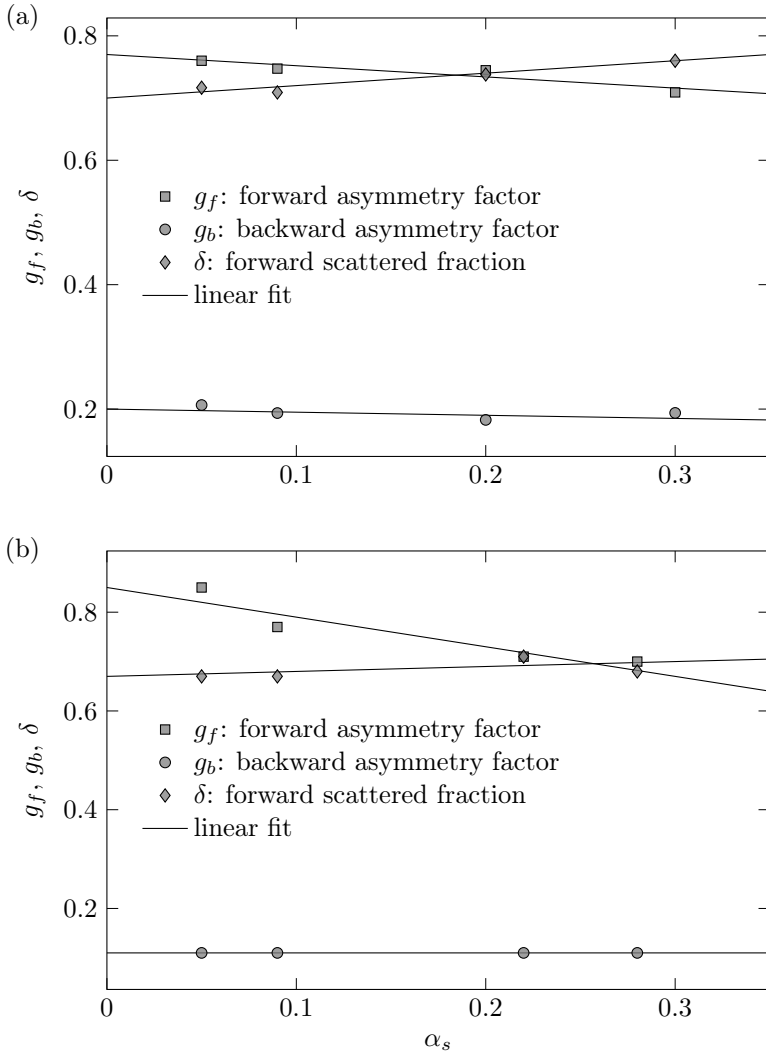


Figure 4.17: Parameters of the DHG scattering phase function derived from the Monte Carlo model for the black (a) and green SiC (b) particle suspensions as a function of the solid fraction together with linear fits.

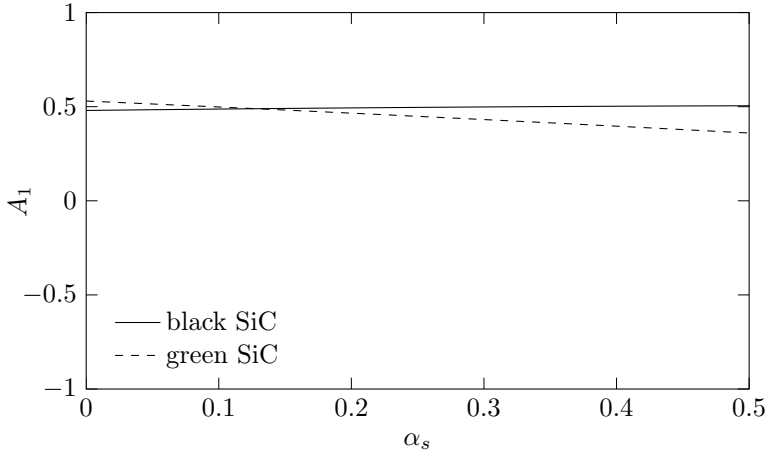


Figure 4.18: Comparison of the single asymmetry factors of the black and green SiC particle suspensions as a function of the solid fraction. The  $y$ -axis is scaled to show the possible range of  $-1 \leq A_1 \leq 1$ .

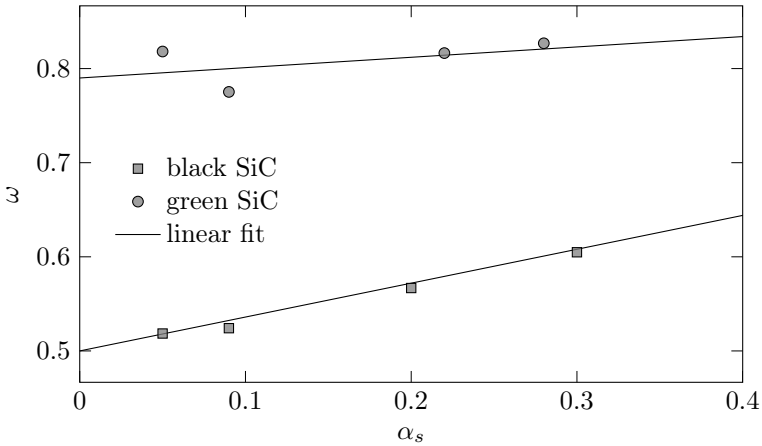


Figure 4.19: Scattering albedo of the black and green SiC particle suspension as a function of the solid fraction derived from the Monte Carlo model together with a linear fit.



### Extinction coefficient

Figure 4.20 shows a comparison of the numerically and experimentally derived extinction coefficients of the black and the green SiC particle suspensions together with the dependent scattering correlation from Singh and Kaviany [52] for a mean particle diameter  $d_p = 63.75 \mu\text{m}$ . The numerically fitted extinction coefficient shows an excellent agreement with the experimental determined value. The dependent scattering correlation from Singh and Kaviany given in Eq. (2.16) extended with Eq. (2.8) and  $Q_{\text{ext}} = 2$  results in

$$\beta(\alpha_s, d_p) = \frac{3}{d_p} (\alpha_s + 1.84\alpha_s^2 - 3.15\alpha_s^3 + 7.20\alpha_s^4) \quad (4.20)$$

With the respective mean diameter, Eq. (4.20) predicts the extinction coefficient of both SiC particle suspensions with good accuracy. The RMSE for the numerical predicted extinction coefficient of the black and green SiC particle suspensions is  $\text{RMSE} = 0.771$  and  $\text{RMSE} = 0.530$ , respectively.

A summary of the numerically derived volume-averaged radiation properties is listed in Table 4.3.

Table 4.3: Numerically derived extinction coefficient  $\beta$ , scattering albedo  $\omega$ , and parameters of the DHG scattering phase function  $g_f$ ,  $g_b$ ,  $\delta$  based on the Monte Carlo model for the black and green SiC particle suspensions.

| SiC   | $\alpha_s$ | $\beta \text{ (mm}^{-1}\text{)}$ | $\omega$ | $g_f$ | $g_b$ | $\delta$ |
|-------|------------|----------------------------------|----------|-------|-------|----------|
| Black | 0.05       | 2.49                             | 0.52     | 0.76  | 0.21  | 0.72     |
|       | 0.09       | 4.40                             | 0.52     | 0.75  | 0.19  | 0.71     |
|       | 0.20       | 13.81                            | 0.57     | 0.75  | 0.18  | 0.74     |
|       | 0.30       | 20.64                            | 0.61     | 0.71  | 0.19  | 0.76     |
| Green | 0.05       | 2.51                             | 0.82     | 0.85  | 0.11  | 0.67     |
|       | 0.09       | 4.15                             | 0.78     | 0.77  | 0.11  | 0.67     |
|       | 0.22       | 13.17                            | 0.82     | 0.71  | 0.11  | 0.71     |
|       | 0.28       | 17.90                            | 0.83     | 0.70  | 0.11  | 0.68     |

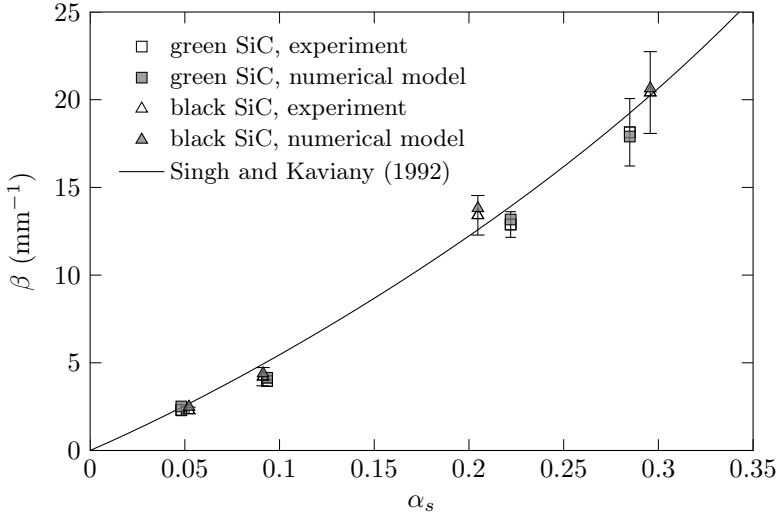


Figure 4.20: Numerically and experimentally derived extinction coefficients of the black and green SiC particle suspensions with indicated 95 % confidence uncertainty of the experimental results compared to the correlation from Singh and Kaviani [52] for a mean diameter of  $d_p = 63.75 \mu\text{m}$ .

## 4.5 Conclusion

A combined experimental-numerical approach was developed to find the volume-averaged radiative properties: extinction coefficient, scattering albedo, and approximated scattering phase function of black and green SiC particle suspensions with different solid fractions. The angular radiation distribution was measured with a spectroscopic goniometry system and used to fit a collision-based Monte Carlo model. The black and green SiC particle suspensions show similar approximated scattering phase functions with a weak dependence on the solid fraction. Compared to Mie theory, the approximated phase functions have a reduced forward scattering peak and an increased probability of backscattering. The extinction coefficient of both SiC particle suspensions is in good agreement with the dependent scattering correlation of Singh and Kaviani, indicating that the extinction coefficient is largely independent of the particle shape. The black SiC particle suspension has a scattering albedo about 40 % smaller than that of the green SiC particle suspension. With a comparable extinction coefficient, the black particle suspension has a considerably higher absorption coefficient than the green particle suspension. The failure of Mie theory to accurately predict the scattering phase function of the SiC particle suspensions indicates the importance of considering the particle shapes, dependent scattering effects, and possible material impurities.

The presented correlations provide a complete set of volume-averaged radiation properties suitable to model radiation heat transfer in gas-particle systems with changing solid fractions. Existing methods like the spherical harmonics, discrete ordinate, or statistical Monte Carlo methods, can directly incorporate the determined radiation properties to solve the radiation transfer equation.



## Part II

# Model of dense gas-particle suspensions



# Chapter 5

## Model and numerical methods<sup>1</sup>

The simulations reported in this thesis were obtained with a modified version of the transient compressible two-phase Euler-Euler solver *twoPhaseEulerFoam* of OpenFOAM 2.3.x [49]. The modifications include the implementation of a radiation heat-transfer model that makes use of the determined radiation properties from Chapter 4 and a model to calculate the effective heat conductivities depending on the local solid volume fraction. In the following, the conservation equations together with the required closure relations of the hydrodynamics and heat transfer are presented. Furthermore, the solution procedure of the model and the applied time- and space-averaging methods are shown.

---

<sup>1</sup>Material from this chapter has been published in:

J. Marti, A. Haselbacher, and A. Steinfeld, “A numerical investigation of gas-particle suspensions as heat transfer media for high-temperature concentrated solar power,” *International Journal of Heat and Mass Transfer*, accepted, 2015

## 5.1 Conservation equations

### 5.1.1 Mass conservation

The basic density-weighted solid-phase mass-conservation equation is given by

$$\frac{\partial \alpha_s \rho_s}{\partial t} + \nabla \cdot (\alpha_s \rho_s \mathbf{U}_s) = 0 \quad (5.1)$$

where  $\alpha_s$  is the solid-phase volume fraction,  $\rho_s$  is the solid-phase density, and  $\mathbf{U}_s$  is the interstitial solid-phase velocity vector. Eq. (5.1) was shown to be very unstable for large density ratios that are common in gas-particle systems [98]. A more stable approach is to handle density-related terms separate from phase-fraction transportation terms by decomposing Eq. (5.1) into

$$\rho_s \frac{\partial \alpha_s}{\partial t} + \alpha_s \frac{\partial \rho_s}{\partial t} + \rho_s \nabla \cdot (\alpha_s \mathbf{U}_s) + \alpha_s \mathbf{U}_s \cdot \nabla \rho_s = 0 \quad (5.2)$$

rearranging and dividing by  $\rho_s$  leads to

$$\frac{\partial \alpha_s}{\partial t} + \nabla \cdot (\alpha_s \mathbf{U}_s) = -\frac{\alpha_s}{\rho_s} \left( \frac{\partial \rho_s}{\partial t} + \mathbf{U}_s \cdot \nabla \rho_s \right) = -\frac{\alpha_s}{\rho_s} \frac{D \rho_s}{Dt} \quad (5.3)$$

and finally to guarantee boundedness of the solid-phase fraction, the solid-phase velocity is decomposed into mean  $\mathbf{U}$  and relative  $\mathbf{U}_r$  parts according to

$$\mathbf{U}_s = \mathbf{U} + \alpha_s \mathbf{U}_r \quad (5.4)$$

where the mean velocity is given by

$$\mathbf{U} = \alpha_s \mathbf{U}_s + \alpha_g \mathbf{U}_g \quad (5.5)$$

and the relative velocity by

$$\mathbf{U}_r = \mathbf{U}_s - \mathbf{U}_g \quad (5.6)$$

where  $\mathbf{U}_g$  is the interstitial gas-phase velocity. Replacing the solid-phase velocity in Eq. (5.3) with Eq. (5.4) leads to

$$\frac{\partial \alpha_s}{\partial t} + \nabla \cdot (\alpha_s \mathbf{U}) + \nabla \cdot (\alpha_s (1 - \alpha_s) \mathbf{U}_r) = -\frac{\alpha_s}{\rho_s} \frac{D \rho_s}{Dt} \quad (5.7)$$



and decomposing further results in

$$\frac{\partial \alpha_s}{\partial t} + \mathbf{U} \cdot \nabla \alpha_s + \nabla \cdot (\alpha_s (1 - \alpha_s) \mathbf{U}_r) = -\alpha_s \nabla \cdot \mathbf{U} - \frac{\alpha_s}{\rho_s} \frac{D \rho_s}{Dt} \quad (5.8)$$

For the gas-phase continuity equation, the same approach leads to a very similar equation given by

$$\frac{\partial \alpha_g}{\partial t} + \mathbf{U} \cdot \nabla \alpha_g - \nabla \cdot (\alpha_g (1 - \alpha_g) \mathbf{U}_r) = -\alpha_g \nabla \cdot \mathbf{U} - \frac{\alpha_g}{\rho_g} \frac{D \rho_g}{Dt} \quad (5.9)$$

Combining Eq. (5.8) and Eq. (5.9) leads to an expression for the divergence of the mean velocity according to

$$\nabla \cdot \mathbf{U} = -\frac{\alpha_s}{\rho_s} \frac{D \rho_s}{Dt} - \frac{\alpha_g}{\rho_g} \frac{D \rho_g}{Dt} \quad (5.10)$$

that can be substitute into Eq. (5.8), resulting in

$$\begin{aligned} \frac{\partial \alpha_s}{\partial t} + \mathbf{U} \cdot \nabla \alpha_s + \nabla \cdot (\alpha_s (1 - \alpha_s) \mathbf{U}_r) \\ = \alpha_s (1 - \alpha_s) \left( -\frac{1}{\rho_s} \frac{D \rho_s}{Dt} - \frac{1}{\rho_g} \frac{D \rho_g}{Dt} \right) \end{aligned} \quad (5.11)$$

and by adding  $\alpha_s \nabla \cdot \mathbf{U}$  on both sides the final form of the compressible mass-conservation equation is obtained by

$$\begin{aligned} \frac{\partial \alpha_s}{\partial t} + \nabla \cdot (\alpha_s \mathbf{U}) + \nabla \cdot (\alpha_s (1 - \alpha_s) \mathbf{U}_r) \\ = \alpha_s \nabla \cdot \mathbf{U} + \alpha_s (1 - \alpha_s) \left( -\frac{1}{\rho_s} \frac{D \rho_s}{Dt} - \frac{1}{\rho_g} \frac{D \rho_g}{Dt} \right) \end{aligned} \quad (5.12)$$

This equation is explicitly solved in time by using MULES (multidimensional limiter for explicit solution) as explained in [99]. After solving Eq. (5.12) for the solid-phase fraction  $\alpha_s$ , the gas-phase volume fraction follows from

$$\alpha_g = 1 - \alpha_s \quad (5.13)$$

### 5.1.2 Momentum conservation

#### Solid phase

The momentum conservation equation of the solid phase is given by

$$\begin{aligned} \frac{\partial \alpha_s \rho_s \mathbf{U}_s}{\partial t} + \nabla \cdot (\alpha_s \rho_s \mathbf{U}_s \mathbf{U}_s) - \left( \frac{\partial \alpha_s \rho_s}{\partial t} + \nabla \cdot (\alpha_s \rho_s \mathbf{U}_s) \right) \mathbf{U}_s - \nabla \cdot \bar{\bar{\boldsymbol{\tau}}}_s \\ = \alpha_s \rho_s \mathbf{g} - \alpha_s \nabla p - \nabla p_s + K_D (\mathbf{U}_g - \mathbf{U}_s) \end{aligned} \quad (5.14)$$

where  $\mathbf{g}$  is the gravitational-acceleration vector,  $p$  is the pressure,  $K_D$  is the interfacial drag coefficient, and  $\bar{\bar{\boldsymbol{\tau}}}_s$  is the solid viscous stress tensor defined by

$$\bar{\bar{\boldsymbol{\tau}}}_s = \rho_s \left( \nu_{s,\text{eff}} \left( (\nabla \mathbf{U}_s)^T + \nabla \mathbf{U}_s - \frac{2}{3} \nabla \cdot \mathbf{U}_s \bar{\bar{\mathbf{I}}} \right) + \nu_{s,\text{bulk}} \nabla \cdot \mathbf{U}_s \bar{\bar{\mathbf{I}}} \right) \quad (5.15)$$

where  $\nu_{s,\text{eff}}$  is the effective particle viscosity,  $\nu_{s,\text{bulk}}$  is the solid bulk viscosity, and  $\bar{\bar{\mathbf{I}}}$  is the identity tensor. The effective and bulk viscosities depend on the solid fraction as well as the kinetic-theory closure relations explained in Section 5.2.1. The solid-phase momentum equation includes a particle-pressure gradient term given by

$$\nabla p_s = \frac{\partial P_s}{\partial \alpha_s} \nabla \alpha_s \quad (5.16)$$

where  $P_s$  is the particle-pressure coefficient accounting for the momentum transport due to the motion and interaction of particles [100].

#### Gas phase

The momentum conservation equation of the gas phase is given by

$$\begin{aligned} \frac{\partial \alpha_g \rho_g \mathbf{U}_g}{\partial t} + \nabla \cdot (\alpha_g \rho_g \mathbf{U}_g \mathbf{U}_g) - \left( \frac{\partial \alpha_g \rho_g}{\partial t} + \nabla \cdot (\alpha_g \rho_g \mathbf{U}_g) \right) \mathbf{U}_g \\ - \nabla \cdot \bar{\bar{\boldsymbol{\tau}}}_g = \alpha_g \rho_g \mathbf{g} - \alpha_g \nabla p + K_D (\mathbf{U}_s - \mathbf{U}_g) \end{aligned} \quad (5.17)$$

where the gas viscous stress tensor is defined by

$$\bar{\bar{\tau}}_g = \alpha_g \rho_g \nu_g \left( (\nabla \mathbf{U}_g)^T + \nabla \mathbf{U}_g - \frac{2}{3} \nabla \cdot \mathbf{U}_g \bar{\mathbf{I}} \right) \quad (5.18)$$

where  $\nu_g$  is the gas viscosity.

The actual discretization of the solid- and gas-phase momentum equations include a predictor and corrector step. In the momentum predictor step the time derivative, convective, diffusion, and drag terms are handled implicitly while the viscous stress term is handled semi-explicitly. During the momentum corrector step the pressure gradient and gravitation terms are added explicitly to the momentum equation. In this way, the terms involving the velocity are solved implicitly and the remaining parts explicitly. Such a discretization method has been proven to be very stable [98].

### 5.1.3 Energy conservation

The energy conservation equations are based on the conservation of the total energy  $E$  defined by

$$E = e + \frac{p}{\rho} + \frac{1}{2} U^2 \quad (5.19)$$

where  $e$  is the specific internal energy, the second term on the right hand side accounts for pressure work, and the third term is the kinetic energy.

#### Solid phase

The energy conservation equation for the solid phase is given by

$$\begin{aligned} & \frac{\partial \alpha_s \rho_s e_s}{\partial t} + \nabla \cdot (\alpha_s \rho_s \mathbf{U}_s e_s) - \left( \frac{\partial \alpha_s \rho_s}{\partial t} + \nabla \cdot (\alpha_s \rho_s \mathbf{U}_s) \right) e_s \\ & + \frac{\partial \alpha_s \rho_s \frac{1}{2} |\mathbf{U}_s|^2}{\partial t} + \nabla \cdot (\alpha_s \rho_s \mathbf{U}_s \frac{1}{2} |\mathbf{U}_s|^2) - \left( \frac{\partial \alpha_s \rho_s}{\partial t} + \nabla \cdot (\alpha_s \rho_s \mathbf{U}_s) \right) \frac{1}{2} |\mathbf{U}_s|^2 \\ & + \frac{\partial \alpha_s}{\partial t} p + \nabla \cdot (\alpha_s \mathbf{U}_s p) - \nabla \cdot \left( \frac{\alpha_s k_{s,\text{eff}}}{c_{p,s}} \nabla e_s \right) = h_{\text{sg}} (T_g - T_s) + S_{\text{rad}} \end{aligned} \quad (5.20)$$

where  $e_s$  is the specific internal energy of the solid phase,  $k_{s,\text{eff}}$  is the effective solid heat conductivity,  $c_{p,s}$  is the specific heat capacity of the solid phase,  $h_{\text{sg}}$  is the interfacial heat-transfer coefficient,  $T_g$  and  $T_s$  are the gas- and solid-phase temperatures, and  $S_{\text{rad}}$  is the radiation source term.

### Gas phase

For the gas phase, the energy conservation equation is given by

$$\begin{aligned} & \frac{\partial \alpha_g \rho_g e_g}{\partial t} + \nabla \cdot (\alpha_g \rho_g \mathbf{U}_g e_g) - \left( \frac{\partial \alpha_g \rho_g}{\partial t} + \nabla \cdot (\alpha_g \rho_g \mathbf{U}_g) \right) e_g \\ & + \frac{\partial \alpha_g \rho_g \frac{1}{2} |\mathbf{U}_g|^2}{\partial t} + \nabla \cdot (\alpha_g \rho_g \mathbf{U}_g \frac{1}{2} |\mathbf{U}_g|^2) - \left( \frac{\partial \alpha_g \rho_g}{\partial t} + \nabla \cdot (\alpha_g \rho_g \mathbf{U}_g) \right) \frac{1}{2} |\mathbf{U}_g|^2 \\ & + \frac{\partial \alpha_g p}{\partial t} + \nabla \cdot (\alpha_g \mathbf{U}_g p) - \nabla \cdot \left( \frac{\alpha_g k_{g,\text{eff}}}{c_{p,g}} \nabla e_g \right) = h_{\text{sg}} (T_s - T_g) \quad (5.21) \end{aligned}$$

where  $e_g$  is the specific internal energy of the gas phase,  $k_{g,\text{eff}}$  is the effective gas heat conductivity, and  $c_{p,g}$  is the specific heat capacity of the gas phase. The transparent gas phase is assumed to be non-participating and the radiation source term is therefore neglected.

The last terms on the left hand side of Eq. (5.20) and (5.21) are the diffusion terms and describe the conduction of heat within the solid or gas phase based on Fourier's law of heat conduction. These terms are derived from the relation

$$c_p \nabla T = \nabla h \quad (5.22)$$

that is valid for ideal gases, solids, and liquids [101]. Eq. (5.22) allows the reformulation of the heat conduction term according to

$$\nabla \cdot (k \nabla T) = \nabla \cdot \left( \frac{k}{c_p} \nabla h \right) \quad (5.23)$$

With this reformulation, the diffusion terms have no direct dependence on the temperature and Eq. (5.20) and Eq. (5.21) can be solved for the specific internal energy. For a practical application, it is usually more convenient to

know the solid- and gas-phase temperatures. This is achieved by using the conversion formula

$$e = h - \frac{p}{\rho} = \int_{T_{\text{ref}}}^T c_p(T) dT - \frac{p}{\rho} \quad (5.24)$$

where  $T_{\text{ref}} = 298.15 \text{ K}$  [49]. With a constant heat capacity, the temperature is calculated from

$$T = T_{\text{ref}} + \frac{1}{c_p} \left( e + \frac{p}{\rho} \right) \quad (5.25)$$

## 5.2 Closure relations for hydrodynamics

### 5.2.1 Solid-phase stress

The solution of the solid-phase momentum conservation equation requires the solid-phase stress tensor. For dense systems, where the particle motion is controlled by particle collisions, the solid-phase stress can be explained with gas kinetic theory, which describes gas by a large number of small particles representing gas molecules [102]. Similar to the thermodynamic temperature for gases, the granular temperature  $\Theta$  describes the ensemble average of particle-velocity fluctuations  $\Theta = 1/3 \langle \mathbf{U}_s'^2 \rangle$ , where  $\mathbf{U}_s'$  is the fluctuating particle velocity. The solid-phase stress is based on these particle-velocity fluctuations. The granular temperature is determined from the transport equation for the granular energy  $3\Theta/2$  given by

$$\frac{3}{2} \left[ \frac{\partial \alpha_s \rho_s \Theta}{\partial t} + \nabla \cdot (\alpha_s \rho_s \mathbf{U}_s \Theta) \right] = \left( -P_s \Theta \bar{\bar{\mathbf{I}}} + \bar{\bar{\tau}}_s \right) : \nabla \mathbf{U}_s + \nabla \cdot (k_\Theta \nabla \Theta) - \gamma_\Theta \Theta - J_1 \Theta + J_2 \quad (5.26)$$

where the first term on the right-hand side accounts for the increase of the granular energy due to shear forces in the solid phase, the second term describes the diffusion along the gradient, the third term accounts for dissipation due to inelastic particle collisions, and  $J_1$  and  $J_2$  describe the dissipation due to viscous damping and the increase of the granular energy due

to slip between the solid and gas phase, respectively [103, 104]. The particle pressure coefficient  $P_s$  and the granular temperature dissipation coefficient  $\gamma_\Theta$  are calculated according to Lun et al. [105]

$$P_s = \rho_s \alpha_s (1 + 2(1 + e_r) \alpha_s g_0) \quad (5.27)$$

$$\gamma_\Theta = 12(1 - e_r^2) \frac{\alpha_s^2 \rho_s g_0}{d_p} \sqrt{\frac{\Theta}{\pi}} \quad (5.28)$$

where  $e_r$  is the restitution coefficient of the particles,  $g_0$  is the radial distribution function, and  $d_p$  is the particle diameter. The solid-phase stress tensor  $\bar{\bar{\tau}}_s$  is given in Eq. (5.15) and the conductivity of the granular temperature  $k_\Theta$  is determined from formulations of Gidaspow [106] given by

$$k_\Theta = \rho_s d_p \sqrt{\pi \Theta} \left( 2\alpha_s^2 g_0 \frac{1 + e_r}{\pi} + \frac{9}{8} g_0 \frac{1 + e_r}{2} \alpha_s^2 + \frac{15}{16} \alpha_s + \frac{25}{64} \frac{1}{(1 + e_r) g_0} \right) \quad (5.29)$$

The two source terms  $J_1$  and  $J_2$  are functions of the interfacial drag coefficient  $K_D$  and derived by Louge et al. [107] based on formulations of Koch [108] given by

$$J_1 = 3K_D \quad (5.30)$$

$$J_2 = \frac{d_p K_D^2 |\mathbf{U}_s - \mathbf{U}_g|^2}{4\alpha_s \rho_s \sqrt{\pi \Theta}} \quad (5.31)$$

where the solid fraction is limited to  $\alpha_s \geq 10^{-6}$  to avoid a singularity at  $\alpha_s = 0$ .

### Solid-phase viscosity

The solid-phase stress tensor given in Eq. (5.15) requires a solid-bulk and effective particle viscosity where both are based on the granular temperature that requires the solution of Eq. (5.26). On the basis of Lun et al. [105], the

solid-bulk viscosity  $\nu_{s,\text{bulk}}$  accounts for the particle-suspension compression and expansion resistance given by

$$\nu_{s,\text{bulk}} = \frac{4}{3} \alpha_s^2 d_p g_0 (1 + e_r) \sqrt{\frac{\Theta}{\pi}} \quad (5.32)$$

The effective particle viscosity  $\nu_{s,\text{eff}}$  combines a kinetic and a collisional contribution determined from formulations of Gidaspow [106] according to

$$\nu_{s,\text{eff}} = \nu_{s,\text{kin}} + \nu_{s,\text{col}} \quad (5.33)$$

where the kinetic contribution is given by

$$\nu_{s,\text{kin}} = d_p \sqrt{\Theta \pi} \left( \frac{1}{15} g_0 (1 + e_r) \alpha_s^2 + \frac{1}{6} \alpha_s + \frac{10}{96} \frac{1}{(1 + e_r) g_0} \right) \quad (5.34)$$

and the collisional contribution by

$$\nu_{s,\text{col}} = \frac{4}{5} \alpha_s^2 d_p g_0 (1 + e_r) \sqrt{\frac{\Theta}{\pi}} \quad (5.35)$$

As soon as the solid fraction exceeds a predefined limit  $\alpha_s > \alpha_{s,\text{fric}}$ , the effective particle viscosity is extended by the frictional-stress contribution defined by Johnson and Jackson [109] calculated from

$$\nu_{s,\text{fric}} = \frac{P_{\text{fric}}}{\rho_s} \sin \phi_{\text{fric}} \quad (5.36)$$

where  $\phi_{\text{fric}}$  is an empirical constant and  $P_{\text{fric}}$  is the normal frictional stress given by

$$P_{\text{fric}} = \text{Fr} \frac{(\alpha_s - \alpha_{s,\text{fric}})^{\eta_1}}{(\alpha_{s,\text{max}} - \alpha_s)^{\eta_2}} \quad (5.37)$$

where Fr,  $\eta_1$ , and  $\eta_2$  are empirical constants and  $\alpha_{s,\text{max}}$  is the predefined solid fraction at the maximum packing limit.

## Radial distribution function

The radial distribution function influences the solid-phase stress when particles are in close contact and can be explained as a non-dimensional distance

between the particles. The function modifies the collision probability for dense solid suspensions [102]. The used formulation of Sinclair and Jackson [110] is calculated from

$$g_0 = \left( 1 - \left( \frac{\min(\alpha_s, \alpha_{s,\text{fric}})}{\alpha_{s,\text{max}}} \right)^{\frac{1}{3}} \right)^{-1} \quad (5.38)$$

and reaches the correct limit in the case of a packed bed [111].

### 5.2.2 Interphase drag

The interphase drag coefficient  $K_D$  in Eq. (5.14) and (5.17) is calculated from correlations by Syamlal and O'Brien [112] or Gidaspow [106] depending on the respective application as mentioned below.

#### Drag formulation by Syamlal and O'Brien

The drag correlation by Syamlal and O'Brien [112] is given by

$$K_D = \alpha_s \alpha_g \frac{3}{4} C_D \frac{\rho_g \nu_g}{v_{r,s}^2 d_p^2} \quad (5.39)$$

where  $C_D$  is the dimensionless drag coefficient calculated from

$$C_D = \left( 0.63 \sqrt{\text{Re}_p} + 4.8 \sqrt{v_{r,s}} \right)^2 \quad (5.40)$$

where  $v_{r,s}$  is the dimensionless terminal solid velocity according to Garside and Al-Dibouni [113]

$$v_{r,s} = \frac{1}{2} \left( a - 0.06 \text{Re}_p + \sqrt{(0.06 \text{Re}_p)^2 + 0.12 \text{Re}_p (2b - a) + a^2} \right) \quad (5.41)$$

with the coefficients

$$a = (1 - \alpha_s)^{4.14} \quad (5.42)$$

$$b = \begin{cases} 0.8 (1 - \alpha_s)^{1.28}, & \alpha_s \geq 0.15 \\ (1 - \alpha_s)^{2.65}, & \alpha_s < 0.15 \end{cases} \quad (5.43)$$



and the particle Reynolds number  $\text{Re}_p$  is defined by

$$\text{Re}_p = \frac{|\mathbf{U}_s - \mathbf{U}_g| d_p}{\nu_g} \quad (5.44)$$

### Drag formulation by Gidaspow

The interphase drag coefficient of Gidaspow [106] is for low solid fractions based on the formulation by Wen and Yu [114] and for higher solid fractions based on the formulation by Ergun [115] leading to

$$K_D = \begin{cases} \alpha_s \alpha_g \frac{3}{4} C_D \frac{\rho_g \nu_g}{d_p^2} (1 - \alpha_s)^{-2.65}, & \alpha_s \leq 0.2 \\ \alpha_s \frac{\rho_g \nu_g}{d_p^2} \left( 150 \frac{1 - \alpha_g}{\alpha_g} + \frac{7}{4} \text{Re}_p \right), & \alpha_s > 0.2 \end{cases} \quad (5.45)$$

where the dimensionless drag coefficient  $C_D$  is calculated according to Rowe and Henwood [116] based on formulations by Schiller and Naumann [117] resulting in

$$C_D = \begin{cases} 0.44 \text{Re}_p, & \text{Re}_p \geq 1000 \\ 24 \left( 1 + 0.15 (\text{Re}_p)^{0.687} \right), & \text{Re}_p < 1000 \end{cases} \quad (5.46)$$

Both drag formulations limit the solid fraction and particle Reynolds number to increase the numerical stability. The solid fraction is limited to  $\alpha_s \geq 10^{-6}$  and the particle Reynolds number is limited to  $\text{Re}_p \geq 10^{-3}$ .

## 5.3 Closure relations for heat transfer

### 5.3.1 Radiation model

The radiation heat-transfer model is based on the  $P_1$ -approximation of the spherical-harmonics method [118]. This approximation is suitable for systems with an optical thickness of  $\tau > 1$  [57]. The dense gas-particle suspension in the present case has a mean optical thickness of  $\tau = O(100)$ . The

radiation source term required by Eq. (5.20) is calculated from

$$S_{\text{rad}} = \kappa (G - 4\sigma T_s^4) \quad (5.47)$$

where  $\kappa$  is the absorption coefficient,  $G$  is the incident radiation, and  $\sigma$  is the Stefan-Boltzmann constant. The incident radiation is defined as the integral of the radiation intensity  $I$  over all solid angles according to

$$G(\mathbf{r}) = \int_{4\pi} I(\mathbf{r}, \mathbf{s}) d\Omega \quad (5.48)$$

where  $\mathbf{r}$  is the position vector and  $\mathbf{s}$  the direction vector of the radiation intensity. The incident radiation is determined from

$$\nabla \cdot \left( \frac{1}{3(\kappa + \sigma_s) - A_1\sigma_s} \nabla G \right) - \kappa G = -4\kappa\sigma T_s^4 \quad (5.49)$$

where  $\sigma_s$  is the scattering coefficient and  $A_1$  is the asymmetry factor given in Eq. (2.13). Once the incident radiation is known, the radiative heat flux is computed from [57]

$$\mathbf{q}_{\text{rad}} = -\frac{1}{3(\kappa + \sigma_s) - A_1\sigma_s} \nabla G \quad (5.50)$$

For the incident radiation at walls, Marshak's wall boundary condition is applied [119, 120]. Radiation heat transfer is only considered in the solid phase since the transparent gas phase is assumed to be non-participating.

### 5.3.2 Effective conductivity

The effective bed conductivity is calculated from formulations of Zehner and Schlunder [121] according to

$$k_{\text{bed}} = k_{s,\text{bed}} + k_{g,\text{bed}} \quad (5.51)$$

where the solid- and gas-phase contributions are calculated from

$$k_{s,\text{bed}} = \frac{1}{\sqrt{\alpha_s}} (\psi a + (1 - \psi) \chi) k_{g,\text{bulk}} \quad (5.52)$$

$$k_{g,\text{bed}} = (1 - \sqrt{\alpha_s}) k_{g,\text{bulk}} \quad (5.53)$$

where  $k_{g,bulk}$  is the bulk gas-phase conductivity,  $\psi$  is a particle-shape factor ( $\psi = 7.26 \times 10^{-3}$  for spherical particles), and  $\chi$  is given by

$$\chi = \frac{2}{1 - \frac{b}{a}} \left( \frac{a-1}{(1 - \frac{b}{a})^2} \frac{b}{a} \ln\left(\frac{a}{b}\right) - \frac{b-1}{1 - \frac{b}{a}} - \frac{1}{2}(b-1) \right) \quad (5.54)$$

with

$$a = \frac{k_{s,bulk}}{k_{g,bulk}} \quad (5.55)$$

$$b = 1.25 \left( \frac{\alpha_s}{1 - \alpha_s} \right)^{\frac{10}{9}} \quad (5.56)$$

The effective solid and gas conductivities, required by Eq. (5.20) and (5.21), are obtained from

$$k_{s,eff} = \frac{k_{s,bed}}{\alpha_s} \quad (5.57)$$

$$k_{g,eff} = \frac{k_{g,bed}}{1 - \alpha_s} \quad (5.58)$$

### 5.3.3 Interphase heat transfer

Assuming spherical particles, the interphase heat-transfer coefficient in Eq. (5.20) and (5.21) is given by

$$h_{sg} = \frac{6\alpha_s}{d_p} h_p \quad (5.59)$$

where the fluid-particle heat-transfer coefficient  $h_p$  is estimated using the Ranz and Marshall [122] correlation expressed as

$$\text{Nu}_p = \frac{h_p d_p}{k_{g,bulk}} = 2 + 0.6 \text{Re}_p^{0.5} \text{Pr}^{0.333} \quad (5.60)$$

where the Prandtl number is defined by

$$\text{Pr} = \frac{\rho_g \nu_g c_{p,g}}{k_{g,bulk}} \quad (5.61)$$

## 5.4 Solution procedure

The solution procedure is based on the finite-volume method and uses the PIMPLE [123] algorithm that merges the SIMPLE [101] and PISO [124] algorithm. The SIMPLE algorithm allows under-relaxation and increases the numerical stability and improves convergence while the PISO algorithm handles the pressure-velocity coupling. For stability and efficiency reasons, the terms involving the velocity are solved implicitly. The chronological operations for each time-step are outlined as follows:

1. Update the particle-pressure gradient according to Eq. (5.16).
2. Begin the phase-fraction iteration:
  - (a) Calculate the phase volume fluxes due to the particle-pressure gradient and include them to the mean and relative phase volume fluxes.
  - (b) Solve the mass conservation equation given by Eq. (5.12) with the MULES algorithm [99] and update the solid-phase volume flux.
  - (c) Calculate the mass flux for the solid phase.
  - (d) Calculate the gas-phase fraction and the volumetric and mass fluxes of the gas phase.
3. Predict the solid- and gas-phase velocities from the momentum equation given by Eq. (5.14) and (5.17) without including pressure gradient, gravitation, and particle-pressure terms.
4. Energy conservation:
  - (a) Calculate the effective solid- and gas-phase thermal conductivities according to Eq. (5.57) and (5.58).
  - (b) Calculate the radiation source term defined in Eq. (5.47) by solving the  $P_1$ -approximation given by Eq. (5.49).
  - (c) Solve the solid- and gas-phase energy conservation equations according to Eq. (5.20) and (5.21).

5. Begin the pressure corrector step (PISO):
  - (a) Correct the predicted phase velocities with the contributions of the corrected pressure gradient, gravitational force, and particle-pressure terms.
  - (b) Update the gas-phase density due to the pressure change.
6. Repeat from step 1. until the predefined number (usually 3) of PIMPLE iterations are met.
7. Solve the granular-energy equation given by Eq. (5.26) and calculate the solid-phase stress terms.

OpenFOAM provides several methods to discretize each term in the used conservation equations separately. With exception of the boundary values, all variables are stored at cell centers. Values at cell faces are found by interpolation [49]. Table 5.1 lists the interpolation methods used in the simulations of this thesis.

Table 5.1: Input keywords for the OpenFOAM solver for various terms where  $\phi$  is a generic scalar,  $\mathbf{V}$  a generic vector, and  $\Gamma$  a generic diffusion coefficient.

| Term  | Input keyword          | Description   |
|---|------------------------|---|
| $\frac{\partial}{\partial t}$               | Euler                  | time derivative: first order, bounded, implicit                             |
| $\nabla \phi$                               | Gauss linear           | default gradient: second order, linear interpolation (central differencing) |
| $\nabla \cdot \mathbf{V}$                   | Gauss limited-Linear 1 | default divergence: second order, limited linear differencing               |
| $\nabla \cdot (\alpha_s \mathbf{U}_s)$      | Gauss vanLeer          | divergence: second order, van Leer limiter                                  |
| $\nabla \cdot \overline{\overline{\tau}}_s$ | Gauss linear           | divergence: second order, Gaussian integration                              |

---

|                                     |             |        |   |
|-------------------------------------|-------------|--------|---|
| $\nabla \cdot (\Gamma \nabla \phi)$ | Gauss       | linear | default Laplacian: central differencing |
|                                     | uncorrected |        | (interpolation), first order, bounded,  |
|                                     |             |        | non-conservative                        |

---



---

## 5.5 Time and space average

The chaotic nature of gas-particle systems, like bubbling fluidized beds, complicates the tasks of interpreting the simulation results and extracting physical mechanisms. To assist these tasks, time and space averaging is used in this thesis. The time average depends on the time-averaging interval defined by the starting  $t_{\text{start}}$  and end time  $t_{\text{end}}$  as well as on the averaging frequency  $f_{\text{ave}}$ . The total number of considered time steps is therefore given by

$$N_t = (t_{\text{end}} - t_{\text{start}}) f_{\text{ave}} \quad (5.62)$$

The applied averaging interval and averaging frequency have a crucial influence on the averaged simulation results and require a convergence study to determine their influence. By storing the simulation results during a specified time interval with a predefined averaging frequency, this convergence study is simplified. Therefore, a computed gas- or solid-phase quantity  $\xi_i^n$  is stored at each averaging time step  $n$  in each cell center  $i$ . The time-averaged quantity in cell  $i$  is given by

$$\bar{\xi}_i = \frac{1}{N_t} \sum_{n=1}^{N_t} \xi_i^n \quad (5.63)$$

The space-averaged quantity at averaging time step  $n$  of a plane crossing  $N_i$  cell centers is defined as

$$\hat{\xi}^n = \frac{1}{A_{\text{tot}}} \sum_{i=1}^{N_i} \xi_i^n A_i \quad (5.64)$$

where  $A_{\text{tot}}$  is the total area of the plane and  $A_i$  is the cross-sectional area of cell  $i$  intersected by the plane. The spatial average of the time-averaged quantity is given by

$$\widehat{\xi} = \frac{1}{A_{\text{tot}}} \sum_{i=1}^{N_i} \frac{1}{N_t} \sum_{n=1}^{N_t} \xi_i^n A_i = \frac{1}{A_{\text{tot}}} \sum_{i=1}^{N_i} \bar{\xi}_i A_i \quad (5.65)$$

A combined quantity, like the spatial average of the time-averaged solid-mass flow rate, is hence calculated from

$$\widehat{\dot{m}}_s = \frac{1}{A_{\text{tot}}} \sum_{i=1}^{N_i} \frac{1}{N_t} \sum_{n=1}^{N_t} \rho_s \alpha_{s,i}^n \mathbf{U}_{s,i}^n \cdot \mathbf{n}_i A_i \quad (5.66)$$

where  $\mathbf{U}_{s,i}^n$  is the interstitial solid velocity and  $\mathbf{n}_i$  the unit normal vector of the considered cross section.

When the time-averaging interval ( $t_{\text{end}} - t_{\text{start}}$ ) and averaging frequency  $f_{\text{ave}}$  required for a converged time-averaged result are known, a moving time average can be used to avoid the storage of data sets. The moving time average of a solid- or gas-phase quantity in cell  $i$  at the time step  $n + 1$  is given by

$$\bar{\xi}_i^{n+1} = \frac{t^{n+1} - t_{\text{start}} - \Delta t_{\text{int}}}{t^{n+1} - t_{\text{start}}} \bar{\xi}_i^n + \frac{\Delta t_{\text{int}}}{t^{n+1} - t_{\text{start}}} \xi_i^{n+1} \quad (5.67)$$

where  $\Delta t_{\text{int}}$  is the time interval between two successive data sets [49]. To reach a converged time-averaged result with the moving time average, the conditions  $t^{n+1} \geq t_{\text{end}}$  and  $\Delta t_{\text{int}} \leq 1/f_{\text{ave}}$  must be satisfied. The spacial average over a plane crossing  $N_i$  cells of a time-averaged quantity using Eq. (5.67) is given by

$$\widehat{\xi}^n = \frac{1}{A_{\text{tot}}} \sum_{i=1}^{N_i} \bar{\xi}_i^n A_i \quad (5.68)$$





## Chapter 6

### Model verification and validation<sup>1</sup>

The verification and validation of the model is divided into two parts. In a first step, the hydrodynamics are verified by comparing the velocity profile of a single-phase tube flow to the analytical solution of the Poiseuille flow and a validation is performed by comparing the pressure drop, bed expansion, and solid fraction in a bubbling fluidized bed with experimental data from literature. Furthermore, comparisons with numerical results from literature are used as benchmark. The second step includes verification and validation studies of the heat transfer using analytical and experimental results. The transient heat transfer is verified by using the analytical result of the transient convective heating of a one-dimensional packed bed. The radiation model is verified by comparing the incoming radiation in a two-dimensional enclosure to approximated analytical and Monte Carlo ray-tracing solutions. Finally, experimental results of steady-state temperature profiles in a packed bed are used to validate the model with respect to conduction combined with radiation heat transfer.

---

<sup>1</sup>Material from this chapter has been published in:

J. Marti, A. Haselbacher, and A. Steinfeld, “A numerical investigation of gas-particle suspensions as heat transfer media for high-temperature concentrated solar power,” *International Journal of Heat and Mass Transfer*, accepted, 2015

## 6.1 Hydrodynamics

### 6.1.1 Single-phase flow verification

The Hagen-Poiseuille equation gives for a laminar incompressible single-phase flow the analytical solution of the fully developed velocity profile in a three-dimensional cylindrical pipe flow [125]. Applied to a two-dimensional flow, the analytical solution of the velocity profile is given by

$$u(x) = \frac{1}{2\mu} \frac{\Delta p}{L} (d^2 - x^2) \quad (6.1)$$

where  $\mu$  is the dynamic viscosity of the fluid,  $\Delta p$  is the pressure drop over the tube length  $L$ ,  $d$  is the tube diameter, and  $x$  is the radial coordinate. The normalization of Eq. (6.1) with the cross-section-averaged flow velocity  $\hat{u}$  gives

$$\frac{u(x)}{\hat{u}} = \frac{3}{2} \frac{d^2 - x^2}{d^2} \quad (6.2)$$

The model uses a parabolic velocity profile at the inlet ( $y = 0$ ), a pressure opening at the outlet ( $y = L$ ), and no-slip boundary conditions at the walls ( $x = -d/2$ ,  $x = d/2$ ). The model parameters are listed in Table 6.1. Figure 6.1 shows the comparison of the normalized velocity profile of the analytical solution with the numerical result. The numerical result shows the fully developed velocity profile at  $y/L = 0.8$  where  $y$  is the axial coordinate in flow direction. The analytical and numerical results are in excellent agreement.

### 6.1.2 Bubbling fluidized bed validation

The investigated dense gas-particle suspension used as HTM behaves from a hydrodynamic point of view very similar than a bubbling fluidized bed. The hydrodynamics were therefore validated by comparison with experimental and numerical results of bubbling fluidized beds. The experimental data were obtained in a pseudo-two-dimensional fluidized bed with a height of 1 m, a width of 0.28 m, and a depth of 0.025 m operated with glass beads of

Table 6.1: Model parameters of the Hagen-Poiseuille verification case.

| Property             | Symbol          | Value                   |
|----------------------|-----------------|-------------------------|
| tube diameter        | $d$             | 0.036 m                 |
| tube length          | $L$             | 1.0 m                   |
| fluid density        | $\rho$          | 1000 kg/m <sup>3</sup>  |
| fluid kin. viscosity | $\mu$           | 0.001 m <sup>2</sup> /s |
| fluid inlet velocity | $U_{\text{in}}$ | 0.1 m/s                 |
| cell size            | $\Delta x$      | 1.0 mm                  |

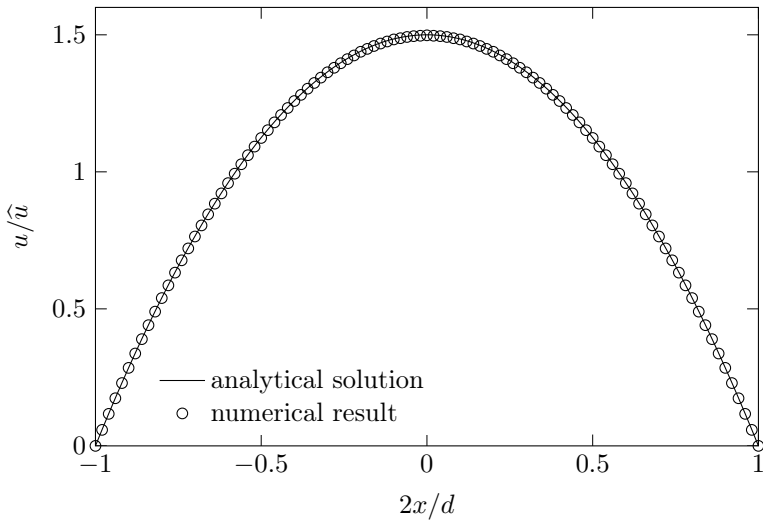


Figure 6.1: Comparison of the analytical solution and the numerical result of the normalized velocity profile of a fully developed two-dimensional incompressible laminar pipe flow. The numerical result is shown for  $y/L = 0.8$ .

250–300  $\mu\text{m}$  diameter [126]. The numerical reference results were computed with the commercial software ANSYS FLUENT [127] and the open-source software MFIX [112] in two dimensions by neglecting the small depth [126, 128]. Table 6.2 lists the dimensions and operating conditions of our two-dimensional simulation with OpenFOAM. As in [126, 128], the Johnson and Jackson wall boundary condition [109] was used for the solid phase. The inlet of the fluidized bed was impermeable for the solid phase while a uniform Dirichlet boundary condition was utilized for the gas-phase velocity in the range of 0.1–0.46 m/s. After a freeboard section, the gas phase exited through a fixed pressure outlet. The drag force was calculated with the Syamlal-O’Brien model [112]. The granular temperature in the reference simulation was based on a simplified algebraic equation while our simulation was based on the full balance equation of the kinetic theory given in Eq. (5.26). Figure 6.2 shows a schematic of the initial packed bed with indicated dimensions and boundary conditions as listed in Table 6.2.

Table 6.2: Model parameters of the hydrodynamics validation case.

| Property               | Symbol                              | Value                                       |
|------------------------|-------------------------------------|---|
| tube width             | $W$                                 | 0.28 m                                      |
| tube height            | $H$                                 | 1.25 m                                      |
| initial bed height     | $H_0$                               | 0.48 m                                      |
| atmospheric pressure   | $p_{\text{atm}}$                    | $0.85 \times 10^5 \text{ Pa}$               |
| particle density       | $\rho_s$                            | $2500 \text{ kg/m}^3$                       |
| particle diameter      | $d_p$                               | $275 \mu\text{m}$                           |
| initial solid fraction | $\alpha_{s,0}$                      | 0.5   |
| max. solid fraction    | $\alpha_{s,\text{max}}$             | 0.6   |
| gas density            | $\rho_g$                            | $1.225 \text{ kg/m}^3$                      |
| gas kin. viscosity     | $\nu_g$                             | $1.485 \times 10^{-5} \text{ m}^2/\text{s}$ |
| gas inlet velocity     | $U_{g,\text{in}}$                   | 0.1–0.46 m/s                                |
| averaging interval     | $t_{\text{end}} - t_{\text{start}}$ | 55 s  |
| averaging frequency    | $f_{\text{ave}}$                    | 20 Hz                                       |

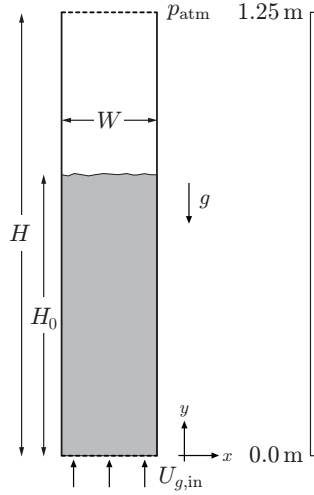


Figure 6.2: Schematic of the fluidized bed with indicated dimensions and boundary conditions. The origin is located at the inlet on the centerline.

### Grid refinement

The influence of the computational grid was evaluated by performing a grid-refinement study with five grid levels. Figure 6.3 shows a comparison of the different grid spacings  $\Delta x$  as a function of the radial direction. The cell size was uniformly refined from 20.0 mm to 1.25 mm. Table 6.3 list the considered grids with the cell size and total number of cells. The tube height of the coarsest grid had to be increased to  $H = 1.4\text{ m}$  due to the higher bed expansion during the start-up phase.

To evaluate the influence of the computational grid on the hydrodynamics, the solid-velocity and solid-fraction profiles as well as the cross-section-averaged solid fraction in the axial direction were compared for the different grid levels. For this grid-refinement study, a constant gas inlet velocity of

$U_{g,\text{in}} = 0.46 \text{ m/s}$  was used. The considered quantities were time averaged with a time-averaging interval between  $t_{\text{start}} = 5 \text{ s}$  and  $t_{\text{end}} = 60 \text{ s}$  and an averaging frequency of  $f_{\text{ave}} = 20 \text{ Hz}$  as explained in Section 5.5.

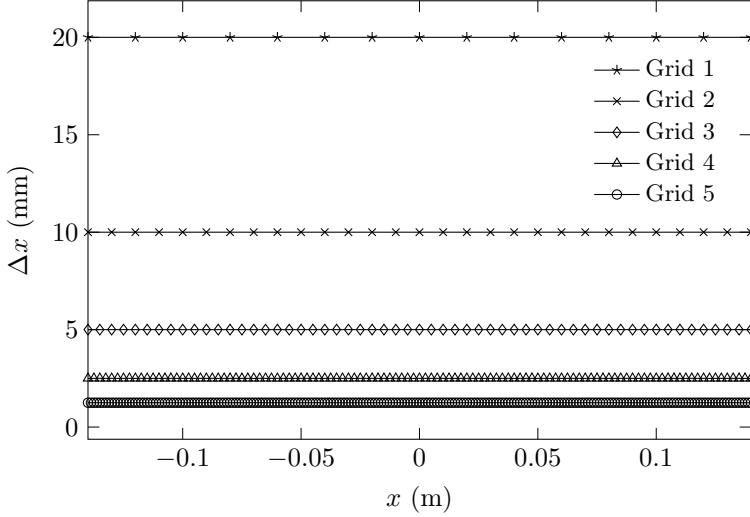


Figure 6.3: Comparison of the considered grid spacings as a function of the radial direction for the grid-refinement study of the hydrodynamics validation case.

Figure 6.4 shows the time-averaged solid-velocity profiles at an axial location of  $y = 0.4 \text{ m}$  (a) and  $y = 0.2 \text{ m}$  (b) for the different grid refinement levels. The results with Grid 1 and 2 distinguish, especially for  $y = 0.2 \text{ m}$ , considerably from the results with Grids 3–5. The agreement between the results with Grids 3–5 is good.

Figure 6.5 shows the time-averaged solid-fraction profiles at an axial location of  $y = 0.4 \text{ m}$  (a) and  $y = 0.2 \text{ m}$  (b) for the different grid refinement levels. The results with Grid 4 and 5 are very similar while the results with Grids 1–3 differ considerably from the results with Grid 5.

Figure 6.6 shows the time- and cross-section-averaged solid fraction in the axial direction for the different grid refinement levels. The axial location of the steep solid fraction decrease at about  $y = 0.65 \text{ m}$  indicates the

Table 6.3: Cell sizes and total number of grid cells used in the grid-refinement study of the hydrodynamics validation case.

| Grid | Cell size (mm) | Number of cells |
|------|----------------|-----------------|
| 1    | 20.0           | 980             |
| 2    | 10.0           | 3500            |
| 3    | 5.0            | 14000           |
| 4    | 2.5            | 56000           |
| 5    | 1.25           | 224000          |

transition from the bubbling fluidized bed (dense region) into the freeboard region. The results with Grid 1 and 2 show a bigger bed expansion compared to the result with Grid 5. The difference between the solid fraction distribution in the axial direction with Grid 4 and 5 is marginal.

The considered solid velocity and solid fraction profiles as well as the solid fraction in the axial direction did not change appreciably when decreasing the cell size from 2.5 mm (Grid 4) to 1.25 mm (Grid 5). It was thus assumed that a cell size of 2.5 mm is adequate and leads to nearly grid-independent results. It should be noted that the grid spacings used by Herzog et al. [128] and Taghipour et al. [126] were two and four times bigger than the grid spacing used in our simulation, respectively.

### Time average

The time averaging of the transient results was assessed by varying the averaging interval between  $t_{\text{start}} = 5$  s and  $t_{\text{end}} = 10\text{--}120$  s and the averaging frequency from 1 Hz to 100 Hz. The first five seconds were neglected to allow enough time for the transition from the initial packed to the bubbling state. Based on the previous grid-refinement study, a grid spacing of 2.5 mm was used. Since the grid spacing is the same for each case, no symbols are used to visualize the cell locations.

Figures 6.7, 6.8, and 6.9 show the time-averaged solid-velocity and solid-

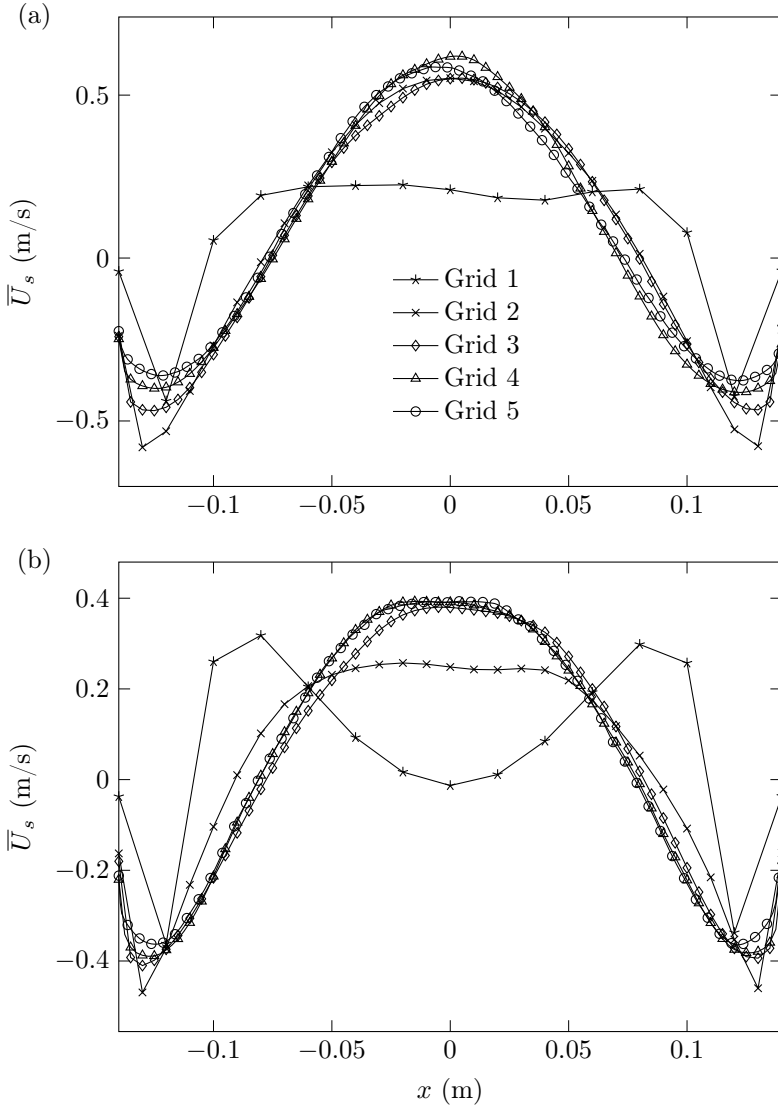


Figure 6.4: Time-averaged solid-velocity profiles at  $y = 0.4$  m (a) and  $y = 0.2$  m (b) for different grid refinement levels with a gas inlet velocity of  $U_{g,\text{in}} = 0.46$  m/s. (To avoid overlapping, the symbols of Grid 4 and 5 are shown ever 2nd and 4th cell location, respectively.)



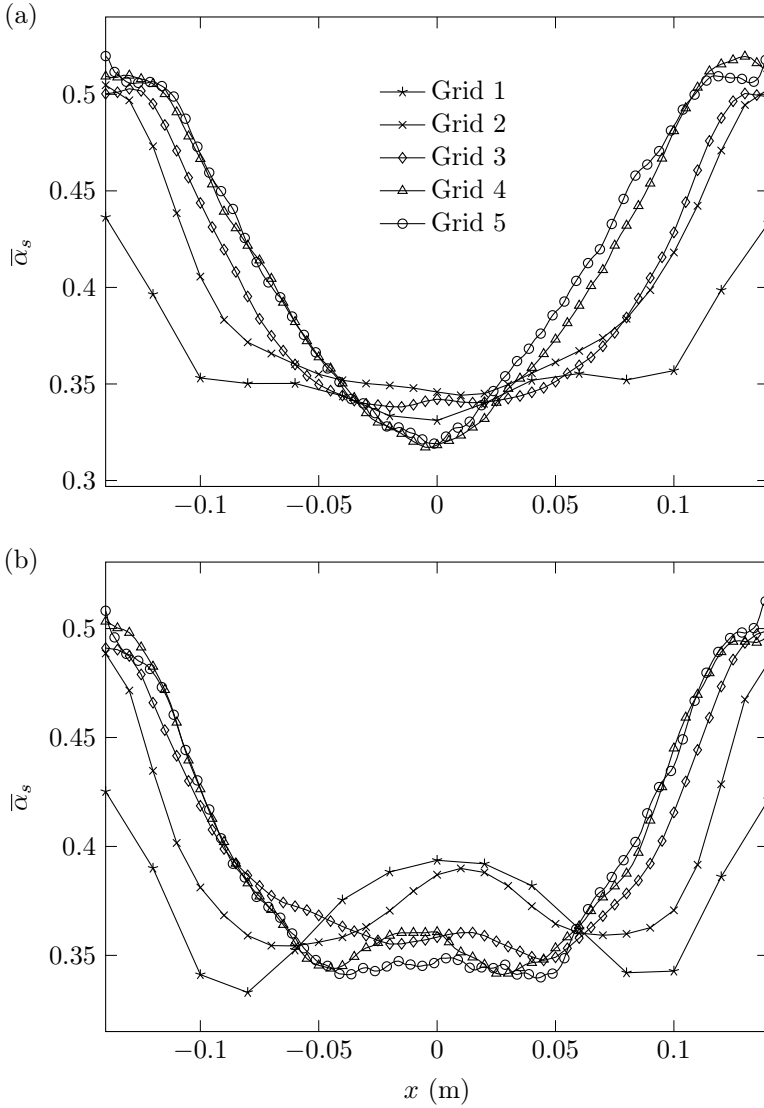


Figure 6.5: Time-averaged solid-fraction profiles at  $y = 0.4$  m (a) and  $y = 0.2$  m (b) for different grid refinement levels with a gas inlet velocity of  $U_{g,\text{in}} = 0.46$  m/s. (To avoid overlapping, the symbols of Grid 4 and 5 are shown ever 2nd and 4th cell location, respectively.)

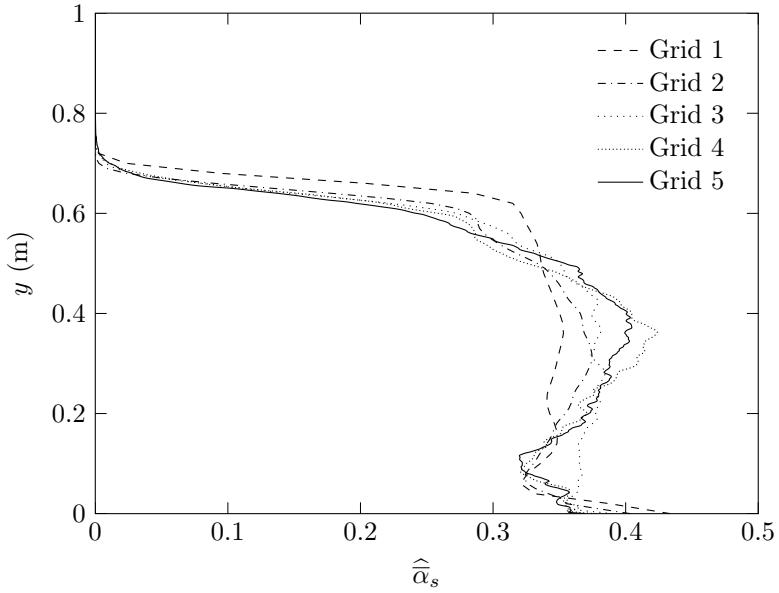


Figure 6.6: Time- and cross-section-averaged solid fraction in the axial direction for different grid refinement levels with a gas inlet velocity of  $U_{g,\text{in}} = 0.46 \text{ m/s}$ . (To avoid overlapping, symbols are not shown.)

fraction profiles at  $y = 0.4$  m (a) and  $y = 0.2$  m (b) as well as the time- and cross-section-averaged solid fraction in the axial direction for different averaging frequencies and a constant averaging interval between  $t_{\text{start}} = 5$  s and  $t_{\text{end}} = 60$  s. Increasing the averaging frequency from 20 Hz to 100 Hz has no considerable influence on the solid velocity or solid fraction. A averaging frequency of 20 Hz was therefore assumed to be sufficient.

Figures 6.10, 6.11, and 6.12 show the time-averaged solid-velocity and solid-fraction profiles at  $y = 0.4$  m (a) and  $y = 0.2$  m (b) as well as the time- and cross-section-averaged solid fraction in the axial direction for different averaging intervals and a constant averaging frequency of 20 Hz. Increasing the averaging interval from 5–60 s to 5–120 s has no considerable influence on the solid velocity or solid fraction. It was thus assumed that an averaging interval between  $t_{\text{start}} = 5$  s and  $t_{\text{end}} = 60$  s is adequate and leads to averaging-interval-independent results.

Based on the presented results, a converged time-averaged solid-fraction and solid-velocity field was achieved by using an averaging frequency of 20 Hz with an averaging interval between  $t_{\text{start}} = 5$  s and  $t_{\text{end}} = 60$  s. The bubbles had a mean bed residence time of approximately 0.9 s. Therefore, the averaging interval corresponds to about 61 bubble mean bed-residence times and about 18 data sets were averaged per bubble mean bed-residence time. Taghipour et al. [126] did not describe their averaging procedure while Herzog et al. [128] used a time-averaging interval of only 3–12 s with an unknown averaging frequency.

## Validation with experimental and numerical results

After a grid-refinement and time-averaging study, the results of the model were compared to experimental and numerical results from literature. Figure 6.13 shows the time- and space-averaged pressure drop through the bed as a function of the inflow velocity. Our result and the reference results of Herzog et al. [128] show the expected increase in the pressure drop with increasing inflow velocity up to fluidization and a nearly constant pressure drop once the bed is fluidized. This constant pressure drop is slightly below

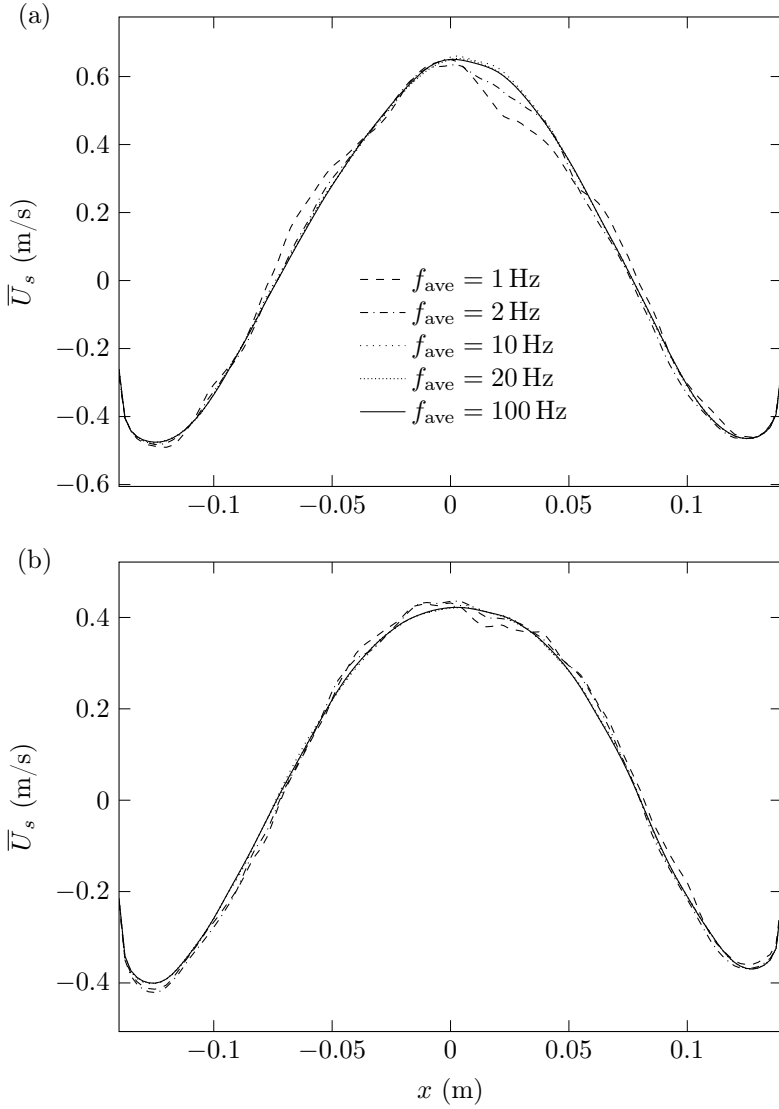


Figure 6.7: Time-averaged solid-velocity profiles at  $y = 0.4$  m (a) and  $y = 0.2$  m (b) for different averaging frequencies and a constant averaging interval between  $t_{\text{start}} = 5$  s and  $t_{\text{end}} = 60$  s with a grid spacing of 2.5 mm and a gas inlet velocity of  $U_{g,\text{in}} = 0.46$  m/s.

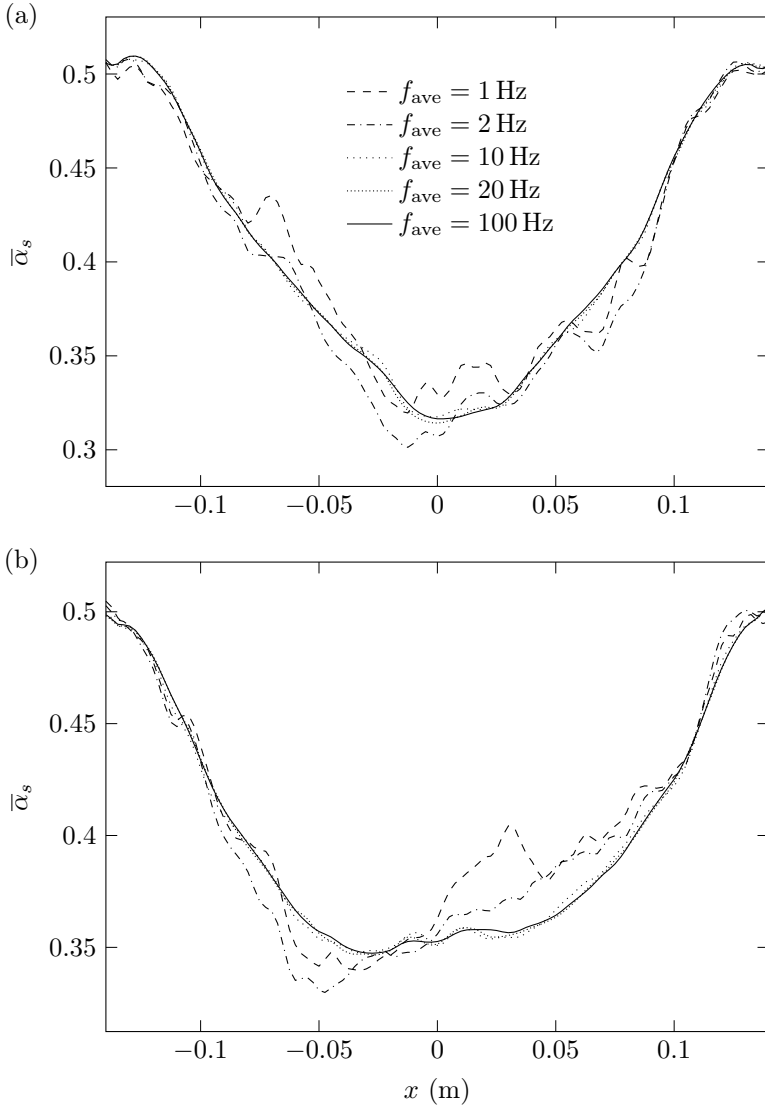


Figure 6.8: Time-averaged solid-fraction profiles at  $y = 0.4$  m (a) and  $y = 0.2$  m (b) for different averaging frequencies and a constant averaging interval between  $t_{\text{start}} = 5$  s and  $t_{\text{end}} = 60$  s with a grid spacing of 2.5 mm and a gas inlet velocity of  $U_{g,\text{in}} = 0.46$  m/s.

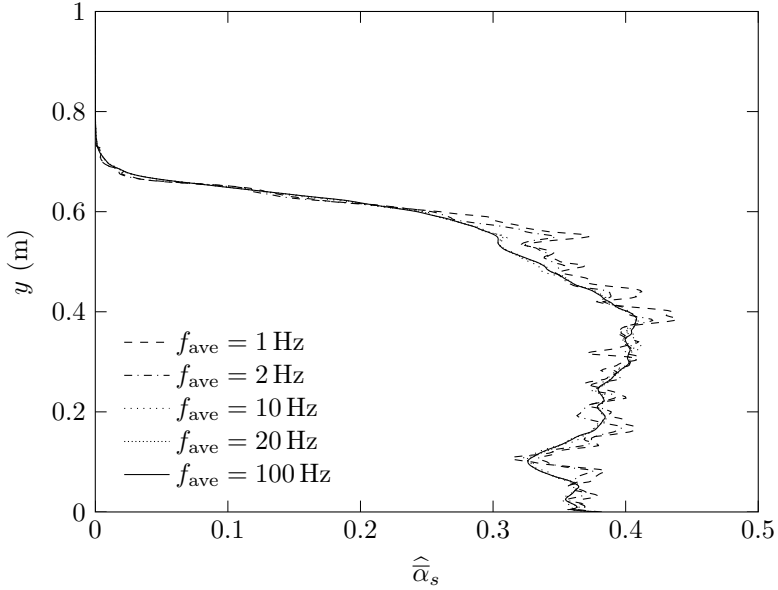


Figure 6.9: Time- and cross-section-averaged solid fraction in the axial direction for different averaging frequencies and a constant averaging interval between  $t_{\text{start}} = 5$  s and  $t_{\text{end}} = 60$  s with a grid spacing of 2.5 mm and a gas inlet velocity of  $U_{g,\text{in}} = 0.46$  m/s.

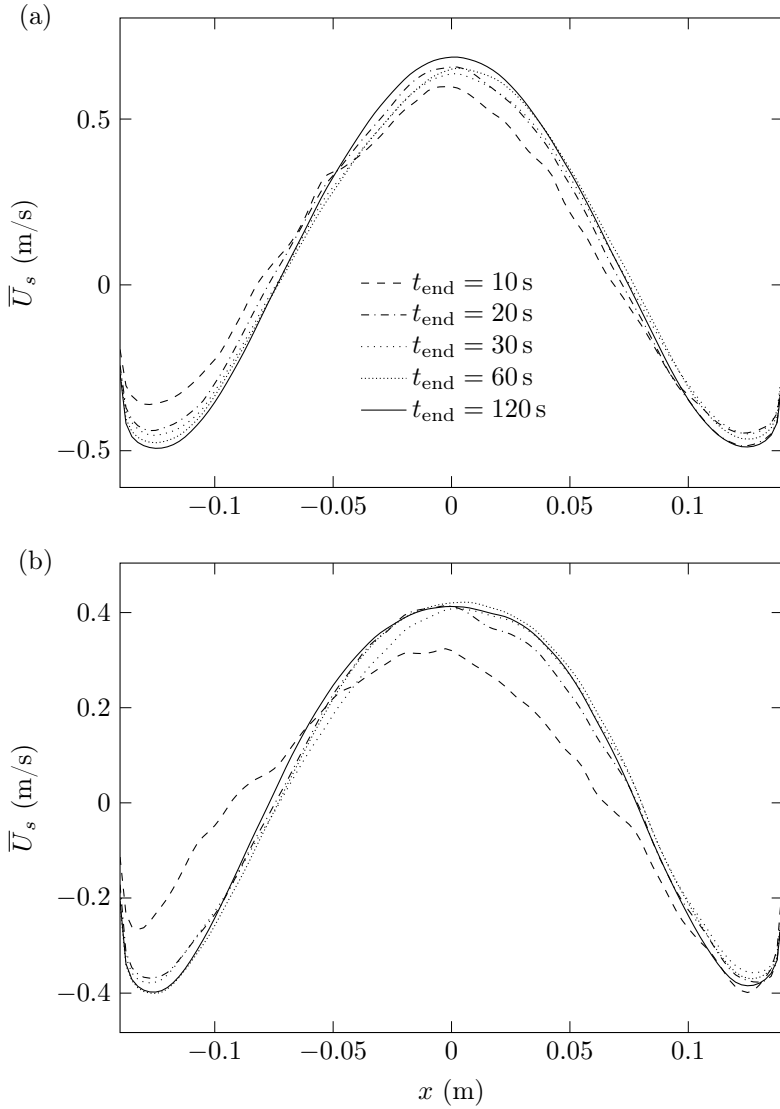


Figure 6.10: Time-averaged solid-velocity profiles at  $y = 0.4$  m (a) and  $y = 0.2$  m (b) for different averaging intervals and a constant averaging frequency of 20 Hz with a grid spacing of 2.5 mm and a gas inlet velocity of  $U_{g,\text{in}} = 0.46$  m/s.

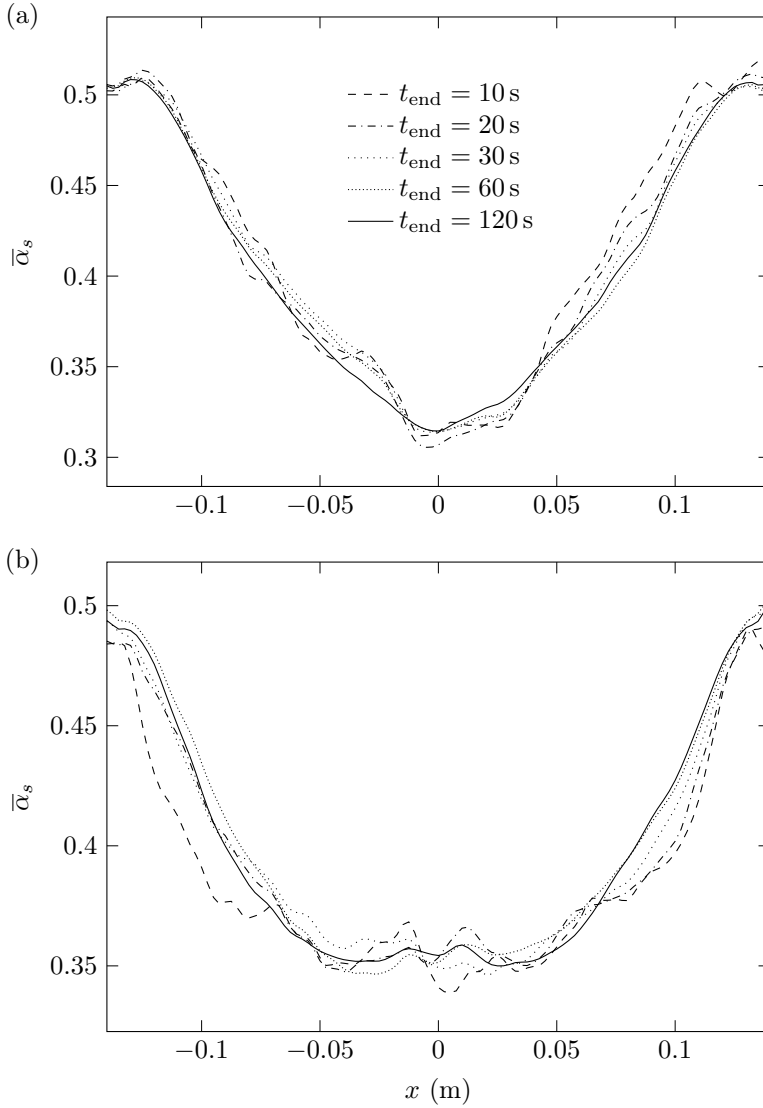


Figure 6.11: Time-averaged solid-fraction profiles at  $y = 0.4$  m (a) and  $y = 0.2$  m (b) for different averaging intervals and a constant averaging frequency of 20 Hz with a grid spacing of 2.5 mm and a gas inlet velocity of  $U_{g,\text{in}} = 0.46$  m/s.



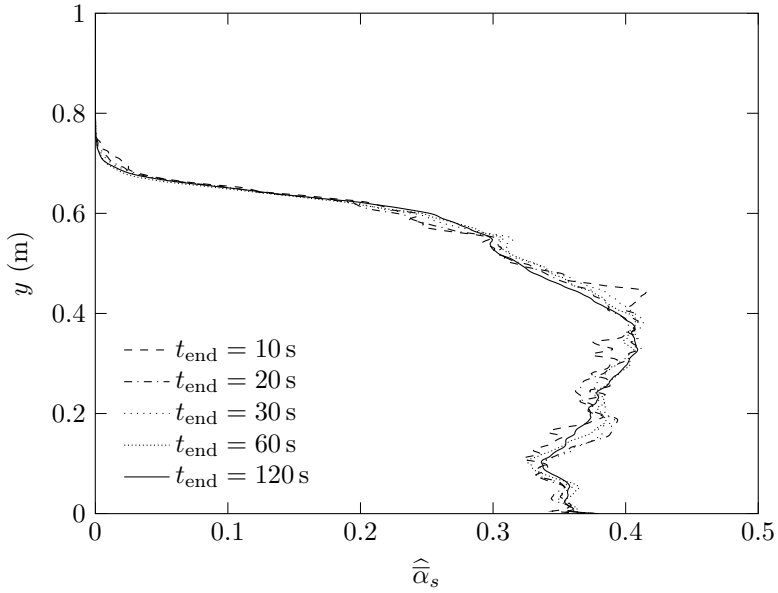


Figure 6.12: Time- and cross-section-averaged solid fraction in the axial direction for different averaging intervals and a constant averaging frequency of 20 Hz with a grid spacing of 2.5 mm and a gas inlet velocity of  $U_{g,\text{in}} = 0.46$  m/s.

the theoretically predicted pressure drop due to the bed weight per cross-sectional area. The maximum pressure drop of our results and the results of Herzog et al. [128] is reached at minimum fluidization velocity. This agrees with theoretical and experimental results [28]. The experimental results of Taghipour et al [126] show a deviation from the expected fluidization curve with an underprediction of the pressure drop at minimum fluidization velocity and an overprediction at high flow velocities. A possible reason for this behavior is incomplete fluidization due to channeling.

The time- and space-averaged bed expansion as a function of the inflow velocity is presented in Figure 6.14. Our results are comparable to those of Herzog et al. [128], while the results of Taghipour et al. [126] show a smaller bed expansion. The experimental measurements show a higher bed expansion for low inflow velocities and a slightly reduced expansion for increased flow velocities.

Figures 6.15 and 6.16 present comparisons of the time-averaged solid-fraction and solid-velocity profiles of our model with the reference results at  $y = 0.2\text{ m}$ . Compared to the results obtained by Herzog et al. [128] with MFIX, our model predicts a similar solid fraction in the core region and a lower solid fraction near the walls. A possible reason for this deviation could be the coarser grid spacing and/or different parameters of the Johnson and Jackson wall boundary condition used by Herzog et al. [128]. The solid velocity shows a similar trend with very good agreement in the core region and deviations near the wall compared to the results obtained with MFIX. Our solid-fraction and solid-velocity profiles are closer to axial symmetry as a result of the increased averaging interval and the higher averaging frequency.

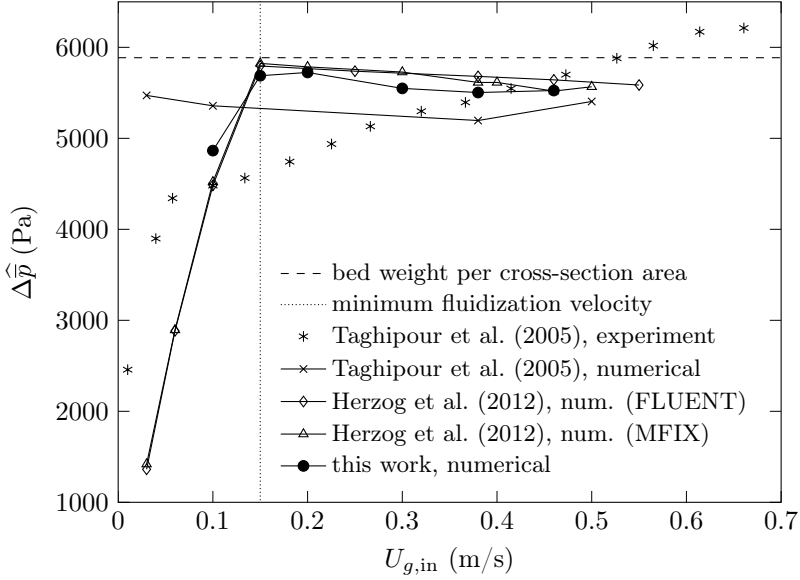


Figure 6.13: Comparison of the time- and space-averaged pressure drop of our model with experimental and numerical reference results by Taghipour et al. [126] and Herzog et al. [128] as a function of the gas inlet velocity  $U_{g,in}$ . Also indicated is the theoretical pressure drop due to the bed weight and the minimum fluidization velocity.

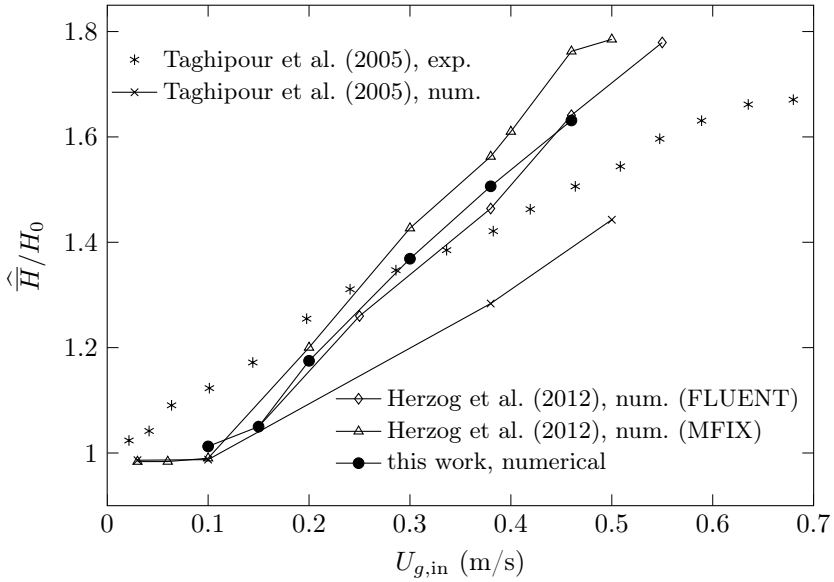


Figure 6.14: Comparison of the time- and space-averaged normalized bed height  $\hat{H}/H_0$  of our model with experimental and numerical results by Taghipour et al. [126] and Herzog et al. [128] as a function of the inlet velocity  $U_{g,in}$ .

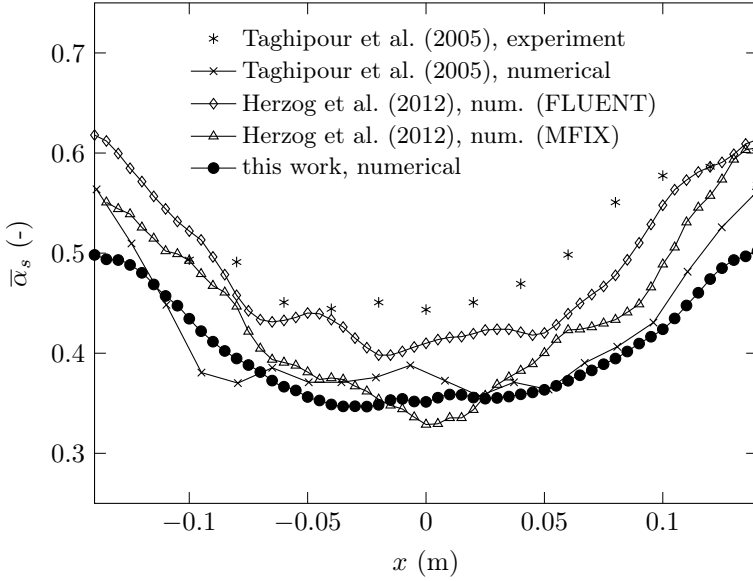


Figure 6.15: Comparison of the time-averaged solid-fraction profile of our model with experimental and numerical reference results by Taghipour et al. [126] and Herzog et al. [128] for a gas inlet velocity of  $U_{g,\text{in}} = 0.46 \text{ m/s}$  at  $y = 0.2 \text{ m}$ . (Due to overlapping symbols, only every second data point is shown in our results.)

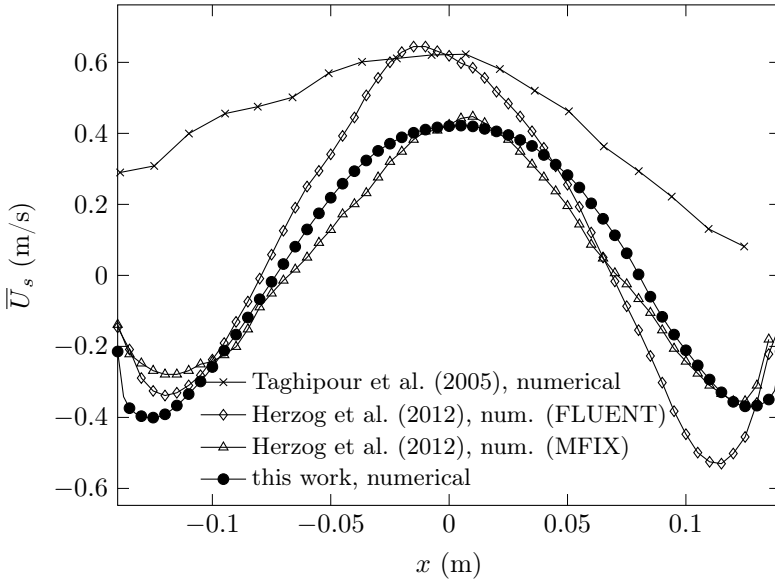


Figure 6.16: Comparison of the time-averaged solid-velocity profile of our model with numerical reference results by Taghipour et al. [126] and Herzog et al. [128] for an inlet velocity of  $U_{g,\text{in}} = 0.46$  m/s at  $y = 0.2$  m. (Due to overlapping symbols, only every second data point is shown in our results.)

## 6.2 Heat transfer

After the verification and validation of the hydrodynamics, this section presents verification and validation studies of the heat transfer.

### 6.2.1 Transient convective heat-transfer verification

The capability of the model to represent transient heat transfer was verified by using an initially cold packed bed that is heated up by a hot fluid flow. For large Péclet numbers ( $Pe > 100$ ), conduction is negligible and neglecting wall effects allows simplification to a one-dimensional convection problem with an interfacial heat-transfer term [129]. The solid- and fluid-phase energy conservation equations to this problem are given by

$$\alpha_s \rho_s c_{p,s} \frac{\partial T_s}{\partial t} = h_{fs} (T_f - T_s) \quad (6.3)$$

$$(1 - \alpha_s) \rho_f c_{p,f} \frac{\partial T_f}{\partial t} + (1 - \alpha_s) \rho_f c_{p,f} U_f \frac{\partial T_f}{\partial x} = h_{fs} (T_s - T_f) \quad (6.4)$$

where the subscript  $f$  describes the fluid phase and  $h_{fs}$  is the fluid-solid heat-transfer coefficient [130]. Together with suitable initial and boundary conditions, this system of equations can be solved analytically as shown by Schumann [131]. Table 6.4 list the applied model parameters. Figure 6.17 shows the normalized fluid-temperature profile in flow direction of the analytical solution compared to the results of our model for several time steps. The results predicted by our model are in excellent agreement with the analytical solution of Schumann.

Table 6.4: Model parameters of the convective heat transfer verification case.

| Property          | Symbol     | Value  |
|-------------------|------------|--------|
| grid cell size    | $\Delta x$ | 0.5 mm |
| tube height       | $h$        | 2.0 m  |
| packed bed height | $h_0$      | 1.5 m  |

|                            |              |                                      |
|----------------------------|--------------|--------------------------------------|
| solid fraction             | $\alpha_s$   | 0.5                                  |
| solid density              | $\rho_s$     | 8500 kg/m <sup>3</sup>               |
| solid heat capacity        | $c_{p,s}$    | 385 J/kg m <sup>3</sup>              |
| solid thermal conductivity | $k_{s,bulk}$ | 0 W/kg K                             |
| particle diameter          | $d_p$        | 3.95 mm                              |
| Prandtl number             | Pr           | 0.8374                               |
| Reynolds number            | Re           | 3950                                 |
| Péclet number              | Pe = RePr    | 3308                                 |
| fluid density              | $\rho_f$     | 1000 kg/m <sup>3</sup>               |
| fluid kin. viscosity       | $\nu_f$      | $1 \times 10^{-7}$ m <sup>2</sup> /s |
| fluid heat capacity        | $c_{p,f}$    | 4187 J/kgK                           |
| fluid thermal conductivity | $k_{f,bulk}$ | 0.5 W/m K                            |
| fluid inlet velocity       | $U_{f,in}$   | 0.15 m/s                             |
| initial temperature        | $T_0$        | 300 K                                |
| fluid inlet temperature    | $T_{f,in}$   | 400 K                                |

### 6.2.2 Radiation heat-transfer verification

The implementation of the  $P_1$ -approximation was verified by comparing the incoming irradiation in a two-dimensional square enclosure predicted by our model with the analytical solution of the  $P_1$ -approximation and the exact solution with Monte Carlo ray tracing [57]. The square enclosure has a purely scattering medium in between, a hot bottom wall at  $T_{w,hot} = 300$  K emitting radiation, and cold side and top walls at  $T_{w,cold} = 0$  K absorbing radiation. The square side length is  $L = 1.0$  m and the medium in between has a scattering coefficient of  $\sigma_s = 1.0$  m<sup>-1</sup>. The incoming irradiation onto a wall was calculated from

$$E_w = \mathbf{q}_{rad,w} \cdot \mathbf{n}_w \quad (6.5)$$



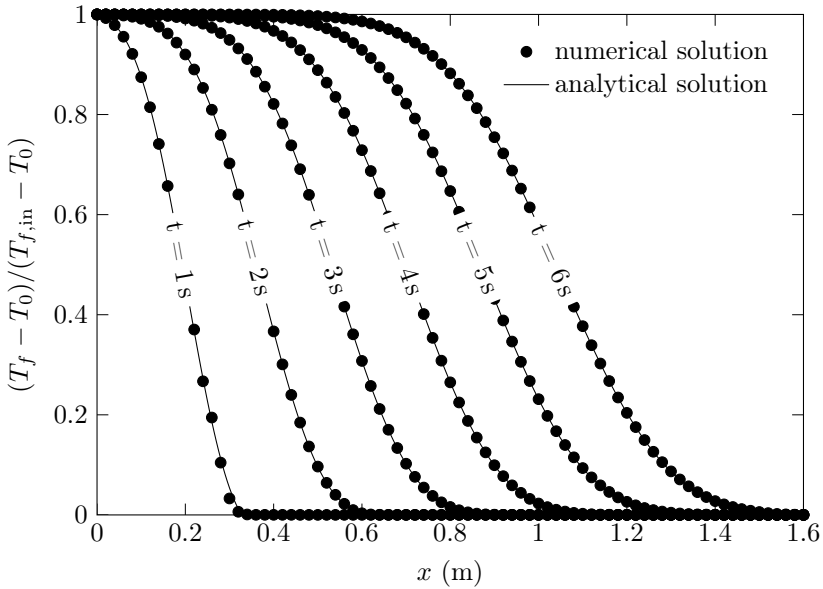


Figure 6.17: Normalized fluid-temperature profile along the flow direction in a one-dimensional packed bed for different time steps. The analytical solution of Schumann [131] is compared to the results predicted by our model. (Symbols are shown for every 4th grid cell.)

where  $\mathbf{q}_{\text{rad},w}$  is the radiative heat flux on the wall and  $\mathbf{n}_w$  is the wall-surface normal vector pointing out of the domain ( $\mathbf{q}_{\text{rad},w} \cdot \mathbf{n}_w > 0$  for net incoming heat flux and  $\mathbf{q}_{\text{rad},w} \cdot \mathbf{n}_w < 0$  for net outgoing heat flux). For the incident radiation Marshak's wall boundary condition [119, 120] was applied. Table 6.5 lists the relevant model parameters.

Figure 6.18 compares the results for the incoming irradiation on the square-enclosure walls. The results of our numerical model agrees well with the analytical solution of the  $P_1$ -approximation but differs from the exact solution computed with the Monte Carlo method. This difference is well known for optically-thin ( $\tau \ll 1$ ) cases [57]. In the present case with a dense suspension of small particles, the mean optical thickness is  $\tau = O(100)$  and therefore suitable for the  $P_1$ -approximation.

Table 6.5: Model parameters of the radiation-model verification case.

| Property                       | Symbol              | Value                |
|--------------------------------|---------------------|----------------------|
| grid cell size                 | $\Delta x$          | 10 mm                |
| side length                    | $L$                 | 1.0 m                |
| scattering coefficient         | $\sigma_s$          | $1.0 \text{ m}^{-1}$ |
| absorption coefficient         | $\kappa$            | $0.0 \text{ m}^{-1}$ |
| wall emissivity                | $\epsilon$          | 1.0                  |
| bottom wall temperature        | $T_{w,\text{hot}}$  | 300 K                |
| top and side wall temperatures | $T_{w,\text{cold}}$ | 0 K                  |

### 6.2.3 Steady-state conduction and radiation validation

Combined conduction and radiation heat transfer was validated with steady-state temperature measurements by Kamiuto et al. [132]. They considered an annular packed bed formed by concentric tubes and cordierite spheres with a mean diameter of 6.94 mm. The inner tube was heated electrically and the outer tube was cooled to maintain a constant temperature gradient. Due to the tube length and uniform heating, axial boundary effects

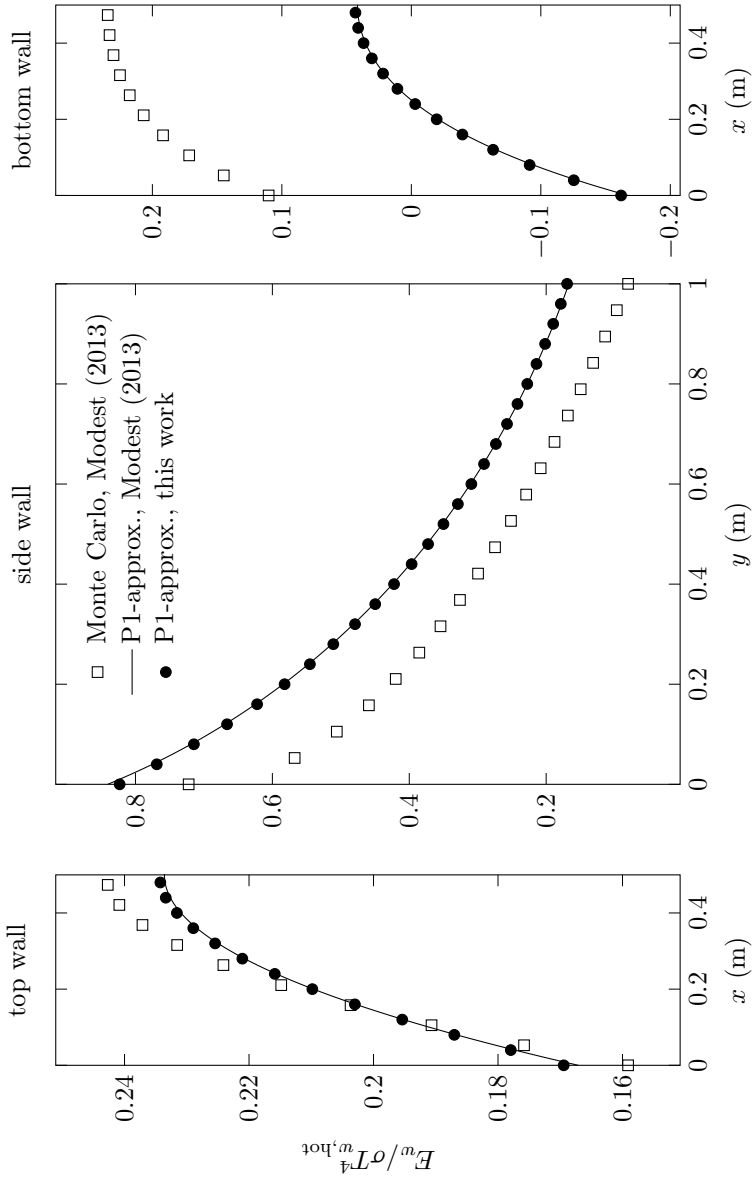


Figure 6.18: Comparison of the normalized incoming irradiation on the walls of a square enclosure with a hot bottom wall and cold top and side walls containing a purely-scattering medium with our  $P_1$ -approximation and the analytical  $P_1$ -approximation and the Monte Carlo results by Modest [57].

were negligible. Coupled with a constant temperature in the circumferential direction, the problem can be treated as one-dimensional. The model parameters are listed in Table 6.6.

Figure 6.19 compares the normalized steady-state solid-temperature profiles predicted by our model with the experimental results as a function of the inner tube wall temperature. Numerical results were obtained with and without the  $P_1$ -approximation. The model is seen to be in good overall agreement with the experimental data. As the inner tube wall temperature increases, good agreement can only be obtained by modeling the effects of radiation.

Table 6.6: Model parameters of the steady-state conduction and radiation heat-transfer validation.

| Property                     | Symbol                      | Value/Correlation       |
|------------------------------|-----------------------------|-------------------------|
| grid cell size               | $\Delta x$                  | 0.5 mm                  |
| characteristic length        | $L$                         | 0.086 m                 |
| solid fraction               | $\alpha_s$                  | 0.562                   |
| solid density                | $\rho_s$                    | 2600 kg/m <sup>3</sup>  |
| solid heat capacity          | $c_{p,s}$                   | 1070 J/kg K             |
| solid thermal conductivity   | $k_{s,bulk}$                | 1.707 W/m K             |
| particle diameter            | $d_p$                       | 6.94 mm                 |
| gas density                  | $\rho_g$                    | 0.746 kg/m <sup>3</sup> |
| gas heat capacity            | $c_{p,g}$                   | 1026 J/kg K             |
| gas thermal conductivity     | $k_{g,bulk}$                | 0.0386 W/m K            |
| cold wall temperature        | $T_{w,cold}$                | 296.2–297.6 K           |
| hot wall temperature         | $T_{w,hot}$                 | 372.8–777.2 K           |
| extinction coefficient       | $\beta = \kappa + \sigma_s$ | correlation from [82]   |
| scattering albedo            | $\omega = \sigma_s/\beta$   | 0.3 [132]               |
| cold and hot wall emissivity | $\epsilon$                  | 1.0 and 0.5 [132, 133]  |

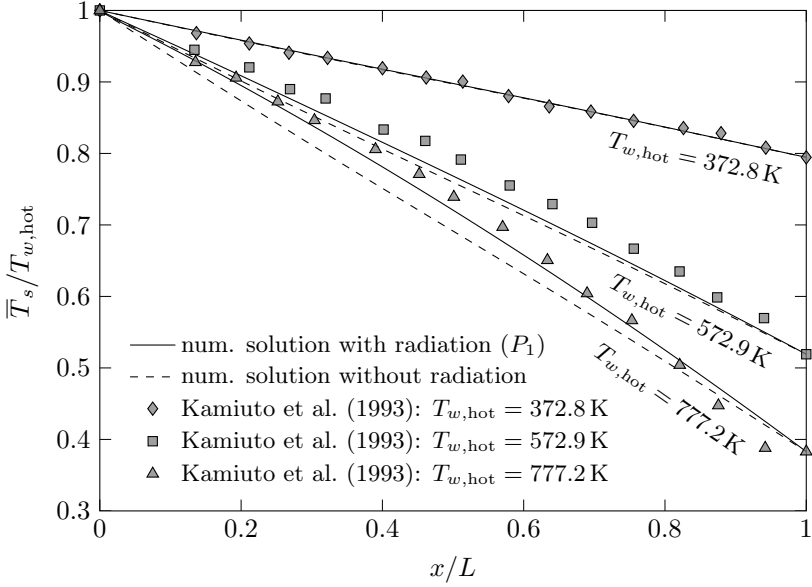


Figure 6.19: Normalized steady-state solid-temperature profiles within a packed bed of cordierite spheres for different temperature gradients. Experimental results from Kamiuto et al. [132] compared to one-dimensional numerical results with and without the  $P_1$  radiation model.

## 6.3 Conclusion

A detailed model to predict the hydrodynamics and heat transfer in dense gas-particle systems was built on the open-source code OpenFOAM. The model is based on a two-phase Euler-Euler approach and uses an existing transient compressible solver that was extended to include radiation heat transfer together with a model to calculate the effective heat conductivities based on the local solid volume fraction.

An extensive verification and validation procedure was performed in which the hydrodynamics and heat transfer were examined separately. A single-phase flow verification was performed by using the analytical solution of the fully developed velocity profile in a two-dimensional pipe flow. The analytical and numerical results were in excellent agreement. An extensive grid-refinement and time-average study was done for a bubbling fluidized bed and the converged results were compared to experimental and numerical results from literature.

The transient convective heat transfer was verified by using the analytical solution of forced convection in a one-dimensional packed bed. The radiation heat-transfer model was verified by comparing the incoming irradiation in a square enclosure predicted by our model with the analytical solution of the  $P_1$ -approximation. For both heat-transfer verification studies, the analytical and numerical results were in excellent agreement. Steady-state conduction combined with radiation was validated with experimental results from literature using an annular packed bed formed by concentric tubes and cordierite spheres. The model showed good agreement with the experimental results over a large range of temperatures.

# Chapter 7

## Results<sup>1</sup>

Having verified and validated the model, attention is now focused on the previously mentioned dense gas-particle-suspension solar receiver [6]. To reduce the computational cost, the simulation uses a two-dimensional planar representation of the CSP plant. This simplification can be justified for the slowly bubbling fluidization regime with small particles (Geldart Group A–B) since the hydrodynamic difference between two and three dimensions is small [134].

### 7.1 Simulation of CSP plant

Figure 7.1 shows a schematic of the model that includes a particle-suspension dispenser in the lower part, a heated riser tube in the middle, and a storage/outlet section in the upper part. A complete description of the setup and the experimental campaign is given in [6]. The riser-tube diameter is  $d_{\text{tube}} = 36 \text{ mm}$  and the heated section height is  $H_{\text{heated}} = 0.5 \text{ m}$  with its center located at the origin as indicated in the figure. SiC particles with a

---

<sup>1</sup>Material from this chapter has been published in:

J. Marti, A. Haselbacher, and A. Steinfeld, “A numerical investigation of gas-particle suspensions as heat transfer media for high-temperature concentrated solar power,” *International Journal of Heat and Mass Transfer*, accepted, 2015

Sauter mean diameter of  $64\text{ }\mu\text{m}$  were used in the experiments.

Based on averaged experimental results, the gas- and solid-phase wall-temperature boundary conditions in the heated tube section ( $-0.25\text{ m} \leq y \leq 0.25\text{ m}$ ) were modeled by assuming a steady parabolic temperature profile  $T(y) = 589 + 86y - 408y^2$  as indicated in the figure. The wall temperature in the upper riser section decreased linearly with  $100\text{ K/m}$ . At all other locations the wall temperature was fixed at  $400\text{ K}$ . The initial solid and the inflow gas temperature were likewise  $400\text{ K}$ . The  $P_1$  radiation model used Marshak's boundary condition [119] with an assumed wall emissivity of  $\epsilon = 0.8$  [135]. The absorption and scattering coefficients of the particle suspension required by Eq. (5.49) were determined in Part I using an experimental-numerical approach. In the lower section, two initially filled particle feeding tubes continuously fed particles to the suspension dispenser. The bottom wall was impermeable for the solid phase and a continuous gas inlet velocity of  $U_{g,\text{in}} = 5.5\text{ mm/s}$  was specified. This inlet velocity is equal to the minimum fluidization velocity of the particles. A lateral aeration inlet in the lower section of the riser tube was needed to control the fluidization behavior of the suspension. The aeration velocity depended on the experimental operating conditions ( $U_{g,\text{aer}} = 0.16\text{--}1.26\text{ mm/s}$ ). In the experimental setup, some of the air leaked through the particle feeder. This leakage volume-flow rate was estimated by subtracting the air volume flow rate at the riser inlet from the air volume-flow rate at the inlet of the suspension dispenser. The riser-inlet velocity  $U_{g,\text{riser,in}}$  is based on the superficial slip velocity between the gas and solid phase, which was determined by a helium-tracking technique [136]. This slip velocity was shown to be similar to the minimum fluidization velocity independent of the operating conditions. With a measured mean solid velocity, the air velocity at the riser inlet can be derived. Since the experimentally determined air-leakage flow rate was not constant, several different leakage flow rates were considered by changing the gas outlet velocity ( $U_{g,\text{leak}} = 1.0\text{--}3.5\text{ mm/s}$ ) in the upper part of the particle feeding tube. These velocities were in the range of the experimentally determined values.



To ease the comparison of experimental and numerical results for different aeration inlet velocities  $U_{g,\text{aer}}$ , a theoretical aeration riser velocity  $U_{g,\text{aer},\text{riser}}$  is calculated by dividing the aeration volume-flow rate in standard cubic meters per second by the riser cross section. This results in a theoretical velocity that is independent of the variable riser inlet velocity  $U_{g,\text{riser},\text{in}}$  and compressibility effects due to pressure and temperature influences.

A no-slip boundary condition was applied to the gas phase while the solid-phase velocity on walls was determined from the Johnson and Jackson partial-slip boundary condition [109]. In the upper part, an opening with imposed atmospheric pressure of  $p_{\text{atm}} = 0.85 \times 10^5$  Pa allowed air and particles to leave the system.

The gas phase was treated as an ideal gas with a constant specific heat capacity. The temperature-dependent gas viscosity was calculated based on the Sutherland's formula [137] and the temperature-dependent thermal conductivity was determined from the modified Eucken relation [138, 139]. The solid-phase heat capacity and the thermal bulk conductivity were calculated with temperature-dependent polynomial correlations [20]. The restitution coefficient of the solid phase and the walls was assumed to be  $e_r = 0.95$ . The gravitational constant was set to  $g = 9.81 \text{ m/s}^2$  in the negative  $y$ -direction. A compilation of the model parameters is listed in Table 7.1.

Table 7.1: Model parameters of the CSP plant.

| Property                   | Symbol                  | Value/Correlation           |
|----------------------------|-------------------------|-----------------------------|
| atmospheric pressure       | $p_{\text{atm}}$        | $0.85 \times 10^5$ Pa       |
| initial solid fraction     | $\alpha_{s,0}$          | 0.4                         |
| max. solid fraction        | $\alpha_{s,\text{max}}$ | 0.5                         |
| solid density              | $\rho_s$                | $3210 \text{ kg/m}^3$       |
| solid heat capacity        | $c_{p,s}$               | correlation from Munro [20] |
| solid thermal conductivity | $k_{s,\text{bulk}}$     | correlation from Munro [20] |

|                               |                     |                                    |
|-------------------------------|---------------------|------------------------------------|
| Sauter mean particle diameter | $d_p$               | 64 $\mu\text{m}$                   |
| restitution coefficient       | $e_r$               | 0.95                               |
| gas density                   | $\rho_g$            | ideal gas                          |
| gas viscosity                 | $\mu_g$             | Sutherland's formula [137]         |
| gas heat capacity             | $c_{p,g}$           | 1005 J/kg K                        |
| gas thermal conductivity      | $k_{g,\text{bulk}}$ | modified Eucken relation [139]     |
| extinction coefficient        | $\beta$             | correlation from Singh et al. [82] |
| scattering albedo             | $\omega$            | correlation from Marti et al. [86] |
| wall emissivity               | $\epsilon$          | 0.8 [135]                          |

### 7.1.1 Grid-refinement and averaging study

In a way similar to the validation case of the hydrodynamics, a grid-refinement and averaging study was performed for the simulation of the CSP plant. To reduce the computational time, these studies were performed by considering a bubbling fluidized bed in the heated riser section only and neglecting the rest of the CSP plant. The solid and gas phase were initially at 750 K and the wall temperature was modeled by assuming a steady parabolic temperature profile given by  $T(y) = 800 - 800 y^2$ .

#### Grid-refinement study

The continuum representation of the solid phase is only valid for a grid spacing much larger than the particle diameter. On the other hand, the near-wall region of the heated riser must be highly resolved for accurate prediction of the temperature gradient. The smallest cell size is therefore a compromise between the particle diameter and the required near-wall resolution. The influence of the computational grid was evaluated by performing a grid-refinement study with five grid levels. Table 7.2 lists the considered grids with the maximum and minimum cell size, maximum stretching ratio,

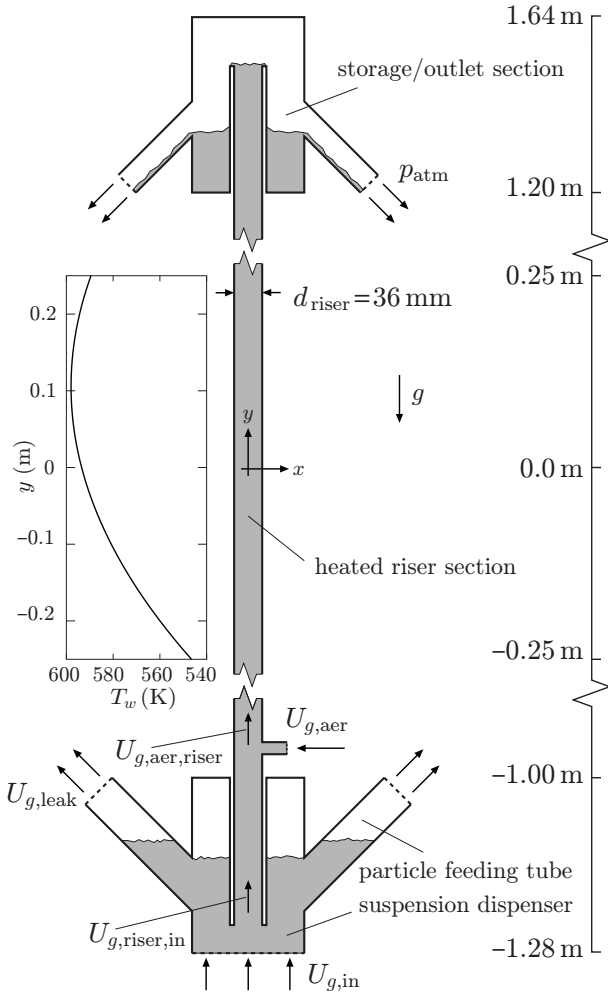


Figure 7.1: Schematic of the numerical model with indicated boundary conditions and system dimensions. The origin is located in the middle of the heated tube section.

and number of cells. The smallest cell at the wall was 0.033 mm and the maximum stretching ratio was less than 1.1 to avoid large numerical errors. The two coarsest grids use a uniform grid spacing over the complete cross section while Grids 3–5 use a uniform grid spacing in the center region and a continuously refined grid in the radial direction towards the wall. Figure 7.2 shows a close-up of Grid 3 with indicated near-wall and center region. The refinement towards the wall starts at a distance of 8.0 mm from the wall.

Figure 7.3 compares the different grid spacings as a function of the radial direction. The minimum cell size of Grid 5 is about half the size of the used particle diameter and therefore clearly below the limit for using the continuum representation of the solid phase. Nevertheless, Grid 5 is used for comparison and to demonstrate the problematic of resolving the near-wall region without using a grid spacing below the particle diameter.

A comparison of the different solid fraction fields for the investigated computational grids is depicted in Figure 7.4. The figure shows on top the solid fraction field at  $t = 1$  s where the initial bubbles start to rise and below the bubbling fluidized bed at  $t = 25$  s. The coarsest grid is not capable of resolving the bubbles properly while the best bubble resolution is achieved with Grid 4, which has the smallest grid spacing in the core region.

To investigate the influence of the computational grid on the hydrodynamics, the solid velocity and solid fraction profiles as well as the cross-section-averaged solid fraction in the axial direction were compared for the different grids levels. The influence on the heat transfer was evaluated by comparing solid-temperature profiles and solid-temperature gradient profiles. For the grid-refinement study, a constant gas inlet velocity of  $U_{g,\text{in}} = 0.04$  m/s was used. This velocity corresponds approximately to the superficial air velocity in the riser of the CSP plant. The considered values were time averaged with a time-averaging interval between  $t_{\text{start}} = 5$  s and  $t_{\text{end}} = 60$  s and an averaging frequency of  $f_{\text{ave}} = 20$  Hz as explained in Section 5.5. The shown values are either cell-centered values if the data points are located within the computational domain or face-centered values if the

Table 7.2: Grid characteristics of the grid-refinement study of the heated riser section with maximum  $\max(\Delta x_i)$  and minimum cell size  $\min(\Delta x_i)$  in millimeters, maximum stretching ratio  $\max(\Delta x_i/\Delta x_{i+1})$ , number of cells in the near-wall region for one side and one row of cells  $N_{i,\text{wall}}$ , and the total number of cells  $N_{i,\text{tot}}$ .

| Grid | $\max(\Delta x_i)$ | $\min(\Delta x_i)$ | $\max\left(\frac{\Delta x_i}{\Delta x_{i+1}}\right)$ | $N_{i,\text{wall}}$ | $N_{i,\text{tot}}$ |
|------|--------------------|--------------------|--|---------------------|--------------------|
| 1    | 2.0                | 2.0                | 1.0  | 4                   | 4500               |
| 2    | 1.0                | 1.0                | 1.0  | 8                   | 18 000             |
| 3    | 1.0                | 0.1984             | 1.099  | 16                  | 26 000             |
| 4    | 0.5                | 0.1                | 1.05   | 32                  | 52 000             |
| 5    | 1.0                | 0.0328             | 1.077  | 32                  | 42 000             |

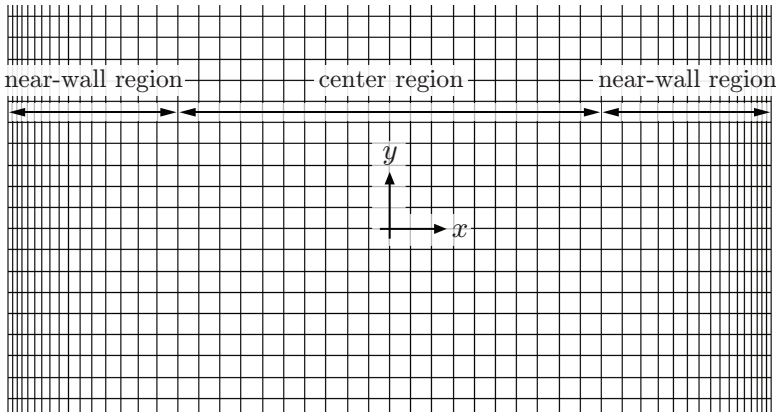


Figure 7.2: Close-up of Grid 3 with indicated near-wall region (refined grid) and center region (uniform grid). The near-wall region starts 8.0 mm from the wall.

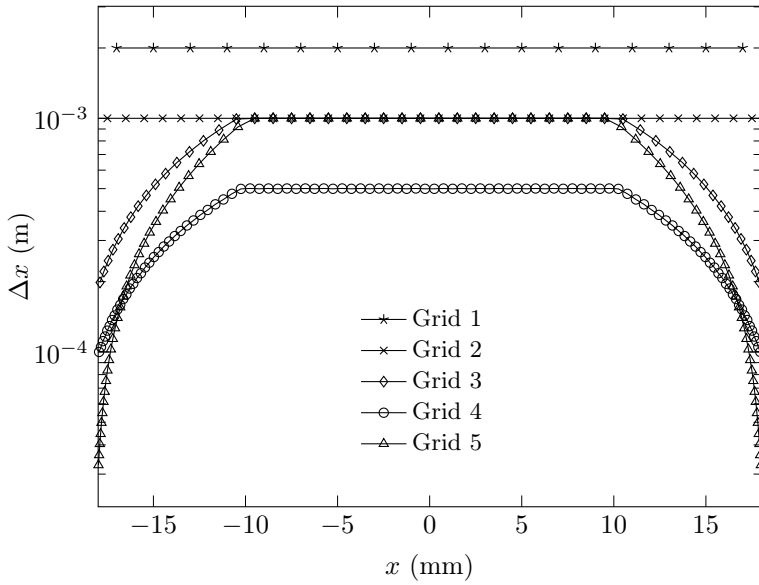


Figure 7.3: Comparison of the considered grid spacings as a function of the radial direction for the grid-refinement study of the heated riser section.

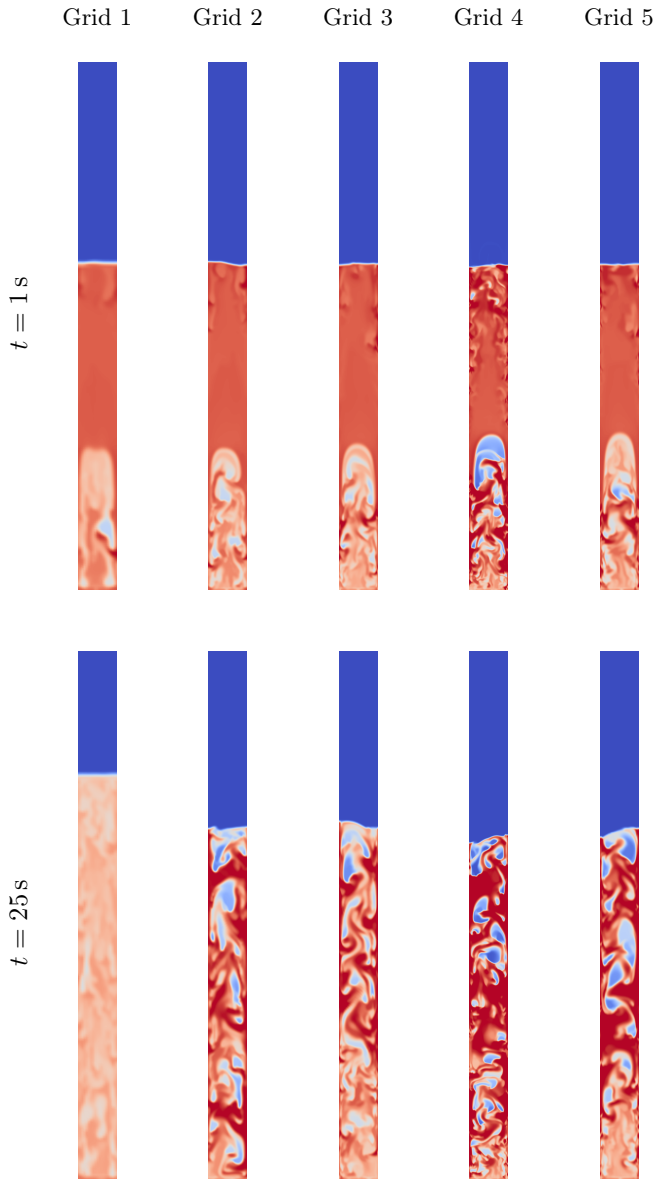


Figure 7.4: Solid fraction of the bubbling fluidized bed for Grids 1–5. On top at  $t = 1 \text{ s}$  and below at  $t = 25 \text{ s}$ .

data points are located on boundaries.

Figure 7.5 shows the time-averaged solid-velocity profiles at the axial locations  $y = 0.0$  m (a) and  $y = -0.1$  m (b) for the different grid-refinement levels. In the center region, the results are similar for the considered grid levels. Towards the walls the differences increase while especially the result with Grid 1 differs considerably from the results with Grids 2–5.

The time-averaged solid-fraction profiles for the different grid levels at the axial locations  $y = 0.0$  m (a) and  $y = -0.1$  m (b) are presented in Figure 7.6. For both axial locations, Grid 1 underpredicts the solid fraction by about 15% compared to the solid-fraction profile with Grids 2–5, which are similar. The predicted solid-fraction profiles with Grids 2–5 have in the center region some fluctuations. This results probably from a time-averaging interval that was not long enough to reach fully converged time-averaged results.

Figure 7.7 shows the time- and cross-section-averaged solid fraction in the axial direction for the different grid levels. The axial location of the steep solid fraction decrease corresponds to the transition from the bubbling fluidized bed (dense region) into the freeboard region and indicates therefore the time-averaged bed height. The result with Grid 1 clearly overestimates the bed expansion predicted with Grids 2–5. The bed heights with Grids 2, 3, and 5 are very similar whereas the result with Grid 4 shows the smallest bed height. A reduction of the grid spacing in the center region leads therefore to a decrease of the bed expansion. This is a known behavior for Euler-Euler simulations with Geldart Group A particles [140, 141]. It is assumed that this reduction of the bed expansion results from a more detailed resolution of the bubbles as the grid spacing decreases. A reduction of the grid spacing from 1.0 mm to 0.5 mm leads to reduction of the time-averaged bed height of about 4%.

To study the influence of the computational grid on the heat transfer, the solid-temperature and solid-temperature-gradient profiles were compared for the different grid levels. The solid-phase temperature did not reach a quasi-steady state for the considered starting time ( $t_{\text{start}} = 5$  s) of the time-



averaging interval. Therefore, the solid phase was heating up during the time averaging.

The time-averaged solid-temperature profiles at the axial locations  $y = 0.0\text{ m}$  (a) and  $y = -0.1\text{ m}$  (b) for the different grid-refinement levels are shown in Figure 7.8. A close-up of the first 1.5 mm from the left wall is indicated in Figure 7.9. The grid spacing of Grids 1 and 2 are too big to capture the steep temperature increase towards the heated wall. The temperature predictions with Grids 3–5 show a very good agreement with a maximum temperature difference of 0.4% located on the centerline. The close-up of the near-wall region shows the importance of the near-wall resolution to accurately predict the steep temperature gradient towards the wall.

Figure 7.10 presents the time-averaged solid-temperature gradients at the axial locations  $y = 0.0\text{ m}$  (a) and  $y = -0.1\text{ m}$  (b) for the different grid levels in the first 1.5 mm from the left wall. The radial temperature gradient was estimated by using second-order Lagrange interpolation polynomials [142]. As for the temperature profiles, Grids 1 and 2 are clearly too coarse to resolve the temperature gradient in the near-wall region. The predicted temperature gradients with Grids 3–5 show good agreement up to a distance of about 0.5 mm from the wall. At the wall, the temperature gradients can differ considerably between the different grid levels and there is no obvious trend. It is expected that this discrepancy is partly due to an averaging-interval not long enough to reach a fully-converged time-averaged result. In addition, the application of the continuum approach to represent the solid phase with highly resolved grids in the near-wall region has probably also an influence on the shown discrepancies of the temperature gradients.

Although there are some differences, it is assumed that Grid 3, with a cell size of 1.0 mm in the center region and a minimum cell size of 0.2 mm, is adequate and leads to nearly grid-independent results. Furthermore, the smallest grid spacing of Grid 3 is three times larger than the particle diameter of  $d_p = 64\text{ }\mu\text{m}$ . This should be appropriate to apply, even in the near-wall region, the continuum representation of the solid phase.

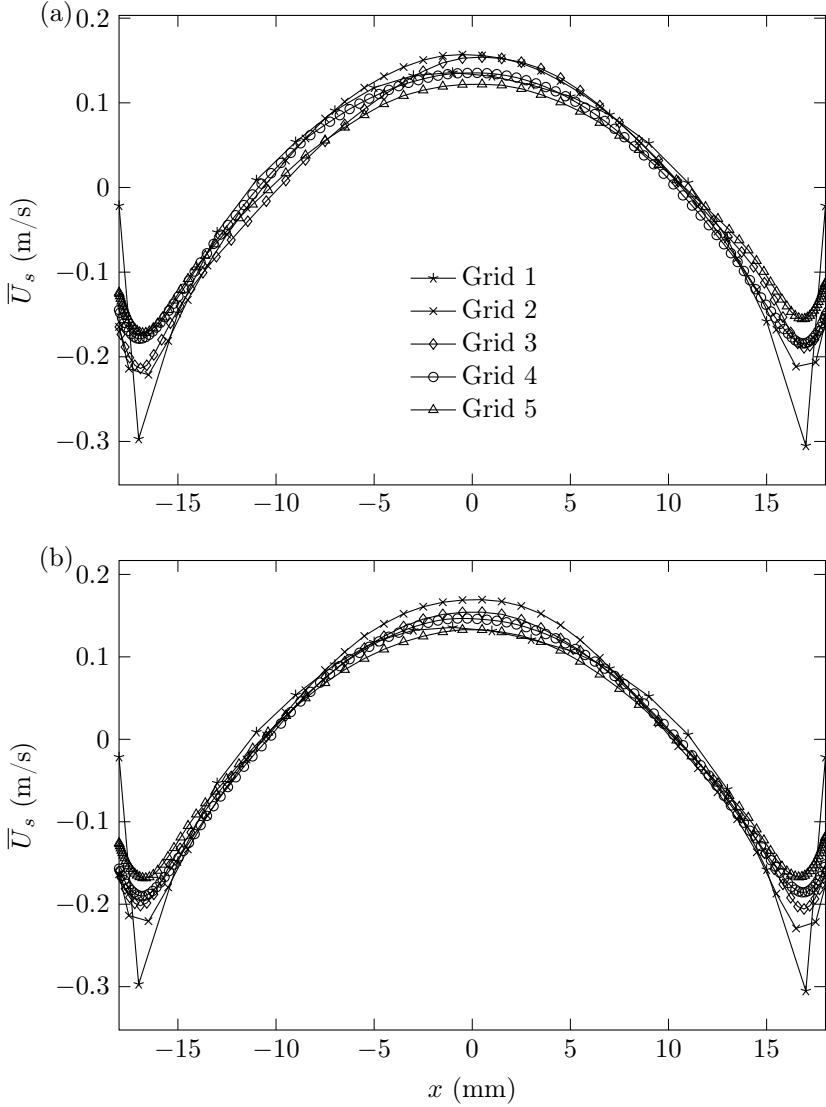


Figure 7.5: Time-averaged solid-velocity profiles at  $y = -0.1$  m (a) and  $y = 0.0$  m (b) for different grid-refinement levels with a gas inlet velocity of  $U_{g,\text{in}} = 0.04$  m/s.

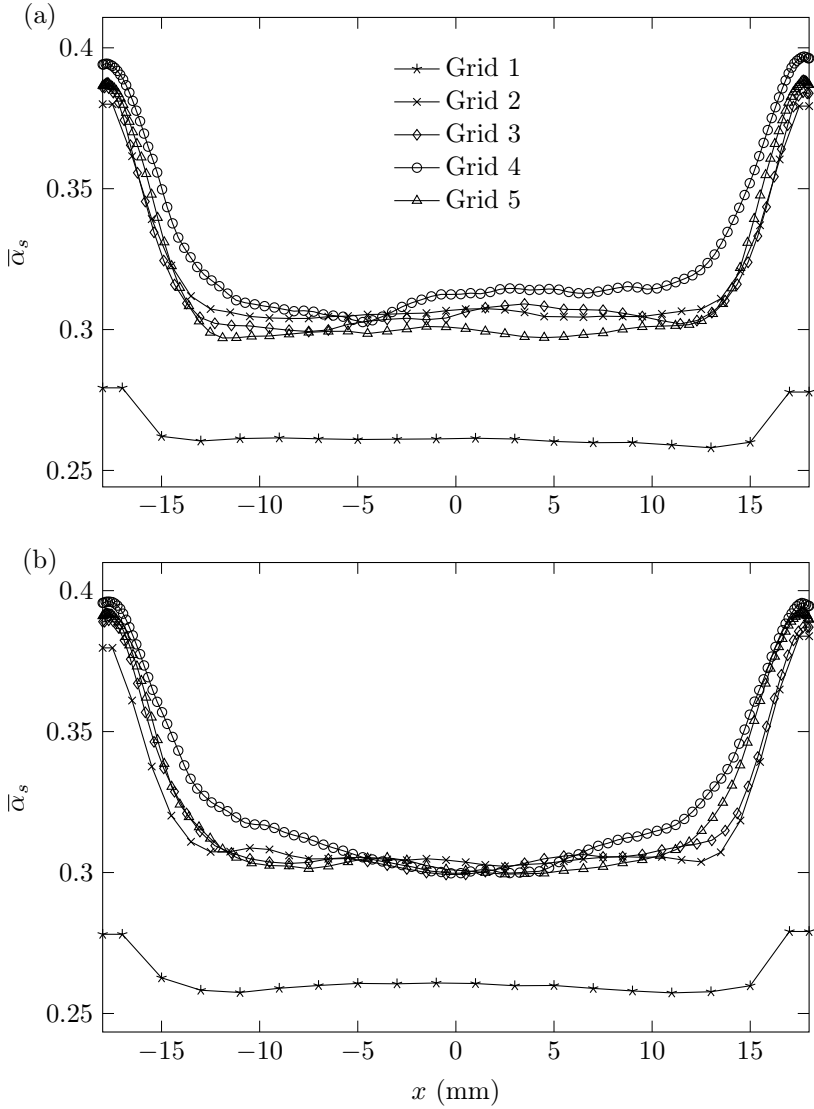


Figure 7.6: Time-averaged solid-fraction profiles at  $y = 0.0$  m (a) and  $y = -0.1$  m (b) for different grid-refinement levels with a gas inlet velocity of  $U_{g,\text{in}} = 0.04$  m/s.

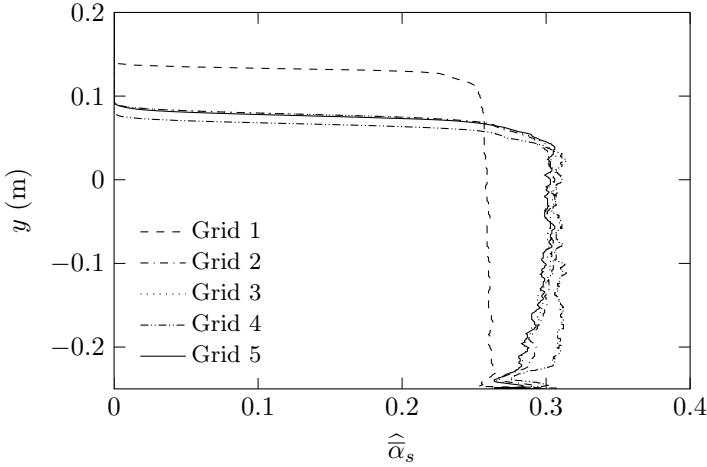


Figure 7.7: Time- and cross-section-averaged solid fraction in the axial direction for different grid-refinement levels with a gas inlet velocity of  $U_{g,\text{in}} = 0.04 \text{ m/s}$ . (To avoid overlapping, symbols are not shown.)

### Time-averaging study of heated riser section

The time averaging of the transient results was assessed by varying the averaging interval between  $t_{\text{start}} = 5 \text{ s}$  and  $t_{\text{end}} = 10\text{--}120 \text{ s}$  and the averaging frequency from 1 Hz to 100 Hz. For each time average, the first five seconds of the simulation run were neglected to allow enough time for the transition from the initial packed bed to the bubbling state. Based on the previous grid-refinement study, Grid 3 was used with a constant gas inlet velocity of  $U_{g,\text{in}} = 0.04 \text{ m/s}$ . Since the grid spacing is the same for each shown curve, no symbols are used to visualize the cell locations.

Figures 7.11, 7.12, 7.14, and 7.13 show the time-averaged solid-velocity, solid-fraction, and solid-temperature profiles at the axial locations  $y = 0.0 \text{ m}$  (a) and  $y = -0.1 \text{ m}$  (b) as well as the time- and cross-section-averaged solid fraction in the axial direction. The results are presented for different averaging frequencies and a constant averaging interval between  $t_{\text{start}} = 5 \text{ s}$

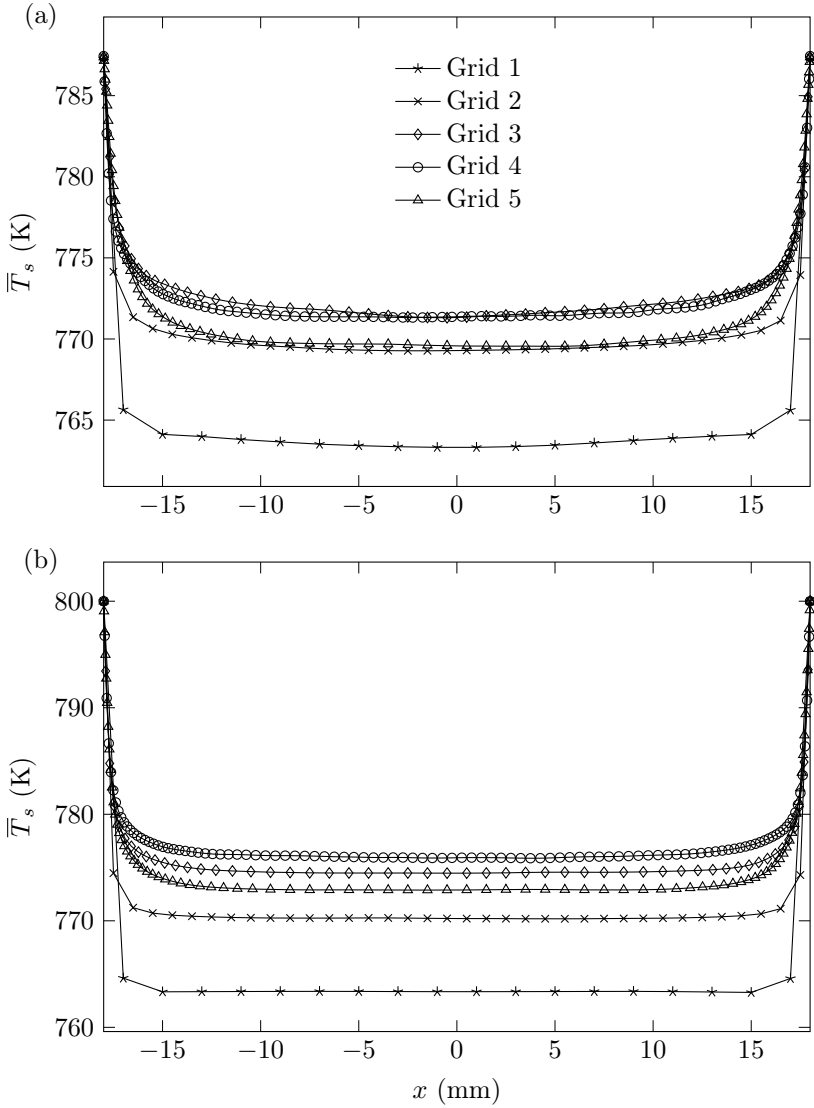


Figure 7.8: Time-averaged solid-temperature profiles at  $y = 0.0$  m (a) and  $y = -0.1$  m (b) for different grid-refinement levels with a gas inlet velocity of  $U_{g,in} = 0.04$  m/s.

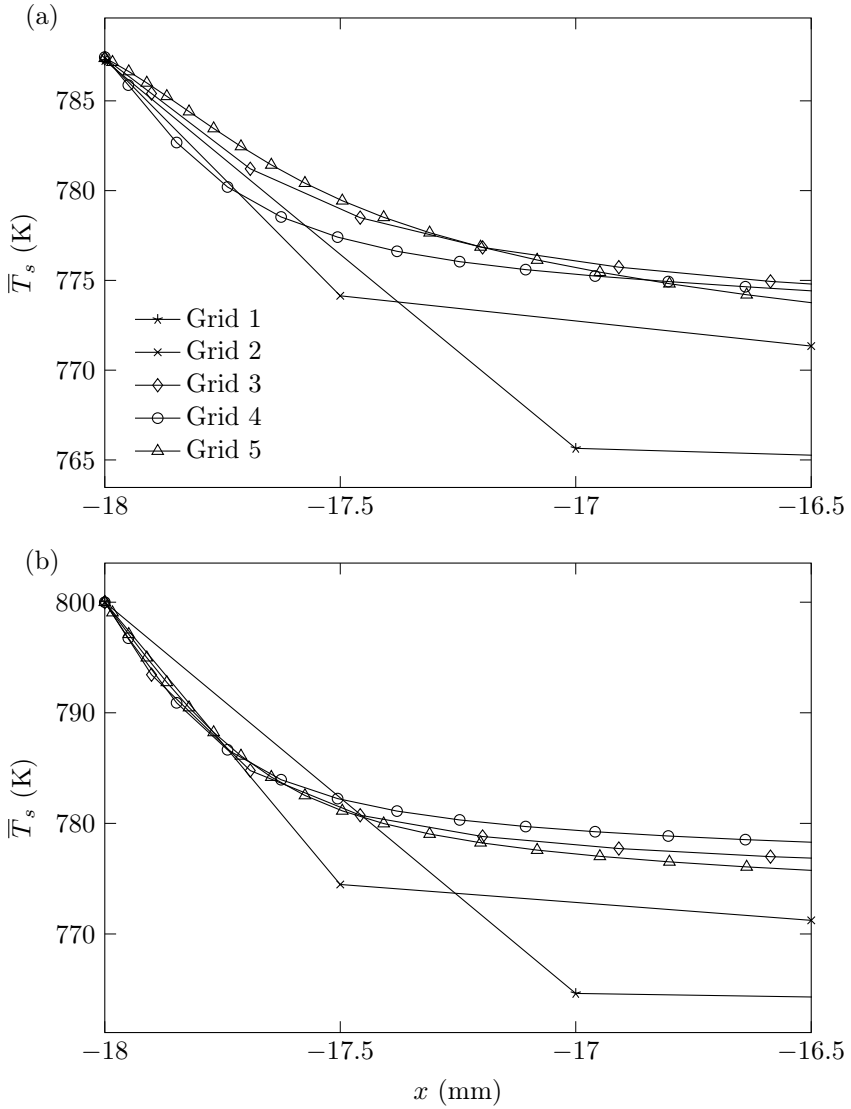


Figure 7.9: Time-averaged solid temperature in the near-wall region at  $y = 0.0$  m (a) and  $y = -0.1$  m (b) for different grid-refinement levels with a gas inlet velocity of  $U_{g,\text{in}} = 0.04$  m/s.

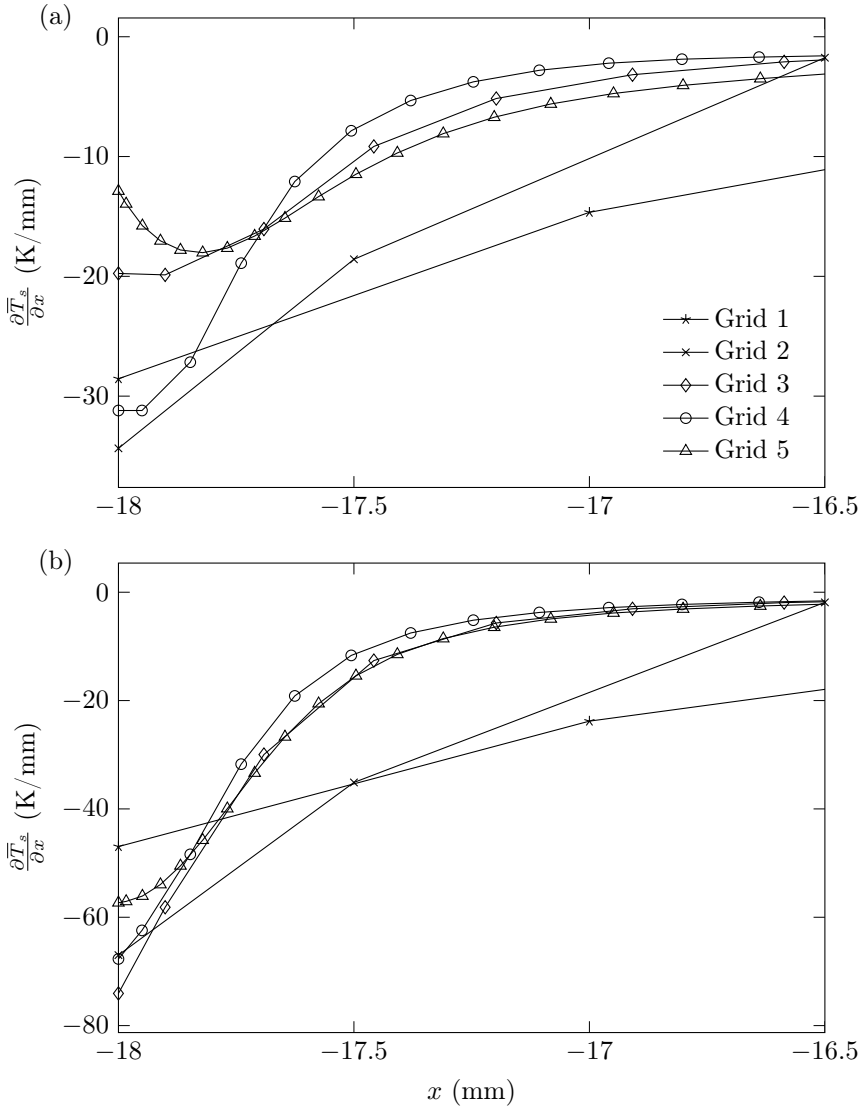


Figure 7.10: Time-averaged solid-temperature gradient in the near-wall region at  $y = 0.0$  m (a) and  $y = -0.1$  m (b) for different grid-refinement levels with a gas inlet velocity of  $U_{g,\text{in}} = 0.04$  m/s.

and  $t_{\text{end}} = 60$  s. Increasing the averaging frequency from 20 Hz to 100 Hz has no considerable influence on the solid velocity, solid fraction, or solid temperature. A averaging frequency of 20 Hz was therefore assumed to be sufficient.

The time-averaged solid-velocity and solid-fraction profiles at the axial locations  $y = 0.0$  m (a) and  $y = -0.1$  m (b) and the time- and cross-section-averaged solid fraction in the axial direction are presented in Figures 7.15, 7.16, and 7.17, respectively. The results are shown for different averaging intervals and a constant averaging frequency of 20 Hz. Increasing the end time of the time average from  $t_{\text{end}} = 60$  s to  $t_{\text{end}} = 120$  s has no considerable influence on the solid velocity or solid fraction. It was thus assumed that an averaging interval between  $t_{\text{start}} = 5$  s and  $t_{\text{end}} = 60$  s is adequate and leads to averaging-interval-independent results. The influence of the time-averaging interval on the solid temperature is not shown since increasing the averaging interval will increase the solid temperature and a comparison is of limited used.

A converged time-averaged solid-fraction and solid-velocity field was therefore achieved by using an averaging frequency of 20 Hz together with an averaging interval between  $t_{\text{start}} = 5$  s and  $t_{\text{end}} = 60$  s. The bubbles had a mean bed-residence time of approximately 1.3 s. As a result, the required averaging procedure corresponds to about 42 bubble mean bed-residence times and about 26 data sets were averaged per bubble mean bed-residence time.

### Time-averaging study of CSP plant

A visualization of the instantaneous solid-fraction field of the complete CSP-plant model together with close-ups of the solid-fraction and solid-temperature field in the heated riser section are depicted in Figure 7.18. Compared to the previously investigated riser section, the complete CSP plant required a longer averaging interval due to the increased length scale in the axial direction. Furthermore, the complete CSP plant needed a longer starting time to reach a quasi-steady state. This results mainly from the



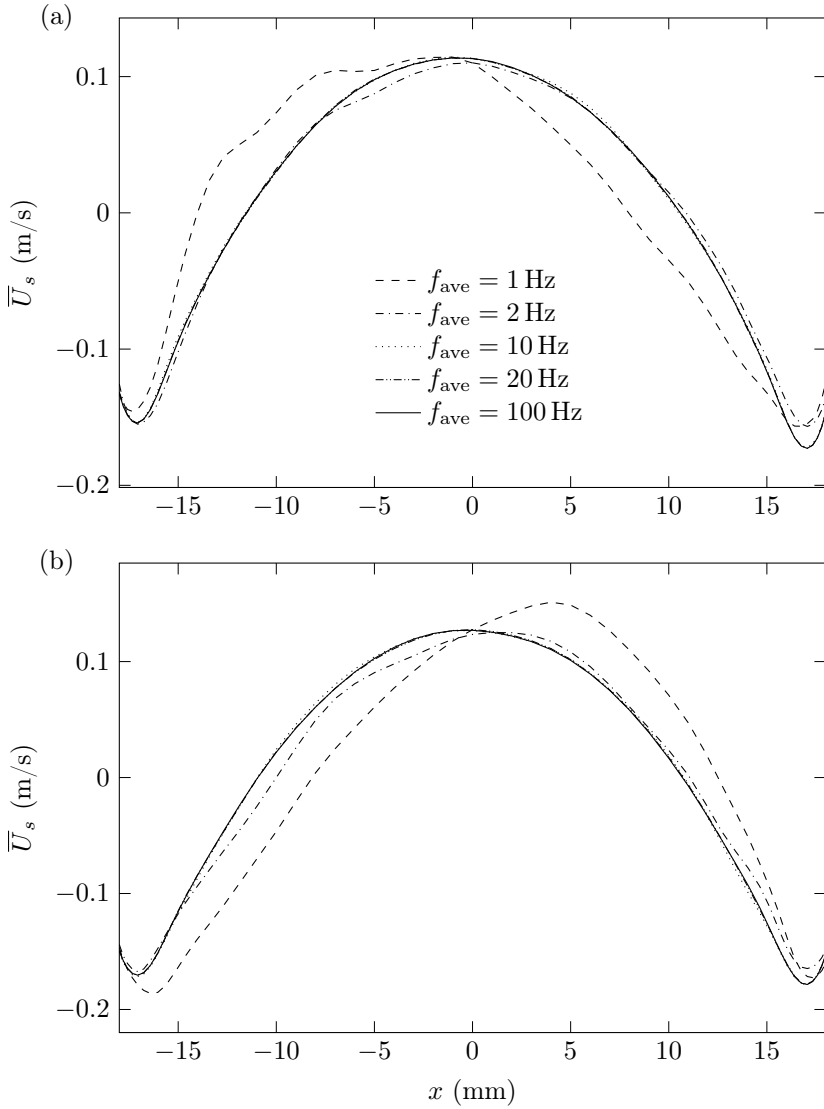


Figure 7.11: Time-averaged solid-velocity profiles at  $y = 0.0$  m (a) and  $y = -0.1$  m (b) for different averaging frequencies and a constant averaging interval between  $t_{\text{start}} = 5$  s and  $t_{\text{end}} = 60$  s with a gas inlet velocity of  $U_{g,\text{in}} = 0.04$  m/s.

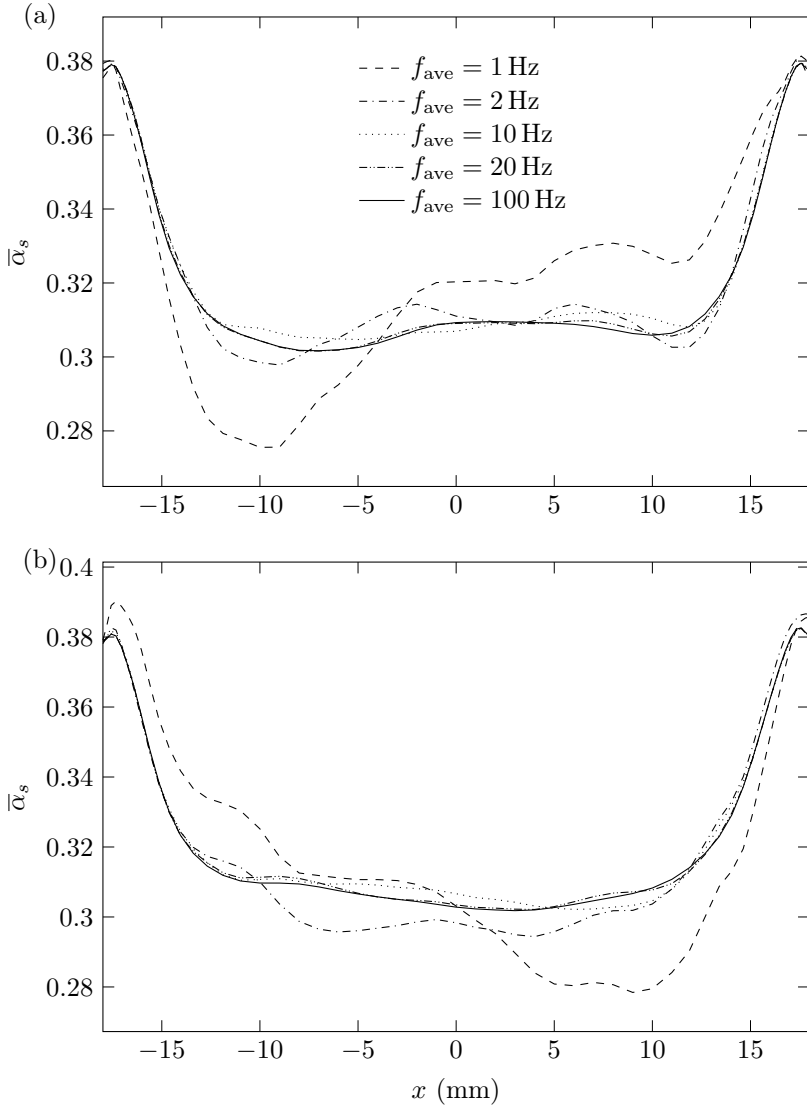


Figure 7.12: Time-averaged solid-fraction profiles at  $y = 0.0$  m (a) and  $y = -0.1$  m (b) for different averaging frequencies and a constant averaging interval between  $t_{\text{start}} = 5$  s and  $t_{\text{end}} = 60$  s with a gas inlet velocity of  $U_{g,\text{in}} = 0.04$  m/s.

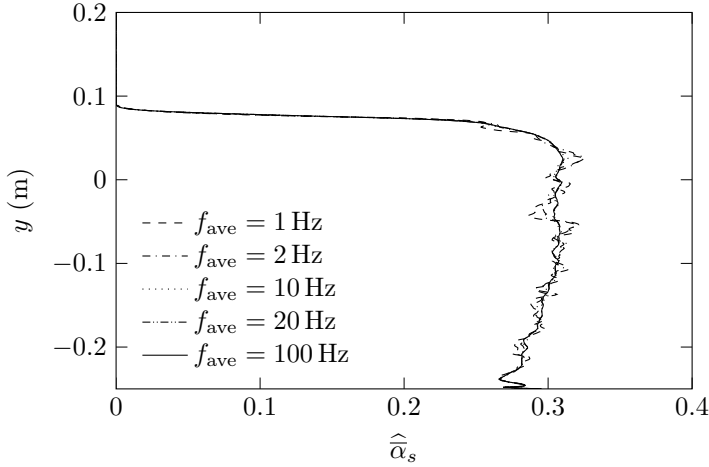


Figure 7.13: Time- and cross-section-averaged solid fraction in the axial direction for different averaging frequencies and a constant averaging interval between  $t_{\text{start}} = 5$  s and  $t_{\text{end}} = 60$  s with a gas inlet velocity of  $U_{g,\text{in}} = 0.04$  m/s.

heating time of the initial cold particles and the required time to reach a quasi-steady mass flow rate.

Figure 7.19 (a) shows the cross-section-averaged solid temperature at the axial locations  $y = -0.25$  m,  $y = 0.25$  m, and  $y = 0.0$  m of the riser of the complete CSP plant. The considered axial locations correspond to the inlet, outlet, and midpoint of the heated riser section. The shown solid temperatures are time averaged by using the moving average given in Eq. (5.67) while storing and resetting the time-averaged result every second. This procedure reduces strong fluctuations to improve the visualization. During the first 50–100 s, the solid phase heats up from the initial 400 K to a quasi-steady temperature that depends on the axial location. A close-up of the cross-section-averaged solid temperatures are presented in Figure 7.19 (b). The results in Figure 7.19 (b) are extended with moving averages starting at  $t = 200$  s. These additional moving averages (solid line) are not reset every second and they approach a statistical steady state after about 150–200 s.

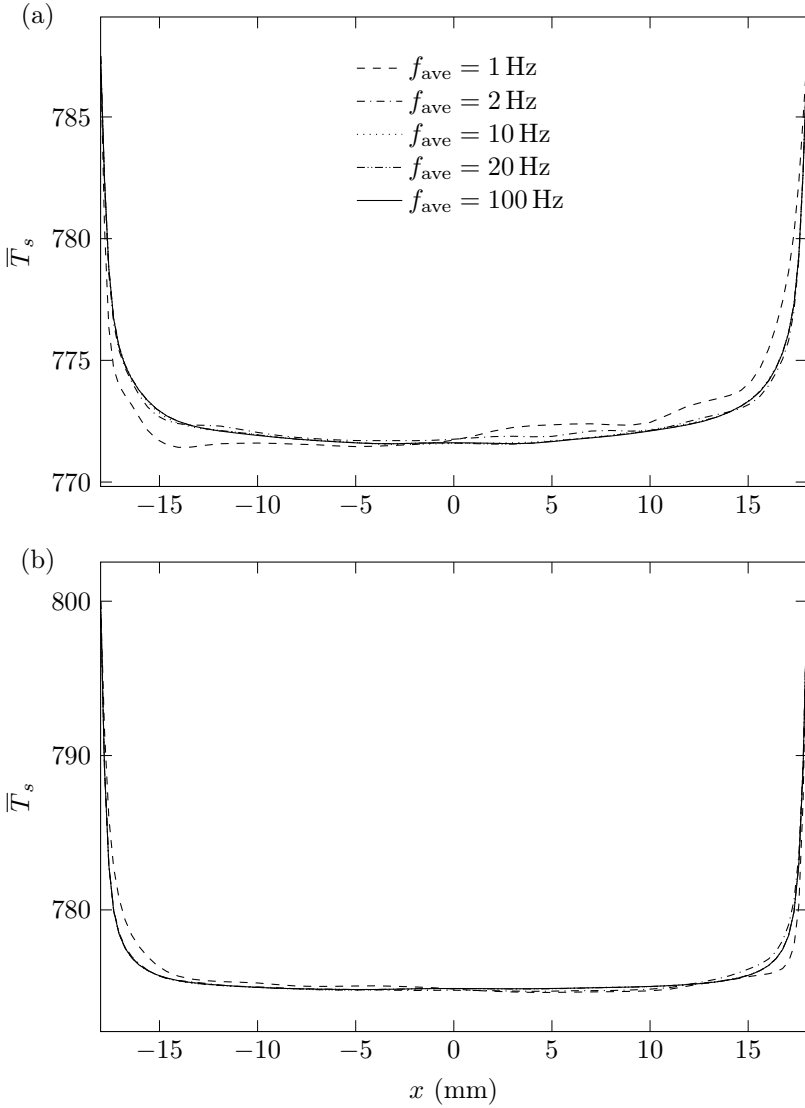


Figure 7.14: Time-averaged solid-temperature profiles at  $y = 0.0$  m (a) and  $y = -0.1$  m (b) for different averaging frequencies and a constant averaging interval between  $t_{\text{start}} = 5$  s and  $t_{\text{end}} = 60$  s with a gas inlet velocity of  $U_{g,\text{in}} = 0.04$  m/s.

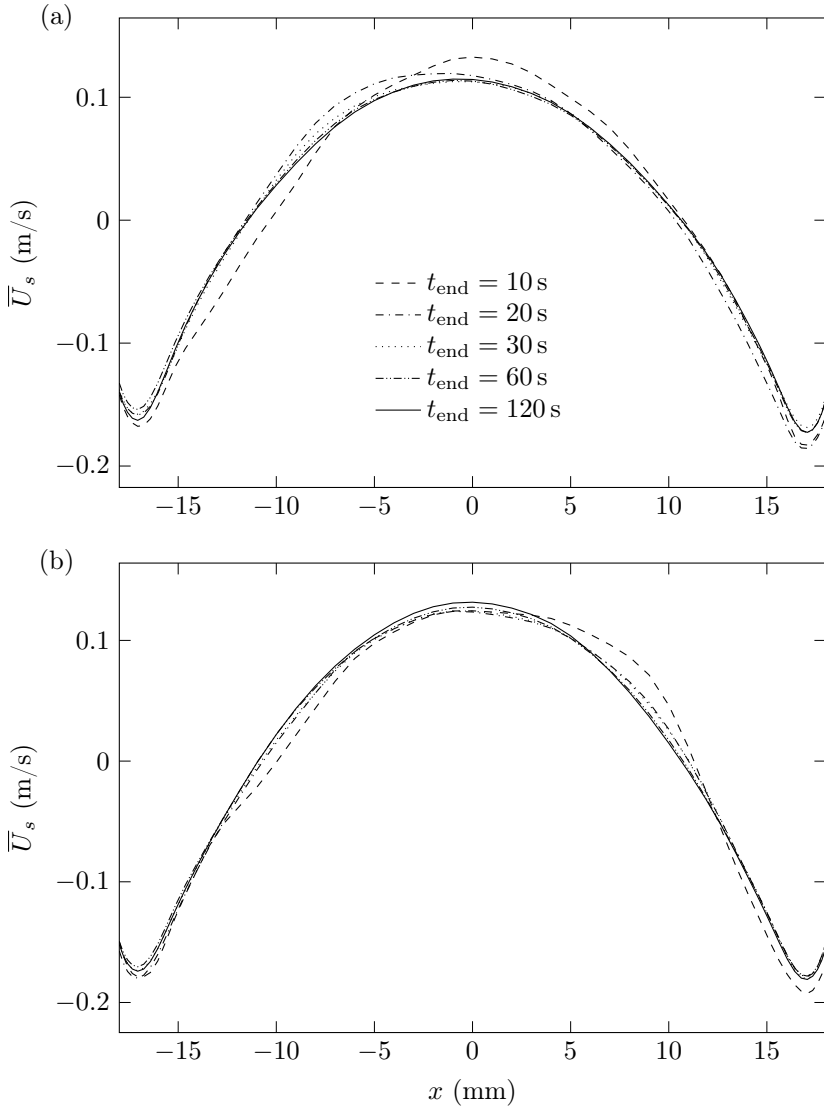


Figure 7.15: Time-averaged solid-velocity profiles at  $y = 0.0$  m (a) and  $y = -0.1$  m (b) for different averaging intervals and a constant averaging frequency of 20 Hz with a gas inlet velocity of  $U_{g,\text{in}} = 0.04$  m/s.

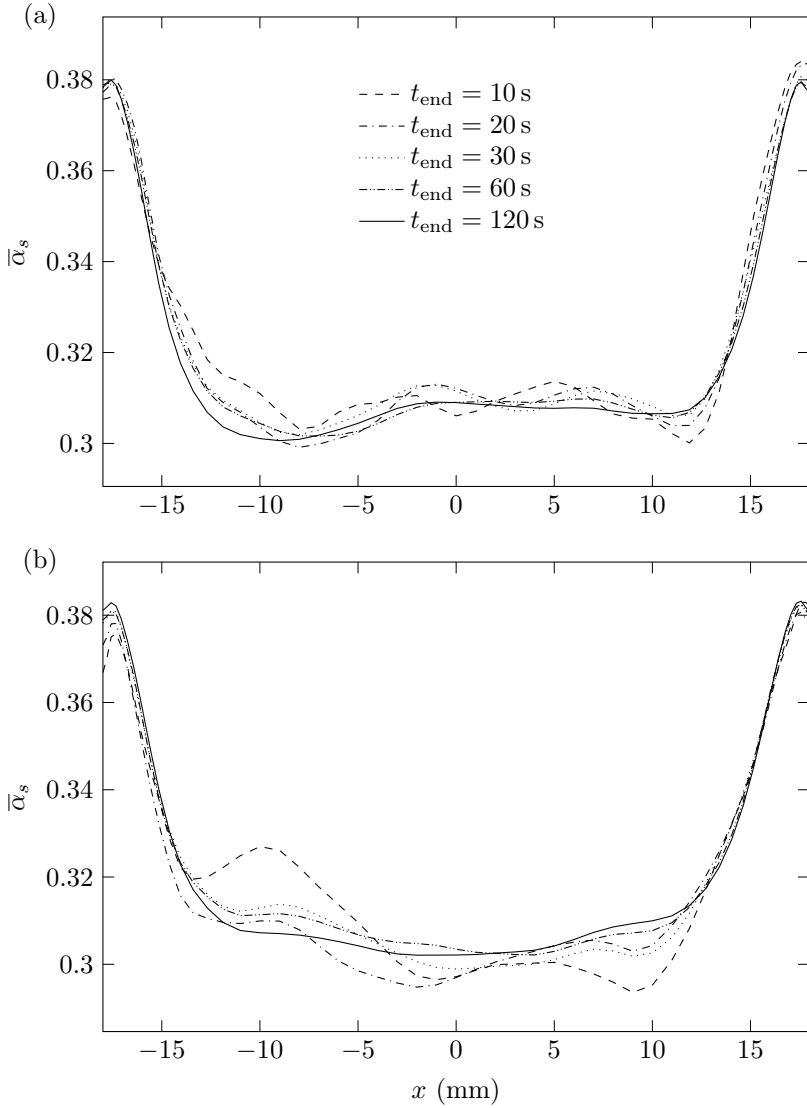


Figure 7.16: Time-averaged solid-fraction profiles at  $y = 0.0$  m (a) and  $y = -0.1$  m (b) for different averaging intervals and a constant averaging frequency of 20 Hz with a gas inlet velocity of  $U_{g,\text{in}} = 0.04$  m/s.

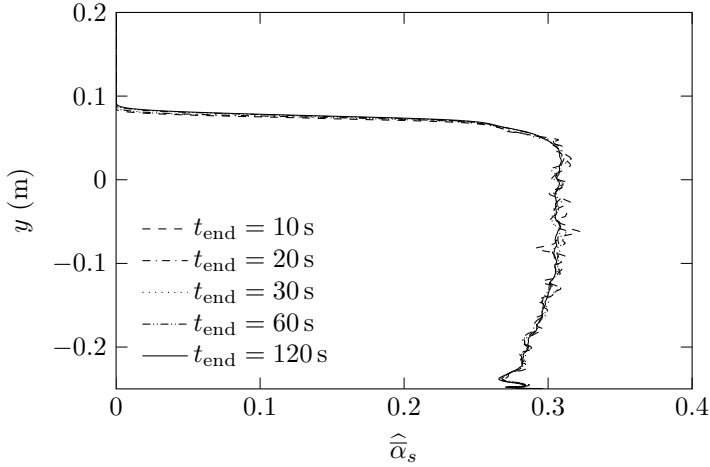


Figure 7.17: Time- and cross-section-averaged solid fraction in the axial direction for different averaging intervals and a constant averaging frequency of 20 Hz with a gas inlet velocity of  $U_{g,\text{in}} = 0.04 \text{ m/s}$ .

Figure 7.20 (a) shows the space-averaged solid-phase mass flow leaving the computational domain through the outlet (see Figure 7.1) per riser cross section. The initial horizontal line indicates the time it takes for the solid phase to reach from the initial state the outlet of the CSP plant. In the present situation this corresponds to about 40 s. Due to the rising bubbles, the solid phase leaves the system in irregular waves. This results in the strong fluctuations shown in the figure and complicates the determination of the time- and cross-section-averaged solid mass flow rate.

To simplify this task, the temporal change of the solid-phase mass located in the computational domain is considered as elaborated in the following. In a quasi-steady state, the time-averaged mass flow rate leaving the computational domain through the outlet is equal to the mass flow rate passing through the riser. The time- and space-averaged solid mass flow

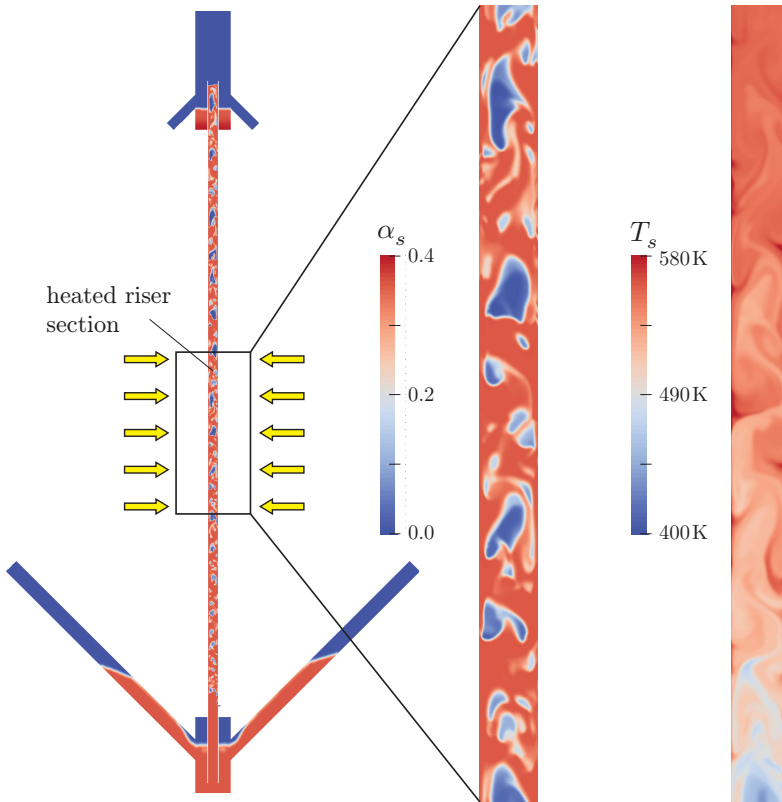


Figure 7.18: Visualization of the instantaneous solid-fraction field of the complete CSP-plant model together with close-ups of the solid-fraction and solid-temperature field in the heated riser section.



rate leaving the system between the  $t_{\text{start}}$  and  $t_{\text{end}}$  is calculated from

$$\begin{aligned} \widehat{\dot{m}}_s &= \frac{\widehat{m}_s}{t_{\text{end}} - t_{\text{start}}} = \frac{\rho_s}{t_{\text{end}} - t_{\text{start}}} (V_s^{t_{\text{start}}} - V_s^{t_{\text{end}}}) = \\ &= \frac{\rho_s}{t_{\text{end}} - t_{\text{start}}} \left( \int_{V_{\text{comp,dom}}} \alpha_s^{t_{\text{start}}} dV - \int_{V_{\text{comp,dom}}} \alpha_s^{t_{\text{end}}} dV \right) \quad (7.1) \end{aligned}$$

where  $V_{\text{comp,dom}}$  is the volume of the computational domain and  $V_s^{t_{\text{start}}}$  and  $V_s^{t_{\text{end}}}$  are the solid-phase volumes in the computational domain at the time  $t_{\text{start}}$  and  $t_{\text{end}}$ , respectively. The influence of local extrema at  $t_{\text{start}}$  or  $t_{\text{end}}$  can be reduced by using a small time interval and taking the average of the individual contributions. This is visualized in Figure 7.20 (b) representing the time integration of the solid-phase mass flow rate leaving the system per riser cross section. The shown result is achieved by using Eq. (7.1) with a time interval of 1 s and summing up the individual contributions. The slope of the indicated linear fit for  $t \geq 200$  s is equal to the time-averaged solid-phase mass flow rate after reaching a quasi-steady state. With this method to determine the time-averaged solid-phase mass flow rate, the numerical errors resulting from the fluctuations of the solid mass flow rate are reduced.

Due to the size of the CSP plant, the low velocities, and the unsteady nature of the system, a start-up phase of about 150–200 s was required to reach from the initial condition a quasi-steady state of the solid mass flow rate and the solid temperature. For the time averaging itself, an additional averaging interval of about 150–200 s with a averaging frequency of 20 Hz was needed to reach converged statistics. This corresponds to about 20–100 bubble residence times over the complete riser and around 30–150 data sets per bubble residence time.

### 7.1.2 Comparison with experimental results

The wall-to-bed heat-transfer coefficient is of central importance to the performance of the CSP plant. For both the experimental and numerical results this coefficient was determined by first calculating the time- and space-

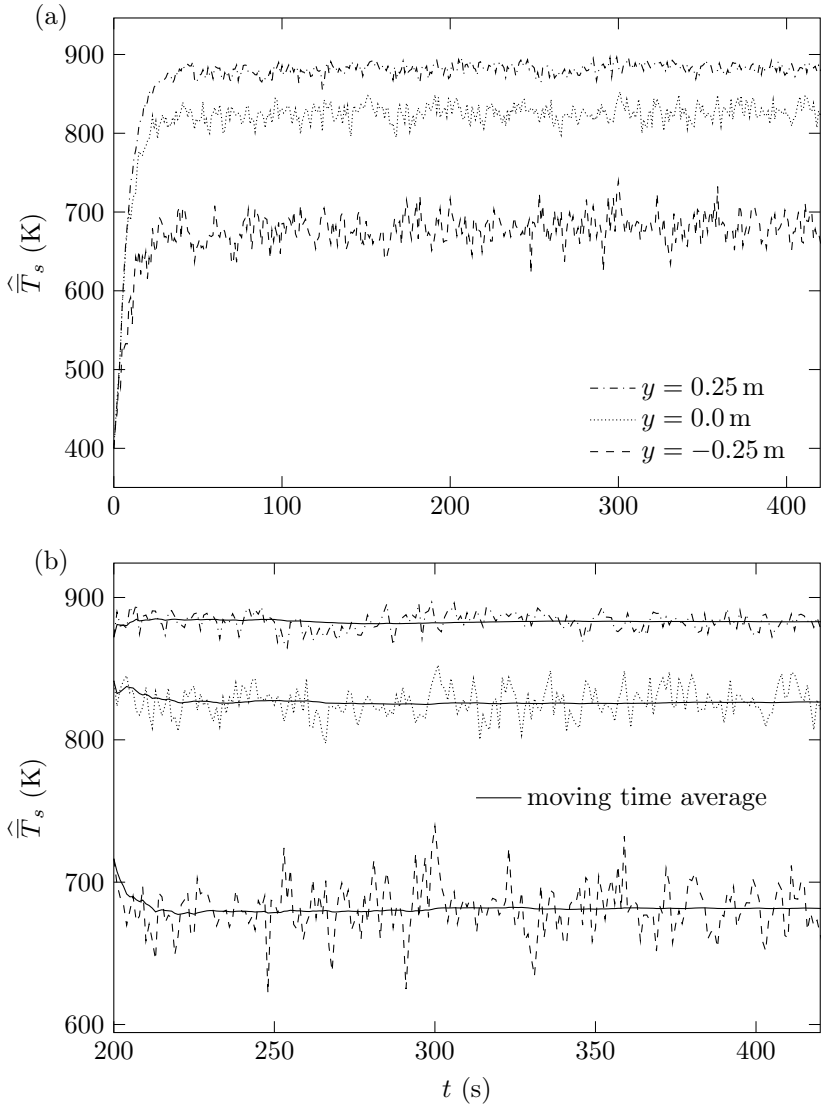


Figure 7.19: Time- and cross-section-averaged solid temperature at the inlet ( $y = -0.25$  m), outlet ( $y = 0.25$  m), and midpoint ( $y = 0.0$  m) of the heated riser section.

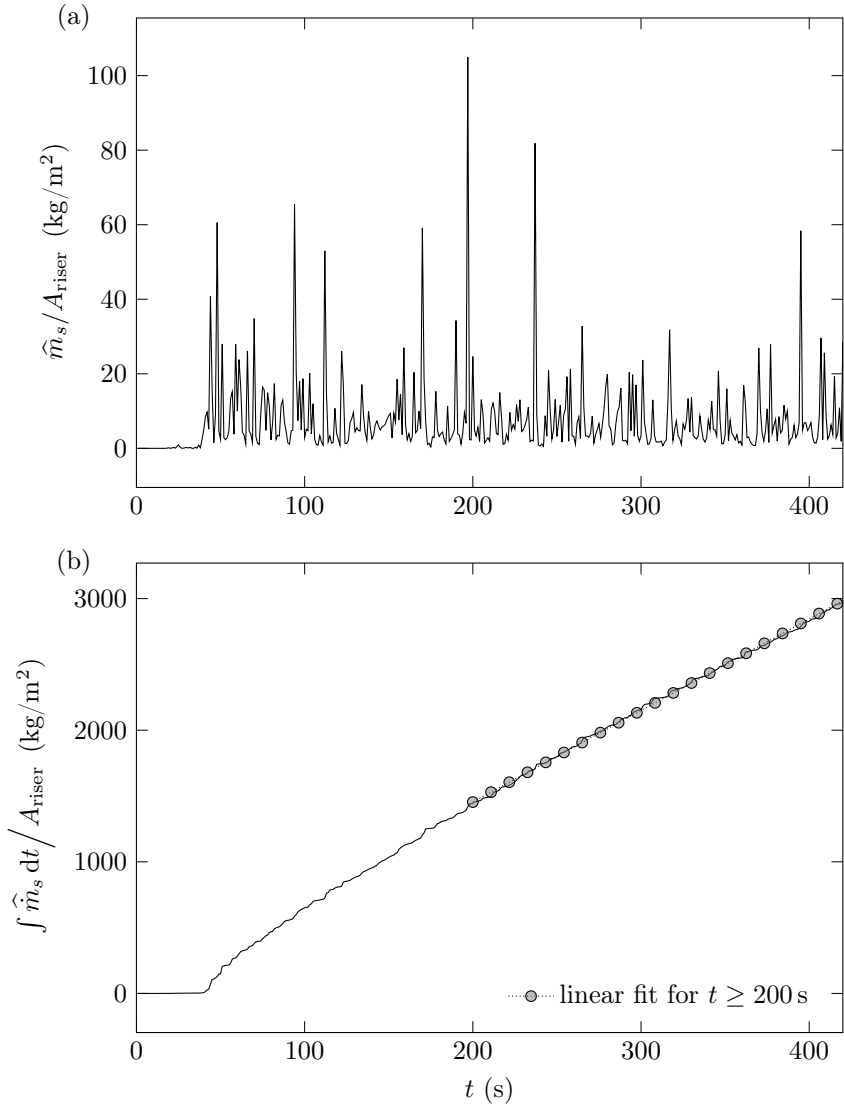


Figure 7.20: (a) Space-averaged solid-phase mass flow leaving the computational domain through the outlet per riser cross section. (b) Time integration of the space-averaged solid-phase mass flow rate per riser cross section together with a linear fit for  $t \geq 200$  s.

averaged power transmitted to the solid phase from

$$\widehat{\bar{Q}}_s = \widehat{\bar{m}}_s \left( \widehat{\bar{T}}_{s,\text{out}} - \widehat{\bar{T}}_{s,\text{in}} \right) c_{p,s} \left( \widehat{\bar{T}}_{s,\text{mean}} \right) \quad (7.2)$$

where  $\widehat{\bar{m}}_s$ ,  $\widehat{\bar{T}}_{s,\text{in}}$ , and  $\widehat{\bar{T}}_{s,\text{out}}$  are the time- and space-averaged solid mass flow rate and inlet and outlet solid-phase temperatures in the heated riser section, respectively, and  $c_{p,s}$  is a function of  $\widehat{\bar{T}}_{s,\text{mean}} = \left( \widehat{\bar{T}}_{s,\text{out}} + \widehat{\bar{T}}_{s,\text{in}} \right) / 2$ . For the experimental results,  $\widehat{\bar{m}}_s$  was determined by weighing the mass of particles leaving the riser tube divided by the elapsed time of each measurement. The temperatures  $\widehat{\bar{T}}_{s,\text{in}}$  and  $\widehat{\bar{T}}_{s,\text{out}}$  were determined by directly measuring the suspension temperature at the in- and outlet of the heated riser section with two K-type thermocouples at each location and averaging the mean temperature of both thermocouples over time. The time- and heated-riser-section averaged wall-to-bed heat-transfer coefficient  $\widehat{\bar{h}}_{\text{wb}}$  was then calculated from

$$\widehat{\bar{h}}_{\text{wb}} = \frac{\widehat{\bar{Q}}_s}{A_w \widehat{\bar{T}}_{\text{LMTD}}} \quad (7.3)$$

where  $A_w$  is the internal wall area and  $\widehat{\bar{T}}_{\text{LMTD}}$  is the time- and space-averaged logarithmic mean temperature difference given by

$$\widehat{\bar{T}}_{\text{LMTD}} = \frac{\left( \bar{T}_{w,\text{in}} - \widehat{\bar{T}}_{s,\text{in}} \right) - \left( \bar{T}_{w,\text{out}} - \widehat{\bar{T}}_{s,\text{out}} \right)}{\ln \left( \left( \bar{T}_{w,\text{in}} - \widehat{\bar{T}}_{s,\text{in}} \right) / \left( \bar{T}_{w,\text{out}} - \widehat{\bar{T}}_{s,\text{out}} \right) \right)} \quad (7.4)$$

where  $\bar{T}_{w,\text{in}}$  and  $\bar{T}_{w,\text{out}}$  are the time-averaged internal wall temperatures at the in- and outlet of the heated riser section, which are constant for the numerical model.

Figure 7.21 compares the experimental and numerical results for the wall-to-bed heat-transfer coefficient as a function of the aeration riser velocity. The numerical results have been obtained for several values of the air-leakage velocity to cover the approximate range of values observed in the experiments. For both the experimental and numerical results an increased aeration riser velocity leads to a decreasing wall-to-bed heat-transfer

coefficient. This is due to increased heat removal by the air flow and the resulting reduction of the solid temperature reduces the thermal energy stored and transported in the solid phase. The numerical results agree quite well with the experimental results for intermediate and high aeration riser velocities with a relative mean difference of 19.9 %. For low aeration riser velocities, the difference between experimental and numerical results can be significant. The substantial difference of the numerical results for different air-leakage velocities reveals the importance of this value on the wall-to-bed heat-transfer coefficient.

Figure 7.22 shows the time- and space-averaged solid mass flux in the riser as a function of the air-leakage velocity. The multiple data points for a given air-leakage velocity correspond to different aeration inflow velocities. For the considered range, the solid mass flux decreases linearly with an increasing air-leakage velocity. This trend is explained by the reduced riser-inlet velocity caused by an increasing air-leakage velocity in the particle feeding tubes.

The influence of the riser-inlet air velocity on the wall-to-bed heat-transfer coefficient is depicted in Figure 7.23. Both experimental and numerical results show that an increase of the riser-inlet velocity leads to an increase of the wall-to-bed heat-transfer coefficient. The numerical results significantly overpredict the measured heat-transfer coefficient for low aeration riser velocities. For medium to high aeration riser velocities, the agreement is quite good.

Figure 7.24 presents the time- and space-averaged pressure drop and solid fraction in the riser tube as a function of the aeration riser velocity. The multiple data points for a given aeration riser velocity correspond to different riser-inlet velocities. The experimental solid fraction was calculated based on the measured pressure drop [6]. Good agreement between experimental and numerical results is obtained for both pressure drop and solid fraction with relative mean differences of 4.6 % and 3.3 %, respectively. Increasing the aeration flow rate decreases the solid fraction in the riser and results, as expected, in a reduced pressure drop.

Experiments with the CSP plant showed that an increase of the aeration flow rate had no influence on the solid mass flow rate [143]. The numerical model reproduced this behavior. In addition, it was observed that in the simulations an increase of the aeration flow rate increased the bubble formation and frequency. The previous results demonstrate that the model can predict the hydrodynamic and heat-transfer processes in a highly complex gas-particle system with good accuracy. The discrepancies are attributed to three main sources: measurement errors and uncertainties, uncertainties in boundary conditions due to incomplete experimental data, and the assumption of a two-dimensional geometry.

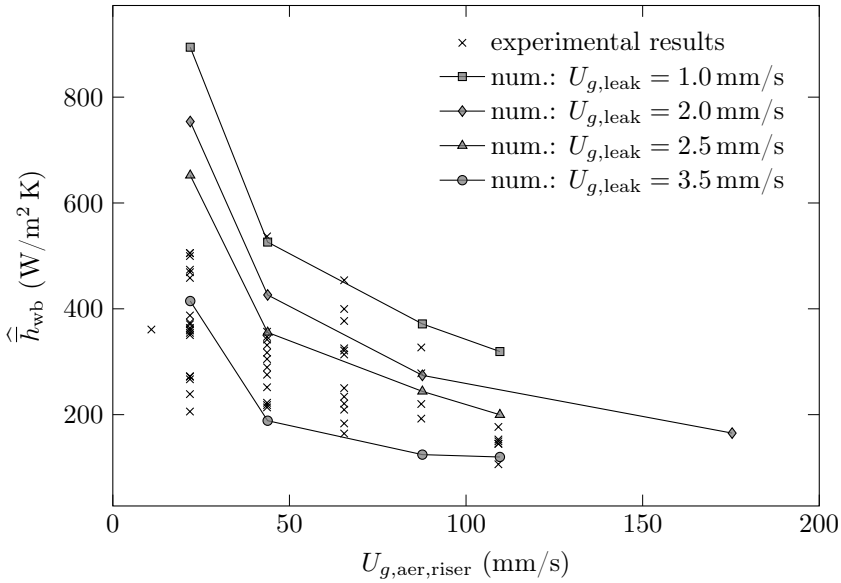


Figure 7.21: Comparison of the experimental and numerical values of the wall-to-bed heat-transfer coefficient as a function of the aeration riser velocity. The numerical results are for different air-leakage velocities.

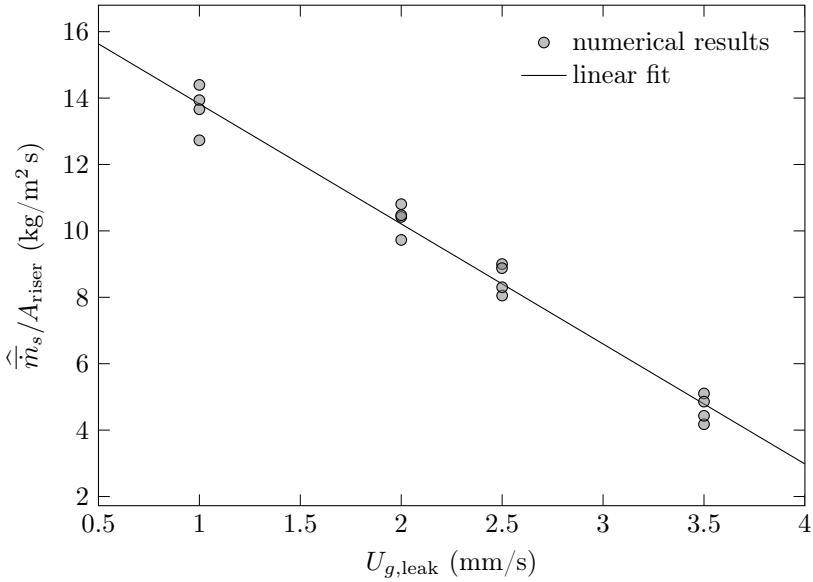


Figure 7.22: Numerical result of the solid mass flux in the riser tube as a function of the air-leakage velocity in the particle feeding tubes. The multiple data points for a given air-leakage velocity correspond to different aeration inflow velocities.

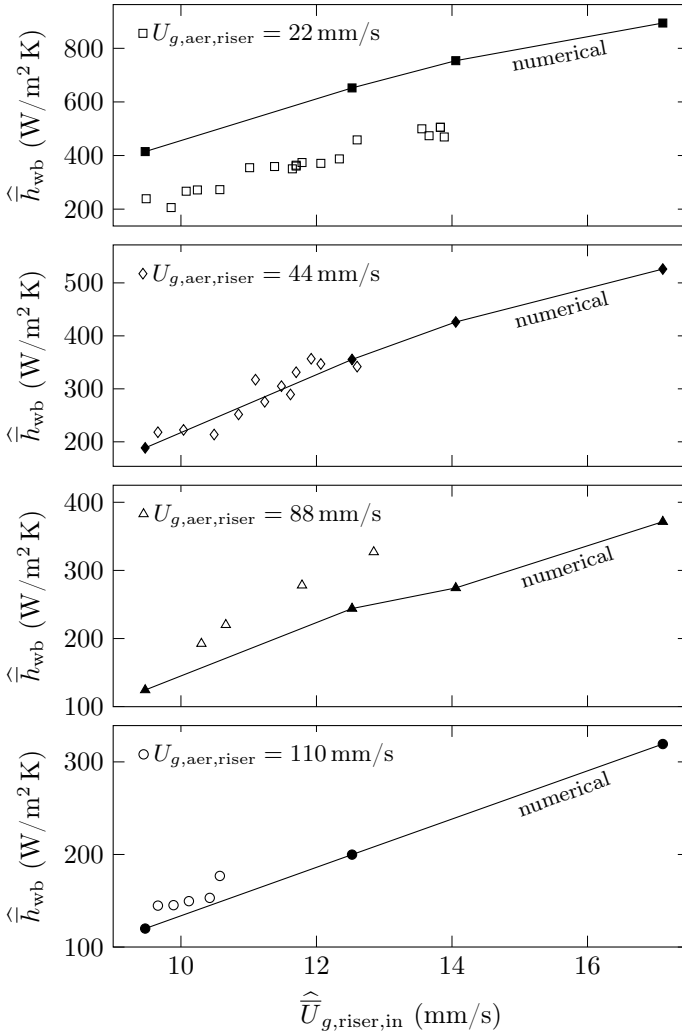


Figure 7.23: Comparison of the experimental and numerical values of the wall-to-bed heat-transfer coefficient as a function of the riser-inlet air velocity for different aeration riser velocities.



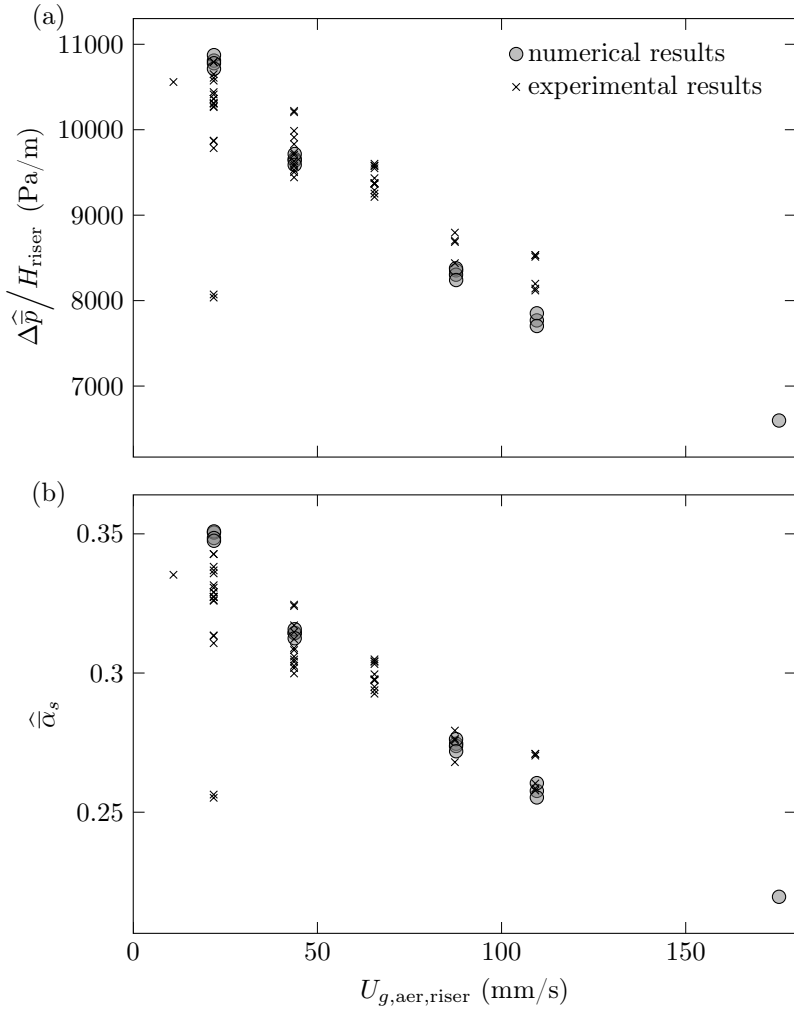


Figure 7.24: Comparison of the experimental and numerical values of the pressure drop (a) and the solid fraction (b) in the riser tube as a function of the aeration riser velocity. The multiple data points for a given aeration riser velocity correspond to different air-leakage velocities.

## 7.2 Parameter study

Having demonstrated good agreement between the simulation and experimental data, the model can now be used to investigate the influence of parameters that were not studied experimentally due to experimental limitations of the CSP plant. Two parameter studies were performed where the influence of the wall temperature of the heated riser section ( $\hat{T}_w = 581, 981,$  and  $1281$  K) and the riser diameter ( $d_{\text{tube}} = 36, 46, 54,$  and  $72$  mm) were analyzed. As before, a start-up phase of about 150–200 s was required to reach a quasi-steady state and an averaging interval of about 150–200 s with a averaging frequency of 20 Hz was needed to reach converged statistics.

### 7.2.1 Influence of riser-wall temperature

The temperature  $\hat{T}_w = 581$  K corresponds to the averaged riser-wall temperature of the experimental campaign [6],  $\hat{T}_w = 981$  K corresponds approximately to the upper limit where conventional refractory-steel riser tubes are still applicable, and  $\hat{T}_w = 1281$  K corresponds approximately to the maximum intended riser-wall temperature for the present CSP application. To investigate the influence of the riser wall temperature, a constant set of gas-phase boundary conditions ( $U_{g,\text{in}} = 5.5$  mm/s,  $U_{g,\text{aer},\text{riser}} = 44.0$  mm/s, and  $U_{g,\text{leak}} = 2.5$  mm/s) with a particle diameter of  $d_p = 64$   $\mu\text{m}$  was used. The different wall temperatures were achieved by scaling the parabolic temperature profile in the heated riser section as shown in Figure 7.1.

Figure 7.25 shows the time- and space-averaged (a) wall-to-bed heat-transfer coefficient, (b) solid temperature at the in- and outlet of the heated riser section, (c) solid mass flow per riser cross section, and (d) solid fraction in the heated riser section as a function of the space-averaged riser-wall temperature. The wall-to-bed heat-transfer coefficient decreases with an increasing riser-wall temperature. To find the reason for this behavior, the calculation method of the wall-to-bed heat-transfer coefficient has to be analyzed in detail. The wall-to-bed heat-transfer coefficient was determined

by Eq. (7.3) and depends on the power transmitted to the solid phase  $\widehat{Q}_s$ , the LMTD, and the internal wall area. The power transmitted to the solid phase was calculated from Eq. (7.2) and depends on the solid mass flow, the solid-phase temperature difference between the in- and outlet of the heated section, and the temperature dependent heat capacity. As depicted in Figure 7.25 (c), the solid mass flow is nearly independent on the riser-wall temperature. The heat capacity depends on the mean solid temperature  $\widehat{T}_{s,\text{mean}}$  that increases from 518–971 K when increasing the riser-wall temperature from 581–1281 K, resulting in an increase of the heat capacity from 942–1162 J/kg K. As indicated in Figure 7.25 (b), the temperature difference between the inlet ( $y = -0.25$  m) and the outlet ( $y = 0.25$  m) of the heated riser section increases from 78–295 K when increasing the riser-wall temperature from 581–1281 K. Therefore, the power transmitted to the solid phase increases considerably with an increasing riser-wall temperature. With an increasing  $\widehat{Q}_s$  and a constant internal wall area, the decrease of the wall-to-bed heat-transfer coefficient for an increasing riser-wall temperature must be, as given by Eq. (7.3), due to an increasing  $\widehat{T}_{\text{LMTD}}$ . This is indicated in Figure 7.26, where  $\widehat{T}_{\text{LMTD}}$  is shown as a function of the riser-wall temperature. Increasing the riser-wall temperature leads to an almost linear increase of  $\widehat{T}_{\text{LMTD}}$ . As depicted in Figure 7.25 (d), due to the temperature dependent gas expansion, the solid fraction in the riser decreases about 20% when increasing the riser-wall temperature by 700 K. Increasing the riser-wall temperature by 700 K leads to an increase of the mean suspension temperature by about 450 K. This indicates that the particles have especially for the highest riser-wall temperature not enough time to heat up and an increase of the particle residence time or an increase of the particle heating rate is required to make full use of the higher riser-wall temperature. A more detailed discussion about this topic is given in Section 7.3.1.

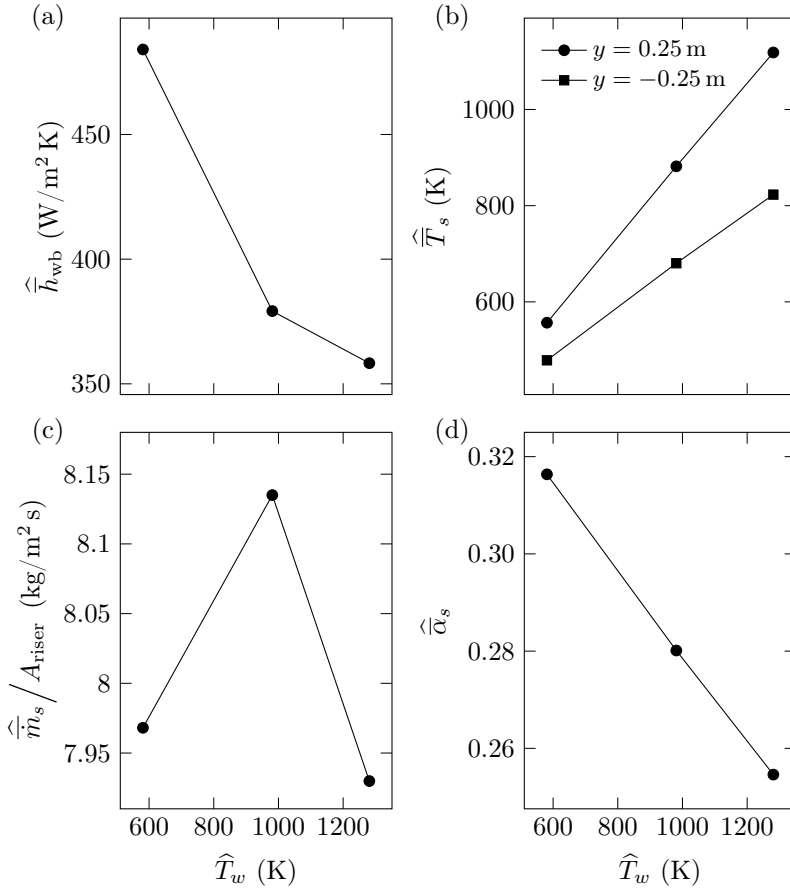


Figure 7.25: Time- and space-averaged (a) wall-to-bed heat-transfer coefficient, (b) solid temperature at the in- and outlet of the heated riser section, (c) solid mass flow per riser cross section, and (d) solid fraction in the heated riser section as a function of the riser-wall temperature.

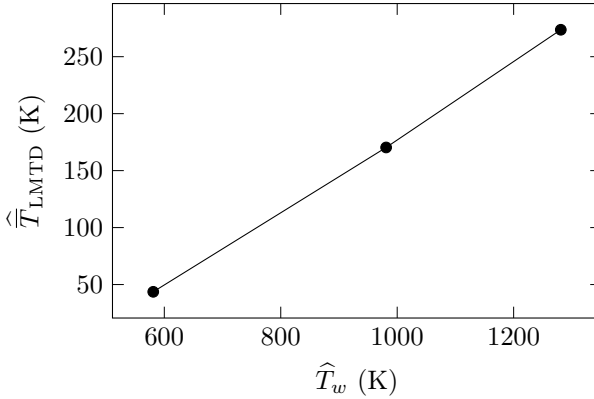


Figure 7.26: Logarithmic mean temperature difference as a function of the average riser-wall temperature.

### 7.2.2 Influence of riser diameter

To investigate the influence of the riser diameter, the gas-phase velocity at the suspension-dispenser inlet was kept constant at  $U_{g,\text{in}} = 5.5$  mm/s. The air leakage  $U_{g,\text{leak}}$  and aeration velocity  $U_{g,\text{aer}}$  were adapted to maintain, independent of the riser diameter, a constant riser-inlet velocity of  $U_{g,\text{riser,in}} = 12.5$  mm/s and an aeration riser velocity of  $U_{g,\text{aer,riser}} = 44.0$  mm/s. For every riser diameter, the heated riser section had the same temperature profile with an average riser-wall temperature of  $\hat{T}_w = 981$  K.

Figure 7.27 shows the time- and space-averaged (a) wall-to-bed heat-transfer coefficient, (b) solid temperature at the in- and outlet of the heated riser section, (c) solid mass flow per riser cross section, and (d) solid fraction in the heated riser section as a function of the riser diameter. An increase of the riser diameter leads to a small increase of the wall-to-bed heat-transfer coefficient. This is mainly due to an increasing solid mass flow rate when increasing the riser diameter as indicated in Figure 7.27 (c). It should be noted that Figure 7.27 (c) depicts the mass flow rate per riser cross section and the total mass flow rate increases even more strongly due to an increas-

ing riser cross section with increasing riser diameter. As seen in Figure 7.27 (b), the solid temperature at the outlet of the heated riser section decreases with increasing riser diameter. This results mainly from the increase of the total solid mass flow rate while keeping the heat-exchange surface the same. Although the overall power transmitted to the solid phase increases, the stronger increase of total solid heat capacity rate  $C_s = c_{p,s} \hat{m}_s$  decreases the suspension temperature. An increase of the riser diameter from 36–72 mm results in an increase of the power transmitted to the solid phase by about 27 % while the solid heat capacity rate increases by about 62 %. This reduces the solid temperature difference over the heated riser section by about 65 K or 30 %. This demonstrates the compromise between increasing the mass flow of the HTM through the riser and the resulting decrease of the HTM temperature. Furthermore, this relation gives the possibility to control the suspension temperature by varying the solid mass flow rate. Indicated in Figure 7.27 (d), the solid fraction in the heated riser section increases with increasing riser diameter. This increase is attributed to the reduced suspension temperature leading to a reduction of the gas expansion. Additionally, the riser diameter influences the rising bubbles that has also an effect on the solid fraction. For Geldart Group A particles, the dynamic equilibrium between bubble coalescence and splitting leads to an increase of the bubble size towards a maximum size as they move in the axial direction [144]. In the present case, the maximum bubble size is similar to the smallest considered riser diameter of  $d_{\text{riser}} = 36$  mm [145]. When the radial extension of a bubble approaches the riser diameter, it will lead to slug flow where the complete riser cross section is covered by the gas phase [27]. With a riser diameter of  $d_{\text{riser}} > 36$  mm, a bubble with a diameter of about 36 mm rises freely and particles can pass the bubble on both sides. This behavior is shown in Figure 7.28 where the instantaneous solid fraction field is compared for the different riser diameters in a riser section of 1.0 m height. For the smallest riser diameter, some bubbles cover almost the entire cross section that leads to slug flow. Increasing the riser diameter avoids, especially for  $d_{\text{riser}} = 72$  mm, these slugs. Reducing slug flow by increasing the riser

diameter decreases the bed expansion and increases therefore the average solid fraction in the riser. In addition, the reduced slug-flow tendency leads to a more uniform bubble size distribution and reduces pressure oscillations, which is a favorable effect for steady operation of such a CSP plant.

## 7.3 Time-averaged heat-transfer mechanisms

After investigating the more general influence of the wall temperature and the riser diameter on the operating conditions and heat transfer of the CSP plant, the model is now used to investigate in detail the heat-transfer mechanisms in dense gas-particle suspensions for which there are no experimental data. The results below were obtained for gas-phase boundary conditions given by  $U_{g,aer,riser} = 44.0 \text{ mm/s}$  and  $U_{g,leak} = 2.5 \text{ mm/s}$ . The influence of the average wall temperature in the heated riser section ( $\hat{T}_w = 581, 981, \text{ and } 1281 \text{ K}$ ) as well as the particle diameter ( $d_p = 64, 200, \text{ and } 400 \text{ }\mu\text{m}$ ) on the heat-transfer mechanisms was analyzed. As for the previous parameter study, the different wall temperatures were achieved by scaling the parabolic temperature profile in the heated riser section. The suspension-dispenser inlet velocity was adapted to the particle diameters listed above to keep the suspension in the lower section just above the minimum fluidization velocity, resulting in  $U_{g,in} = 5.5, 42.0, \text{ and } 159.3 \text{ mm/s}$ .

### 7.3.1 Temperature distribution in the solid phase

Figure 7.29 shows the normalized time-averaged solid temperature and the temperature-gradient as a function of the normalized radial coordinate for different wall temperatures and  $d_p = 64 \text{ }\mu\text{m}$  at  $y = 0.0 \text{ m}$  and  $y = 0.245 \text{ m}$ . Since the radial profiles are virtually symmetric only the values from the wall to the tube centerline are shown. Each marker location corresponds to a cell-centered value in the computational grid. For both axial locations, the solid temperature peaks at the hot tube wall and approaches constant values near the centerline. Along the axial direction, the temperature profiles differ

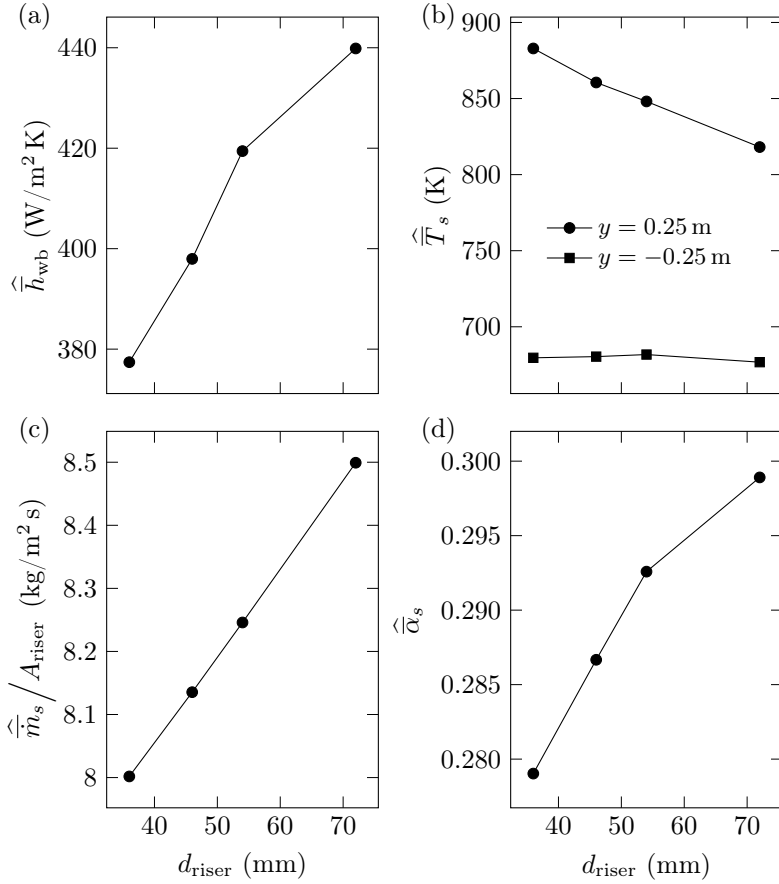


Figure 7.27: Time- and space-averaged (a) wall-to-bed heat-transfer coefficient, (b) solid temperature at the in- and outlet of the heated riser section, (c) solid mass flow per riser cross section, and (d) solid fraction in the heated riser section as a function of the riser diameter.



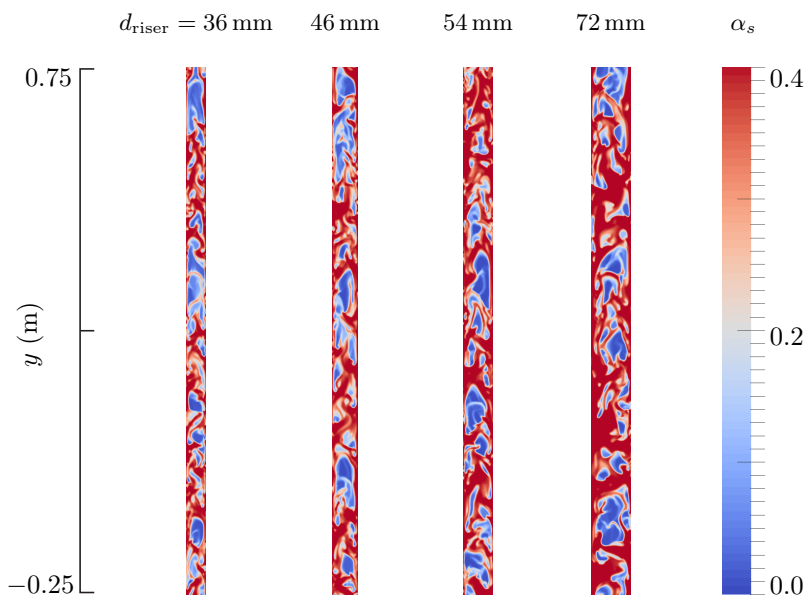


Figure 7.28: Instantaneous solid fraction field in a 1.0 m high riser section for different riser diameters.

mainly by a reduction of the temperature difference between the heated riser wall and the bulk flow in the tube center. The normalized temperature gradients peak likewise at the wall and decrease within the near-wall region to a negligible value. The different wall temperatures have thereby a minor influence on the normalized temperature gradient.

Figure 7.30 depicts  $\bar{T}_s(x=0, y)$  normalized with the local wall temperature  $T_w(y)$  for  $d_p = 64 \mu\text{m}$  and different wall temperatures along the axial direction of the heated riser section. Increasing the wall temperature leads to an increased temperature difference between  $\bar{T}_s(x=0, y)$  and  $T_w(y)$ . This difference is largest at the beginning of the heated riser section where the cold particles enter. As the particles move upwards through the heated zone, the difference between  $\bar{T}_s(x=0, y)$  and  $T_w(y)$  decreases as expected. For the highest wall temperature, the temperature difference between the solid phase in the centerline and the riser wall at the upper end of the heater riser section is about 186 K. This indicates that there is a potential to increase the solid-phase temperature further by either increasing the residence time of the particles in the heated riser section or by increasing the heating rate of the particles. The residence time can be increased by increasing the length of the heated riser section or by reducing the riser-inlet air velocity  $U_{g,\text{riser,in}}$  to decrease the solid mass flow rate while keeping the same solid fraction. In the former case, the solar power input would need to be increased to retain the same heat flux on the larger riser section. The heating rate can be increased by reducing the particle size, which could, however, lead to different fluidization conditions especially when moving towards cohesive (Geldart Group C) particles.

### 7.3.2 Heat-transfer contributions in the solid phase

The detailed modeling approach enables a direct calculation of individual heat-transfer contributions in the solid phase. To distinguish between individual contributions, the terms of Eq. (5.20) responsible for a specific heat-transfer mechanism are time-averaged. This leads to time-averaged

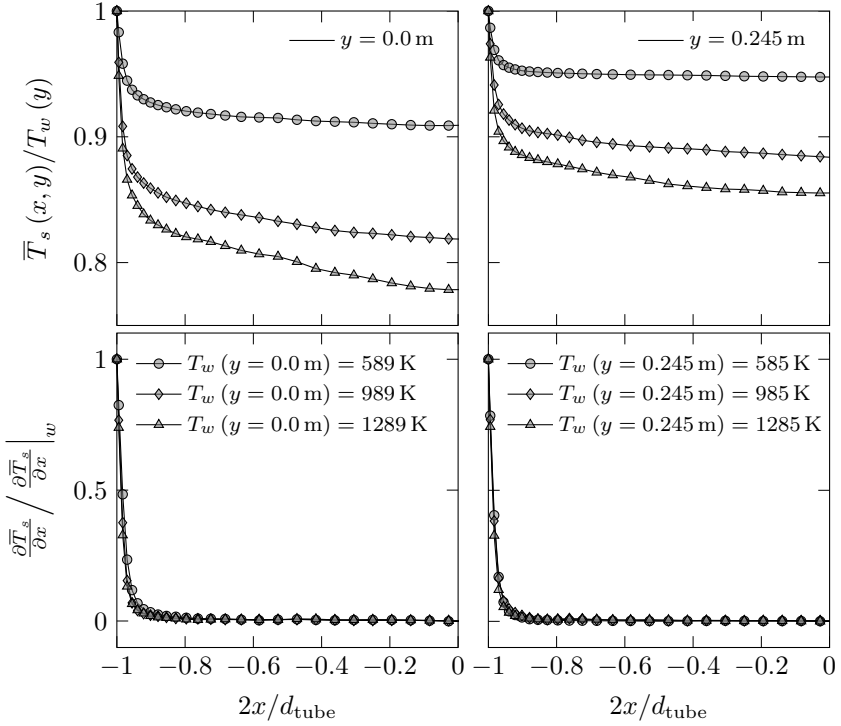


Figure 7.29: Normalized time-averaged solid-phase temperature and temperature gradient at  $y = 0.0$  m (left) and  $y = 0.245$  m (right) as a function of the normalized radial direction for  $d_p = 64 \mu\text{m}$  and different wall temperatures.

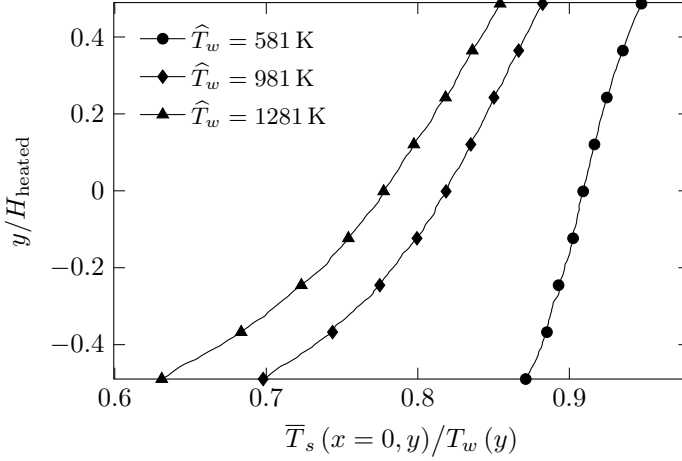


Figure 7.30: Normalized time-averaged solid-phase temperature at  $x = 0.0$  m for  $d_p = 64 \mu\text{m}$  and different wall temperatures as a function of the normalized axial location. (Symbols are shown every 61 cells.)

volumetric heat-transfer contributions as follows:

- Heat conduction:

$$\overline{Q'''_{\text{cond}}} = \overline{Q'''_1} = \overline{\nabla \cdot \left( \frac{\alpha_s k_{s,\text{eff}}}{c_{p,s}} \nabla e_s \right)} \quad (7.5)$$

- Convection of internal energy:

$$\begin{aligned} \overline{Q'''_{\text{conv,int}}} = \overline{Q'''_2} = \overline{e_s \nabla \cdot (\alpha_s \rho_s \mathbf{U}_s)} - \overline{\nabla \cdot (\alpha_s \rho_s \mathbf{U}_s e_s)} - \\ \left( \frac{\partial \overline{\alpha_s \rho_s e_s}}{\partial t} - \frac{\partial \overline{\alpha_s \rho_s}}{\partial t} \overline{e_s} \right) \approx \alpha_s \rho_s \overline{\left( \frac{De_s}{Dt} \right)} \end{aligned} \quad (7.6)$$

- Radiation heat transfer:

$$\overline{Q'''_{\text{rad}}} = \overline{Q'''_3} = \overline{\kappa (G - 4\sigma T_s^4)} \quad (7.7)$$

- Interfacial heat transfer:

$$\overline{Q'''_{\text{intf}}} = \overline{Q'''_4} = \overline{h_{sg} (T_g - T_s)} \quad (7.8)$$

- Convection of kinetic energy:

$$\begin{aligned} \overline{Q}_{\text{conv,kin}}''' = \overline{Q}_5''' = & \overline{\nabla \cdot (\alpha_s \rho_s \mathbf{U}_s) \frac{1}{2} |\mathbf{U}_s|^2} - \overline{\nabla \cdot (\alpha_s \rho_s \mathbf{U}_s \frac{1}{2} |\mathbf{U}_s|^2)} \\ & - \left( \overline{\frac{\partial \alpha_s \rho_s \frac{1}{2} |\mathbf{U}_s|^2}{\partial t}} - \overline{\frac{1}{2} |\mathbf{U}_s|^2 \frac{\partial \alpha_s \rho_s}{\partial t}} \right) \approx \overline{\alpha_s \rho_s \left( \frac{D \frac{1}{2} |\mathbf{U}_s|^2}{Dt} \right)} \end{aligned} \quad (7.9)$$

- Pressure terms:

$$\overline{Q}_{\text{pres}}''' = \overline{Q}_6''' = \overline{p \frac{\partial \alpha_s}{\partial t}} - \overline{\nabla \cdot (\alpha_s \mathbf{U}_s p)} \quad (7.10)$$

By definition, in a quasi-steady state, the sum of all volumetric heat-transfer contributions in a specific computational grid cell must be equal to zero

$$\sum_{k=1}^6 \overline{Q}_{k,i,j}''' = 0 \quad (7.11)$$

where  $i$  and  $j$  are the grid cell indices in  $x$ - and  $y$ -directions. For example, the case  $\overline{Q}_{1,i,j}''' > 0$  corresponds to a positive heat transfer to cell  $i, j$  by conduction from neighboring cells or boundaries while  $\overline{Q}_{2,i,j}''' < 0$  corresponds to heat removal in cell  $i, j$  by convection of internal energy to neighboring cells or boundaries. To identify the relative impact of a specific heat-transfer mechanism within a defined range of grid cells, it is useful to normalize the individual heat-transfer contributions with the absolute value of the maximum heat-transfer contribution within this defined range of grid cells. The maximum heat-transfer contribution for a horizontal row  $j$  of grid cells is defined by

$$\overline{Q}_{\text{max},j}''' = \max_i \left( \max_{1 \leq k \leq 6} \left( \left| \overline{Q}_{k,i,j}''' \right| \right) \right) \quad (7.12)$$

On the other hand, if the relative impact of the heat-transfer mechanism within a specific grid cell is of interest, it is useful to normalized the individual heat-transfer contributions within a specific grid cell with the absolute value of the total incoming (or outgoing) volumetric heat transfer of this particular grid cell given by

$$\overline{Q}_{\text{sum},i,j}''' = \frac{1}{2} \sum_{k=1}^6 \left| \overline{Q}_{k,i,j}''' \right| \quad (7.13)$$

This local normalization enables the identification of relative heat-transfer contributions in grid cells with a small volumetric heat transfer compared to  $\overline{Q}_{\max,j}'''$  given by Eq. (7.12).

In the following, the time-averaged volumetric heat-transfer contributions are shown only for the axial location  $y = 0.245$  m since they are nearly constant along the heated riser section. Due to near-perfect radial symmetry only the results of the left riser side are presented. Furthermore, the radial profiles are limited to the near-wall region where the main heat transfer takes place.

Figure 7.31 presents the time-averaged heat-transfer contributions normalized with  $\overline{Q}_{\max,j}'''$  for  $T_w(y = 0.245 \text{ m}) = 985 \text{ K}$  and  $d_p = 64 \mu\text{m}$  as a function of the normalized radial coordinate. When moving from the riser wall towards the centerline, the normalized heat-transfer contributions decrease within 2 mm to a negligible value. In this region of high gradients, the dominant heat-addition mechanism is conduction and the dominant heat-removal mechanism is convection of internal energy. This behavior reflects the basic mechanism of forced convection heat transfer from a hot surface where the fluid in direct contact with the wall is heated by conduction and the transport of energy into the bulk flow is mainly by convection. The heat transfer contribution due to convection of kinetic energy given by Eq. (7.9) is negligible since the considered particles are conveyed with small velocities ( $U_{s,\max} \approx 0.05 \text{ m/s}$ ). Similarly insignificant are the pressure terms given by Eq. (7.10) as a result of the small pressure difference of  $\Delta p_{\max} \approx 0.25 \text{ bar}$  in the system. The reduction of the dominant heat-transfer contributions towards the centerline is due to the almost constant temperature in the center region. The decrease of the heat-transfer contributions follows roughly the progression of the normalized time-averaged temperature gradient as shown in Figure 7.29.

The most significant with  $\overline{Q}_{\max,j}'''$  normalized time-averaged heat-transfer contributions are depicted in Figure 7.32 (a) for  $T_w(y = 0.245 \text{ m}) = 585, 985, \text{ and } 1285 \text{ K}$  and  $d_p = 64 \mu\text{m}$  as a function of the normalized radial coordinate. For increasing wall temperatures, the normalized heat-

transfer contributions decrease quicker toward the centerline but negligible values are reached at approximately the same distance from the wall. The faster decrease for increased wall temperatures is related to steeper temperature gradients close to the wall. Although the high wall temperature of  $T_w (y = 0.245 \text{ m}) = 1285 \text{ K}$  leads to the expectation that radiative heat transfer is important, it is in fact negligible compared to conduction and convection of internal energy. This finding can be explained by two factors. First, there is only a small temperature difference between the hot wall and the adjacent solid phase. This limited temperature difference is due to the very high heating rate of the particles leading to an almost instantaneous adjustment to the surrounding temperature. For all the considered cases, the Biot number of the particles is  $\text{Bi} \ll 1$ . Second, the large extinction coefficient of the solid phase reduces the radiation exchange between hot regions near the wall and colder regions towards the centerline.

Figure 7.32 (b) shows the same time-averaged heat-transfer contributions as Figure 7.32 (a) but uses  $\overline{Q}_{\text{sum},i,j}'''$  for the normalization. It should be noted that  $\overline{Q}_{\text{sum},i,j}'''$  changes for each cell location. In the considered near-wall region, the relative heat-transfer contributions within individual cells stay nearly constant and heat is only removed by convection of internal energy for all considered wall temperatures. Increasing the wall temperature from 585 K to 1285 K reduces the relative heat addition by conduction close to the heated wall by about 5–6 % while radiation and interfacial heat transfer increase slightly and compensate the reduced heat addition by conduction.

Figure 7.33 (a) depicts the most significant with  $\overline{Q}_{\text{max},j}'''$  normalized time-averaged heat-transfer contributions for  $T_w (y = 0.245 \text{ m}) = 985 \text{ K}$  and  $d_p = 64, 200, \text{ and } 400 \mu\text{m}$  as a function of the normalized radial coordinate. As before, the dominant heat-transfer mechanisms are conduction and convection of internal energy. An increase of the particle diameter shifts the maximum heat transfer by one grid cell towards the centerline while negligible values are reached at approximately the same distance from the wall. The same time-averaged heat-transfer contributions normalized with  $\overline{Q}_{\text{sum},i,j}'''$  are

shown in Figure 7.33 (b). When moving from the heated wall towards the centerline, the relative heat addition by radiation increases while the relative conduction contribution likewise decreases. This effect is mainly present for  $d_p = 400 \mu\text{m}$ . It is expected that this results from an increased radiation exchange between hot and colder particles farther apart due to the reduced extinction coefficient of the suspension with bigger particles. The relative contribution of the interfacial heat transfer stays over the considered near-wall region for each particle diameter at a constant positive value of about 0.02–0.03. This indicates that about 2–3 % of the total heat gain are due to interfacial heat transfer and hence the time-averaged solid-phase temperature is slightly lower than the temperature of the surrounding gas phase.

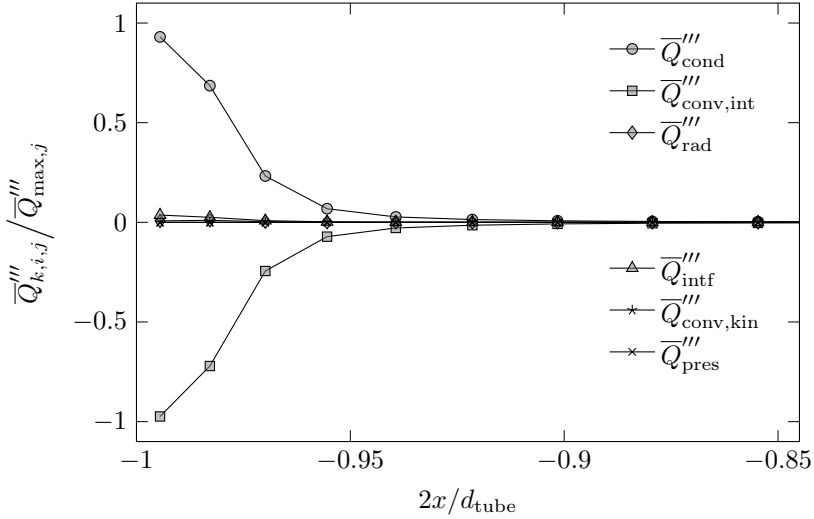


Figure 7.31: Normalized time-averaged heat-transfer contributions at  $y = 0.245 \text{ m}$  for  $d_p = 64 \mu\text{m}$  and  $T_w(y = 0.245 \text{ m}) = 985 \text{ K}$  as a function of the normalized radial direction.



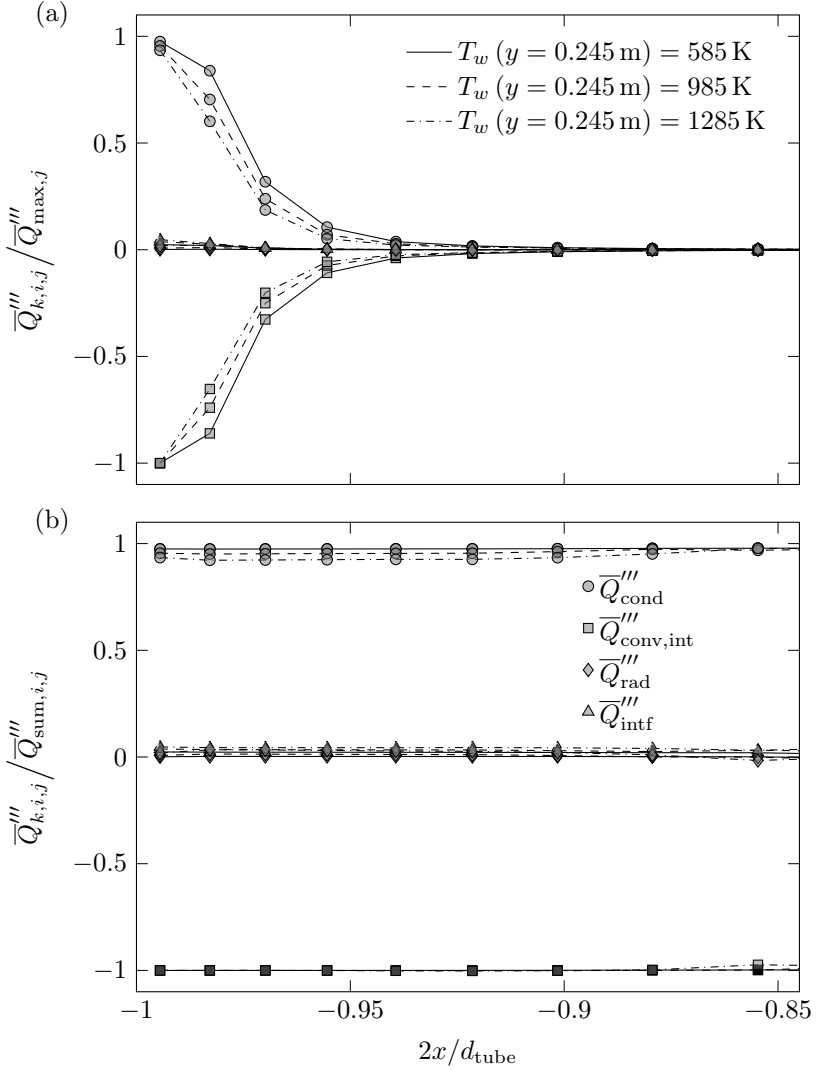


Figure 7.32: Normalized time-averaged main heat-transfer contributions at  $y = 0.245 \text{ m}$  for  $d_s = 64 \mu\text{m}$  and different wall temperatures as a function of the normalized radial direction. The heat-transfer contributions are normalized with (a)  $\overline{Q}'''_{\text{max},j}$  and (b) with the local value of  $\overline{Q}'''_{\text{sum},i,j}$ .

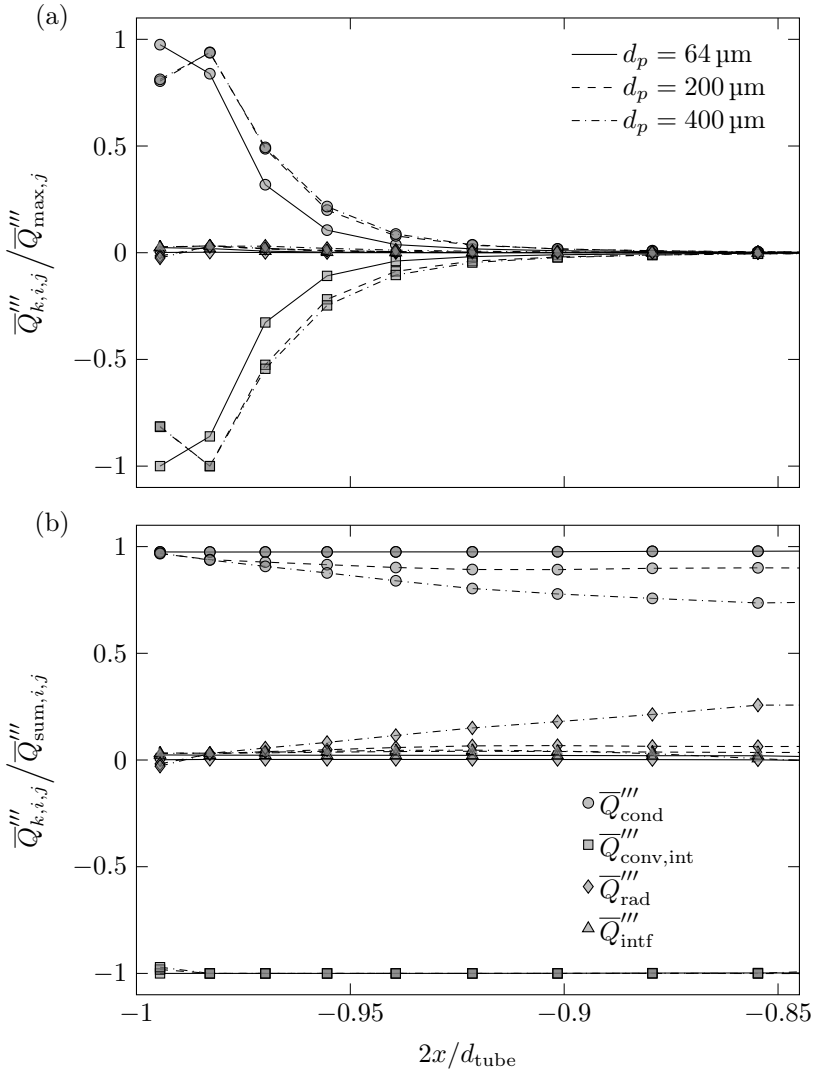


Figure 7.33: Normalized time-averaged main heat-transfer contributions at  $y = 0.245 \text{ m}$  for  $T_w(y = 0.245 \text{ m}) = 985 \text{ K}$  and different particle diameters as a function of the normalized radial direction. The heat-transfer contributions are normalized with (a)  $\bar{Q}'''_{\max,j}$  and (b) with the local value of  $\bar{Q}'''_{\text{sum},i,j}$ .

### 7.3.3 Local wall-to-suspension heat flux

Following the investigation of the heat-transfer within the solid phase, attention is now focused on to the wall-to-suspension heat flux. Based on the temperature gradient at the wall and the radiation wall heat flux, the time-averaged local heat flux from the wall to the suspension is given by

$$\bar{q}_{\text{sus}}(y) = \bar{q}_s(y) + \bar{q}_g(y) + \bar{q}_{\text{rad}}(y) = \bar{\alpha}_s \bar{k}_{s,\text{eff}} \left| \frac{\partial \bar{T}_s}{\partial n} \right|_w + (1 - \bar{\alpha}_s) \bar{k}_{g,\text{eff}} \left| \frac{\partial \bar{T}_g}{\partial n} \right|_w + |\bar{\mathbf{q}}_{\text{rad},w} \cdot \mathbf{n}_w| \quad (7.14)$$

where the first two terms on the right-hand side correspond to the conductive heat flux by the solid and gas phase and the third term is the radiative heat flux. The two conduction terms are based on Fourier's law of heat conduction. It should be noted that  $\bar{k}_{s,\text{eff}}$  does not include radiation effects. The temperature gradient at the wall was computed from one-sided second-order Lagrange interpolation polynomials [142].

Figure 7.34 depicts the normalized time-averaged wall-heat-flux contributions in the heated riser section for  $\hat{T}_w = 581 \text{ K}$ ,  $981 \text{ K}$ , and  $1281 \text{ K}$  and  $d_p = 64 \mu\text{m}$  as a function of the normalized axial coordinate. The heat-flux contributions are normalized with the local value of  $\bar{q}_{\text{sus}}(y)$  given in Eq. (7.14). The dominant contribution is seen to be solid conduction at about 90–97 % of the total suspension heat flux. Gas conduction and radiation heat flux account for about 2–5 % and 1–5 %, respectively. Increasing the wall temperature leads to increases of  $\bar{q}_{\text{rad}}/\bar{q}_{\text{sus}}$  and  $\bar{q}_g/\bar{q}_{\text{sus}}$  while  $\bar{q}_s/\bar{q}_{\text{sus}}$  decreases. The relative increase of  $\bar{q}_{\text{rad}}/\bar{q}_{\text{sus}}$  is partly due to the temperature dependence to the forth power while the conductive terms depend on the temperature gradients that showed an almost linear dependence on the temperature. It is expected that the increase of  $\bar{q}_g/\bar{q}_{\text{sus}}$  is due to thermal gas expansion at higher temperatures and the resulting decrease of the solid fraction that also favors the radiation exchange. In addition, Figure 7.34 shows a relative change of the wall-heat-flux contribution in the axial direction:  $\bar{q}_s/\bar{q}_{\text{sus}}$  decreases while  $\bar{q}_{\text{rad}}/\bar{q}_{\text{sus}}$  and  $\bar{q}_g/\bar{q}_{\text{sus}}$  increase. This results

probably from the increase of the suspension temperature in the axial direction (as indicated in Figure 7.30) and the consequential decrease of the solid fraction due to thermal gas expansion. This tendency is particularly pronounced for higher temperatures.

Figure 7.35 shows the normalized time-averaged wall-heat-flux contributions in the heated riser section for  $d_p = 64\text{ }\mu\text{m}$ ,  $200\text{ }\mu\text{m}$ , and  $400\text{ }\mu\text{m}$  and a mean wall temperature of  $\hat{T}_w = 981\text{ K}$  as a function of the normalized axial coordinate. As before, the dominant contribution is solid conduction with a relative importance of about 86–94 % while gas conduction and radiation account for about 4–5 % and 2–9 %, respectively. An increase of the particle diameter increases  $\bar{q}_{\text{rad}}/\bar{q}_{\text{sus}}$  since radiation can penetrate deeper into the suspension due to a reduced extinction coefficient. Furthermore, the higher heat capacity of bigger particles increases the temperature difference between the wall and the nearby particles, which enhances the radiation heat flux also. For a particle diameter of  $d_p = 400\text{ }\mu\text{m}$  and a mean wall temperature of  $\hat{T}_w = 981\text{ K}$ , the relative radiation-heat-flux contribution can exceed 10 %. This maximum is reached on the top of the heated riser section where the highest suspension temperature is reached and the increased gas expansion leads to a minimum solid fraction.

## 7.4 Instantaneous heat-transfer mechanisms

In the previous section, the time-averaged heat-transfer mechanisms were analyzed. These time-averaged mechanisms depend on the instantaneous flow and temperature fields. To point this out, this section investigates the influence of the solid-fraction, solid-temperature, and solid-velocity field on the local and instantaneous heat flux from the riser wall to the solid phase. This local and instantaneous heat flux is calculated from

$$q_s(y) = \alpha_s k_{s,\text{eff}} \left| \frac{\partial T_s}{\partial n} \right|_w \quad (7.15)$$

where as in Eq. (7.14), the solid-temperature gradient at the wall was computed from one-sided second-order Lagrange interpolation polynomials.

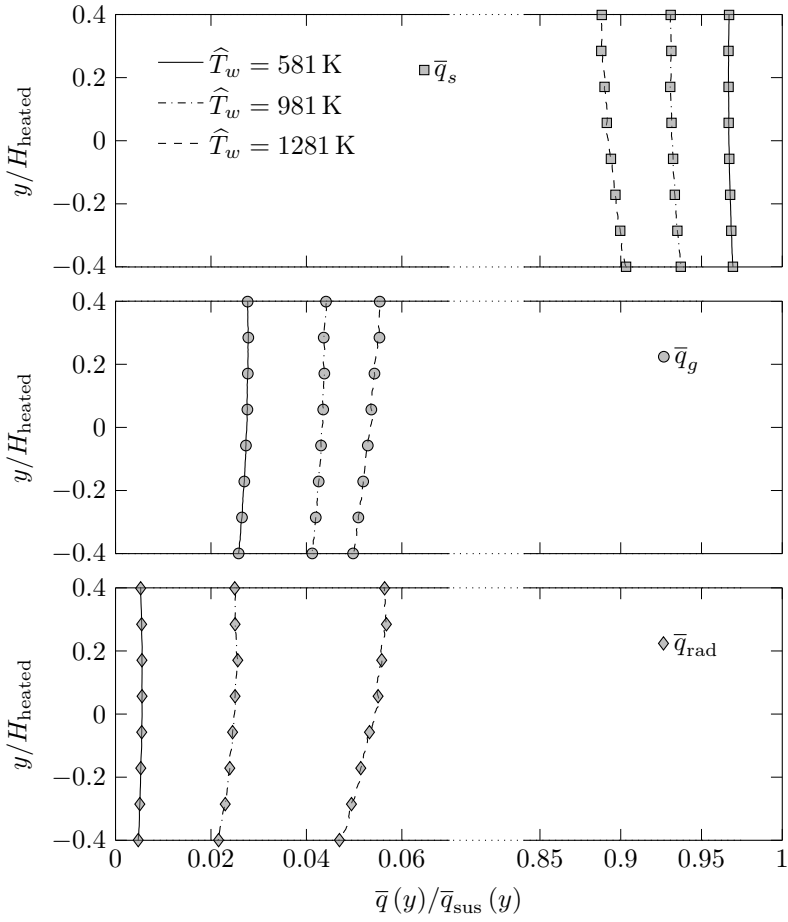


Figure 7.34: Normalized time-averaged local wall heat flux in the heated riser section for different wall temperatures and  $d_p = 64 \mu\text{m}$  as a function of the normalized axial coordinate. (Symbols are shown for every 57 cells.)

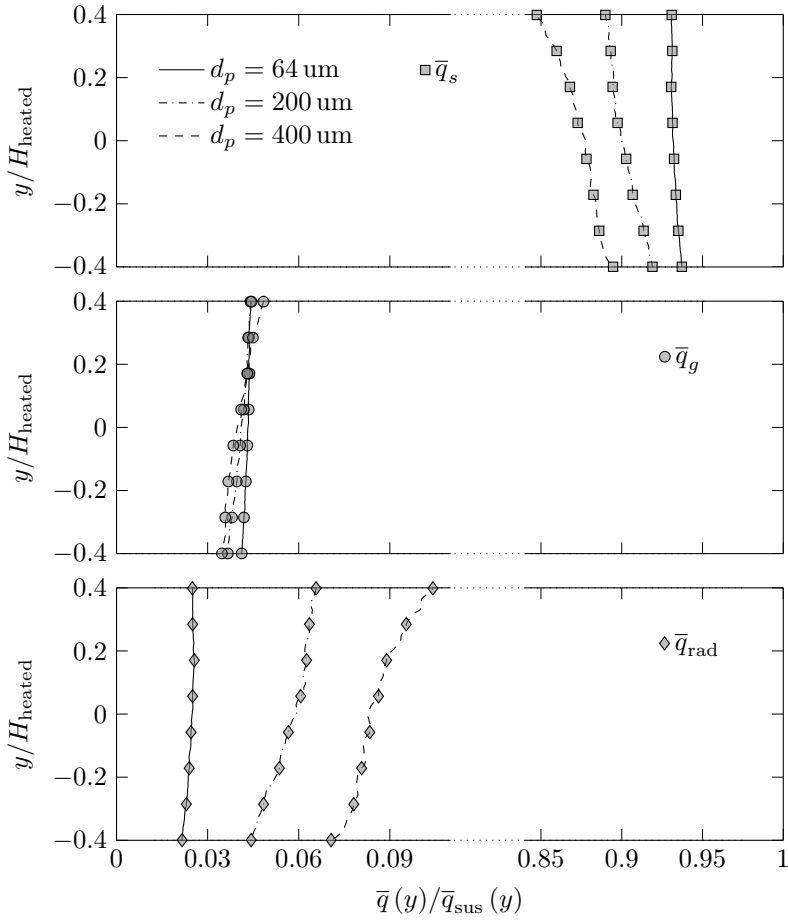


Figure 7.35: Normalized time-averaged wall heat flux in the heated riser section for different particle diameters and  $\hat{T}_w = 981 \text{ K}$  as a function of the normalized axial coordinate. (Symbols are shown for every 57 cells.)

Figure 7.36 shows the local wall-to-solid heat flux along the heated riser section for both the left and right wall at different times and for a mean riser-wall temperature of  $\hat{T}_w = 581$  K. The local heat flux is normalized with the maximum value of  $q_s$  for  $t_1 \leq t \leq t_4$  where  $t_1$ – $t_4$  are the investigated times. The heat flux values are normalized for each wall independently. The results shown are for a time interval after reaching a quasi-steady state. To demonstrate the influence of the solid fraction, each time step includes a snapshot of the solid fraction field. The fast bubble dynamics require a short time interval of 0.025 s to visualize transient effects. The wall-to-solid heat flux shows a wave-like shape with peak values usually at locations where a bubble is in the immediate vicinity of the left or right wall. Especially the bigger bubbles have the tendency to move from one wall to the other as they rise through the heated riser section. When the bubbles approach one side, they force the solid phase to move along the wall in either up- or downward direction. During this process, colder solid regions from the center replace the solid phase adjacent to the heated wall. This effect increases the local heat flux.

Further characteristics of the instantaneous wall-to-solid heat flux are locations where the wall heat flux almost vanishes. These local minima are directly related to the solid temperature field as indicated in Figure 7.37, showing the same wall-to-solid heat-flux curves as in Figure 7.36 together with the instantaneous solid-temperature fields for the investigated times. As seen from the solid temperature fields, every local minimum of the wall-to-solid heat-flux is exactly located at a local hot spot, visualized with the darker color. These hot spots indicate a reduced temperature difference between the heated wall and the adjacent solid phase resulting in a decrease of the local solid-phase temperature gradient. As given in Eq. (7.15), the wall-to-solid heat flux vanishes if the temperature gradient tends towards zero. The relative small heat conductivity of the gas-particle suspension reduces the heat transfer by conduction from these hot regions to the adjacent colder regions.

The locations of these hot spots are strongly dependent on the velocity

field. This is shown in Figure 7.38, comparing the instantaneous solid-velocity field with indicated velocity vectors to the wall-to-solid heat flux on the left and right riser wall over the same time interval as before. In general, when a bubble moves upwards, the front of the rising bubble pushes the solid phase into the positive axial direction while along the bubble sides, the solid phase is pushed into the negative axial direction. This effect can be seen at an axial location of around  $y = 0.0\text{ m}$  on the right wall: the solid phase is pushed downwards as the rising bubble moves from the left to the right wall. This downwards flow drags the local hot spot in negative  $y$ -direction and shifts thereby the local heat-flux minimum accordingly. The formation of these hot spots results from stagnation zones where a reduced convective exchange gives the solid phase enough time to heat up by wall-to-solid conduction. These stagnation zones appear because bubbles tend to follow the path of the previous bubble and hence they do not pass through certain solid regions. The preferred bubble path changes in irregular intervals due to hydrodynamic variations like bubble coalescence or breakup. When a rising bubble induces a renewal of a hot solid region at the wall, the convective heat transfer reduces the local solid temperature by moving the hot region adjacent to the wall into the bulk flow and replacing it with a colder region from the center, which improves the local wall heat flux.

As shown above, the heat transfer is influenced by a complex interplay between the solid-fraction, solid-temperature, and solid-velocity field whereas the rising bubbles have a strong impact on the overall heat exchange. Moreover, the observed instantaneous mechanisms explain the results of the time-averaged heat transfer analyzed in Section 7.3.2 where it was shown that the time-averaged heat-transfer contributions are dominated by heat addition due to conduction at the wall and by heat removal due to convection.



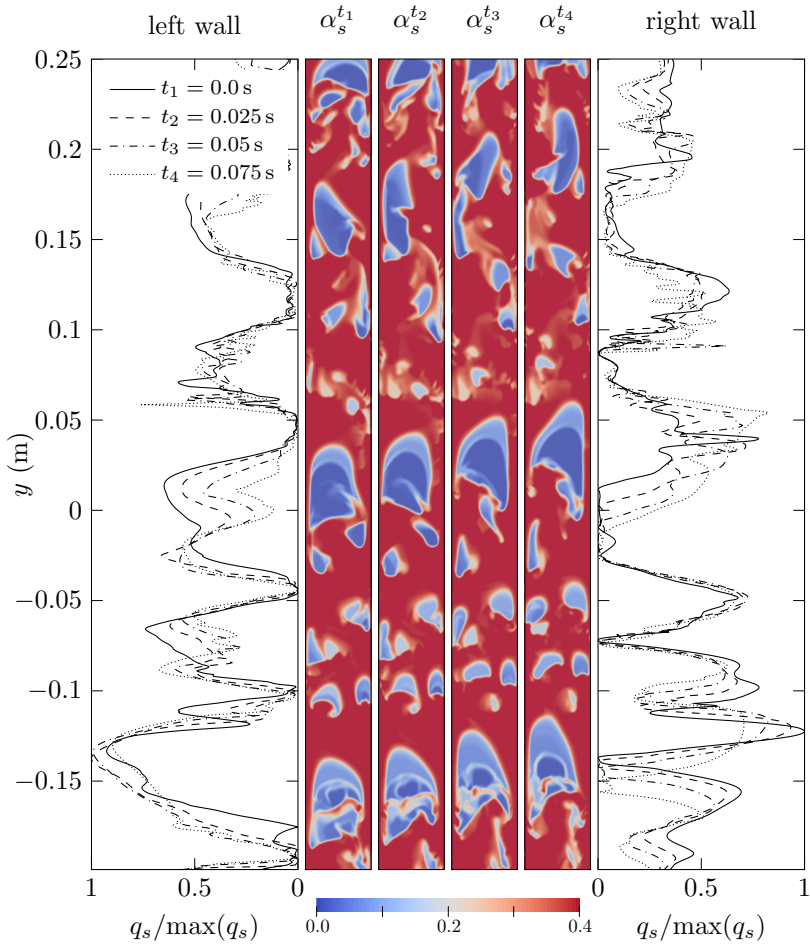


Figure 7.36: Local and normalized wall-to-solid heat flux along the axial direction of the left and right heated riser wall at different times for a mean wall temperature of  $\hat{T}_w = 581$  K with indicated instantaneous solid-fraction fields.

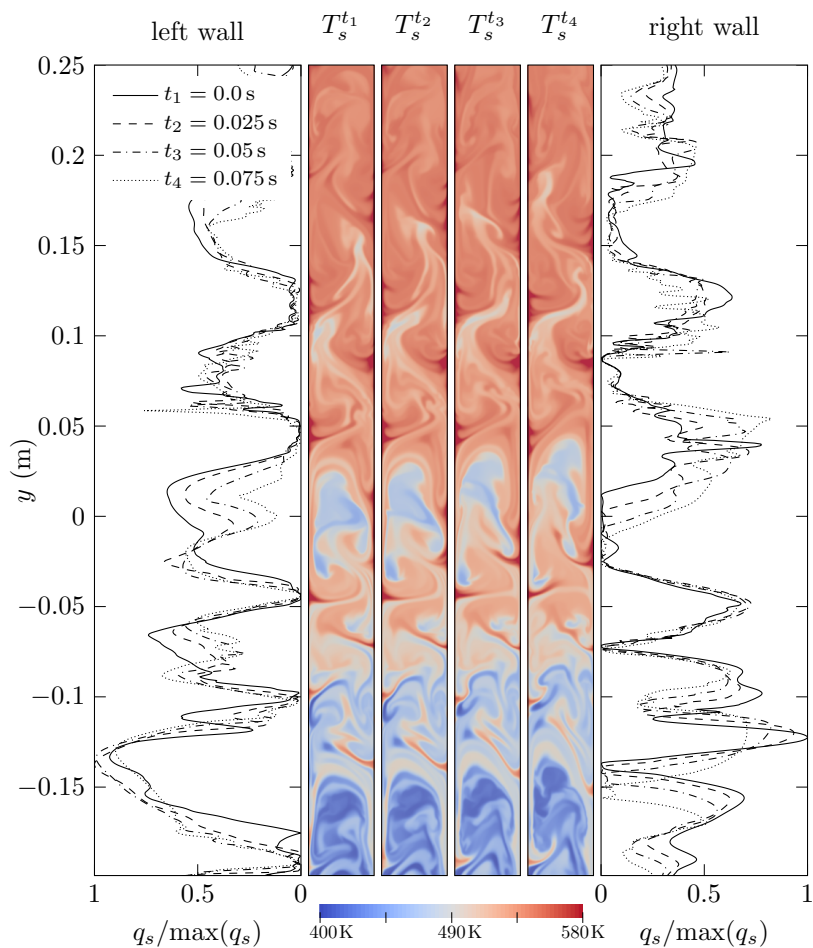


Figure 7.37: Local and normalized wall-to-solid heat flux along the axial direction of the left and right heated riser wall at different times for a mean wall temperature of  $\hat{T}_w = 581$  K with indicated instantaneous solid-temperature fields.

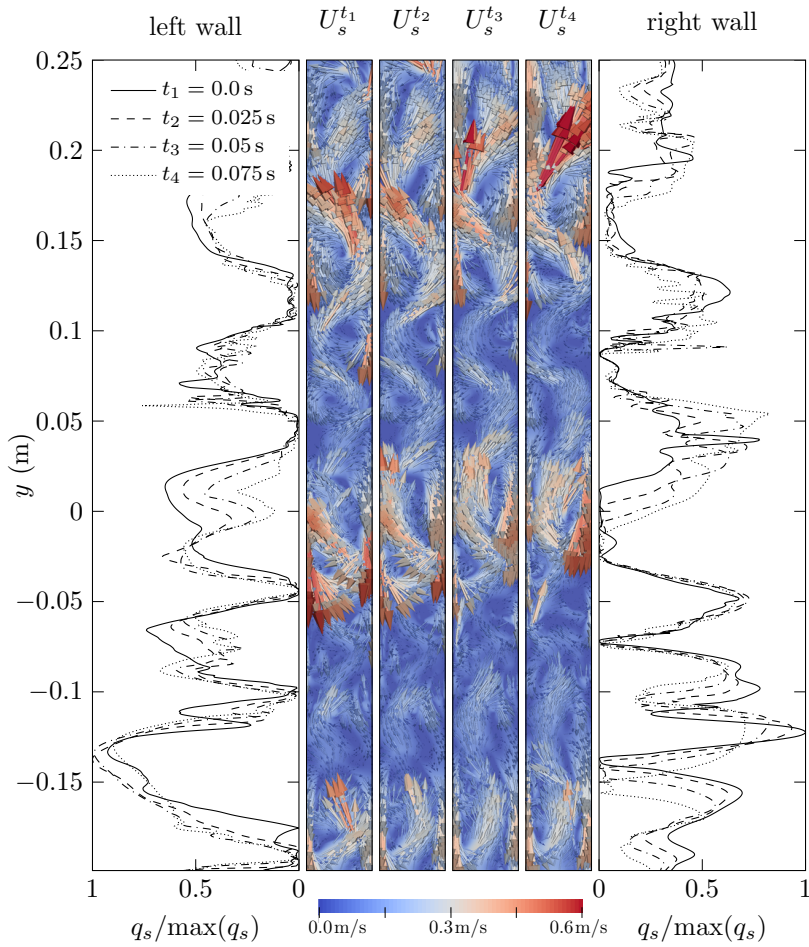


Figure 7.38: Local and normalized wall-to-solid heat flux along the axial direction of the left and right heated riser wall at different times for a mean wall temperature of  $\hat{T}_w = 581$  K with indicated instantaneous solid-velocity fields.

## 7.5 Conclusion

A comparison of the two-phase model with on-sun experimental results of a CSP plant using a dense gas-particle suspension as HTM showed good agreement. The comparison included the wall-to-bed heat-transfer coefficient, the pressure drop, and the solid fraction in the riser for different operating conditions. In a subsequent step, the verified and validated model was used for three independent investigations for which there are either no experimental data available or the investigations reach beyond experimental possibilities. First, a parameter study was performed to investigate the influence of the riser-wall temperature and the riser diameter on the wall-to-bed heat-transfer coefficient, the solid temperature, the solid mass flow rate, and the solid fraction in the heated riser section. Second, a detailed analysis of the involved time-averaged heat-transfer mechanisms was performed by separating the total heat transfer into the individual heat-transfer contributions. This separation was performed for the heat transfer within the solid phase and for the wall-to-suspension heat flux. Finally, the instantaneous solid-fraction, solid-temperature, and solid-velocity fields were analyzed to investigate their influence on the instantaneous wall-to-solid heat flux.

The parameter study showed that for a constant solid mass flow rate an increase of the riser wall temperature leads to a decrease of the heat-transfer coefficient. This results from a strong decrease of the logarithmic mean temperature difference between the in- and outlet of the heated riser section. Furthermore, the increased suspension temperature causes a gas-phase expansion and a resulting decrease of the solid fraction in the heated riser section. While keeping the gas velocity at the riser inlet and the riser-wall temperature constant, an increase of the riser diameter from 36 mm to 72 mm reduces the solid temperature difference over the heated riser section by about 30 %. This results from an increase of the total heat capacity rate by about 62 %, while the total power transmitted to the suspension increases only by about 27 %. In addition, increasing the riser diameter above the maximum bubble size prevents slug flow, leads to a more uniform bubble

size distribution, and reduces pressure oscillations, which is favorable for the power plant operation. Although the wall-to-bed heat-transfer coefficient gives important information, it is not necessarily an indicator for good performance of a CSP plant or a desirable value to optimize. Moreover, due to its dependence on several parameters, the heat-transfer coefficient should always be considered in relation to other properties like the solid temperature or the solid mass flow rate.

The total heat transfer was separated into the fundamental contributions to gain insights into the importance of the involved time-averaged heat-transfer mechanisms. The results were compared for a range of wall temperatures and different particle diameters. Within the solid phase, heat transfer is dominated by conduction and convection of internal energy, while radiation heat transfer has, even for an average wall temperature of 1281 K, a minor influence. This is due to the combination of a small temperature difference between the wall and the adjacent solid phase and the high extinction coefficient of the dense suspension. Consequently, radiation exchange between hot regions near the wall and colder regions towards the center-line is extinguished by the intermediate suspension. Furthermore, radiation exchange between adjacent solid regions is insignificant due to the reduced temperature difference. The major heat exchange takes place within a distance of a few particle diameters from the hot wall where the particles are mainly heated by conduction and most of the heat is transferred to the bulk flow by solid convection.

The wall-to-suspension heat flux was found to be dominated by solid-phase conduction that accounts for about 97 % for an average wall temperature of 581 K. For an increased average wall temperature of 981 K together with a particle diameter of 400  $\mu\text{m}$ , the radiation heat-flux contribution can locally exceed 10 %. The radiation wall heat flux is not only favored by the strong temperature dependence of radiation itself, it also increases due to the gas expansion at higher temperatures and the resulting reduction of the solid-phase volume fraction that decreases the extinction coefficient of the suspension. This results in an increase of the relative radiation heat flux

contribution along the heated riser.

In a final analysis, the influence of the instantaneous solid-fraction, solid-temperature, and solid-velocity field on the wall-to-solid heat flux was investigated. A comparison of sequential snapshots with the local wall-to-solid heat flux revealed the complex interplay between the examined flow and temperature fields and the wall heat flux. The rising bubbles induce a convective transport of the solid phase and replace hot solid regions adjacent to the heated riser wall with colder regions from the center. Local hotspots have another important influence on the wall-to-solid heat transfer: due to temporal stagnation zones at the wall, the solid phase has enough time to heat up by conduction and approaches the local wall temperature. With a reduced temperature gradient between these hot spots and the wall, the local wall heat flux vanishes. Furthermore, the observed instantaneous flow and heat transfer characteristics explain and confirm the previously determined time-averaged heat-transfer mechanisms.

# Chapter 8

## Summary and outlook

### 8.1 Summary

A major improvement of the solar-to-electricity efficiency of CSP power plants requires an increase of the working-fluid temperature to enable a more efficient thermodynamic cycle. With an increase of the working-fluid temperature above 873 K, commonly used subcritical Rankine cycles can be replaced with supercritical or even ultra-supercritical Rankine cycles. This increases the thermal-to-electricity efficiency by about 10 %. Moreover, the costs of thermal-energy storage systems have to be reduced to allow cost-effective and round-the-clock electricity generation using CSP. At these high temperatures, conventional HTM like molten nitrate salts will decompose and direct steam generation is unsuitable for thermal-energy storage. These problems can be avoided by using heat-resistant particles with a high heat capacity like SiC particles. As a consequence, the operating temperatures of CSP plants can be increased towards 1300 K and the SiC particles can directly be used as thermal-energy storage media. In order to transfer the incident solar energy to such particles, a new CSP concept uses a slowly upward moving, dense gas-particle suspension as HTM for solar power towers. The dense gas-particle suspension heats up by moving through directly irra-

diated riser tubes located in the solar receiver of such a power plant. After passing the solar receiver, the HTM can be either stored or directly routed through a heat exchanger to transfer the thermal energy to a working fluid that is subsequently used in a thermodynamic cycle to generate electricity.

To evaluate this new CSP concept in more detail, an in-depth understanding of the involved hydrodynamic and heat-transfer mechanisms is required. Therefore, a detailed model to predict the hydrodynamics and heat transfer in dense gas-particle systems was built in this thesis. To include radiation heat transfer, an experimental-numerical approach was developed to determine radiation properties of dense particle suspensions that can directly be applied to solve the RTE with commonly used numerical methods.

### 8.1.1 Determination of radiation properties

The developed experimental-numerical approach enables the determination of the volume-averaged extinction coefficient, scattering albedo, and approximated scattering phase function of particle suspensions as a function of the solid fraction. This allows the accurate prediction of radiation heat transfer in gas-particle systems. A spectroscopic goniometry system was used to measure the intensity distribution around irradiated samples of SiC particle suspensions. For this reason, the particles were suspended in a transparent epoxy resin and the mixture was put between two glass slides. With this method, the solid fraction and thickness of the particle suspension can be set precisely. A numerical fitting procedure was applied for each solid fraction to determine the approximated radiation properties of the particle suspension. This was achieved by using a Monte Carlo model representing the experimental setup and approximating the particle suspension with an idealized continuous participating medium. The radiation properties of the participating medium were adjusted in a fitting routine until the numerical intensity distribution showed good agreement with the experimental intensity distribution. Three different suspension thicknesses were considered for each solid fraction. The resulting set of approximated radiation properties



corresponded to the values that led to the best agreement for all considered suspension thicknesses together.

Two different types of SiC particles were investigated: black particles with a purity of 97 % and green particles with a purity of 99 %. The scattering phase function was best approximated with the double Henyey-Greenstein phase function featuring a strong forward and small backward scattering peak. In the investigated range of solid volume fractions, the approximated scattering phase functions were similar for both SiC particle types and they showed a weak dependence on the solid fraction. The determined extinction coefficient was for both particles in excellent agreement with the dependent scattering correlation from Singh and Kaviani indicating a very strong dependence on the solid fraction. The scattering albedo increased slightly with increasing solid fraction while the black SiC particle suspensions showed a scattering albedo about 40 % smaller than the green SiC particle suspensions. With a similar extinction coefficient, the black SiC particle suspensions have therefore a considerably higher absorption coefficient. A comparison of the approximated scattering phase function with the theoretical scattering phase function calculated from Mie theory showed a substantial disagreement. This emphasizes the importance to take dependent scattering effects, actual particle shapes, and possible impurities into account to accurately determine volume-averaged radiation properties of dense particle suspensions.

### 8.1.2 Model of dense gas-particle suspensions

The developed model to predict the hydrodynamics and heat transfer in dense gas-particle systems uses a transient compressible two-phase Euler-Euler approach and was built on the open-source code OpenFOAM. The model is capable of capturing the dynamics of bubble formation, coalescence, and breakup together with conduction, convection, and radiation heat transfer. With the determined volume-averaged radiation properties of the SiC particle suspensions, the implemented radiation model calculates

the effective radiation properties at each time step depending on the solid volume fraction in each computational cell.

The continuum representation of the solid phase requires a grid spacing larger than the particle diameter and the smallest grid size was therefore limited by the particle size. This is in contrast to the grid in the near-wall region of the heated riser that required a high resolution to accurately predict the temperature gradient. As a result, the smallest grid spacing was a compromise between the continuum representation of the solid phase and the appropriate near-wall grid resolution.

In separate studies, the hydrodynamics and heat transfer were verified and validated before comparing the model to on-sun experimental results of a CSP plant using a dense gas-particle suspension as HTM. The comparison showed good agreement and the verified and validated model was subsequently used for a parameter study and in-depth investigations of the heat-transfer mechanisms.

In the parameter study, the influences of the riser wall temperature and the riser diameter on the wall-to-bed heat-transfer coefficient, solid temperature, solid mass flow rate, and solid fraction were investigated. It was shown that for a constant solid mass flow rate through the riser tube an increase of the riser wall temperature reduces the heat-transfer coefficient. This is mainly due to the strong increase of the LMTD between the in- and outlet of the heated riser section. With a constant gas velocity at the riser inlet, an increase of the riser diameter from 36 mm to 72 mm increased the total heat capacity rate by about 62% while the total power transmitted to the suspension increased only by about 27%. As a consequence, the solid temperature difference over the heated riser section decreased by about 30%. This indicates the compromise between increasing the mass flow of the HTM through the riser and the resulting reduction of the HTM temperature.

The detailed investigation of the heat-transfer mechanisms was split into three parts: the time-averaged heat transfer within the solid phase, the time-averaged wall-to-suspension heat flux, and the instantaneous wall-to-solid heat flux. In the former, the combined heat transfer was separated by

splitting the energy conservation equation into individual heat-transfer contributions. Within the solid phase, the main heat transfer is by conduction and convection, while radiation has for a particle diameter of  $64\text{ }\mu\text{m}$  a minor influence. This is even the case for an average wall temperature of  $1281\text{ K}$ . The minor influence of radiation results from a small temperature difference between the wall and the adjacent solid phase together with the high extinction coefficient of the dense suspension. The major heat exchange takes place within a few millimeters from the hot wall where heat is added by conduction and transferred to the bulk flow by solid convection.

The time-averaged wall-to-suspension heat flux is controlled by wall-to-solid conduction that accounts, for a particle diameter of  $64\text{ }\mu\text{m}$  and an average wall temperatures of  $581\text{ K}$ , for about 97 %. Increasing the particle diameter to  $400\text{ }\mu\text{m}$  together with an average wall temperature of  $981\text{ K}$  leads in the upper area of the heated riser section to a radiation heat-flux contribution of around 10 %. The radiation wall heat flux is favored by the strong temperature dependence of radiation heat transfer and the increasing gas expansion for higher suspension temperatures. As a consequence of the gas expansion, the solid fraction is reduced and therefore the extinction coefficient of the gas-particle suspension decreases.

The analysis of the instantaneous wall-to-solid heat flux confirmed the above conclusions that the heat transfer is dominated by wall-to-solid conduction in combination with heat removal through solid convection to the bulk flow. This was observed by comparing sequential snapshots of the solid-fraction, solid-temperature, and solid-velocity field. Furthermore, the exchange of hot solid regions adjacent to the heated wall is strongly influenced by the path of the rising bubbles, which tend to follow the previous bubble. This leads to local stagnation zones at the wall where the solid phase approaches the wall temperature and the local wall heat flux decreases significantly.

Altogether, the presented model differs from previous models by allowing detailed insights into the hydrodynamics and heat-transfer mechanisms over a very broad range of operating conditions. The detailed modeling approach

allowed thereby a level of detail that is beyond experimental techniques. The in-depth prediction and distinction of individual contributions of the heat transfer within the solid-phase and the wall-to-suspension heat flux give an important understanding to evaluate and optimize the performance of dense gas-particle suspensions as high-temperature HTM for this new CSP concept.

## 8.2 Outlook

On the basis of the applied experimental-numerical approach to determine radiation properties and the modeling of the hydrodynamics and heat transfer in dense gas-particle suspensions, there is some potential for further research.

### 8.2.1 Determination of radiation properties

The arrangement of the optical instruments required by the used spectroscopic goniometry system limited the measurement of the angular intensity distribution to a range of 0–156°. The backscattering from 156–180° could therefore not be captured and its influence on the approximated scattering phase function was accordingly not considered. Since a continuous function, covering the complete angular range from 0–180°, was used to fit the discrete measurements, the absence of certain measuring points will increase the statistical uncertainty. One way of measuring the backscattered intensity above 156° could be realized by using a beam splitter placed directly in the path of the incoming radiation. In this way, part of the incoming radiation will be lost but the backscattered radiation from the sample can be reflected towards a detector. Difficulties may arise from the alignment and possible offsets due to the beam splitter as well as from the reduced radiation intensity reaching the detector.

The radiation properties of the SiC particle suspensions were determined in the visible spectrum where they showed a negligible dependence on the

wavelength. Based on reported values from literature, the scattering coefficient of SiC particles stays also constant within the infrared region. Although this justifies the assumption of a spectrally independent approximated scattering phase function, it was not demonstrated. The investigation in the infrared region would require a fundamental adjustment of the experimental method since the used epoxy resin and the glass slides of the samples and the optical lenses of the experimental setup have reduced transmissivities for wavelengths above 2000–3000 nm. The experimental setup could be adjusted by replacing the lenses with appropriate mirrors to direct the incident radiation to the sample. Achieving a uniform suspension of particles in combination with a precisely controllable solid fraction and a small optical thickness without using epoxy resin or glass slides is more complex. One possibility could be a freely falling curtain of particles whereas the controlling of a uniform curtain with a constant solid fraction may lead to major experimental challenges.

### 8.2.2 Model of dense gas-particle suspensions

The gained insights and knowledge of the heat transfer in dense gas-particle suspensions will be used within the CSP2 project to develop a simplified model for optimization and scale-up studies. Compared to the detailed model developed in this thesis, the simplified model will cover basic mass and heat balances to reduce the computational time considerably.

To increase the confidence in the developed model further, additional experimental studies are desirable. Especially the exact measurement of the air flow rate at the riser inlet is a key value to accurately compare the experimentally determined and numerically predicted wall-to-bed heat-transfer coefficient. This air flow rate could be determined by measuring the mass flow of air bypassing the riser through the particle feeding tube in combination with pressure and temperature measurements at the riser inlet. With a known air mass flow at the suspension dispenser inlet and the air density at the riser entrance, a simple mass balance would lead to the

superficial air velocity at the riser inlet. In addition, the used experimental results were determined from an on-sun experimental campaign where the operating conditions depended on the solar irradiation and environmental temperature changes. To simplify the task of validating the model, the construction of a lab-scale experimental setup with an electrically heated riser could be beneficial to extract more controllable experimental results together with accurately defined boundary conditions.

Since the smallest grid spacing was limited by the particle size, higher-order spatial discretization methods should be considered to improve the accuracy of the predicted near-wall temperature gradient. Another possibility to improve the resolution and accuracy of the predicted near-wall hydrodynamics and heat transfer could be a combination of a discrete representation of the particles in the near-wall region and a continuum representation of the solid phase in the center region. However, the numerical implementation of combining an Euler-Lagrange with an Euler-Euler approach is expected to be very challenging.

To reduce the computational time of the detailed model, it should be considered to implement an adaptive grid refinement strategy. With such a method, the grid could be dynamically adapted during the calculation depending on the required accuracy of the solution in certain regions of the computational domain.

In the framework of the CSP2 project, the experimental testing of a scaled-up CSP plant with several parallel riser tubes is planned to follow the experimental campaign of the single-tube riser used for comparison in this thesis. The experimental results of the multi-tube CSP plant would be useful to extend the model validation with a different setup. In addition, the influence of non-uniform heating between parallel riser tubes would be an interesting field for additional numerical investigations.

Furthermore, the influence of circumferential temperature differences on the riser wall is of interest. For directly irradiated riser tubes, it is expected that the front- and backside temperature of the riser will differ. Due to the temperature dependent gas expansion, an influence on the hydrodynamics

is expected. The increased gas expansion on the irradiated side leads most likely to an increased bubble frequency and an intensified particle replacement. This could enhance the wall-to-suspension heat flux on the irradiated riser wall.

An important task is the comparison of the heat transfer between two- and three-dimensional systems. Due to the extremely high computational costs, it was not possible to model a complete CSP plant with a reasonable grid resolution in three dimensions. Consideration should be given to model a small section of the riser in two and in three dimensions and compare the resulting hydrodynamic and heat-transfer mechanisms. One problem of modeling only a section of the riser is the lack of axial periodicity. The temperature increases along the riser and the size of gas bubbles increase as they move in the axial direction due to coalescence and gas expansion. This prevents the application of periodic boundary conditions to represent the complete riser with a small riser section. A solution would be to consider a bubbling fluidized bed without a net solid mass flow rate. The comparison between the bubbling fluidized bed and the dense gas-particle suspensions used as HTM can be justified with the very slow upward movement of the HTM that behaves from a hydrodynamic point of view basically like a steady bubbling fluidized bed.

Finally, the applied model uses an idealized representation of monosized particles to reduce the computational time considerably. An investigation with two different particle sizes having the same mean diameter as the monosized case showed a slight increase of the bed expansion. This study could be extended to more than two different particle sizes, whereas the increase of the computational costs would lead to a very time-consuming investigation. The influence of polysized particles on the heat transfer is not fully known and could be beneficial for further modeling approaches. As a result of the determined radiation properties where the influence of different particle sizes balanced each other out, it is expected that with the same mean particle diameter the heat transfer between mono- and polysized particles will be similar.





# List of Figures

|     |   |    |
|-----|---|----|
| 1.1 | Aerial view of Gemasolar, a 20 MW <sub>el</sub> solar power tower CSP plant using molten nitrate salt as HTM. The plant was constructed and is operated by Torresol Energy [9]. . . . .   | 3  |
| 1.2 | Schematic of a CSP plant using a dense gas-particle suspension as HTM with a storage of hot and cold particles and a generic thermodynamic cycle. . . . .   | 5  |
| 2.1 | Polar plot of different scattering phase functions. The HG and DHG phase function have the same shape factor for the forward peak. The incident radiation travels from the left to the right. . . . .                                       | 23 |
| 3.1 | Photograph of the investigated black (a) and green (b) SiC particles with indicated scale. . . . .  | 27 |
| 3.2 | SEM images of the black (a) and green (b) SiC particles with indicated scale. . . . .   | 28 |
| 3.3 | Density ( $q_0$ ) and cumulative ( $Q_0$ ) distribution of the black (a) and green (b) SiC volume-based particle diameter. The distributions are based on the number of particles. Also shown is the volume-mean particle diameter. . . . . | 29 |
| 3.4 | Photograph of the investigated black (a) and green (b) SiC particle samples. The sample height is 76 mm and the width is 26 mm. . . . .   | 31 |

|     |  |    |
|-----|--|----|
| 3.5 | Schematic of the spectroscopic goniometry system with a xenon-arc lamp, double monochromator, mechanical chopper, plano-convex spherical $\text{MgF}_2$ lens pairs, sample, dual Si/MCT sandwich detector, lock-in amplifier, and data acquisition system. . . . .   | 33 |
| 3.6 | Geometric representation of the Monte Carlo model. With description on top and indicated stochastic rays below. Only a small number of rays are shown for clarity. The yellow lines are rays that are either absorbed in the participating medium or by a detector and the black lines are rays that are lost to the surrounding. A green plus sign indicates an absorption event and a red cross sign indicates the last scattering event of a ray that is lost to the surrounding. . . . . | 38 |
| 3.7 | Schematic of the sample including the epoxy-particle suspension and the glass slides together with generic ray paths. . . .  | 39 |
| 4.1 | SEM image of the glass microspheres used for the validation study with indicated scale. . . . .  | 42 |
| 4.2 | Density ( $q_0$ ) and cumulative ( $Q_0$ ) distribution of the glass microspheres volume-based particle size. The distributions are based on the number of particles. Also indicated is the volume-mean particle diameter. . . . .   | 42 |
| 4.3 | Mie scattering phase function of glass microspheres with a refractive index of $n_G = 1.515 - i1.5 \times 10^{-7}$ and a wavelength of $\lambda = 500$ nm. . . . .   | 44 |
| 4.4 | Measured normalized detector signal of packed beds with glass microspheres as a function of the viewing angle compared to the numerical results of the Monte Carlo model with Mie scattering. . . . .  | 45 |

|      |  |    |
|------|--|----|
| 4.5  | Spectral dependence of the normalized detector signal at $\theta_s = 0^\circ$ for a) the glass slides, a sample with epoxy only, and b) samples with black and green SiC particles for different sample thicknesses. . . . .   | 48 |
| 4.6  | Normalized and scaled detector signal at a viewing angle of $\theta_s = 0^\circ$ for different solid fractions as a function of the sample thickness together with an exponential fit through each sample series. (a) shows the results of the black SiC particles and (b) the results of the green SiC particles together with the 95 % confidence uncertainty. . . . . | 51 |
| 4.7  | Experimentally determined extinction coefficients of the black and green SiC samples compared to the independent scattering theory and the dependent scattering correlation from Singh and Kaviany [52] with indicated 95 % confidence uncertainty of the experimental results. . . . .  | 52 |
| 4.8  | Normalized detector signal of the black SiC samples with $\alpha_s = 0.05$ (a) and $\alpha_s = 0.09$ (b) as a function of the viewing angle with indicated 95 % confidence uncertainty. . . . .  | 55 |
| 4.9  | Normalized detector signal of the black SiC samples with $\alpha_s = 0.20$ (a) and $\alpha_s = 0.30$ (b) as a function of the viewing angle with indicated 95 % confidence uncertainty. . . . .  | 56 |
| 4.10 | Normalized detector signal of the green SiC samples with $\alpha_s = 0.05$ (a) and $\alpha_s = 0.09$ (b) as a function of the viewing angle with indicated 95 % confidence uncertainty. . . . .  | 57 |
| 4.11 | Normalized detector signal of the green SiC samples with $\alpha_s = 0.22$ (a) and $\alpha_s = 0.28$ (b) as a function of the viewing angle with indicated 95 % confidence uncertainty. . . . .  | 58 |
| 4.12 | Normalized detector signal of the black and green SiC samples with a solid fraction of $\alpha_s = 0.09$ and similar sample thicknesses as a function of the viewing angle with indicated 95 % confidence uncertainty. . . . .   | 59 |

|      |   |    |
|------|---|----|
| 4.13 | (a) Investigated scattering phase functions. (b) Experimental measured (green SiC, $\alpha_s = 0.28$ , $s = 0.19$ mm) and normalized detector signal as a function of the viewing angle compared to the Monte Carlo model with the different scattering phase functions shown in (a). . . . . | 61 |
| 4.14 | Normalized detector signal for different solid fractions and similar sample thicknesses of the black SiC (a) and green SiC (b) samples as a function of the viewing angle in comparison with the Monte Carlo model. . . . .   | 62 |
| 4.15 | Comparison of the numerically derived DHG scattering phase function for black SiC (a) and green SiC (b) particle suspensions with different solid fractions as a function of the scattering angle. . . . .  | 63 |
| 4.16 | Numerically derived DHG scattering phase functions of the black and green SiC particle suspensions ( $\alpha_s = 0.05$ ) compared to the scattering phase function based on Mie theory for $n_{\text{SiC}} = 2.7 - i0.1$ and using the measured green SiC particle size distribution. . . . . | 64 |
| 4.17 | Parameters of the DHG scattering phase function derived from the Monte Carlo model for the black (a) and green SiC (b) particle suspensions as a function of the solid fraction together with linear fits. . . . .  | 67 |
| 4.18 | Comparison of the single asymmetry factors of the black and green SiC particle suspensions as a function of the solid fraction. The $y$ -axis is scaled to show the possible range of $-1 \leq A_1 \leq 1$ . . . . .  | 68 |
| 4.19 | Scattering albedo of the black and green SiC particle suspension as a function of the solid fraction derived from the Monte Carlo model together with a linear fit. . . . .   | 68 |

|      |  |     |
|------|--|-----|
| 4.20 | Numerically and experimentally derived extinction coefficients of the black and green SiC particle suspensions with indicated 95 % confidence uncertainty of the experimental results compared to the correlation from Singh and Kaviany [52] for a mean diameter of $d_p = 63.75 \mu\text{m}$ . . . . .   | 70  |
| 6.1  | Comparison of the analytical solution and the numerical result of the normalized velocity profile of a fully developed two-dimensional incompressible laminar pipe flow. The numerical result is shown for $y/L = 0.8$ . . . . .   | 95  |
| 6.2  | Schematic of the fluidized bed with indicated dimensions and boundary conditions. The origin is located at the inlet on the centerline. . . . .  | 97  |
| 6.3  | Comparison of the considered grid spacings as a function of the radial direction for the grid-refinement study of the hydrodynamics validation case. . . . .   | 98  |
| 6.4  | Time-averaged solid-velocity profiles at $y = 0.4 \text{ m}$ (a) and $y = 0.2 \text{ m}$ (b) for different grid refinement levels with a gas inlet velocity of $U_{g,\text{in}} = 0.46 \text{ m/s}$ . . . . .  | 100 |
| 6.5  | Time-averaged solid-fraction profiles at $y = 0.4 \text{ m}$ (a) and $y = 0.2 \text{ m}$ (b) for different grid refinement levels with a gas inlet velocity of $U_{g,\text{in}} = 0.46 \text{ m/s}$ . . . . .  | 101 |
| 6.6  | Time- and cross-section-averaged solid fraction in the axial direction for different grid refinement levels with a gas inlet velocity of $U_{g,\text{in}} = 0.46 \text{ m/s}$ . . . . .  | 102 |
| 6.7  | Time-averaged solid-velocity profiles at $y = 0.4 \text{ m}$ (a) and $y = 0.2 \text{ m}$ (b) for different averaging frequencies and a constant averaging interval between $t_{\text{start}} = 5 \text{ s}$ and $t_{\text{end}} = 60 \text{ s}$ with a grid spacing of $2.5 \text{ mm}$ and a gas inlet velocity of $U_{g,\text{in}} = 0.46 \text{ m/s}$ . . . . . | 104 |

|      |  |     |
|------|--|-----|
| 6.8  | Time-averaged solid-fraction profiles at $y = 0.4$ m (a) and $y = 0.2$ m (b) for different averaging frequencies and a constant averaging interval between $t_{\text{start}} = 5$ s and $t_{\text{end}} = 60$ s with a grid spacing of 2.5 mm and a gas inlet velocity of $U_{g,\text{in}} = 0.46$ m/s. . . . .  | 105 |
| 6.9  | Time- and cross-section-averaged solid fraction in the axial direction for different averaging frequencies and a constant averaging interval between $t_{\text{start}} = 5$ s and $t_{\text{end}} = 60$ s with a grid spacing of 2.5 mm and a gas inlet velocity of $U_{g,\text{in}} = 0.46$ m/s. . . . .  | 106 |
| 6.10 | Time-averaged solid-velocity profiles at $y = 0.4$ m (a) and $y = 0.2$ m (b) for different averaging intervals and a constant averaging frequency of 20 Hz with a grid spacing of 2.5 mm and a gas inlet velocity of $U_{g,\text{in}} = 0.46$ m/s. . . . .   | 107 |
| 6.11 | Time-averaged solid-fraction profiles at $y = 0.4$ m (a) and $y = 0.2$ m (b) for different averaging intervals and a constant averaging frequency of 20 Hz with a grid spacing of 2.5 mm and a gas inlet velocity of $U_{g,\text{in}} = 0.46$ m/s. . . . .   | 108 |
| 6.12 | Time- and cross-section-averaged solid fraction in the axial direction for different averaging intervals and a constant averaging frequency of 20 Hz with a grid spacing of 2.5 mm and a gas inlet velocity of $U_{g,\text{in}} = 0.46$ m/s. . . . .   | 109 |
| 6.13 | Comparison of the time- and space-averaged pressure drop of our model with experimental and numerical reference results by Taghipour et al. [126] and Herzog et al. [128] as a function of the gas inlet velocity $U_{g,\text{in}}$ . Also indicated is the theoretical pressure drop due to the bed weight and the minimum fluidization velocity. . . . . | 111 |
| 6.14 | Comparison of the time- and space-averaged normalized bed height $\widehat{H}/H_0$ of our model with experimental and numerical results by Taghipour et al. [126] and Herzog et al. [128] as a function of the inlet velocity $U_{g,\text{in}}$ . . . . .  | 112 |

|      |   |     |
|------|---|-----|
| 6.15 | Comparison of the time-averaged solid-fraction profile of our model with experimental and numerical reference results by Taghipour et al. [126] and Herzog et al. [128] for a gas inlet velocity of $U_{g,\text{in}} = 0.46 \text{ m/s}$ at a bed height of $y = 0.2 \text{ m}$ . . . . . | 113 |
| 6.16 | Comparison of the time-averaged solid-velocity profile of our model with numerical reference results by Taghipour et al. [126] and Herzog et al. [128] for an inlet velocity of $U_{g,\text{in}} = 0.46 \text{ m/s}$ at $y = 0.2 \text{ m}$ . . . . .                                     | 114 |
| 6.17 | Normalized fluid-temperature profile along the flow direction in a one-dimensional packed bed for different time steps. The analytical solution of Schumann [131] is compared to the results predicted by our model. . . . .  | 117 |
| 6.18 | Comparison of the normalized incoming irradiation on the walls of a square enclosure with a hot bottom wall and cold top and side walls containing a purely-scattering medium with our $P_1$ -approximation and the analytical and the Monte Carlo results by Modest [57]. . . . .        | 119 |
| 6.19 | Normalized steady-state solid-temperature profiles within a packed bed of cordierite spheres for different temperature gradients. Experimental results from Kamiuto et al. [132] compared to one-dimensional numerical results with and without the $P_1$ radiation model. . . . .        | 121 |
| 7.1  | Schematic of the numerical model with indicated boundary conditions and system dimensions. The origin is located in the middle of the heated tube section. . . . .  | 127 |
| 7.2  | Close-up of Grid 3 with indicated near-wall region (refined grid) and center region (uniform grid). The near-wall region starts 8.0 mm from the wall. . . . .   | 129 |
| 7.3  | Comparison of the considered grid spacings as a function of the radial direction for the grid-refinement study of the heated riser section. . . . .   | 130 |

|      |   |     |
|------|---|-----|
| 7.4  | Solid fraction of the bubbling fluidized bed for Grids 1–5. On top at $t = 1$ s and below at $t = 25$ s. . . . .  | 131 |
| 7.5  | Time-averaged solid-velocity profiles at $y = -0.1$ m (a) and $y = 0.0$ m (b) for different grid-refinement levels with a gas inlet velocity of $U_{g,\text{in}} = 0.04$ m/s. . . . .   | 134 |
| 7.6  | Time-averaged solid-fraction profiles at $y = 0.0$ m (a) and $y = -0.1$ m (b) for different grid-refinement levels with a gas inlet velocity of $U_{g,\text{in}} = 0.04$ m/s. . . . .   | 135 |
| 7.7  | Time- and cross-section-averaged solid fraction in the axial direction for different grid-refinement levels with a gas inlet velocity of $U_{g,\text{in}} = 0.04$ m/s. . . . .  | 136 |
| 7.8  | Time-averaged solid-temperature profiles at $y = 0.0$ m (a) and $y = -0.1$ m (b) for different grid-refinement levels with a gas inlet velocity of $U_{g,\text{in}} = 0.04$ m/s. . . . .  | 137 |
| 7.9  | Time-averaged solid temperature in the near-wall region at $y = 0.0$ m (a) and $y = -0.1$ m (b) for different grid-refinement levels with a gas inlet velocity of $U_{g,\text{in}} = 0.04$ m/s. . . . .   | 138 |
| 7.10 | Time-averaged solid-temperature gradient in the near-wall region at $y = 0.0$ m (a) and $y = -0.1$ m (b) for different grid-refinement levels with a gas inlet velocity of $U_{g,\text{in}} = 0.04$ m/s. . . . .  | 139 |
| 7.11 | Time-averaged solid-velocity profiles at $y = 0.0$ m (a) and $y = -0.1$ m (b) for different averaging frequencies and a constant averaging interval between $t_{\text{start}} = 5$ s and $t_{\text{end}} = 60$ s with a gas inlet velocity of $U_{g,\text{in}} = 0.04$ m/s. . . . . | 141 |
| 7.12 | Time-averaged solid-fraction profiles at $y = 0.0$ m (a) and $y = -0.1$ m (b) for different averaging frequencies and a constant averaging interval between $t_{\text{start}} = 5$ s and $t_{\text{end}} = 60$ s with a gas inlet velocity of $U_{g,\text{in}} = 0.04$ m/s. . . . . | 142 |
| 7.13 | Time- and cross-section-averaged solid fraction in the axial direction for different averaging frequencies and a constant averaging interval between $t_{\text{start}} = 5$ s and $t_{\text{end}} = 60$ s with a gas inlet velocity of $U_{g,\text{in}} = 0.04$ m/s. . . . .        | 143 |



|      |  |     |
|------|--|-----|
| 7.14 | Time-averaged solid-temperature profiles at $y = 0.0$ m (a) and $y = -0.1$ m (b) for different averaging frequencies and a constant averaging interval between $t_{\text{start}} = 5$ s and $t_{\text{end}} = 60$ s with a gas inlet velocity of $U_{g,\text{in}} = 0.04$ m/s. . . . . | 144 |
| 7.15 | Time-averaged solid-velocity profiles at $y = 0.0$ m (a) and $y = -0.1$ m (b) for different averaging intervals and a constant averaging frequency of 20 Hz with a gas inlet velocity of $U_{g,\text{in}} = 0.04$ m/s. . . . .   | 145 |
| 7.16 | Time-averaged solid-fraction profiles at $y = 0.0$ m (a) and $y = -0.1$ m (b) for different averaging intervals and a constant averaging frequency of 20 Hz with a gas inlet velocity of $U_{g,\text{in}} = 0.04$ m/s. . . . .   | 146 |
| 7.17 | Time- and cross-section-averaged solid fraction in the axial direction for different averaging intervals and a constant averaging frequency of 20 Hz with a gas inlet velocity of $U_{g,\text{in}} = 0.04$ m/s. . . . .  | 147 |
| 7.18 | Visualization of the instantaneous solid-fraction field of the complete CSP-plant model together with close-ups of the solid-fraction and solid-temperature field in the heated riser section. . . . .   | 148 |
| 7.19 | Time- and cross-section-averaged solid temperature at the inlet ( $y = -0.25$ m), outlet ( $y = 0.25$ m), and midpoint ( $y = 0.0$ m) of the heated riser section. . . . .   | 150 |
| 7.20 | (a) Space-averaged solid-phase mass flow leaving the computational domain through the outlet per riser cross section. (b) Time integration of the space-averaged solid-phase mass flow rate per riser cross section together with a linear fit for $t \geq 200$ s. . . . .             | 151 |
| 7.21 | Comparison of the experimental and numerical values of the wall-to-bed heat-transfer coefficient as a function of the aeration riser velocity. The numerical results are for different air-leakage velocities. . . . .   | 154 |

- 7.22 Numerical result of the solid mass flux in the riser tube as a function of the air-leakage velocity in the particle feeding tubes. The multiple data points for a given air-leakage velocity correspond to different aeration inflow velocities. . . . . 155
- 7.23 Comparison of the experimental and numerical values of the wall-to-bed heat-transfer coefficient as a function of the riser-inlet air velocity for different aeration riser velocities. . . . . 156
- 7.24 Comparison of the experimental and numerical values of the pressure drop (a) and the solid fraction (b) in the riser tube as a function of the aeration riser velocity. The multiple data points for a given aeration riser velocity correspond to different air-leakage velocities. . . . . 157
- 7.25 Time- and space-averaged (a) wall-to-bed heat-transfer coefficient, (b) solid temperature at the in- and outlet of the heated riser section, (c) solid mass flow per riser cross section, and (d) solid fraction in the heated riser section as a function of the riser-wall temperature. . . . . 160
- 7.26 Logarithmic mean temperature difference as a function of the average riser-wall temperature. . . . . 161
- 7.27 Time- and space-averaged (a) wall-to-bed heat-transfer coefficient, (b) solid temperature at the in- and outlet of the heated riser section, (c) solid mass flow per riser cross section, and (d) solid fraction in the heated riser section as a function of the riser diameter. . . . . 164
- 7.28 Instantaneous solid fraction field in a 1.0 m high riser section for different riser diameters. . . . . 165
- 7.29 Normalized time-averaged solid-phase temperature and temperature gradient at  $y = 0.0$  m (left) and  $y = 0.245$  m (right) as a function of the normalized radial direction for  $d_p = 64 \mu\text{m}$  and different wall temperatures. . . . . 167

- 7.30 Normalized time-averaged solid-phase temperature at  $x = 0.0$  m for  $d_p = 64 \mu\text{m}$  and different wall temperatures as a function of the normalized axial location. . . . . 168
- 7.31 Normalized time-averaged heat-transfer contributions at  $y = 0.245$  m for  $d_p = 64 \mu\text{m}$  and  $T_w(y = 0.245 \text{ m}) = 985 \text{ K}$  as a function of the normalized radial direction. . . . . 172
- 7.32 Normalized time-averaged main heat-transfer contributions at  $y = 0.245$  m for  $d_s = 64 \mu\text{m}$  and different wall temperatures as a function of the normalized radial direction. The heat-transfer contributions are normalized with (a)  $\overline{Q}_{\text{max},j}'''$  and (b) with the local value of  $\overline{Q}_{\text{sum},i,j}'''$ . . . . . 173
- 7.33 Normalized time-averaged main heat-transfer contributions at  $y = 0.245$  m for  $T_w(y = 0.245 \text{ m}) = 985 \text{ K}$  and different particle diameters as a function of the normalized radial direction. The heat-transfer contributions are normalized with (a)  $\overline{Q}_{\text{max},j}'''$  and (b) with the local value of  $\overline{Q}_{\text{sum},i,j}'''$ . . . . . 174
- 7.34 Normalized time-averaged local wall heat fluxes in the heated riser section for different wall temperatures and  $d_p = 64 \mu\text{m}$  as a function of the normalized axial coordinate. . . . . 177
- 7.35 Normalized time-averaged wall heat fluxes in the heated riser section for different particle diameters and  $\hat{T}_w = 981 \text{ K}$  as a function of the normalized axial coordinate. . . . . 178
- 7.36 Local and normalized wall-to-solid heat flux along the axial direction of the left and right heated riser wall at different times for a mean wall temperature of  $\hat{T}_w = 581 \text{ K}$  with indicated instantaneous solid-fraction fields. . . . . 181
- 7.37 Local and normalized wall-to-solid heat flux along the axial direction of the left and right heated riser wall at different times for a mean wall temperature of  $\hat{T}_w = 581 \text{ K}$  with indicated instantaneous solid-temperature fields. . . . . 182

|      |  |     |
|------|--|-----|
| 7.38 | Local and normalized wall-to-solid heat flux along the axial direction of the left and right heated riser wall at different times for a mean wall temperature of $\hat{T}_w = 581$ K with indicated instantaneous solid-velocity fields. . . . . | 183 |
|------|--|-----|

# List of Tables

|     |   |    |
|-----|---|----|
| 3.1 | Measured volume-mean, median (D50), D10, and D90 diameter based on the number distribution of the black and green SiC particles. The indicated particle diameters are volume equivalent sphere diameters. . . . .                                       | 26 |
| 3.2 | Maximum precision limit of the measured detector signal $P_V$ , bias limit $B$ , and the overall uncertainty of the normalized detector signal $U_{V/V_0}$ as a function of the viewing angle $\theta_s$ for a confidence level of 95 %. . . . .        | 35 |
| 4.1 | Solid fraction and sample thickness of the investigated black and green SiC particle suspensions with indicated 95 % uncertainty. . . . .   | 49 |
| 4.2 | Experimental derived extinction coefficient $\beta$ for the black and green SiC particles together with the 95 % confidence uncertainty. . . . .  | 52 |
| 4.3 | Numerically derived extinction coefficient $\beta$ , scattering albedo $\omega$ , and parameters of the DHG scattering phase function $g_f$ , $g_b$ , $\delta$ based on the Monte Carlo model for the black and green SiC particle suspensions. . . . . | 69 |
| 5.1 | Input keywords for the OpenFOAM solver for various terms where $\phi$ is a generic scalar, $\mathbf{V}$ a generic vector, and $\Gamma$ a generic diffusion coefficient. . . . .   | 89 |

|     |   |     |
|-----|---|-----|
| 6.1 | Model parameters of the Hagen-Poiseuille verification case. . .   | 95  |
| 6.2 | Model parameters of the hydrodynamics validation case. . . .  | 96  |
| 6.3 | Cell sizes and total number of grid cells used in the grid-refinement study of the hydrodynamics validation case. . . . .   | 99  |
| 6.4 | Model parameters of the convective heat transfer verification case. . . . .   | 115 |
| 6.5 | Model parameters of the radiation-model verification case. . .  | 118 |
| 6.6 | Model parameters of the steady-state conduction and radiation heat-transfer validation. . . . .   | 120 |
| 7.1 | Model parameters of the CSP plant. . . . .  | 125 |
| 7.2 | Grid characteristics of the grid-refinement study of the heated riser section with maximum and minimum cell size, maximum stretching ratio, number of cells in the near-wall region for one side and one row of cells, and the total number of cells. . | 129 |

# Bibliography

- [1] C. K. Ho and B. D. Iverson, “Review of high-temperature central receiver designs for concentrating solar power,” *Renewable and Sustainable Energy Reviews*, vol. 29, pp. 835–846, 2014.
- [2] R. Pitz-Paal, A. Amin, M. O. Bettzuge, P. Eames, G. Flamant, F. Fabrizio, J. Holmes, A. Kribus, H. van der Laan, C. Lopez, F. G. Novo, P. Papagiannakopoulos, E. Pihl, P. Smith, and H.-J. Wagner, “Concentrating solar power in Europe, the Middle East and North Africa: a review of development issues and potential to 2050,” *Journal of Solar Energy Engineering*, vol. 134, no. 2, pp. 024501–1–6, 2012.
- [3] C. Singer, R. Buck, R. Pitz-Paal, and H. Müller-Steinhagen, “Economic potential of innovative receiver concepts with different solar field configurations for supercritical steam cycles,” *Journal of Solar Energy Engineering*, vol. 136, no. 2, pp. 021009–1–10, 2014.
- [4] R. Pitz-Paal, *Future Energy: Improved, Sustainable and Clean Options for our Planet*, ch. Concentrating Solar Power, pp. 405–428. Elsevier, Oxford, 2nd ed., 2013.
- [5] A. L. Ávila-Marín, “Volumetric receivers in solar thermal power plants with central receiver system technology: A review,” *Solar Energy*, vol. 85, pp. 891–910, 2011.
- [6] G. Flamant, D. Gauthier, H. Benoit, J.-L. Sans, R. Garcia, B. Boissière, R. Ansart, and M. Hemati, “Dense suspension of solid particles

- as a new heat transfer fluid for concentrated solar thermal plants: On-sun proof of concept,” *Chemical Engineering Science*, vol. 102, pp. 567–576, 2013.
- [7] M. Romero and A. Steinfeld, “Concentrating solar thermal power and thermochemical fuels,” *Energy & Environmental Science*, vol. 5, no. 11, pp. 9234–9245, 2012.
- [8] R. I. Dunn, P. J. Hearps, and M. N. Wright, “Molten-salt power towers: newly commercial concentrating solar storage,” *Proceedings of the IEEE*, vol. 100, no. 2, pp. 504–515, 2012.
- [9] Torresol Energy, “Press Dossier,” Getxo-Vizcaya, Spain, 2014.
- [10] R. W. Bradshaw and R. W. Carling, “A review of the chemical and physical-properties of molten alkali nitrate salts and their effect on materials for solar central receivers,” *Journal of the Electrochemical Society*, vol. 134, no. 8B, pp. C510–C511, 1987.
- [11] A. Belmiloudi, ed., *Heat Transfer - Theoretical Analysis, Experimental Investigations and Industrial Systems*. InTech, 2011.
- [12] J. Pacio and T. Wetzel, “Assessment of liquid metal technology status and research paths for their use as efficient heat transfer fluids in solar central receiver systems,” *Solar Energy*, vol. 93, pp. 11–22, 2013.
- [13] A. J. Hunt, “Small particle heat exchangers,” Tech. Rep. 7841, Lawrence Berkeley National Laboratory, Berkeley, CA, 1978.
- [14] A. J. Hunt, “A new solar thermal receiver utilizing a small particle heat exchanger,” in *14th Intersociety Energy Conversion Engineering Conference*, (Boston, MA), August 5–10 1979.
- [15] M. Abdelrahman, P. Fumeaux, and P. Suter, “Study of solid-gas-suspensions used for direct absorption of concentrated solar radiation,” *Solar Energy*, vol. 22, no. 1, pp. 45–48, 1979.



- [16] G. Flamant, "Theoretical and experimental study of radiant heat transfer in a solar fluidized-bed receiver," *AIChE Journal*, vol. 28, no. 4, pp. 529–535, 1982.
- [17] J. Martin and J. Vitko Jr, "ASCUAS: A solar central receiver utilizing a solid thermal carrier," tech. rep., Sandia National Laboratories, Livermore, CA, 1982.
- [18] P. K. Falcone, J. E. Noring, and J. M. Hraby, "Assessment of a solid particle receiver for a high temperature solar central receiver system," tech. rep., Sandia National Laboratories, Livermore, CA (USA), 1985.
- [19] T. Tan and Y. Chen, "Review of study on solid particle solar receivers," *Renewable and Sustainable Energy Reviews*, vol. 14, no. 1, pp. 265–276, 2010.
- [20] R. G. Munro, "Material properties of a sintered  $\alpha$ -SiC," *Journal of Physical and Chemical Reference Data*, vol. 26, no. 5, pp. 1195–1203, 1997.
- [21] D. Kearney, U. Herrmann, P. Nava, B. Kelly, R. Mahoney, J. Pacheco, R. Cable, N. Potrovitza, D. Blake, and H. Price, "Assessment of a molten salt heat transfer fluid in a parabolic trough solar field," *Journal of Solar Energy Engineering*, vol. 125, no. 2, pp. 170–176, 2003.
- [22] D. Geldart, "Types of gas fluidization," *Powder Technology*, vol. 7, no. 5, pp. 285–292, 1973.
- [23] A. Gallo, J. Spelling, M. Romero, and J. González-Aguilar, "Preliminary design and performance analysis of a multi-megawatt scale dense particle suspension receiver," in *International Conference on Concentrating Solar Power and Chemical Energy Systems*, (Beijing, China), September 2014.
- [24] G. Cáceres, N. Anrique, A. Girard, J. Degrevé, J. Baeyens, and H. Zhang, "Performance of molten salt solar power towers in chile,"

- Journal of Renewable and Sustainable Energy*, vol. 5, no. 5, p. 053142, 2013.
- [25] J. Spelling, A. Gallo, M. Romero, and J. González-Aguilar, “A high-efficiency solar thermal power plant using a dense particle suspension as the heat transfer fluid,” in *International Conference on Concentrating Solar Power and Chemical Energy Systems*, (Beijing, China), September 2014.
- [26] R. Yusuf, M. C. Melaaen, and V. Mathiesen, “Convective heat and mass transfer modeling in gas-fluidized beds,” *Chemical Engineering & Technology*, vol. 28, no. 1, pp. 13–24, 2005.
- [27] L.-S. Fan and C. Zhu, *Principles of Gas-Solid Flows*. Cambridge Series in Chemical Engineering, Cambridge University Press, 2005.
- [28] D. Kunii and O. Levenspiel, *Fluidization Engineering*. Butterworth-Heinemann, 2nd ed., 1991.
- [29] M. A. Van der Hoef, M. van Sint Annaland, N. G. Deen, and J. A. M. Kuipers, “Numerical simulation of dense gas-solid fluidized beds: A multiscale modeling strategy,” *Annual Review of Fluid Mechanics*, vol. 40, pp. 47–70, 2008.
- [30] A. Prosperetti and G. Tryggvason, *Computational Methods for Multiphase Flow*. Cambridge University Press, 2009.
- [31] M. J. V. Goldschmidt, R. Beetstra, and J. A. M. Kuipers, “Hydrodynamic modelling of dense gas-fluidised beds: Comparison and validation of 3D discrete particle and continuum models,” *Powder Technology*, vol. 142, no. 1, pp. 23–47, 2004.
- [32] M. Syamlal and D. Gidaspow, “Hydrodynamics of fluidization: prediction of wall to bed heat transfer coefficients,” *AIChE Journal*, vol. 31, no. 1, pp. 127–135, 1985.

- [33] J. A. M. Kuipers, W. Prins, and W. P. M. Van Swaaij, "Numerical calculation of wall-to-bed heat-transfer coefficients in gas-fluidized beds," *AIChE Journal*, vol. 38, no. 7, pp. 1079–1091, 1992.
- [34] D. J. Patil, J. Smit, M. van Sint Annaland, and J. A. M. Kuipers, "Wall-to-bed heat transfer in gas-solid bubbling fluidized beds," *AIChE Journal*, vol. 52, no. 1, pp. 58–74, 2006.
- [35] R. Yusuf, B. Halvorsen, and M. C. Melaaen, "An experimental and computational study of wall to bed heat transfer in a bubbling gas-solid fluidized bed," *International Journal of Multiphase Flow*, vol. 42, pp. 9–23, 2012.
- [36] L. M. Armstrong, S. Gu, and K. H. Luo, "Study of wall-to-bed heat transfer in a bubbling fluidised bed using the kinetic theory of granular flow," *International Journal of Heat and Mass Transfer*, vol. 53, no. 21–22, pp. 4949–4959, 2010.
- [37] N. H. Dong, L. M. Armstrong, S. Gu, and K. H. Luo, "Effect of tube shape on the hydrodynamics and tube-to-bed heat transfer in fluidized beds," *Applied Thermal Engineering*, vol. 60, no. 1–2, pp. 472–479, 2013.
- [38] L. M. Armstrong, S. Gu, and K. H. Luo, "The influence of multiple tubes on the tube-to-bed heat transfer in a fluidised bed," *International Journal of Multiphase Flow*, vol. 36, no. 11–12, pp. 916–929, 2010.
- [39] R. Yusuf, B. Halvorsen, and M. C. Melaaen, "Eulerian-Eulerian simulation of heat transfer between a gas-solid fluidized bed and an immersed tube-bank with horizontal tubes," *Chemical Engineering Science*, vol. 66, no. 8, pp. 1550–1564, 2011.
- [40] J. Chang, F. Meng, L. Wang, K. Zhang, H. Chen, and Y. Yang, "CFD investigation of hydrodynamics, heat transfer and cracking reaction in

- a heavy oil riser with bottom airlift loop mixer,” *Chemical Engineering Science*, vol. 78, pp. 128–143, 2012.
- [41] B. Yaghoub, S. Shahhosseini, and S. H. Hashemabadi, “CFD modeling of hydrodynamic and heat transfer in fluidized bed reactors,” *International Communications in Heat and Mass Transfer*, vol. 35, no. 3, pp. 357–368, 2008.
- [42] K. Papadikis, A. V. Bridgwater, and S. Gu, “CFD modelling of the fast pyrolysis of biomass in fluidised bed reactors, part A: Eulerian computation of momentum transport in bubbling fluidised beds,” *Chemical Engineering Science*, vol. 63, no. 16, pp. 4218–4227, 2008.
- [43] K. Papadikis, S. Gu, and A. Bridgwater, “CFD modelling of the fast pyrolysis of biomass in fluidised bed reactors. part B: Heat, momentum and mass transport in bubbling fluidised beds,” *Chemical Engineering Science*, vol. 64, no. 5, pp. 1036–1045, 2009.
- [44] G. Flamant, N. Fatah, and Y. Flitris, “Wall-to-bed heat transfer in gas-solid fluidized beds: Prediction of heat transfer regimes,” *Powder Technology*, vol. 69, no. 3, pp. 223–230, 1992.
- [45] W. Yang, *Handbook of Fluidization and Fluid-Particle Systems*. Chemical Industries, Taylor & Francis, 2003.
- [46] J. C. Lee, G. Y. Han, and C. K. Yi, “Heat transfer in a high temperature fluidized bed,” *Korean Journal of Chemical Engineering*, vol. 16, no. 2, pp. 260–264, 1999.
- [47] H. Liu, A. Elkamel, A. Lohi, and M. Biglari, “Computational fluid dynamics modeling of biomass gasification in circulating fluidized-bed reactor using the Eulerian-Eulerian approach,” *Industrial & Engineering Chemistry Research*, vol. 52, no. 51, pp. 18162–18174, 2013.
- [48] D. Jing, L. Jing, H. Liu, S. Yao, and L. Guo, “Photocatalytic hydrogen production from refinery gas over a fluidized-bed reactor I: Numerical

- simulation,” *Industrial & Engineering Chemistry Research*, vol. 52, no. 5, pp. 1982–1991, 2013.
- [49] OpenCFD, *OpenFOAM — The Open Source CFD Toolbox — Programmer’s Guide*. OpenCFD Ltd., United Kingdom, 2.3.0 ed., 2014.
- [50] L. Hespel, S. Mainguy, and J. J. Greffet, “Radiative properties of scattering and absorbing dense media: Theory and experimental study,” *Journal of Quantitative Spectroscopy and Radiative Transfer*, vol. 77, no. 2, pp. 193–210, 2003.
- [51] D. Baillis and J. F. Sacadura, “Thermal radiation properties of dispersed media: Theoretical prediction and experimental characterization,” *Journal of Quantitative Spectroscopy and Radiative Transfer*, vol. 67, no. 5, pp. 327–363, 2000.
- [52] B. P. Singh and M. Kaviany, “Modelling radiative heat transfer in packed beds,” *International Journal of Heat and Mass Transfer*, vol. 35, no. 6, pp. 1397–1405, 1992.
- [53] C. Coquard and D. Baillis, “Radiative characteristics of opaque spherical particle beds: A new method of prediction,” *Journal of Thermophysics and Heat Transfer*, vol. 18, no. 2, pp. 178–186, 2004.
- [54] J. Randrianalisoa and D. Baillis, “Radiative properties of densely packed spheres in semitransparent media: A new geometric optics approach,” *Journal of Quantitative Spectroscopy and Radiative Transfer*, vol. 111, no. 10, pp. 1372–1388, 2010.
- [55] P. Coray, W. Lipinski, and A. Steinfeld, “Experimental and numerical determination of thermal radiative properties of ZnO particulate media,” *ASME Journal of Heat Transfer*, vol. 132, no. 1, p. 012701, 2010.
- [56] P. Coray, W. Lipinski, and A. Steinfeld, “Spectroscopic goniometry system for determining thermal radiative properties of participating media,” *Experimental Heat Transfer*, vol. 24, no. 3, pp. 300–312, 2011.

- [57] M. F. Modest, *Radiative Heat Transfer*. Academic Press, San Diego, 3rd ed., 2013.
- [58] J. Walker, D. Halliday, and R. Resnick, *Fundamentals of Physics*. John Wiley & Sons, 10th ed., 2013.
- [59] J. R. Howell, R. Siegel, and M. P. Mengüç, *Thermal Radiation Heat Transfer*. CRC Press, 5th ed., 2001.
- [60] J. C. Maxwell, “A dynamical theory of the electromagnetic field,” *Philosophical Transactions of the Royal Society of London*, vol. 155, pp. 459–512, 1865.
- [61] J. M. Stone, *Radiation and Optics*. New York: McGraw-Hill, 1963.
- [62] G. Mie, “Beiträge zur Optik trüber Medien, speziell kolloidaler Metallösungen,” *Annalen der Physik*, vol. 330, no. 3, pp. 377–445, 1908.
- [63] M. I. Mishchenko, J. W. Hovenier, and L. D. Travis, *Light Scattering by Nonspherical Particles: Theory, Measurements, and Applications*. Academic Press, 1999.
- [64] M. Tancrez and J. Taine, “Direct identification of absorption and scattering coefficients and phase function of a porous medium by a Monte Carlo technique,” *International Journal of Heat and Mass Transfer*, vol. 47, no. 2, pp. 373–383, 2004.
- [65] J. Petrasch, P. Wyss, and A. Steinfeld, “Tomography-based Monte Carlo determination of radiative properties of reticulate porous ceramics,” *Journal of Quantitative Spectroscopy and Radiative Transfer*, vol. 105, no. 2, pp. 180–197, 2007.
- [66] S. Suter, A. Steinfeld, and S. Haussener, “Pore-level engineering of macroporous media for increased performance of solar-driven thermochemical fuel processing,” *International Journal of Heat and Mass Transfer*, vol. 78, pp. 688–698, 2014.

- [67] J. Bear, *Dynamics of Fluids in Porous Media*. New York: Elsevier, 1972.
- [68] P. Coray, *Experimental determination of spectral radiative heat transfer properties in participating media*. PhD thesis, ETH Zurich, 2010.
- [69] J. F. Sacadura and D. Baillis, “Experimental characterization of thermal radiation properties of dispersed media,” *International Journal of Thermal Sciences*, vol. 41, no. 7, pp. 699–707, 2002.
- [70] Z. Ivezic and P. Menguc, “An investigation of dependent/independent scattering regimes using a discrete dipole approximation,” *International Journal of Heat and Mass Transfer*, vol. 39, no. 4, pp. 811–822, 1996.
- [71] B. L. Drolen and C. L. Tien, “Independent and dependent scattering in packed-sphere systems,” *Journal of Thermophysics and Heat Transfer*, vol. 1, no. 1, pp. 63–68, 1987.
- [72] C.-L. Tien and B. L. Drolen, “Thermal radiation in particulate media with dependent and independent scattering,” *Annual Review of Heat Transfer*, vol. 1, no. 1, pp. 1–32, 1987.
- [73] F. R. S. Lord Rayleigh, “On the electromagnetic on the electromagnetic theory of light,” *Philosophical Magazine Series 5*, vol. 12, no. 73, pp. 81–101, 1881.
- [74] C.-M. Chu and S. W. Churchill, “Representation of the angular distribution of radiation scattered by a spherical particle,” *Journal of the Optical Society of America*, vol. 45, no. 11, pp. 958–961, 1955.
- [75] J. R. Hodgkinson and I. Greenleaves, “Computations of light-scattering and extinction by spheres according to diffraction and geometrical optics, and some comparisons with the Mie theory,” *Journal of the Optical Society of America*, vol. 53, no. 5, pp. 577–588, 1963.

- [76] L. G. Henyey and J. L. Greenstein, "Diffuse radiation in the galaxy," *The Astrophysical Journal*, vol. 93, pp. 70–83, 1941.
- [77] M. F. Modest and F. H. Azad, "The influence and treatment of Mie-anisotropic scattering in radiative heat transfer," *ASME Journal of Heat Transfer*, vol. 102, no. 1, pp. 92–98, 1980.
- [78] D. Toubanc, "Henyey-Greenstein and Mie phase functions in Monte Carlo radiative transfer computations," *Applied Optics*, vol. 35, no. 18, pp. 3270–3274, 1996.
- [79] G. W. Kattawar, "A three-parameter analytic phase function for multiple scattering calculations," *Journal of Quantitative Spectroscopy and Radiative Transfer*, vol. 15, no. 9, pp. 839–849, 1975.
- [80] W. M. Irvine, "Multiple scattering by large particles," *Astrophysical Journal*, vol. 142, pp. 1563–1575, 1965.
- [81] M. Q. Brewster, "Volume scattering of radiation in packed beds of large, opaque spheres," *Journal of Heat Transfer*, vol. 126, no. 6, pp. 1048–1050, 2004.
- [82] B. P. Singh and M. Kaviany, "Independent theory versus direct simulation of radiation heat transfer in packed beds," *International Journal of Heat and Mass Transfer*, vol. 34, no. 11, pp. 2869–2882, 1991.
- [83] K. Kamiuto, "Correlated radiative transfer in packed-sphere systems," *Journal of Quantitative Spectroscopy and Radiative Transfer*, vol. 43, no. 1, pp. 39–43, 1990.
- [84] K. Kamiuto, "Radiative properties of packed-sphere systems estimated by the extended emerging-intensity fitting method," *Journal of Quantitative Spectroscopy and Radiative Transfer*, vol. 47, no. 4, pp. 257–261, 1992.
- [85] J. Marti, M. Roesle, and A. Steinfeld, "Experimental determination of the radiative properties of particle suspensions for high-temperature



- solar receiver applications,” *Heat Transfer Engineering*, vol. 35, no. 3, pp. 272–280, 2014.
- [86] J. Marti, M. Roesle, and A. Steinfeld, “Combined experimental–numerical approach to determine radiation properties of particle suspensions,” *Journal of Heat Transfer*, vol. 136, no. 9, pp. 092701–092708, 2014.
- [87] S. J. Kline and F. A. McClintock, “Description uncertainties in single-sample experiments,” *Mechanical Engineering*, vol. 75, pp. 3–8, 1953.
- [88] J. H. Kim, T. W. Simon, and R. Viskanta, “Journal of heat transfer policy on reporting uncertainties in experimental measurements and results,” *Journal of Heat Transfer*, vol. 115, no. 1, pp. 5–6, 1993.
- [89] J. Petrasch, “A free and open source Monte Carlo ray tracing program for concentrating solar energy research,” in *ASME 2010 4th International Conference on Energy Sustainability*, (Phoenix, Arizona, USA), pp. 125–132, 2010.
- [90] W. J. Wiscombe, “Improved Mie scattering algorithms,” *Applied Optics*, vol. 19, no. 9, pp. 1505–1509, 1980.
- [91] H. Du, “Mie-scattering calculation,” *Applied Optics*, vol. 43, no. 9, pp. 1951–1956, 2004.
- [92] D. Deirmendjian, *Electromagnetic Scattering on Spherical Polydispersions*. Elsevier Science Ltd., 1969.
- [93] M. A. Postlethwait, K. K. Sikka, M. F. Modest, and J. R. Hellmann, “High-temperature, normal spectral emittance of silicon carbide based materials,” *Journal of Thermophysics and Heat Transfer*, vol. 8, no. 3, pp. 412–418, 1994.
- [94] W. Lipiński, E. Guillot, G. Olalde, and A. Steinfeld, “Transmittance enhancement of packed-bed particulate media,” *Experimental Heat Transfer*, vol. 21, no. 1, pp. 73–82, 2008.

- [95] B. Pegourie, "Optical properties of alpha silicon carbide," *Astronomy and Astrophysics*, vol. 194, no. 1–2, pp. 335–339, 1988.
- [96] G. L. Harris, *Properties of Silicon Carbide*. INSPEC, Institution of Electrical Engineers, 1995.
- [97] J. Marti, A. Haselbacher, and A. Steinfeld, "A numerical investigation of gas-particle suspensions as heat transfer media for high-temperature concentrated solar power," *International Journal of Heat and Mass Transfer*, accepted, 2015.
- [98] H. G. Weller, "Derivation, modelling and solution of the conditionally averaged two-phase flow equations," Tech. Rep. HGW/02, OpenCFD Ltd., 2005.
- [99] K. Kissling, J. Springer, H. Jasak, S. Schutz, K. Urban, and M. Piesche, "A coupled pressure based solution algorithm based on the volume-of-fluid approach for two or more immiscible fluids," in *V European Conference on Computational Fluid Dynamics*, (Lisbon, Portugal), 14–17 June 2010.
- [100] C. S. Campbell and D. G. Wang, "Particle pressures in gas-fluidized beds," *Journal of Fluid Mechanics*, vol. 227, pp. 495–508, 1991.
- [101] S. V. Patankar, *Numerical Heat Transfer and Fluid Flow*. Taylor & Francis, 1980.
- [102] S. Chapman and T. G. Cowling, *The Mathematical Theory of Non-uniform Gases*. Cambridge University Press, Cambridge, 3rd ed., 1970.
- [103] B. van Wachem, *Derivation, Implementation, and Validation of Computer Simulation Models for Gas-Solid Fluidized Beds*. PhD thesis, Delft University of Technology, 2000.

- [104] A. Passalacqua and R. Fox, "Implementation of an iterative solution procedure for multi-fluid gas-particle flow models on unstructured grids," *Powder Technology*, vol. 213, no. 1–3, pp. 174–187, 2011.
- [105] C. K. K. Lun, S. B. Savage, D. J. Jeffrey, and N. Chepurniy, "Kinetic theories for granular flow: inelastic particles in Couette flow and slightly inelastic particles in a general flow field," *Journal of Fluid Mechanics*, vol. 140, pp. 223–256, 1984.
- [106] D. Gidaspow, *Multiphase Flow and Fluidization*. San Diego: Academic Press, 1994.
- [107] M. Y. Louge, E. Mastorakos, and J. T. Jenkins, "The role of particle collisions in pneumatic transport," *Journal of Fluid Mechanics*, vol. 231, pp. 345–359, 1991.
- [108] D. L. Koch, "Kinetic theory for a monodisperse gas-solid suspension," *Physics of Fluids A: Fluid Dynamics*, vol. 2, no. 10, pp. 1711–1723, 1990.
- [109] P. C. Johnson and R. Jackson, "Frictional-collisional constitutive relations for granular materials, with application to plane shearing," *Journal of Fluid Mechanics*, vol. 176, pp. 67–93, 1987.
- [110] J. L. Sinclair and R. Jackson, "Gas-particle flow in a vertical pipe with particle-particle interactions," *AIChE Journal*, vol. 35, no. 9, pp. 1473–1486, 1989.
- [111] B. G. M. Van Wachem, J. C. Schouten, C. M. Van den Bleek, R. Krishna, and J. L. Sinclair, "Comparative analysis of CFD models of dense gas-solid systems," *AIChE Journal*, vol. 47, no. 5, pp. 1035–1051, 2001.
- [112] M. Syamlal, W. Rogers, and T. J. O'Brien, *MFIX Documentation: Theory Guide*. U.S. Department of Energy, Morgantown, WV, 1999.

- [113] J. Garside and M. R. Al-Dibouni, "Velocity-voidage relationships for fluidization and sedimentation in solid-liquid systems," *Industrial & Engineering Chemistry Process Design and Development*, vol. 16, no. 2, pp. 206–214, 1977.
- [114] C. Y. Wen and Y. H. Yu, "A generalized method for predicting the minimum fluidization velocity," *AIChE Journal*, vol. 12, no. 3, pp. 610–612, 1966.
- [115] S. Ergun, "Fluid flow through packed columns," *Chemical Engineering Progress*, vol. 48, pp. 89–94, 1952.
- [116] P. Rowe and G. Henwood, "Drag forces in hydraulic model of a fluidized bed — Part I," *Transactions of the Institution of Chemical Engineers*, vol. 39, no. 1, pp. 43–54, 1961.
- [117] L. Schiller and A. Naumann, "Über die grundlegende Berechnung bei der Schwerkraftaufbereitung," *Zeitschrift Verein Deutscher Ingenieure*, vol. 44, pp. 318–320, 1933.
- [118] J. H. Jeans, "The equations of radiative transfer of energy," *Monthly Notices of the Royal Astronomical Society*, vol. 78, no. 1, pp. 28–36, 1917.
- [119] R. E. Marshak, "Note on the spherical harmonic method as applied to the Milne problem for a sphere," *Physical Review*, vol. 71, no. 7, pp. 443–446, 1947.
- [120] M. N. Özışık, *Radiative Transfer and Interactions with Conduction and Convection*. Wiley, New York, 1973.
- [121] P. Zehner and E. U. Schlünder, "Wärmeleitfähigkeit von Schüttungen bei mässigen Temperaturen," *Chemie Ingenieur Technik*, vol. 42, no. 14, pp. 933–941, 1970.
- [122] W. E. Ranz and W. R. Marshall, "Evaporation from drops, part II," *Chemical Engineering Progress*, vol. 48, no. 4, pp. 173–180, 1952.

- [123] OpenCFD, *OpenFOAM — The Open Source CFD Toolbox — User Guide*. OpenCFD Ltd., United Kingdom, 2.3.0 ed., 2014.
- [124] R. Issa, “Solution of the implicitly discretised fluid flow equations by operator-splitting,” *Journal of Computational Physics*, vol. 62, no. 1, pp. 40–65, 1986.
- [125] F. M. White, *Viscous Fluid Flow*. New York: McGraw-Hill, 3rd ed., 2006.
- [126] F. Taghipour, N. Ellis, and C. Wong, “Experimental and computational study of gas solid fluidized bed hydrodynamics,” *Chemical Engineering Science*, vol. 60, no. 24, pp. 6857–6867, 2005.
- [127] ANSYS, Inc., Canonsburg, PA, *ANSYS FLUENT Theory Guide*, 2013.
- [128] N. Herzog, M. Schreiber, C. Egbers, and H. J. Krautz, “A comparative study of different CFD-codes for numerical simulation of gas-solid fluidized bed hydrodynamics,” *Computers & Chemical Engineering*, vol. 39, pp. 41–46, 2012.
- [129] B. Weigand, *Analytical Methods for Heat Transfer and Fluid Flow Problems*. Springer Berlin Heidelberg, 2004.
- [130] F. R. Villatoro, J. Pérez, F. Domínguez-Muñoz, and J. M. Cejudo-López, “Approximate analytical solution for the heat transfer in packed beds for solar thermal storage in building simulators,” in *Proceedings of the Eleventh International IBPSA Conference*, (Glasgow, Scotland), pp. 709–715, July 2009.
- [131] T. E. W. Schumann, “Heat transfer: A liquid flowing through a porous prism,” *Journal of the Franklin Institute*, vol. 208, no. 3, pp. 405–416, 1929.

- [132] K. Kamiuto, M. Iwamoto, and Y. Nagumo, "Combined conduction and correlated-radiation heat transfer in packed beds," *Journal of Thermophysics and Heat Transfer*, vol. 7, no. 3, pp. 496–501, 1993.
- [133] K. Kamiuto and M. Iwamoto, "Analytical and experimental study of combined conductive and radiative heat transfer through a layer of glass beads," *JSME International Journal*, vol. 31, pp. 537–544, aug 1988.
- [134] N. Xie, F. Battaglia, and S. Pannala, "Effects of using two- versus three-dimensional computational modeling of fluidized beds: Part I, hydrodynamics," *Powder Technology*, vol. 182, pp. 1–13, 2 2008.
- [135] A. J. Baldwin and J. E. R. Lovell-Smith, "The emissivity of stainless steel in dairy plant thermal design," *Journal of Food Engineering*, vol. 17, pp. 281–289, 1992.
- [136] B. Boissière, R. Ansart, M. Hemati, D. Gauthier, and G. Flamant, "Etude hydrodynamique d'un nouveau concept de récepteur solaire à suspension dense de particules," in *STP2012 – 7ème colloque Science et Technologie des Poudres*, (Toulouse, France), 4–6 July 2012.
- [137] W. Sutherland, "The viscosity of gases and molecular force," *The London, Edinburgh, and Dublin Philosophical Magazine and Journal of Science*, vol. 36, no. 223, pp. 507–531, 1893.
- [138] R. A. Svehla, "Estimated viscosities and thermal conductivities of gases at high temperatures," tech. rep., NASA, Lewis Research Center, Cleveland, Ohio, 1962.
- [139] B. E. Poling, J. M. Prausnitz, O. John Paul, and R. C. Reid, *The Properties of Gases and Liquids*. McGraw-Hill New York, 5th ed., 2001.
- [140] S. Zimmermann and F. Taghipour, "CFD modeling of the hydrodynamics and reaction kinetics of FCC fluidized-bed reactors," *Industrial*

- & Engineering Chemistry Research*, vol. 44, no. 26, pp. 9818–9827, 2005.
- [141] S. Pannala, M. Syamlal, and T. J. O’Brien, *Computational Gas-solids Flows and Reacting Systems: Theory, Methods and Practice*. IGI Global, 2011.
- [142] P. J. Davis, *Interpolation and Approximation*. Courier Dover Publications, 1975.
- [143] H. Benoit. private communication, 4 April 2014.
- [144] M. Horio and A. Nonaka, “A generalized bubble diameter correlation for gas-solid fluidized beds,” *AIChE Journal*, vol. 33, no. 11, pp. 1865–1872, 1987.
- [145] V. R. Patil, “A computational approach to investigate the bubble size distribution in a fluidized bed,” *Semester project*, ETH Zurich, 2014.
- [146] J. Marti, M. Roesle, and A. Steinfeld, “Combined experimental-numerical approach to determine radiation properties of particle suspensions,” in *ASME Proceedings – Heat Transfer in Energy Systems*, (Minneapolis, Minnesota, USA), July 14–19 2013.





# List of publications

## Journal articles

J. Marti, A. Haselbacher, and A. Steinfeld, “A numerical investigation of gas-particle suspensions as heat transfer media for high-temperature concentrated solar power,” *International Journal of Heat and Mass Transfer*, accepted, 2015

J. Marti, M. Roesle, and A. Steinfeld, “Combined experimental–numerical approach to determine radiation properties of particle suspensions,” *Journal of Heat Transfer*, vol. 136, no. 9, pp. 092701–092708, 2014

J. Marti, M. Roesle, and A. Steinfeld, “Experimental determination of the radiative properties of particle suspensions for high-temperature solar receiver applications,” *Heat Transfer Engineering*, vol. 35, no. 3, pp. 272–280, 2014

## Conference proceedings

J. Marti, M. Roesle, and A. Steinfeld, “Combined experimental–numerical approach to determine radiation properties of particle suspensions,” in *ASME Proceedings – Heat Transfer in Energy Systems*, (Minneapolis, Minnesota, USA), July 14–19 2013